Tire-Road Friction Coefficient Estimation and Control of Autonomous Vehicles

Juqi Hu

A Thesis

In the Department

of

Mechanical, Industrial & Aerospace Engineering

Presented in Partial Fulfillment of the Requirements

for the Degree of

Doctor of Philosophy (Mechanical Engineering) at

Concordia University

Montréal, Québec, Canada

May 2021

CONCORDIA UNIVERSITY

SCHOOL OF GRADUATE STUDIES

This is to certify that the thesis prepared

By: **Juqi Hu**

Entitled: **Tire-Road Friction Coefficient Estimation and Control of Autonomous Vehicles**

and submitted in partial fulfillment of the requirements for the degree of

Doctor of Philosophy (Mechanical Engineering)

complies with the regulations of this University and meets the accepted standards with respect to originality and quality.

Signed by the Final Examining Committee:

_____ Chair
Dr. Liangzhu Wang

_____ External Examiner
Dr. Yang Shi

_____ External to Program
Dr. Amir G. Aghdam

_____ Examiner
Dr. A. K. Waizuddin Ahmed

_____ Examiner
Dr. Ramin Sedaghati

_____ Co-Supervisor
Dr. Subhash Rakheja

_____ Co-Supervisor
Dr. Youmin Zhang

Approved by _____
Dr. Ivan Contreras Graduate Program Director

April 20, 2021
Date of Defense

_____
Dr. Mourad Debbabi Dean, Gina Cody School of Engineering and Computer Science

Abstract

Tire-Road Friction Coefficient Estimation and Control of Autonomous Vehicles

Juqi Hu, Ph.D.

Concordia University, 2021

This thesis aims to design and develop trajectory planning and tracking strategies integrating with the estimated tire-road friction coefficient (TRFC) so as to enhance the safety and reliability of the autonomous vehicles (AVs) under varying road friction conditions. A two-stage hierarchical framework is firstly developed for estimating TRFC in a computationally efficient manner considering vehicle's lateral dynamic responses to double (DLC) and single (SLC) lane-change maneuvers.

An alternate two-stage TRFC estimation framework is developed further on the basis of the longitudinal dynamics of the vehicle. A sequence of braking pressure pulses is designed in the first stage to identify desired minimal pulse pressure needed for reliable estimation of TRFC with minimal interference with the vehicle motion. In the second stage, a constrained unscented Kalman filter (CUKF) algorithm is subsequently proposed to identify the precise TRFC for achieving rapid convergence and enhanced estimation accuracy.

A trajectory planning scheme integrating the estimated TRFC is subsequently developed for path-change maneuvers considering both the maneuver safety and the occupant's comfort. For this purpose, a 7th-order polynomial function is constructed to ensure continuity up to the derivative of the acceleration (jerk). The friction-adaptive acceleration and speed-adaptive jerk limits are further defined and integrated in the framework to enhance occupant's comfort and acceptance. Both numerical simulation and Quanser self-driving car (QCar) experimental results have revealed

the effectiveness and practicability of the proposed lane change trajectory planning scheme.

An adaptive model predictive control (MPC) tracking scheme is proposed for tracking the desired lane-change path considering wide variations in vehicle speed and TRFC. With integrated consideration of output weights in the cost function together with constraints on the magnitude of the outputs, the proposed MPC scheme required only lateral position for tracking the planned path. An interesting way of integrating adaptive control gains with consideration of steering saturation by using the backstepping technique is also designed for low-speed AVs to enhance trajectory tracking, while respecting to the input boundaries. The effectiveness of the proposed tracking control scheme is verified experimentally using the QCar test platform.

Acknowledgments

I would like to express my deepest gratitude and appreciation to my two supervisors, Prof. Youmin Zhang and Prof. Subhash Rakheja, for their warm guidance, continuous support and encouragement during my Ph.D. study. Without their consistent support and great help as well as insightful guidance, I wouldn't have accomplished this research work. Their passion, meticulosity, diligence and wisdom always inspire me and these are the great gifts for me to take into my life.

I would also like to thank all my colleagues in my research group and collaborators who have helped me a lot during my Ph.D. study. It is my great pleasure to do research and share ideas with them and learn from them. My special thanks go to Hejia Gao, Qianbo Sun, Xia Wu and Xiaobin Zhou, for their accompany through the hardest and happiest time.

Last but not least, I would like to thank my parents and elder sister for their love, understanding, consistent support, and countless sacrifices, which have played an indispensable role in my life. It can never be enough for me to thank them.

Table of Contents

List of Figures

List of Tables

Nomenclature

α_f	Front tire side-slip angle
α_i	Tire side-slip angle
α_r	Rear tire side-slip angle
δ_f	Front tires' steer angle
$\dot{\psi}$	Vehicle's yaw rate
$\hat{\mu}_f$	Estimated tire-road friction coefficient at front tires
$\hat{\mu}_r$	Estimated tire-road friction coefficient at rear tires
$\hat{F}_{xi}$	Estimated individual longitudinal tire force
$\hat{F}_{xr\bullet,l}$	Estimated longitudinal force of rear tires under large braking pulse torque
$\hat{F}_{xr\bullet,s}$	Estimated longitudinal force of rear tires under small constant braking torque
$\hat{F}_{yf}$	Estimated cornering tire force of front-axle
$\hat{F}_{yr}$	Estimated cornering tire force of rear-axle
$\hat{v}_x$	Filtered wheel speed
$\hat{v}_y$	Estimated vehicle lateral velocity
κ_i	Tire longitudinal slip ratio

$\kappa_{r\bullet,s}$ Computed longitudinal slip ratio of rear tires under large braking pulse torque

$\kappa_{r\bullet,s}$ Computed longitudinal slip ratio of rear tires under small constant braking torque

μ_i Individual tire-road friction coefficient

$\mu_{r\bullet}$ Tire-road friction coefficient of rear tires

ω_i Wheel rotation angular speed

ω_{rl} Angular speed of rear-left wheel

ω_{rr} Angular speed of rear-right wheel

ψ Vehicle's yaw angle

ρ_i Positive gain in braking force estimator

ρ_{air} Mass density of air

$\tilde{t}_{slc}$ Lane change duration used for steering prediction

A_f Frontal area of the vehicle

a_P^m Maximum deceleration of the preceding vehicle

a_x Vehicle longitudinal acceleration/deceleration

a_y Vehicle lateral acceleration

a_{xmax} Maximum longitudinal acceleration of host vehicle

a_{ymax} Maximum lateral acceleration of host vehicle

C_d Aerodynamic drag coefficient

C_{xi} Individual tire longitudinal stiffness

$C_{xr\bullet}$ Longitudinal stiffness of rear tires

C_{yf} Cornering stiffness of front-axle

C_{yi} Individual tire cornering stiffness

C_{yr} Cornering stiffness of rear-axle

d_0 Initial longitudinal distance between host vehicle and preceding vehicle

d_0^* Vehicle standstill distance

d_c Longitudinal distance between host and preceding vehicle when crossing the lane boundary

d_s Longitudinal distance between host and preceding vehicle's center of gravity at lane change starting point

d_{th} Minimum threshold of d_s

f_r Rolling resistance coefficient

F_{ri} Individual tire rolling resistance force

F_{xf} Longitudinal tire force of front-axle

F_{xi} Individual longitudinal tire force

F_{xr} Longitudinal tire force of rear-axle

F_{yf} Cornering tire force of front-axle

F_{yi} Individual lateral tire force

F_{yr} Cornering tire force of rear-axle

F_{zf} Normal tire force of front-axle

F_{zi} Individual normal tire force

F_{zr} Normal tire force of rear-axle

g Gravity acceleration

h_0 Vehicle headway time

H_c Control horizon

h_c Height of the vehicle's center of gravity

H_p Predictive horizon

I_z Vehicle's yaw moment of inertia

I_ω Moment of inertia of an individual wheel

j_{ymax} Maximum lateral jerk of host vehicle

k Time step index

K_{Bi} Individual wheel brake force gain

l Vehicle's wheel base

l_f Distance from the center of gravity to the front-axle

l_r Distance from the center of gravity to the rear-axle

l_v Host vehicle's geometric length

L_x Longitudinal distance between lane change starting and ending point

m Vehicle total mass

n_{th} Normalized throttle position

p_p^* Threshold pressure leading to triggering of the anti-lock braking system (ABS)

p_s Magnitude of the braking pressure pulse in the second stage

p_i Individual wheel hydraulic fluid pressure

p_{mc} Master cylinder brake pressure

p_{pi} Magnitude of the ith braking pressure pulse in the first stage

R_e Tire effective radius

T Width of the vehicle

T_s Sampling interval

$T_{b\bullet,l}$ Large braking pulse torque

$T_{b\bullet,s}$ Small constant braking torque

T_{bi} Individual wheel braking torque

$T_{d\bullet,l}$ Driving torque of front tires when applying large braking pulse torque to rear tires

$T_{d\bullet,s}$ Driving torque of front tires when applying small constant braking torque to rear tires

T_{di} Individual wheel driving torque

t_{slc} Single-lane change duration of host vehicle

t_{stop} Time required to stop the preceding vehicle at its maximum deceleration

v_H Forward speed of host vehicle

v_H^* Host vehicle's forward speed in km/h

v_P Forward speed of preceding vehicle

v_x Vehicle longitudinal velocity

v_y Vehicle lateral velocity

v_{lim} Vehicle speed limit on highway (km/h)

v_{th} Vehicle threshold speed on highway (km/h)

v_x^m Mean velocity of the rear wheels

v_{ymax} Maximum lateral velocity of host vehicle

X_s Longitudinal position of host vehicle where the lane change maneuver starts

Acronyms

ABS	Anti-lock braking system
ACC	Adaptive cruise control
AVs	Autonomous vehicles
CG	Center of gravity
CUKF	Constrained unscented Kalman filter
DEKF	Dual extended Kalman filter
DGPS	Differential global positioning system
DLC	Double-lane change
DOF	Degrees-of-freedom
EKF	Extended Kalman filter
GNC	Guidance, navigation and control
GPS	Global positioning system
INS	Inertia navigation system
KF	Kalman filter
LPs	Lattice planners
LQR	Linear quadratic regulator
MF	Magic formula
MPC	Model predictive control
MSE	Mean squared error
NN	Neural network

PID	Proportional-integral-derivative
PSO	Particle swarm optimization
QCar	Quanser self-driving car
QP	Quadratic programming
RLS	Recursive least squares
RRTs	Rapidly-exploring random trees
SLAM	Simultaneous localization and mapping
SLC	Single-lane change
SMC	Sliding mode control
TCS	Traction control system
TRFC	Tire-road friction coefficient
UKF	Unscented Kalman filter
V2VC	Vehicle-to-vehicle communication

Chapter 1

Introduction and Literature Review

1.1 Introduction

Autonomous vehicles (AVs) refer to vehicles whose operations and actuations are partially or fully controlled by on-board processors [1]. AVs have attracted considerable research and development efforts due to their multi-faceted advantages such as enhanced road safety, efficient traffic flow, reduced fuel consumption and emission [2–4]. The significant advances in sensing, computing and artificial intelligence technologies, particularly during the last two decades, have further inspired the society's expectation and passion for the commercially viable AVs [4]. Automotive industry is making notable advances for launching fully-autonomous vehicles within the current decade [5–7].

The operation of an AV is generally categorized in three stages, commonly described by the *sense*, *plan* and *act* (SPA) cycle. Three corresponding subsystems, **guidance, navigation and control (GNC)**, constitute the general architecture of the entire AV system (as shown in Figure 1.1), which are briefly described below [8–11]:

- **Guidance subsystem**, also referred to as the path planning, concerns with determination of the AVs' desired path from its current location to a designated target in accordance with the traffic rules, safety, comfortability and vehicular dynamics. Path planning for on-road

AVs is generally divided into two hierarchical classes as global planning and local planning. Global planning or route planning defines an optimal route or trip (normally represented by a sequence of waypoints) between two geographical locations based on the environment information (map) and some other criterion such as shortest distance, minimum travel time or other pre-defined constraints. Local planning, on the other hand, determines vehicle's behavior more tactically and locally in response to environmental conditions and driving scenarios. Path searching, maneuver planning and trajectory planning (often combined as one) make up the local planning system. After the waypoints that the vehicle should follow are generated from global planning, the local planning concentrates on finding the best trajectory for the vehicle to follow while taking into account the constraints of the vehicle's motion and the traffic environment including both static and dynamic obstacles.

- **Navigation subsystem** is responsible for determination of the AVs' current states including location, velocity as well as heading direction. The operation of an AV requires the knowledge of its instantaneous position and direction with respect to a global coordinate system, in addition to a series of positions ahead in order to reach the destination. Global positioning system (GPS) or differential global positioning system (DGPS) together with inertia navigation system (INS) have been widely used in vehicle localization. The fusing of the data from the environment perception module together with the vehicle states is used to locate and track the static/dynamic obstacles and the lanes [12, 13]. Furthermore, an available global map could contain lane geometric information, lane markings, stop signs, parking lots, check points and provide global environment information. When the AVs travel in an unknown environment, dual tasks of localizing the vehicle and modeling the environment should be handled simultaneously, which is known as simultaneous localization and mapping (SLAM) [12, 14].

- **Control subsystem** is designed to generate the appropriate control commands necessary to track the trajectory generated by the guidance subsystem, while ensuring vehicle stability.

The smoothened command inputs are computed for the low-level actuators including throttle, brake pedal and steering wheel. Vehicle motion control can be broadly divided into longitudinal and lateral path control. The longitudinal control is related to distance-velocity control between vehicles to ensure occupant's safety and comfort, while the lateral control is designed to minimize the lane deviations. It should be noted that the longitudinal and lateral dynamics of a vehicle are coupled in a combined lateral and longitudinal control, where the degree of coupling is a function of the tire and vehicle parameters in addition to the available road friction.

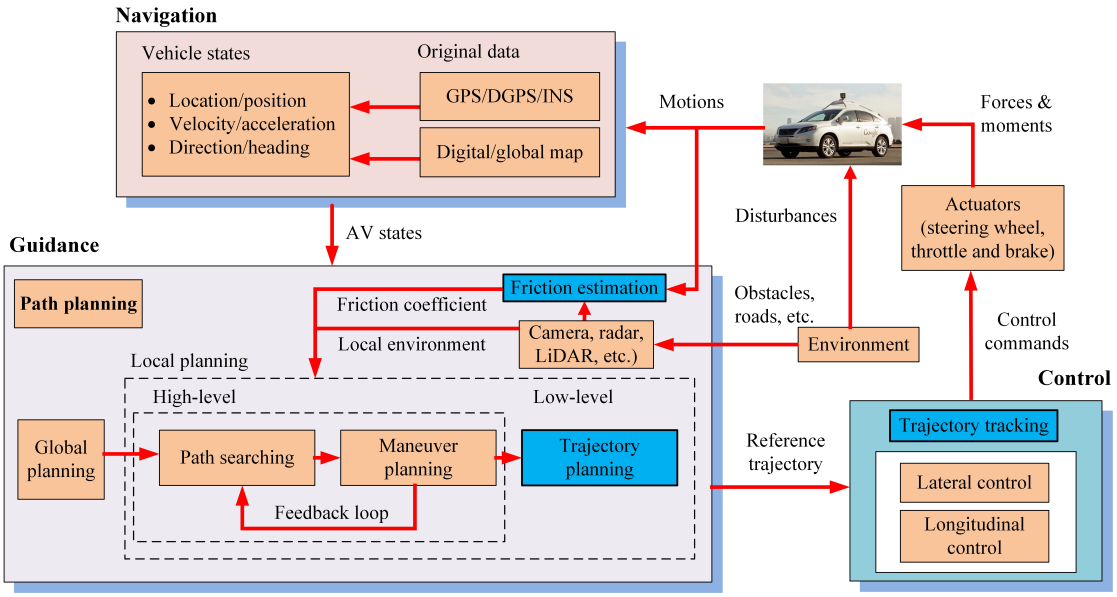

Figure 1.1: The general architecture of guidance, navigation and control (GNC) system for on-road autonomous vehicles (AVs).

It is worth mentioning that global perception system (localization in the navigation subsystem) alone is not sufficient to enable AVs routing to its destination due to potential variations in the environment related factors. Local environment perception via real-time sensing is thus also required. This module is responsible for sensing the environment structures in a multi-sensor manner that enables a model of surrounding environment for the AVs. The original data collected by various sensors like vision, radar, light detection and ranging (LiDAR) sensor, are processed to obtain information about the surrounding environment features (road/object's color, shape, edges, etc.),

traffic objects (both moving and static obstacles/vehicles, pedestrians, etc.), traffic situations (traffic density, traffic signs, intersections, lane markings, etc.). The local dynamic driving environment is constructed on the basis of these on-board sensors [12, p. 3-9].

Highly- or fully-autonomous vehicles are controlled agents integrating environment perception and modeling, localization and map building, path planning and decision-making, and motion control. Despite the significant advances in sensing technologies, signal processing, control system design and computational power, the operation of a fully-autonomous vehicle in both structured and unstructured environment continues to be the long-term goal [14, p. 8]. The development of such an autonomy in turn demands the syntheses of more effective and reliable GNC technologies. These include the reliable situation awareness and risk assessment methods, fast algorithms for generating safe and comfortable paths/trajectories, effective methods for accurate state estimations, and robust controllers designed for accurate path tracking. Furthermore, variations in the road friction add to the complexities for the GNC system since the vehicle motion is directly related to the tire-road adhesion limits. Since the motion of a road vehicle is directly related to the available road friction, a knowledge of the friction is vital for effective path planning and controller's designs. The reported GNC architectures for AVs generally ignore the road friction, which is likely due to complexities associated with its real-time estimation. Besides these issues, wide applications of AVs generally encompass emerging issues with regard to implementations, such as liability, legislation, infrastructure and security [1, 6, 15].

This thesis research is focused on development of trajectory planning and tracking strategies for AVs integrating the available tire-road friction coefficient (TRFC) so as to enhance the vehicle performance towards fully-autonomous driving of AVs under varying road friction conditions. Computationally efficient TRFC estimation strategies are proposed so as to minimize disturbance to the vehicle motion during the identification process. An adaptive trajectory planning scheme under a typical lane change maneuver is subsequently developed to illustrate significance of the TRFC in the trajectory planning algorithm. Using the model predictive control (MPC) and the

estimated TRFC, a path planning and tracking framework is also developed for lane-change maneuvers at different speeds. Considering input constraints, an adaptive trajectory tracking control algorithm based on the backstepping technique is finally designed for low-speed AVs. The effectiveness of the proposed control scheme is also assessed through experiments conducted by using the latest Quanser self-driving car (QCar) test platform.

1.2 Review of Relevant Literature

Guidance, navigation and control (GNC) of autonomous vehicles encompass multiple technical challenges involving trajectory planning, vehicle localization, vehicle state and parameter estimation, and controllers' synthesis for effective trajectory tracking. The real-time estimation of TRFC constitutes an additional challenge though it can not only greatly simplify the path planning and tracking control tasks but also enhance the vehicle performance towards full-autonomy of AVs. The studies reporting TRFC estimation, path planning and trajectory tracking methods have been thoroughly reviewed to build essential background on the reported methods and to formulate the scope of the thesis research. The reported studies on each aspect are briefly discussed in the following subsections, while more thorough reviews of the relevant studies have been presented in the published/submitted manuscripts presented in Chapters 2 to 6.

1.2.1 TRFC: Significance and Real-Time Estimation

As an integral component of the on-road AVs, tires represent the only contact with the ground surface. The vehicle motion on a road is mostly governed by the forces generated by the tires at the tire-ground interface, which in-turn are primarily determined by the TRFC defined as [16]:

$$\mu_i = \max\left(\frac{\sqrt{F_{xi}^2 + F_{yi}^2}}{F_{zi}}\right) \tag{1–1}$$

where F_{xi}, F_{yi} and F_{zi} are the longitudinal, lateral and normal forces, respectively, developed by tire i $(i = 1, ..., n)$ of a vehicle, and μ_i is the tire-road friction coefficient reflecting the maximum force the tire can provide. Although a prior knowledge of the TRFC can facilitate the designs of effective vehicle control and safety systems [17], the role of TRFC has been mostly ignored in the current GNC architectures. This is likely due to challenges associated with real-time estimation of the TRFC and wide variations in the TRFC. Advanced control systems including adaptive cruise control (ACC), anti-lock braking system (ABS), traction control system (TCS), and collision warning or collision avoidance system, could yield enhanced performances with the knowledge of the available TRFC [17–20]. For instance, an ABS can be designed more effectively rather than conservatively to provide improved vehicle deceleration, handling performance and stability control during braking through maximum utilization of the available TRFC [21]. Moreover, the variations in TRFC directly relate to the vehicle dynamic limits (e.g., maximum longitudinal or lateral acceleration, safe forward speed) [11]. The knowledge of TRFC in the path planning stage is thus vital for realizing more intelligent and safer driving performance through designing adaptive control strategies that enable the utilization of the maximum available tire-road adhesion.

Considerable efforts have been made in the recent decades to obtain reliable on-line estimation of available TRFC considering widely different operating conditions and longitudinal or lateral dynamics of the vehicle (e.g., [16,22–24]). The direct measurement of TRFC involves considerable complexities and high cost of sensors. Significant efforts have thus been devoted for estimating TRFC via indirect methods based on the measurable states of the vehicle.

The reported TRFC estimation methods may be grouped as either qualitative or quantitative approaches. Although both methods have been developed with a common objective of estimating the TRFC, the outcomes of the two approaches differ from each other. The qualitative methods generally provide an indication of the adhesion quality and classify the road surface by its condition in a crude manner using sensors such as optical instruments, voice recorder and three-axis accelerometers [25–27]. Apart from the lack of accurate quantitative information of TRFC, these methods invariably neglect contributions due to many important design and operating factors including the

tire type, tire inflation pressure and wear condition [17,28]. In addition, the friction prediction performance of the measured sensors can be severely affected by the external disturbances like dust, vibration and noise. A few studies have focused on identification of tire slip-slope, relating the tire slip ratio and the longitudinal tire force for identifying peak tire-road adhesion [29–31]. The linear force-slip relationship, however, is considered only valid in the low-slip region. Moreover, a road adhesion indicator based on the slip-slope alone cannot be considered reliable when variations in the road friction are encountered.

The quantitative methods generally estimate the TRFC based on tire response measures such as slip ratio and side-slip angle. A few studies have used advanced sensors embedded in the tires to identify the TRFC. These included wireless piezoelectric sensors [32], six-degrees-of-freedom inertial sensors [33] and wheel load sensors [34]. Apart from the high costs and unproven reliability, such methods may involve complex signal processing. Alternatively, a large number of studies have focused on designing algorithms for indirect TRFC estimation from the measured or predicted vehicle states. Such quantitative methods can yield more accurate estimation of the TRFC, although these methods may involve relatively higher levels of tire excitations. Compared to the qualitative methods, most of the quantitative methods may thus lead to notable disturbances in the driving condition. These methods generally obtain TRFC estimation in two stages. Unknown vehicle states and tire forces/torques are estimated in the first stage on the basis of measurable or known longitudinal and/or lateral vehicle dynamic responses. These estimated variables are subsequently employed in a parameter identification problem to obtain an estimate of the TRFC [35,36]. Hu et al. [37] employed a hierarchical linear quadratic regulator (LQR) control methodology to obtain tire forces. The same estimator was also used to estimate TRFC considering the longitudinal and lateral forces. A data fusion method was further proposed to reduce TRFC estimation error. Wang et al. [24] proposed a sequential tire cornering stiffness and TRFC estimation method with minimal interference with the desired vehicle motion and trajectory. The study employed a robust observer based on wheel rotational dynamics in a simplified form for obtaining tire longitudinal forces,

which were subsequently used to estimate lateral tire forces. Ahn et al. [17] proposed an adaptive non-linear observer for simultaneous estimations of tire side-slip angle and TRFC based on tire lateral force and aligning moment. Both the simulation and experimental results demonstrated the effectiveness of the proposed method. Shao et al. [38] identified TRFC from the combined estimation of front-axle lateral force and alignment torque, while ensuring both the stability and robustness.

Considering that the road adhesion varies only slowly, the TRFC can be considered as a system parameter or state that is hidden within the tire model [17, 39]. The powerful Kalman filter (KF) technique and its non-linear extensions, such as the extended Kalman filter (EKF) and the unscented Kalman filter (UKF), have been widely used for effective estimations of vehicle states [35, 40]. Although the forces developed by a tire are known to be strongly nonlinear functions of the slip ratio, side-slip angle and normal load, the TRFC can also be estimated using linear system parameter identification methods by linearizing the non-linear tire model. Zhao et al. [21] proposed a robust TRFC estimation method via triggering of the ABS, where individual longitudinal tire forces and axles' lateral forces were observed via the KF, followed by TRFC estimation using the recursive least squares (RLS) method. Choi et al. [41] observed the tire forces in a similar manner and used the RLS technique with adaptive multiple forgetting factors to estimate TRFC and the tire stiffness. Qi et al. [42] obtained estimates of maximum friction coefficient as well as tire longitudinal and lateral slip slopes using two EKFs together with a novel tire model. Zong et al. [39] employed the dual extended Kalman filter (DEKF) technique with a three-degrees-of-freedom (DOF) vehicle model to estimate vehicle states (yaw rate, side-slip angle and roll rate) and the TRFC. UKF, which is based on the unscented transform theory, has also been applied for estimating TRFC. In [23], two UKF-based estimators communicated simultaneously to estimate both the vehicle states and the TRFC. An integrated road friction estimator was further designed considering different excitation levels to enhance implementation of the approach. Considering the TRFC as a state in the non-linear tire model, Chen et al. [43] employed UKF technique for estimating TRFC from the longitudinal and lateral dynamics. The estimated information was subsequently

fused using mean squared error (MSE) minimization technique to ensure a higher accuracy of the TRFC estimation.

The vast majority of the aforementioned studies have shown that an accurate estimation of TRFC necessitates relatively higher magnitude of the disturbance in terms of longitudinal slip ratio or side-slip angle. The previous studies have thus employed maneuvers leading to high magnitudes of braking/deceleration [22,44] or lateral acceleration [39,45]. A few studies have even considered sinusoidal steering inputs or severe double-lane change (DLC) and slalom-type maneuvers for realizing higher lateral acceleration of the vehicle [41, 46]. Such maneuvers cause considerable interference with the vehicle motion and would be perceived annoying, unsafe and impractical in real driving situations. It is thus desirable to obtain estimations of TRFC under more practical driving circumstance or adequate excitations while minimizing the interference with the vehicle motion.

1.2.2 Trajectory Planning of AVs

Trajectory planning, also referred to as trajectory generation, is an integral module and a key enabler for autonomous driving [47]. This module is concerned with generating a trajectory that satisfies the safety requirements and motion model or state constraints, while ensuring occupant's comfort at the same time. Motivated by the increasing interests in autonomous driving, considerable developments in trajectory planning algorithms have been reported for the AVs. The reported trajectory planning algorithms can be grouped in three broad categories on the basis of the methodology used, namely, the search-based methods, the geometric methods and the optimal control methods. Owing to the limited detection range of the on-board sensors and the processors' memory, incremental approaches are generally employed in the reported search-based methods. These approaches refer to the searching algorithms, where search configurations or states are not fully specified in advance. Rapidly-exploring random trees (RRTs) and lattice planners (LPs) are the two primary techniques used in the incremental approaches [10]. With quick exploration of the tree space, RRTs [48] and their variants including closed-loop RRT [49] and RRT* [50] have been

implemented for AVs during the last two decades. While the RRTs family is specifically designed to handle vehicle nonholonomic constraints (including dynamics) and high degrees-of-freedom (DOF), their main drawbacks lie in the jerky paths and computational complexity [10, 48]. In contrast, the LP techniques require relatively lower computational power, and are generally considered appropriate for dynamic environments. A few studies have shown that evasive type of maneuvers cannot be performed efficiently using the LP techniques [10, 51–53]. Another issue related to the incremental approaches is that the collision checking functions are needed for safety since the planning horizon is claimed to be relatively large [10].

When considering the highly constrained driving scenarios, in particular the autonomous lane change maneuvers on the highways, the complexity of the trajectory planning can be largely reduced. The search-based methods may not be advisable for use in highway environment since they can become highly inefficient in time-critical situations [54].

The geometric methods generally solve the trajectory planning problem by selecting a geometric curve to ensure smoothened target path. The quintic polynomial was firstly introduced in [55] to realize a continuous-curvature transition between the parallel lanes of travel. The proposed function required only the initial and the ending point of the maneuver to define the planned trajectory. The proposed polynomial curve has also been employed to describe the desired lateral position of the vehicle's center of gravity (CG) under high-speed lane change maneuvers [56]. Vehicle trajectory planning using polynomial curvature spirals, which exhibit intuitive parametric representation of trajectories and computational efficiency, can be found in [52, 57]. With combined consideration of maximum admissible curvature and velocity profile, Kahya and Schmidt [58] designed lane change trajectories based on bi-elementary paths, which were composed of a sequence of clothoid curves. Although the smooth transition between different segments of a roadway was guaranteed, numerical calculation of Fresnel integration to determine the clothoids imposes considerable computational demand. Alternatively, Cubic Bezier curves have been employed as the path generator to achieve feasible paths for AVs in dynamic on-road directional maneuvers [59]. Similarly, the reference trajectory of a single-lane change (SLC) maneuver was proposed based on two symmetrical

Bezier curves which were optionally supplemented with a straight-line segment [60]. It should be noted that the performance of the Bezier curves largely depends on the position and the number of the control points. Some studies have also derived the reference lane change trajectory from a desired lateral acceleration profile. Guo et al. [61] employed a trapezoidal acceleration profile for planning a lane change trajectory on a curved road. By assuming the reference acceleration as a 3rd-order polynomial function of time, Feng et al. [62] derived a lane change trajectory that could satisfy the defined acceleration and the jerk constraints. In another study, an optimal lane change trajectory consisting of two symmetrical circular arcs was proposed to achieve a trade-off between the computational efficiency and the occupant's comfort [63]. The cubic spline interpolation was introduced to achieve improvements in computational efficiency while generating the optimal trajectories for typical highway maneuvers such as merging, overtaking and lane changes [64].

The desired trajectory for lane change maneuver can also be generated using optimal control methods that involve minimization of a performance index under a set of constraints (e.g., velocity, acceleration and jerk limits, road friction, duration, change in kinetic energy). The optimal control methods, invariably, utilize the geometric methods for trajectory planning. A safe and comfortable lane change trajectory was designed using the quadratic programming (QP) optimization algorithm in [65]. The time-variant safety margins were further designed for trajectory correction in a dynamic traffic situation. Wei et al. [66] proposed a two-stage approach for planning a lane-change trajectory. A series of candidate paths was initially generated using the quintic polynomial function. The best trajectory with designated velocity profile was subsequently obtained through a nonlinear programming optimization model considering the limiting constraints of the acceleration, jerk and the lane change duration. Realizing the advantages of vehicle-to-vehicle communication (V2VC) in achieving more accurate path and environmental information than that from the on-board sensors alone, Bai et al. [67] used quintic polynomial curves to establish an accelerated lane changing trajectory. The study employed a composite cost function considering deceleration coordination, jerk and lane change duration. Luo et al. [68] proposed an automated

lane change generator based on V2VC considering the potential collision situations. The constrained optimization problem was formulated and sloved considering different safety distances. A number of studies have also employed MPC methods for trajectory planning in the presence of constraints and system nonlinearities [10, 11]. Cesari et al. developed lane change trajectories using the Scenario MPC considering the uncertainty in the environment, safety and occupant's comfort [69]. Considering a lane change maneuver as primarily a longitudinal planning problem, Nilsson et al. [70] converted the lane change trajectory planning problem to loosely coupled longitudinal and lateral MPC problems, which could be efficiently solved in form of low-complexity quadratic programs. The best collision-free path representing by cubic spirals was generated by a unified MPC local trajectory planning and control framework for the autonomous ground vehicle driving along a roughly predefined path in [71]. Although the optimal control methods can yield effective path planning for AVs considering the constraints and system nonlinearities, the solutions of the optimization problem generally impose high computational demand, especially in the presence of nonlinear vehicle dynamics, time-varying states and input constraints.

Although the bounds of vehicle motion and safety are directly related to the available TRFC, the reported path planning strategies either neglect the influence of the varying TRFC or assume constant level of road friction condition. The path planning with the knowledge of available TRFC can ensure greater robustness of the AVs under varying road conditions. Consideration of the road adhesion limit in the trajectory planning can further ensure the physical feasibility of the generated trajectory with reliable safety margin, in addition to the already achieved objectives relevant to occupant's comfort and continuous curvature in the reported studies. The knowledge of TRFC can also simplify the design of trajectory tracking controllers, and help achieve the realization of more human-like or even personalized driving style of the AVs.

1.2.3 Trajectory Tracking of AVs

The AVs' driving tasks involve a tracking control system for tracking the reference or planned trajectory. The main purpose of the trajectory tracking control module is to minimize the position

and orientation errors between the vehicle's actual path and the defined trajectory, and to smoothen the motions while maintaining vehicle stability [72]. A wide range of tracking control algorithms have evolved during the past two decades as a part of the driver assistance technologies. Amer et al. [73] proposed two feedback proportional-integral-derivative (PID) controllers for the steering control of an armoured vehicle to follow a pre-defined trajectory using a 7-DOF directional dynamic model of the vehicle. Optimal control algorithms based on LQR have been widely reported for vehicle path tracking by regulating the yaw moment and corrective steering angle. The parameters of the LQR controller were optimized using particle swarm optimization (PSO) for various dynamic conditions [74]. A robust H_∞ static output-feedback controller was designed based on the mixed genetic algorithm/linear matrix inequality approach for path following without the lateral velocity measurements in [75]. The study considered the roles of uncertainties in vehicle parameters and vehicle states in addition to the external disturbances.

Elbanhawi et al. [76] combined receding horizon strategy with pure pursuit control to improve path tracking performance at high speeds. Further efforts, however, are desirable with regard to the performances under steering angle saturation, control signal limitations, and cross track errors. Based on both the kinematic and dynamic models, the backstepping control algorithm was used to design a robust full-speed range path following system in the presence of the side-slip angle [77]. Wilson and Robinett [78] developed a robust adaptive backstepping control system for mobile robots to compensate for external disturbance caused by the change in ground friction. Both the kinematic and dynamic effects were considered, and the control input were bounded within the maximum value. Setlur et al. [79] designed a Lyapunov-based controller considering the steering system, vehicle chassis and tire-road interface dynamics that ensured globally uniformly ultimately bounded tracking for ground vehicles. The controller design, however, was based on unconstrained control inputs. Hiraoka et al. [80] applied the sliding mode control (SMC) theory to design an automatic path tracking controller for a four-wheel steering vehicle, with the advantage of decoupling the front-and-rear-wheel steering. Hajjaji et al. [81] proposed the design of a stabilizing fuzzy controller for path following using a nonlinear dynamic model. Lyapunov's

method combined with a linear matrix inequality approach was used to analyze the stability of the nonlinear system. Gu and Hu [82] proposed a neural predictive control approach to realize path tracking of a robot car. The method incorporated neural network to model non-linear kinematics of the robot car. Kapania et al. [83] applied a quadratically optimal iterative learning controller to an autonomous race vehicle for multiple-lap path tracking of highly dynamic trajectories. Cheein et al. [84] introduced an algebraic damped controller, whose performance was better than pure pursuit and mixed controllers [85] in various simulations and field experiments. However, the controller showed oscillations when the velocity was fixed for lateral control purposes.

Among the various path tracking control methods, the MPC technique is considered meritorious to address the AVs' trajectory tracking control problem since it can adequately incorporate various constraints in a systematic manner. The MPC approach involves minimization of a performance index subject to various operational constraints with respect to a sequence of control inputs to track a given trajectory by applying the first element of such optimal input sequence to the vehicle system [11,86]. The reported studies have mostly focused on two common approaches. Some studies recognized strong coupling between the path planning and tracking control of AVs, and thus proposed the designs of integrated control module with the path planner. For instance, Jalalmaab et al. [87] investigated a road-adaptive MPC strategy to track the centerline of the lane while avoiding the obstacle. Although path planning and tracking were realized within one linear MPC framework, the vehicle model was limited to only a kinematic point-mass to facilitate real-time implementation. Gao et al. [86] developed a nonlinear MPC using a four-wheel vehicle model together with the Magic formula (MF) tire model considering the tire force saturation and the vehicle nonlinearities. The experimental results revealed rapid increase in the computation time with increasing speed. The proposed controller design thus posed real-time implementation challenge when the vehicle speed exceeded 40 km/h.

Owing to the high computational demand associated with complex optimization process of the integrated path planning and tracking control, other studies have addressed the path planning and tracking problem separately in a hierarchical architecture. As part of the PRORETA

3 project, Bauer et al. [88] utilized a potential field-based trajectory planner to calculate the optimal vehicle trajectory, which was then fed into the control layer to achieve collision avoidance in critical traffic situations. In [89], the collision-free path for AVs was generated based on a three-dimensional potential field method considering road boundary conditions and vehicle's kinematic model. The steering angle command to track the generated path was subsequently obtained from a multi-constrained MPC framework. Similarly, Schim et al. [90] designed a collision avoidance system which determined a collision-free trajectory based on sixth-order polynomials. The front steering and individual wheel torques were controlled by a MPC scheme to track the reference path. Owing to the nonlinearities of the vehicle model, the studies reporting MPC have generally employed computationally efficient linearization techniques (e.g., [91]). Apart from the high computational demand, the performance of the MPC is known to be influenced by the structure of the cost function and the weights imposed on the outputs and inputs, although such issues have been reported in relatively fewer studies.

The studies reporting tracking control using a hierarchical architecture introduce TRFC to the trajectory tracking module as an input and/or a state constraint (e.g. [86, 89, 91]). The controller designs may not thus yield its best performance under widely different road adhesion limits. Moreover, the tracking control performance is strongly related to the quality or smoothness of the reference trajectory. Consideration of the TRFC during the planning process can greatly enhance the quality of the reference trajectory and thereby the tracking control performance. The TRFC based trajectory can also simplify the design of the low-level tracking controller with improved computational efficiency, which is of critical concern for AVs.

1.3 Scope and Objectives of the Thesis Research

From the review of the reported studies, it is evident that the developments in the GNC modules for AVs lack consideration of potential variations in the tire-road friction, which directly relates to performance limits of the vehicle and the controller. The primary scope of this thesis research

is thus to develop trajectory planning and tracking strategies with practical applications to AVs by integrating with the estimated TRFC so as to enhance the performances of the AVs under varying road friction conditions. The term 'practical' in this context denotes the developments in the planning and tracking methods incorporating the friction information from the TRFC estimation strategies that impose minimal interference with the vehicle motion. Specific objectives of the thesis research are summarized below:

(1) Develop a computationally efficient and robust hierarchical TRFC estimation framework using the on-board sensors, and the EKF as well as the UKF techniques, while ensuring the estimation accuracy.

(2) Design excitations for the TRFC estimation module in the form of short duration braking pressure pulses so as to reduce the magnitude of disturbance to the vehicle motion.

(3) Develop a constrained unscented Kalman filter (CUKF) framework to achieve rapid convergence and improved accuracy of the TRFC estimation.

(4) Design TRFC-adaptive acceleration and speed-adaptive jerk limits for high quality trajectory planning with applications to the AVs, while ensuring occupant's comfort.

(5) Develop a computationally efficient and flexible trajectory planning scheme considering broad ranges of TRFC and vehicle speed.

(6) Develop a path planning and tracking framework using the model predictive control (MPC) and the estimated TRFC, and evaluate its performance for path-change maneuvers at different forward speeds.

(7) Develop an adaptive trajectory tracking control scheme for low-speed AVs based on the backstepping technique, while considering the input constraints. Validate this tracking scheme through experiments using a scaled model QCar platform.

1.4 Thesis Layout

This thesis is prepared according to the manuscript-based format described in the "Thesis Preparation, Examination and Regulations" guidelines of the School of Graduate Studies, Concordia University. The thesis research is organized into 7 chapters, which address the research objectives mentioned above, including the introduction and literature review chapter (Chapter 1). Chapters 2 and 3 present TRFC estimation methods based on lateral and longitudinal dynamics of the vehicle, respectively. Chapter 4 describes an efficient trajectory planning scheme for lane change maneuvers considering wide range of speed and road friction in addition to vehicle safety and occupant's comfort. Chapter 5 demonstrates an MPC-based adaptive trajectory tracking method for typical lane chagne maneuvers by making use of the TRFC and vehicle speed. Chapter 6 presents an adaptive trajectory tracking control framework integrating adaptive control gains with consideration of steering saturation by using the backstepping technique, together with laboratory experiments performed with the QCar self-driving platform. The major contributions and conclusions of the thesis research are summarized in Chapter 7 together with recommendations for future studies.

Chapter 2 presents the following article:

- Juqi Hu, Subhash Rakheja and Youmin Zhang, "Real-time estimation of tire-road friction coefficient based on lateral vehicle dynamics," *Proceedings of the Institution of Mechanical Engineers, Part D: Journal of Automobile Engineering*, vol. 234, no. 10-11, pp. 2444-2457, 2020. (DOI: 10.1177/0954407020929233)

This study proposed a two-stage framework for real-time estimation of TRFC of a vehicle on the basis of lateral dynamics of the vehicle. The estimation framework employs a new cascade structure consisting of an EKF and two UKFs to reduce the computational burden. In the first stage, EKF is utilized to estimate lateral velocity of the vehicle and thereby both the front and rear tires' side-slip angles. In the second stage, a two–UKFs sub-framework is formulated in sequence to observe both the front- and rear-axle tire forces, and to subsequently identify their respective

TRFC, regarded as two unknown states. All the measured signals required in the study could be realized from the conventional on-board sensors. Typical DLC and SLC maneuvers were designed and the developed algorithm was verified considering high-, mid-, and low-friction road conditions. The simulation results show that the proposed method can yield accurate and rapid estimations of the TRFC for mid- and low-friction road conditions even under a SLC maneuver, although DLC maneuver is needed to accurately estimate the TRFC for high friction road condition.

Chapter 3 presents the following article:

- Juqi Hu, Subhash Rakheja, and Youmin Zhang, "Tire-road friction coefficient estimation under designed braking pressure pulse," *Proceedings of the Institution of Mechanical Engineers, Part D: Journal of Automobile Engineering*, vol. 235, no. 7, pp. 1876-1891, 2021. (DOI: 10.1177/0954407020983580)

This study investigated the TRFC estimation on the basis of longitudinal vehicle dynamics. A two-stage TRFC estimation scheme is proposed that limits the disturbances to the vehicle motion. A sequence of braking pressure pulses is designed in the first stage to identify desired minimal pulse pressure for reliable estimation of TRFC with minimal interference with the vehicle motion. This stage alone can also provide a qualitative estimation of TRFC. In the second stage, tire normal force and slip ratio are directly calculated from the measured signals, a modified force observer based on the wheel rotational dynamics is developed for estimating the tire braking force. A CUKF algorithm is subsequently proposed to identify the TRFC for achieving rapid convergence and enhanced estimation accuracy. The effectiveness of the proposed methodology is evaluated considering vehicle motions on high-, medium-, and low-friction roads at different speeds. The simulation results suggest that the proposed two-stage methodology can yield an accurate estimation of the road friction with a relatively lower effect on the vehicle speed.

Chapter 4 presents the following submitted paper:

- Juqi Hu, Youmin Zhang, and Subhash Rakheja, "Adaptive lane change trajectory planning scheme for autonomous vehicles with consideration of road friction and vehicle speed," *IEEE Transactions on Intelligent Vehicles*. (Under revision).

This paper proposed a highway lane change trajectory planning scheme for autonomous driving considering both the maneuver safety and the occupant's perception of comfort. A 7th-order polynomial function is constructed to ensure continuity of the planned trajectory up to the derivative of the curvature (jerk). Constraints related to vehicle speed and road friction coefficient are defined by friction-adaptive acceleration and speed-adaptive jerk limits for intelligent trajectory planning with enhanced occupant's comfort and acceptance. It is shown that the proposed planning algorithm reduces to identification of only the lane change duration given a constant forward speed. Illustrative simulation examples have been conducted to verify the effectiveness of the proposed scheme for driving scenarios involving broad variations in vehicle speed and road friction coefficient. The acceptable traceability of the planned lane change trajectories is further demonstrated through path tracking analysis of a full-vehicle model. Finally, experimental tests have been conducted based on Quanser latest QCar to verify the practical effectiveness of the proposed trajectory planning scheme. The results have shown that the proposed scheme can generate safe and comfortable lane change trajectories, which can be well tracked by the AVs.

Chapter 5 presents the following article:

- Juqi Hu, Youmin Zhang and Subhash Rakheja, "Path planning and tracking for autonomous vehicle collision avoidance with consideration of tire-road friction coefficient," in the *21st IFAC World Congress*, Jul. 13-17, 2020, Berlin, Germany.

This study mainly discussed the development of a path planning and tracking framework based on MPC with consideration of the estimated TRFC. The planned path in terms of lateral position is generated based on the safety distance between the host and the obstacle vehicle, which is related to TRFC and vehicle speed. A new structure of MPC is further designed so that only lateral position is required to track the planned path. Moreover, the adaptive weights on the outputs to a wide range of vehicle speeds have been identified. The effectiveness of the proposed planning and tracking framework is validated through co-simulations on both high- and low-friction roads.

Chapter 6 presents the following article:

- Juqi Hu, Youmin Zhang, and Subhash Rakheja, "Adaptive trajectory tracking for car-like vehicles with input constraints," *IEEE Transactions on Industrial Electronics*. (Early Access), Date of Publication: Mar. 30, 2021. (DOI:10.1109/TIE.2021.3068672)

This study proposed an adaptive trajectory tracking control scheme for low-speed AVs with less efforts in tuning of the control gains. An interesting way of integrating adaptive control gains and steering saturation with the backstepping technique is designed to ensure the commanded inputs within the input boundaries. Moreover, the design of such adaptive control gains is also based on enhancing the convergence rate of tracking errors, especially for lateral deviation from the reference trajectory. It is further theoretically proven that, even under the influence of steering saturation, the proposed controller can make the closed-loop system approximately globally asymptotically stable at zero errors. Comparative simulations and experimental tests have been conducted to verify the effectiveness of the proposed control scheme in accurate tracking without violating the input constraints.

The contents of the above-stated manuscripts are interrelated to ensure the flow of the dissertation according to the thesis regulations. A few repetitions in the vehicle and tire modeling and results, however, are evident. The manuscripts presented in the dissertation have been reformatted, while the references have been grouped together and renumbered according to the thesis regulations.

Chapter 2

TRFC Estimation based on Lateral Vehicle Dynamics

2.1 Introduction

Directional control and safety of a road vehicle are strongly related to the forces generated by the tires at the tire-ground interface. Such forces are primarily governed by the TRFC for a given normal load on the tire [16]. A prior knowledge of the TRFC can facilitate the designs of effective vehicle control and safety systems [17, 92]. Considerable efforts have been made in the recent decades to obtain reliable on-line estimation of available TRFC considering widely different operating conditions. These efforts have proposed diverse methods, which may be classified into three broad categories: longitudinal dynamics-based, lateral dynamics-based and coupled dynamics-based approaches. While the coupled dynamics model the real vehicle more accurately, they may make the TRFC estimation algorithm become more complex. Choi et al. [41] employed linearized RLS technique for real-time identification of TRFC together with the tire stiffness on the basis of vehicle responses to combined braking and steering inputs. Qi et al. [42] proposed a modified Dugoff tire model and used two EKFs to estimate the friction coefficient, as well as longitudinal and cornering stiffness of the tire. When certain situations are considered (such as lane change

maneuver under constant speed and driving on straight highway), the vehicle modeling is reasonably simplified by utilizing pure lateral or longitudinal dynamics. TRFC estimation from lateral dynamic response of the vehicle may be relatively simpler since it does not require large longitudinal motions and excitations [24]. Relatively fewer studies, however, have estimated TRFC from lateral dynamic responses to a steering input. In the study by Yoon et al. [46], a cascade structure consisting of a sensor fusion framework based on KF was utilized to simultaneously estimate the vehicle side-slip angle and TRFC. The study employed relatively severe DLC and slalom steering inputs. Chen et al. [45] proposed a novel online gradient descent algorithm for vehicle side-slip angle and road friction estimation, though the effectiveness has not yet been verified by experiments in real vehicle. Ahn et al. [17] proposed an adaptive state and parameter observer to estimate friction coefficient and tire side-slip angle using the lateral acceleration and tire-aligning moment responses to a 0.25 Hz sinusoidal steering input, assuming negligible longitudinal tire force. Using total aligning torque of front-axle during steering, a stability and robustness guaranteed TRFC estimation method is designed by Shao et al. in [38]. Ren et al. [23] proposed a hybrid friction estimator based on a 3-DOF vehicle model responses to a rapidly varying fish-hook steering maneuver. The lateral tire force or self-alignment was chosen to estimate TRFC depending on the excitation levels.

The above studies have shown that the TRFC can be accurately estimated considering lateral dynamics of the vehicle, although effectiveness of the methods have been demonstrated under relatively large tire side-slip angles. TRFC estimation under different steering inputs such as continuous sinusoidal, slalom and fish-hook maneuvers considered in the reported studies may not be practical for real applications. Effective real-time TRFC estimation methods under reasonable levels of tire side-slip angles encountered during typical steering maneuvers would thus be desirable for practical implementations. Motivated by the practicality, in this chapter, we focus on a TRFC estimation method considering lateral dynamic responses of the vehicle to more practical DLC and SLC maneuvers compared to those considered in the reported studies.

2.2 Estimation Framework

The proposed hierarchical two-stage estimation framework making full use of the EKF and UKF techniques for TRFC identification is illustrated in Figure 2.1. In the first stage, EKF is used to linearize transformations between the measured states such as longitudinal and lateral accelerations (a_x, a_y) and the desired states, namely, the longitudinal and lateral velocities (v_x, v_y). The estimated lateral velocity $(\hat{v}_y)$ together with the measured yaw rate $(\dot{\psi})$ and steer angle (δ_f) yield side-slip angles of the front- and rear-axle tires (α_f, α_r). A UKF-based estimator is subsequently used to obtain estimations of lateral tire forces developed at the front and rear tire road interfaces $(\hat{F}_{yf}, \hat{F}_{yr})$. The road friction coefficients at the front and rear tires (μ_f, μ_r), regarded as unknown states of the system, for known normal loads on the tires (F_{zf}, F_{zr}), are then estimated using the brush tire model.

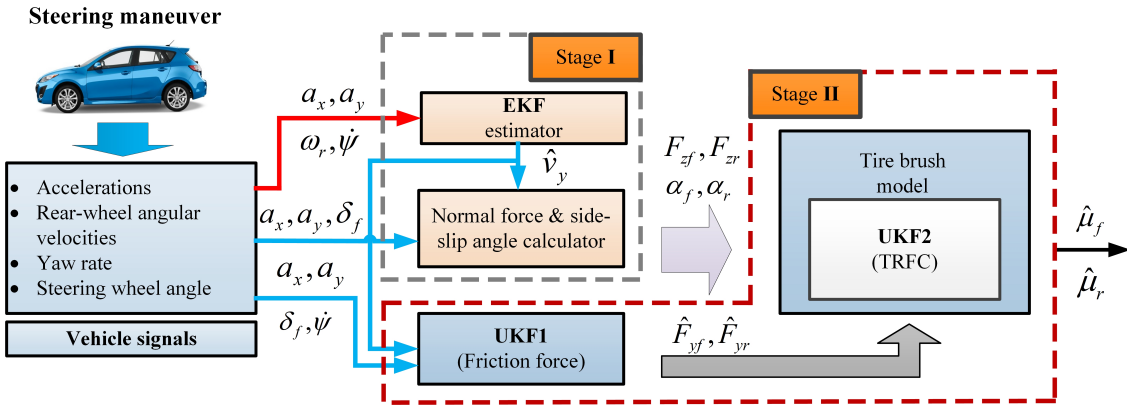

Figure 2.1: Block diagram of the proposed TRFC estimation framework based on lateral vehicle dynamics.

2.3 System Models and Estimation Algorithm

2.3.1 Vehicle Model

Vehicle is assumed driving on a straight flat road under constant forward speed, the wind speed, pitch and roll motions are all assumed negligible. A simple 3-DOF yaw plane model of a two-axle

vehicle, widely used in the reported studies [17, 46] as shown in Figure 2.2, is used to describe longitudinal, lateral and yaw dynamic responses to a steering input. The equations of motion of the simple model are obtained as:

$$\begin{aligned} m(\dot{v}_x - v_y\dot{\psi}) &= F_{xf}\cos\delta_f - F_{yf}\sin\delta_f + F_{xr} - F_R \\ m(\dot{v}_y + v_x\dot{\psi}) &= F_{yf}\cos\delta_f + F_{xf}\sin\delta_f + F_{yr} \\ I_z\ddot{\psi} &= l_f(F_{xf}\sin\delta_f + F_{yf}\cos\delta_f) - l_rF_{yr} \end{aligned} \tag{2–1}$$

where $F_R = f_r mg + 0.5\rho_{air}A_fC_dv_x^2$ represents the total resistance attributed to rolling resistance of tires and the aerodynamic drag force. Furthermore, F_{xr} is neglected considering only front-wheel drive vehicle. The steer angle δ_f is taken as the average of right- and left-tires' steer angle.

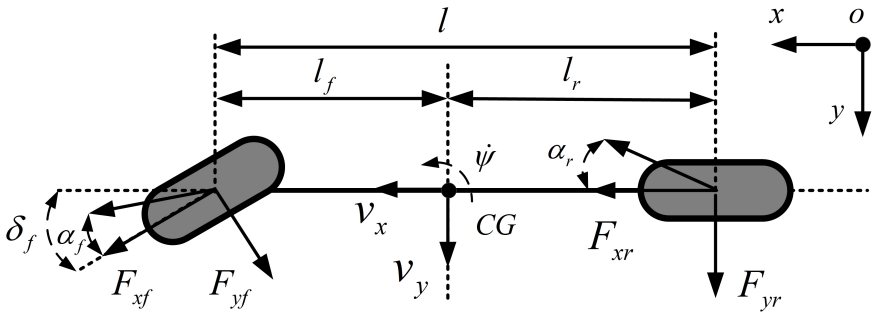

Figure 2.2: Schematic diagram of the bicycle vehicle model.

As the study by Ahn et al. [17] shows, the side-slip angles of the front- and rear-tires (α_f, α_r) can be obtained using small angle approximation by:

$$\begin{aligned} \alpha_f &= \frac{v_y + l_f\dot{\psi}}{v_x} - \delta_f \\ \alpha_r &= \frac{v_y - l_r\dot{\psi}}{v_x} \end{aligned} \tag{2–2}$$

The instantaneous normal forces acting on the front- and rear-axle tires (F_{zf}, F_{zr}) are computed

considering vehicle acceleration or deceleration, a_x, as:

$$\begin{aligned} F_{zf} &= \frac{mgl_r - ma_x h_c}{l} \\ F_{zr} &= \frac{mgl_f + ma_x h_c}{l} \end{aligned} \tag{2–3}$$

From (2–2) and (2–3), it is evident that the instantaneous tire side-slip angles and normal forces can be computed from known measurements $a_x, \delta_f, \dot{\psi}$ and the vehicle longitudinal and lateral velocities v_x, v_y.

2.3.2 Tire Model

It has been reported that nonlinear cornering properties of a tire including the force saturation can be accurately described by a brush tire model, reported in the studies by Choi et al. [41] and Singh and Taheri [18], which directly relates to road friction coefficient and requires considerably fewer parameters compared to the MF tire formula [93]. The brush tire model, comprising a row of elastic bristles representing the tread elements in contact with the road surface, is thus used in this study. In the absence of longitudinal slip, the model describes cornering force as a nonlinear function of normal load, road friction and tire side-slip angle, as:

$$F_{yi} = -\frac{C_{yi} \tan \alpha_i}{q} F$$

where

$$\begin{aligned} q &= \sqrt{C_{yi}^2 (\tan \alpha_i)^2} \\ F &= \begin{cases} q - \frac{q^2}{3\mu_i F_{zi}} + \frac{q^3}{27\mu_i^2 F_{zi}^2}, \text{ if } q \leqslant 3\mu_i F_{zi} \\ \mu_i F_{zi}, \text{ if } q > 3\mu_i F_{zi} \end{cases} \end{aligned} \tag{2–4}$$

where front- and rear-tires are lumped as front-axle and rear-axle tires, respectively, $i = f, r$ refers to front- and rear-axle, respectively, and C_{yi} and μ_i are the respective axle cornering stiffness and friction coefficient. For a typical passenger car tire, the cornering stiffness gradually increases

with tire normal load when the normal load is small, reaches the maximum value at some normal load, and decreases with a further increase in the normal load [94]. The variations in instantaneous normal loads acting on the front- and rear-axle can be neglected since the vehicle is driving under a constant forward speed. It is thus reasonable to assume axle cornering stiffness as constant values. Although tires of the identical type are installed on the front and rear axle, the axle cornering stiffness C_{yf} and C_{yr} may differ due to possible differences in instantaneous normal load. Figure 2.3 shows variations in tire cornering force characteristics, obtained from the brush model for cornering stiffness of 80 kN/rad, with variations in the tire side-slip angle, normal load and TRFC. These facts clearly illustrate strong dependence of cornering force on the TRFC and tire normal load. The dependence on μ, however, is not clearly identifiable, when the tire side-slip angle is very small. This suggests that the TRFC estimation in the vicinity of very small tire side-slip angles may yield errors and is likely the reason for using relatively large or rapidly varying steer inputs in the reported studies [24, 41].

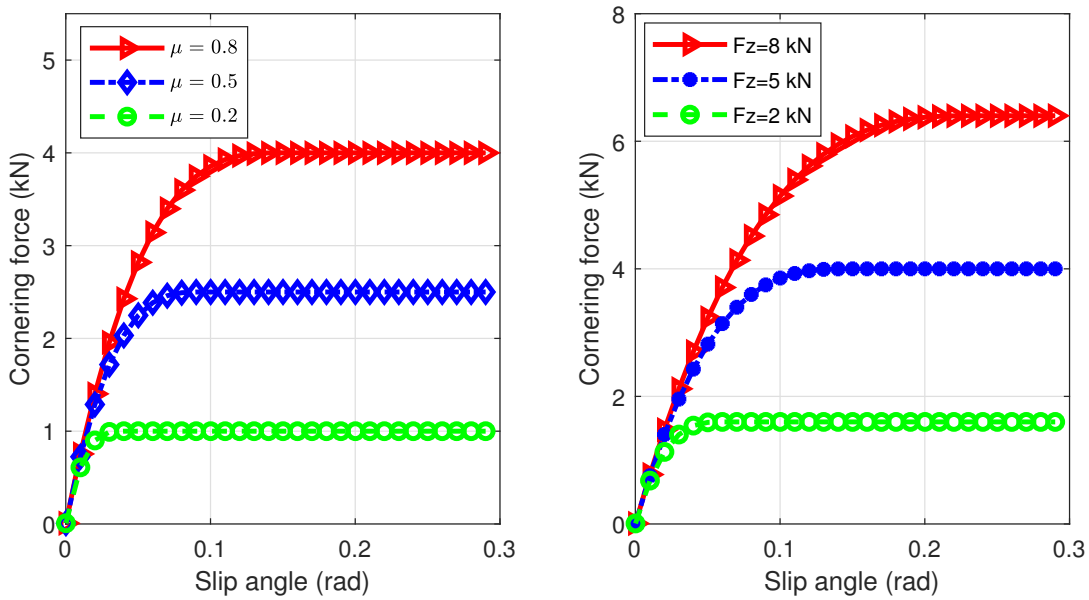

Figure 2.3: Cornering force-slip angle characteristics obtained from the brush tire model: (a) influence of friction coefficient ($F_z = 5$ kN) and (b) influence of normal load ($\mu = 0.8$).

2.3.3 Steering Maneuver

The referenced trajectory is designed based on the path coordinates defined in ISO 3888-1 [95] for a severe DLC maneuver, as shown in Figure 2.4(a). The standardized maneuver, however, is slightly modified to achieve relatively smooth steering and relatively lower tire side-slip angles by increasing the segment lengths, as summarized in Figure 2.4(c). The slightly modified segment lengths are designed so as to generate least tire side-slip angle required by TRFC estimation on high-μ road surface. Thus, sufficiently large tire side-slip angle can also be attained through tracking this referenced trajectory on both mid- and low-friction road conditions since identification of lower frictions requires lower tire side-slip excitations. The coordinates for the SLC maneuver are subsequently extracted from those of the DLC path, as shown in Figure 2.4(b). The steer inputs to the vehicle model are determined by the inner controller accordingly.

2.3.4 Estimation of Vehicle Velocity

A two-stage TRFC estimation scheme is formulated, where the initial stage is concerned with estimation of vehicle lateral velocity using the EKF technique. From (2–2), it is evident that the tire side-slip angles are directly related to instantaneous longitudinal and lateral velocities of the vehicle. Assuming small angles, the kinematic relationships between the accelerations and the derivatives of the vehicle velocities can be expressed as:

$$\begin{aligned} a_x &= \dot{v}_x - v_y\dot{\psi} \\ a_y &= \dot{v}_y + v_x\dot{\psi} \end{aligned} \tag{2–5}$$

The above relations are used to derive the following state-space system in the discrete-time as:

$$\begin{aligned} x_k^E &= f^E(x_{k-1}^E, u_k^E) + w_k^E, \\ z_k^E &= h^E(x_k^E) + v_k^E \end{aligned} \tag{2–6}$$

where k is the index for time step, w_k^E is the process noise with covariance Q^E and v_k^E is the

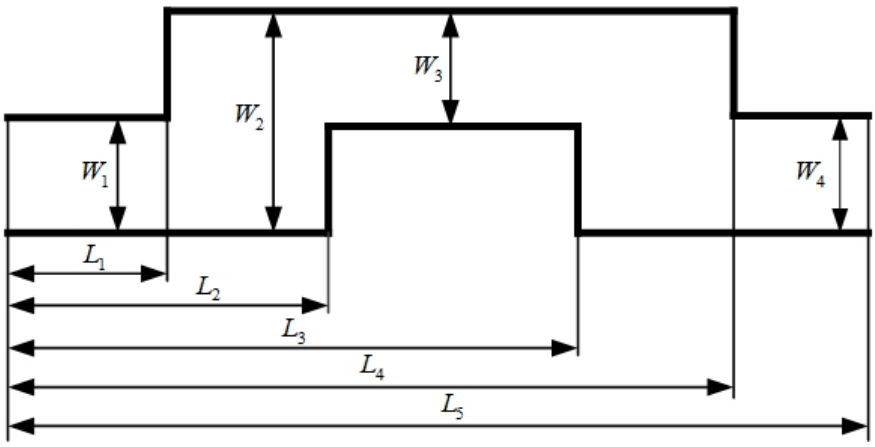

(a)

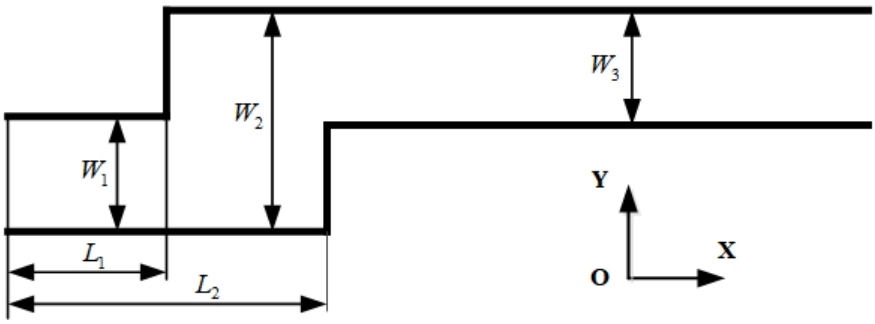

(b)

Maneuver	Track geometry (m)								
	W_1	W_2	W_3	W_4	L_1	L_2	L_3	L_4	L_5
Standard	1.1T+0.25	1.2T+3.75	1.2T+0.25	1.3T+0.25	15	45	70	95	125
Modified DLC	1.1T+0.25	1.2T+3.75	1.2T+0.25	1.3T+0.25	15	50	80	110	140
SLC	1.1T+0.25	1.2T+3.75	1.2T+0.25	---	15	50	---		

(c)

Figure 2.4: Path coordinates in the fixed axis system (XOY) as function of the vehicle width T: (a) DLC, (b) SLC, and (c) track specifications.

measurement noise with covariance R^E. In the above equations, x_k^E and z_k^E are system state and measurement vector, respectively, and u_k^E is input vector, which are defined as:

$$\begin{aligned} x_k^E &= [v_{x,k}, v_{y,k}]^T, \\ z_k^E &= v_{x,k}^m, \\ u_k^E &= [a_{x,k}, a_{y,k}, \dot{\psi}_k]^T \end{aligned} \tag{2–7}$$

where $v_{x,k}^m$ refers to mean velocity of the rear wheels at the ground interface, which can be obtained from angular speed of the wheels (ω_{rl}, ω_{rr}). Considering a front-wheel drive vehicle is selected, it is possible to approximate the vehicle longitudinal velocity in this way. This is because the slip ratios of rear tires are very close to zero when the vehicle is driving on a straight flat road under a constant forward speed. The states' evolution equations $f^E(\cdot)$ and observation functions $h^E(\cdot)$ in (2–6) are expressed as:

$$f^E = \begin{bmatrix} f_1^E \\ f_2^E \end{bmatrix} = \begin{bmatrix} v_{x,k-1} + T_s\dot{\psi}_k v_{y,k-1} + T_s a_{x,k} \\ v_{y,k-1} - T_s\dot{\psi}_k v_{x,k-1} + T_s a_{y,k} \end{bmatrix} \tag{2–8}$$

$$h^E = v_{x,k} \tag{2–9}$$

Following the standard EKF prediction and update scheme, as shown in [96, p. 409], the vehicle lateral velocity can be estimated.

Remark 2.1 *As longitudinal velocity is an element in both the system state (x_k^E) and the measurement vector (z_k^E) in (2–7), the EKF serves as a filter for the measured wheel angular speed. By doing so, the effect of the measurement noise on tire side-slip angle can be reduced.*

2.3.5 Tire Force Estimation

Two UKFs, referred to as UKF1 and UKF2, are implemented in sequence for tire force estimation and TRFC identification in the second stage (Figure 2.1). For estimating the tire forces, the state and measurement vectors are defined with input $u_k^U = \delta_{f,k}$ as:

$$x_k^U = [v_{x,k}, \dot{\psi}_k, v_{y,k}, F_{xf,k}, F_{yf,k}, F_{yr,k}]^T \tag{2–10}$$

$$z_k^U = [\hat{v}_{x,k}, \dot{\psi}_k, \hat{v}_{y,k}, a_{x,k}, a_{y,k}]^T \tag{2–11}$$

The filtered wheel velocity ($\hat{v}_{x,k}$) and the estimated lateral velocity ($\hat{v}_{y,k}$) obtained from the EKF estimator are regarded as known measurements for the force estimation. A random-walk

model [97] is chosen to describe the rate of change of axle forces. Governing equations of motion of the vehicle, (2–1) and (2–5), together with (2–10) and (2–11) are used to formulate the discrete-time state-space system model by integrating the process and measurement noises, as:

$$\begin{aligned} x_k^U &= f^U(x_{k-1}^U, u_k^U) + w_k^U, \\ z_k^U &= h^U(x_k^U) + v_k^U \end{aligned} \tag{2–12}$$

where w_k^U is the process noise with covariance Q^U, and v_k^U is the measurement noise with covariance R^U. The evolution function vector, $f^U(\cdot)$, is obtained as:

$$\begin{bmatrix} f_1^U \\ f_2^U \\ f_3^U \\ f_{4,5,6}^U \end{bmatrix} = \begin{bmatrix} v_{x,k-1} + T_s \dot{\psi}_{k-1} v_{y,k-1} + \dfrac{T_s}{m}[F_{xf,k-1}\cos\delta_{f,k} - F_{yf,k-1}\sin\delta_{f,k} \\ \qquad -0.5\rho_{air} C_d A_f v_{x,k-1}^2], \\ \dot{\psi}_{k-1} + T_s \dfrac{l_f}{I_z}[F_{xf,k-1}\sin\delta_{f,k} + F_{yf,k-1}\cos\delta_{f,k}] - T_s \dfrac{l_r}{I_z} F_{yr,k-1}, \\ v_{y,k-1} - T_s v_{x,k-1}\dot{\psi}_{k-1} + \dfrac{T_s}{m}[F_{xf,k-1}\sin\delta_{f,k} + F_{yf,k-1}\cos\delta_{f,k} + F_{yr,k-1}], \\ F_{xf,k-1},\ F_{yf,k-1},\ F_{yr,k-1} \end{bmatrix} \tag{2–13}$$

In the above formulation, it is assumed that the motion resistance is dominated by the aerodynamic drag, while the rolling resistance is negligibly small compared to the aerodynamic drag. The aerodynamic resistance is obtained considering a constant aerodynamic drag coefficient C_d, frontal area A_f and mass density of air ρ_{air}, assuming negligible wind velocity.

Similarly, the measurement function vector $h^U(\cdot)$ in (2–12) is formulated as:

$$\begin{bmatrix} h_1^U \\ h_2^U \\ h_3^U \\ h_4^U \\ h_5^U \end{bmatrix} = \begin{bmatrix} v_{x,k} \\ \dot{\psi}_k \\ v_{y,k} \\ \dfrac{1}{m}[F_{xf,k}\cos\delta_{f,k} - F_{yf,k}\sin\delta_{f,k} - 0.5\rho_{air} C_d A_f v_{x,k}^2] \\ [F_{xf,k}\sin\delta_{f,k} + F_{yf,k}\cos\delta_{f,k} + F_{yr,k}]\dfrac{1}{m} \end{bmatrix} \tag{2–14}$$

The UKF algorithm parameters $(\alpha_u, \beta_u, \kappa_u)$ together with the dimension of the system state

vector L ($L = 6$) determine the distribution of sigma points and the corresponding weights. A matrix of $2L + 1$ sigma vectors $\Gamma^i_{k|k}$ is computed as:

$$\Gamma^i_{k-1|k-1} = \begin{cases} \hat{x}^U_{k-1|k-1}, i = 0 \\ \hat{x}^U_{k-1|k-1} + \tilde{x}^U_{k-1|k-1}, i = 1, ..., 2L \end{cases} \tag{2–15}$$

where

$$\tilde{x}^U_{k-1|k-1} = \begin{cases} (\sqrt{(L+\lambda)P^U_{k-1|k-1}})_i, i = 1, ..., L \\ -(\sqrt{(L+\lambda)P^U_{k-1|k-1}})_{i-L}, i = L+1, ..., 2L \end{cases} \tag{2–16}$$

and $\lambda = \alpha_u^2(L + \kappa_u) - L$ is a scaling parameter, subscript i ($i = 1, ..., 2L$) denotes the column number of square root of $(L + \lambda)P^U_{k-1|k-1}$. The constant α_u determines the spread of the sigma points around the mean of x^U_k, which is usually set to a small positive value ranging from 10^{-4} to 1, while κ_u is a secondary scaling parameter that is usually set to 0 [98, 99]. In this study, the scaling parameters are selected as $\alpha_u = 1$ and $\kappa_u = 0$, which provided satisfactory estimations of tire forces in the entire tire side-slip range. The weighting coefficients for $2L + 1$ sigma points are calculated by:

$$\begin{aligned} W^0_s &= \frac{\lambda}{L+\lambda} = 0 \\ W^0_c &= 1 - \alpha_u^2 + \beta_u \\ W^i_s &= W^i_c = \frac{1}{2L},\ i = 1, ..., 2L \end{aligned} \tag{2–17}$$

where the constant β_u permits the use of prior knowledge of the distribution of x^U_k, which is selected as 2 for the Gaussian distribution, as suggested in the study by Wan and Van Der Merwe [99]. For more details about the UKF algorithm, see the reference book written by Simon [96, p. 448-450].

Remark 2.2 *The filtered wheel speed ($\hat{v}_{x,k}$) and the estimated lateral velocity ($\hat{v}_{y,k}$) from EKF in the first stage are considered as measurements in the UKF1 algorithm. Tire forces ($F_{xf,k}$,*

$F_{yf,k}, F_{yr,k}$) remain the only unknown states to be estimated. As a result, the overall computational demand for tire force estimation is reduced, although the system state dimension (L) is 6.

Remark 2.3 *Re-setting of the sigma points during each interval is not attempted since the tire longitudinal and cornering forces are not expected to vary abruptly over the chosen sampling duration, which also helps to improve computational efficiency.*

2.3.6 TRFC Estimation

Estimated lateral tire forces of the two axles ($\hat{F}_{yf}, \hat{F}_{yr}$), together with tire side-slip angles of front- and rear-axle (α_f, α_r), and normal forces of front- and rear-axle (F_{zf}, F_{zr}) are all known at this stage. It is known that the cornering stiffness of a typical passenger car tire is largely affected by the normal load. The variations in instantaneous normal loads acting on front- and rear-axle can be neglected since the vehicle is driving under a constant forward speed. Thus, it is reasonable to assume that C_{yf} and C_{yr} are two known constant parameters. The TRFC at the front and rear tires, (μ_f, μ_r), remain the only two parameters to be identified according to the pure side-slip brush tire model (2–4). Considering that the road adhesion condition varies very slowly, the TRFC can be considered as a vehicle state embedded within the brush tire model [39].

Denote the two states by $\tau_k = [\mu_{f,k}, \mu_{r,k}]^T$, and the two measurements by the estimated front- and rear-axle lateral forces from UKF1, $z_k^B = [\hat{F}_{yf,k}, \hat{F}_{yr,k}]^T$, the pure side-slip brush tire model is described as a two-state and two-measurement discrete-time nonlinear system as:

$$\begin{aligned} \tau_k &= \tau_{k-1} + w_k^B \\ z_k^B &= h_B(\tau_k) + v_k^B \end{aligned} \tag{2–18}$$

where w_k^B is the process noise with covariance Q^B, v_k^B is the measurement noise with covariance

R^B and the observation function $h_B(\cdot)$ is expressed as:

$$h_B = \begin{bmatrix} h_{B_1} \\ h_{B_2} \end{bmatrix} = \begin{bmatrix} F_{yf}(\alpha_{f,k}, F_{zf,k}, \hat{\mu}_{f,k-1}) \\ F_{yr}(\alpha_{r,k}, F_{zr,k}, \hat{\mu}_{r,k-1}) \end{bmatrix} \tag{2–19}$$

where $F_{yi}(\cdot)$ is lateral force due to axle ($i = f, r$) obtained from the brush tire model function of the instantaneous normal force $F_{zi,k}$ and tire side-slip angle $\alpha_{i,k}$, together with the TRFC estimated at the previous step, $\hat{\mu}_{i,k-1}$. The TRFC of front- and rear-tires are subsequently identified using the UKF algorithm identical to the UKF1 used for estimating the tire forces, as $\hat{\mu}_{f,k}$ and $\hat{\mu}_{r,k}$. While identical values of α_u, β_u and κ_u are used for the UKF2, the sigma points are updated during each sampling interval for estimating the TRFC. Updating of the sigma points permits rapid convergence of TRFC, although it imposes higher computational demand. Since there are only two parameters to be identified, the overall computational demand is reasonable. The estimated TRFC, $\hat{\mu}_{f,k}$ and $\hat{\mu}_{r,k}$, are confined to 1 if they are larger than 1 to avoid fluctuations and unexpected estimation errors when tire force and tire side-slip angle are extremely small.

2.4 Simulation Results

The proposed friction estimation algorithm was implemented in the MATLAB/Simulink and CarSim software platform to evaluate its performance. The responses of the CarSim vehicle simulation model were considered as the reference or measured states for the purpose of assessing prediction performance of the proposed algorithm. White Gaussian noise, however, was added to the CarSim model outputs in order to study the effectiveness of the algorithm in the presence of measurement noise. The parameters for the vehicle model used in simulation are listed in Table 2.1. The process and measurement covariance matrices for the EKF, UKF1 and UKF2 were chosen

Table 2.1: Class-C hatchback parameters.

Symbol	Parameter	Value	Unit
m_s	Sprung mass	1274	kg
m_{us}	Unsprung mass	142	kg
R_e	Tire radius	0.316	m
C_{yf}	Front-axle cornering stiffness	94	kN/rad
C_{yr}	Rear-axle cornering stiffness	76	kN/rad
l_f	Distance from *CG* to front-axle	1.016	m
l_r	Distance from *CG* to rear-axle	1.562	m
l	Vehicle's wheelbase	2.578	m
T	Width of the vehicle	1.739	m
h_c	Height of the *CG* of the vehicle	0.54	m
I_z	Yaw moment of inertia	1523	kgm^2
A_f	Front area of the vehicle	1.6	m^2
C_d	Aerodynamic drag coefficient	0.35	–

as:

$$\begin{aligned} Q^E &= \text{diag}([10^{-3}\ \ 10^{-3}]),\ R^E = 10, \\ Q^U &= \text{diag}([10^{-3}\ \ 10^{-7}\ \ 10^{-3}\ 400\ \ 850\ \ 675]), \\ R^U &= \text{diag}([2\times10^{-2}\ \ 9.4\times10^{-5}\ \ 2\times10^{-2} \\ &\quad\ 8.6\times10^{-5}\ \ 6.5\times10^{-4}]) \end{aligned} \tag{2–20}$$

and

$$\begin{aligned} Q^B &= 5\times\text{diag}([10^{-6}\ \ 10^{-6}]), \\ R^B &= 6\times\text{diag}([10^{5}\ \ 10^{5}]) \end{aligned} \tag{2–21}$$

where superscripts E, U and B refer to EKF, UKF1 and UKF2, respectively.

Simulations of constant forward speed DLC and SLC maneuvers were conducted on three different road surfaces with coefficients of 0.8, 0.4 and 0.2, denoted as high-μ, mid-μ and low-μ, respectively. The vehicle is permitted to operate on a 55 m long straight road segment prior to entering the DLC or SLC paths (Figure 2.4). The constant forward speed, $v_x = 100$ km/h, is considered for maneuvers performed on high- and mid-μ road conditions, and the maneuver on

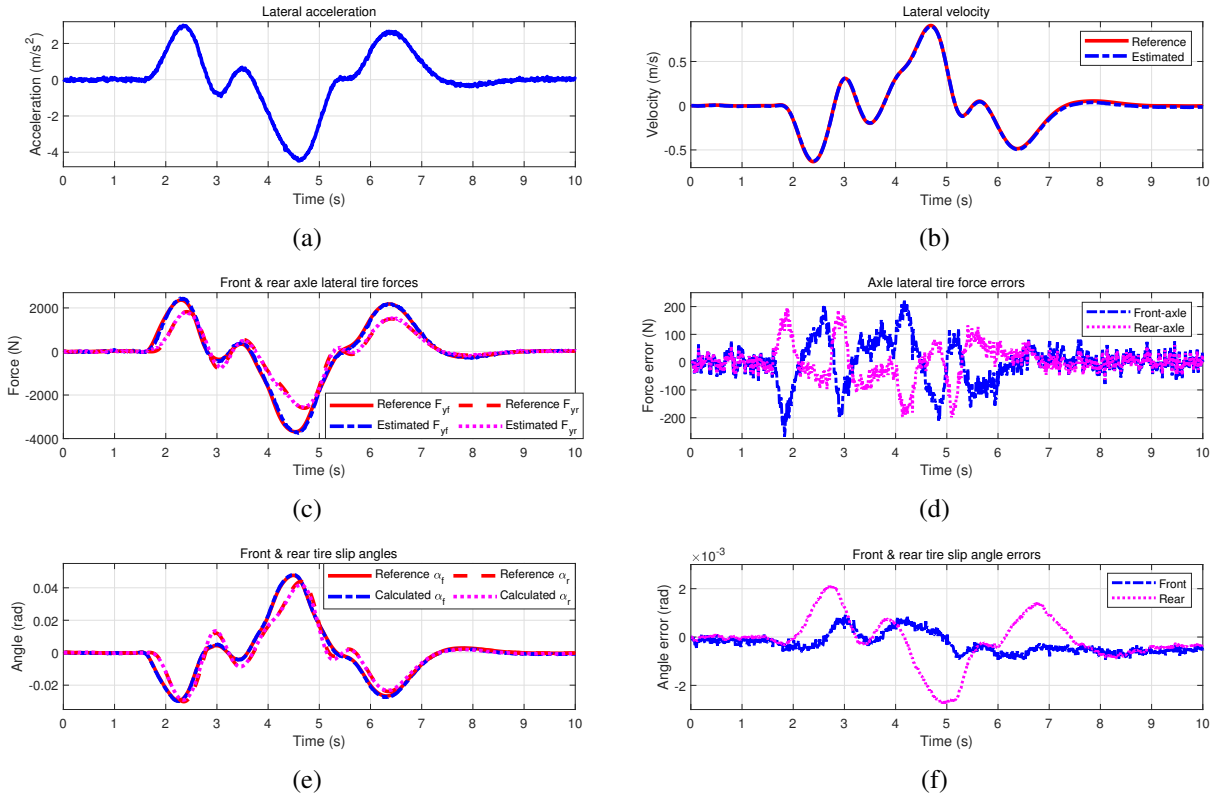

Figure 2.5: DLC simulation results on high-μ road condition: (a) measured lateral acceleration, (b) estimated lateral velocity, (c) and (d) estimated axle forces and their errors, and (e) and (f) calculated tire slip angles and their errors.

low-μ road condition is conducted at a lower speed of 40 km/h.

2.4.1 TRFC Estimation during DLC Maneuvers

2.4.1.1 High-μ Surface

The measured lateral acceleration (a_y), estimated lateral velocity ($\hat{v}_y$), side forces ($\hat{F}_{yf}, \hat{F}_{yr}$) and calculated tire side-slip angles (α_f, α_r) for the high-μ road condition are presented in Figure 2.5. The figure also presents the prediction errors in side forces (Figure 2.5(d)) and tire side-slip angles (Figure 2.5(f)) to show more clear estimation results. The estimated friction coefficients as a function of the time is shown in Figure 2.6(a). The results show accurate estimations of tire side-slip angles and side forces, while notable prediction errors in TRFC is evident for $t \leqslant 2$ s, likely due to very small tire side-slip angles as the vehicle traverses the straight-line segment. As

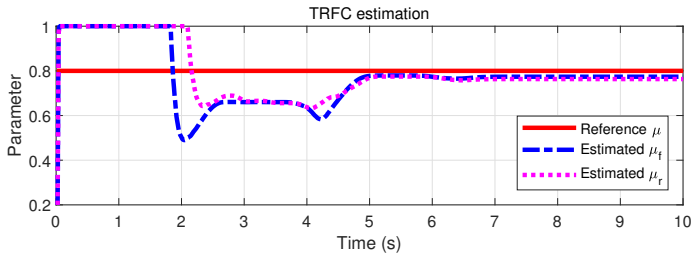

(a)

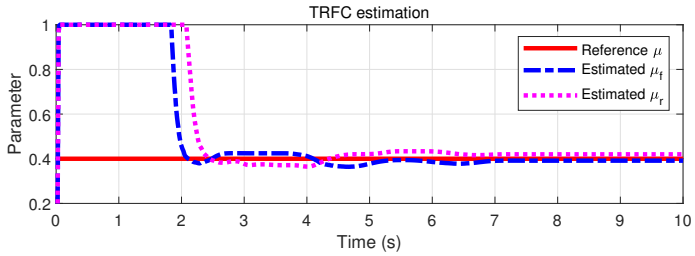

(b)

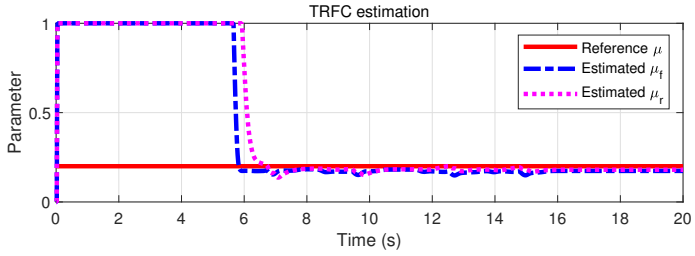

(c)

Figure 2.6: TRFC estimation under DLC maneuver on three different road conditions: (a) high-μ road, (b) mid-μ road, and (c) low-μ road.

seen in Figures 2.5(e) and 2.5(f), accurate lateral velocity estimation (Figure 2.5(b)) yields equally accurate predictions of tire side-slip angles, although the slip angle error of rear tires is larger than that of front tires. Notable errors are also evident in the predicted side forces, as seen in Figure 2.5(d). Peak errors are observed in the $t = 2 - 6$ s interval, which occur mostly in the vicinity of low tire side-slip angle response. The estimated TRFC ($\hat{\mu}_f$ and $\hat{\mu}_r$) values quickly approach 0.65 immediately after the vehicle enters the curved path and the tire side-slip angles approach peak values prior to reversal of the steering input. The error in TRFC estimation in this region is likely due to small tire side-slip angle. As the vehicle starts the second path change, the estimated TRFC increases gradually and converges to about 0.78 near $t = 4.8$ s. The estimated TRFC values remain steady thereafter, irrespective of the tire side-slip angle, as seen in Figure 2.6(a). It is further seen

that $\hat{\mu}_f$ slightly leads $\hat{\mu}_r$, which is consistent with the fact that the contact of the front tires leads that of the rear tires. The error in the estimated TRFC values are partly attributable to the errors in estimated side forces and signal noise, in addition to potential errors in cornering force estimations from the brush tire model.

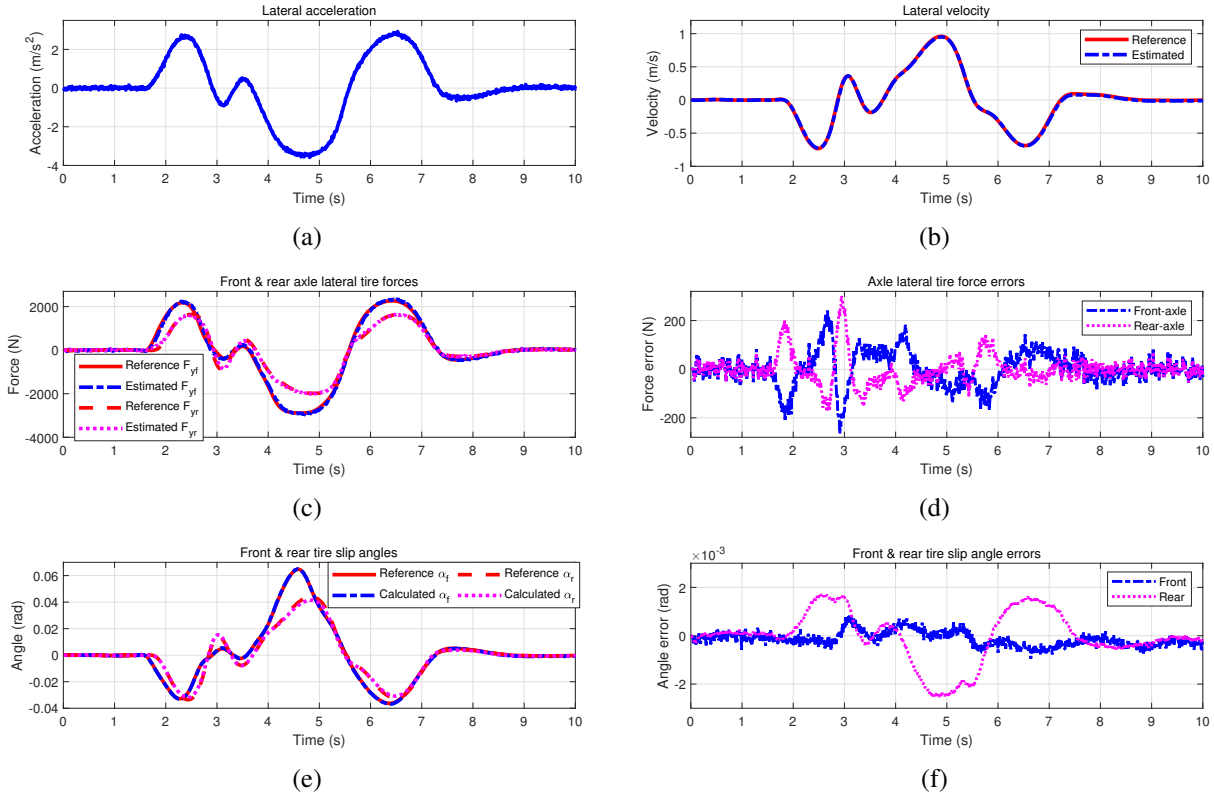

Figure 2.7: DLC simulation results on mid-μ road condition: (a) measured lateral acceleration, (b) estimated lateral velocity, (c) and (d) estimated axle forces and their errors, and (e) and (f) calculated tire slip angles and their errors.

2.4.1.2 Mid-μ Surface

Figure 2.7 illustrates the estimated lateral velocity ($\hat{v}_y$), side forces ($\hat{F}_{yf}$, $\hat{F}_{yr}$) and the calculated tire side-slip angles for the mid-μ road condition together with the side forces and side-slip angle prediction errors. The measured lateral acceleration with the noise, obtained from CarSim, is shown in Figure 2.7(a). Compared to the high-μ road condition (Figure 2.5), the lateral velocity,

side forces and side-slip angles are estimated with the same degree of accuracy (Figures 2.7(b)-2.7(f)). Although notable errors in estimated side forces are evident, the estimated TRFC values rapidly approach the target value of 0.4 near $t = 2$ s, as the vehicle enters the initial curved segment of the DLC path (Figure 2.6(b)). While the side-slip angle developed at the rear tires is close to that obtained for high-μ road condition, the front tire side-slip angle is higher, as shown in Figures 2.5(e) and 2.7(e). More effective prediction of TRFC in this case is partly due to the fact that sufficiently large tire side-slip angles have been developed on mid-μ road surface compared to the high-μ surface, as seen in Figure 2.7(e). Noting that the lower the μ is, the smaller tire side-slip angle it is required to effectively identify this parameter. The UKF-based force observer tracks the actual tire force per-axle reasonably well, which suggests effectiveness of the UKF technique in dealing with system nonlinearities. Relatively large errors, however, are evident when the magnitude of side forces is small, which also implies small tire side-slip angles. The estimated TRFC values, $\hat{\mu}_f$ and $\hat{\mu}_r$, vary within a small range, between 0.39 and 0.42, during rest of the maneuver, as seen in Figure 2.6(b).

2.4.1.3 Low-μ Surface

The simulation results to a DLC maneuver on the low-μ road condition at a speed of 40 km/h are shown in Figure 2.8. The results exhibit considerable oscillations when compared to those obtained with high- and mid-μ road conditions. This is attributed to relatively poor adhesion of the tires with the low friction road surface. High magnitude oscillations in the lateral acceleration responses contribute to higher estimation errors in the lateral velocity and side forces, as seen in Figures 2.8(a) to 2.8(d). The EKF velocity estimator, however, exhibits satisfactory performance for reasonably accurate estimations of the tire side-slip angles based on Eq. (2–2). The estimated tire side-slip angles are close to the reference values, as seen in Figures 2.8(e) and 2.8(f). The observed front- and rear-axle tire forces (Figure 2.8(c)), however, show considerable deviations when compared to the reference values. The results show large peak force errors in the vicinity of zero tire side-slip angles (Figure 2.8(d)), which can be attributed to higher uncertainties in the tire

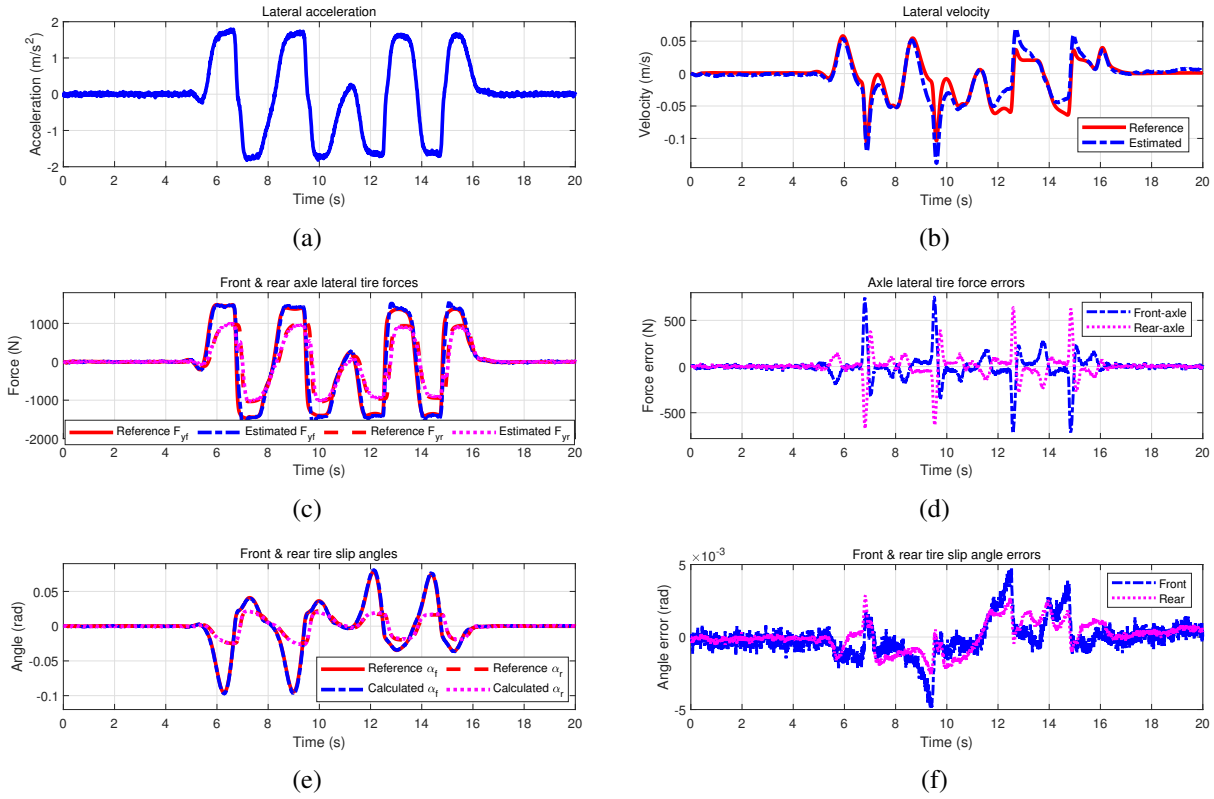

Figure 2.8: DLC simulation results on low-μ road condition: (a) measured lateral acceleration, (b) estimated lateral velocity, (c) and (d) estimated axle forces and their errors, and (e) and (f) calculated tire slip angles and their errors.

forces during wheel slippage. The wheel slippage, however, imposes greater tire side-slip angles to meet the side-force demand (Figure 2.8(e)) compared to those observed with high- and mid-μ road conditions, which contributes to more effective predictions of the TRFC values. The estimated TRFC values rapidly approach the reference value of 0.2, as the vehicle enters the curved segment of the DLC track near $t = 6$ s, as seen in Figure 2.6(c). The estimated values vary between 0.18 and 0.2 during the entire maneuver thereafter. The generated high magnitude of tire side-slip angles may partly explain the slight underestimation of the TRFC, as the modeling errors of brush tire model increase at large tire side-slip angles.

Figure 2.9(a) compares the actual trajectories of the vehicle *CG* obtained during the DLC maneuvers performed on three different road surfaces. The results show that the vehicle trajectories remain within the defined bounds throughout the maneuver, irrespective of the TRFC, although the

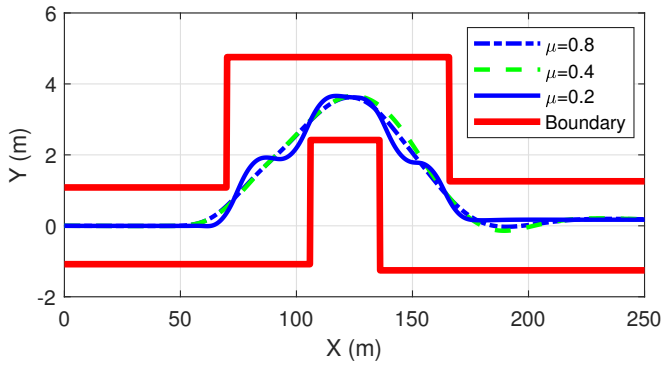

(a)

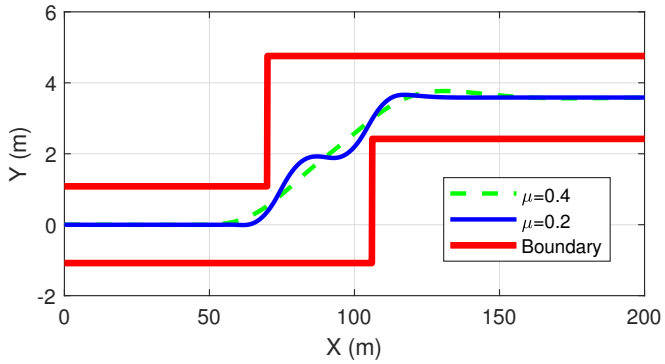

(b)

Figure 2.9: The *CG* trajectory of the vehicle on different road conditions: (a) DLC maneuver and (b) SLC maneuver.

DLC maneuver on the low-μ road condition yields greater path oscillations. The results suggest that the proposed algorithm can yield rapid and accurate estimations of TRFC values from the vehicle responses during a DLC maneuver, especially for the mid- and low-μ road conditions. The estimations on the high-μ road condition, however, revealed great error and time lapse, which is attributed to relatively lower tire side-slip angles developed during the first lane change.

The peak lateral acceleration during the DLC maneuver varies considerably with the road friction, although the vehicle tracks the same path, shown in Figure 2.4(c). While the peak lateral acceleration on high-μ road condition ($\mu = 0.8$) is 0.57μg, the peak acceleration values on mid-μ road condition ($\mu = 0.4$) and low-μ road condition ($\mu = 0.2$) are close to the limit value of μg (0.90μg and 0.92μg, respectively). The designed path thus represents relatively severe maneuvers on mid- and low-μ road conditions, which is neither safe nor practical in real application. However,

the results presented in Figures 2.6(b) and 2.6(c) show that accurate estimations of TRFC can be realized during the initial curved segment of the DLC track. This suggests that the TRFC values could be effectively estimated from the lateral responses to a SLC maneuver, which is considered to be a simpler as well as more practical maneuver for real-time TRFC estimations. It is worthy to note that the peak lateral acceleration corresponding to the first lane change is much smaller than that encountered during the second path change, especially for high- and mid-μ road conditions. The effectiveness of the proposed algorithm is thus further verified considering the lateral responses to a SLC maneuver, which has not been adequately investigated in the reported studies.

2.4.2 TRFC Estimation during SLC Maneuvers

As shown in Figure 2.6(a), the TRFC can not be accurately estimated until the second lane change ($t = 4.8$ s) on high-μ road condition. The SLC results and discussions in this section are limited only to estimations on mid- and low-μ road conditions, which are known to be more critical in view of directional stability and thus safety dynamic performance of the vehicle. The SLC simulation results on mid- and low-μ road conditions at the nominal forward speed of 100 km/h and 40 km/h, respectively, are presented in Figures 2.10 to 2.12.

Compared to the DLC maneuver (Figure 2.7(a)), the peak value of the lateral acceleration under SLC maneuver on the mid-μ road condition is much smaller (Figure 2.10(a)). However, the peak value under SLC maneuver on the low-μ road condition is comparable with that measured under DLC maneuver (Figures 2.8(a) and 2.11(a)). This is due to wheel slippage during both the DLC and SLC maneuver on the very low friction road surface. Figures 2.10 and 2.11 also present the estimated lateral velocity, tire side forces and side-slip angles for the mid- and low-μ road conditions, respectively, together with the tire side forces and side-slip prediction errors. For the mid-μ road condition, the peak tire side-slip angles attained during the SLC maneuver are in the order of 0.03 rad, as seen in Figure 2.10(e). These are quite comparable with those observed during the initial curved segment of the DLC track (Figure 2.7(e)). The proposed algorithm yields accurate estimations of lateral velocity, side forces and side-slip angles, as in the case of the DLC

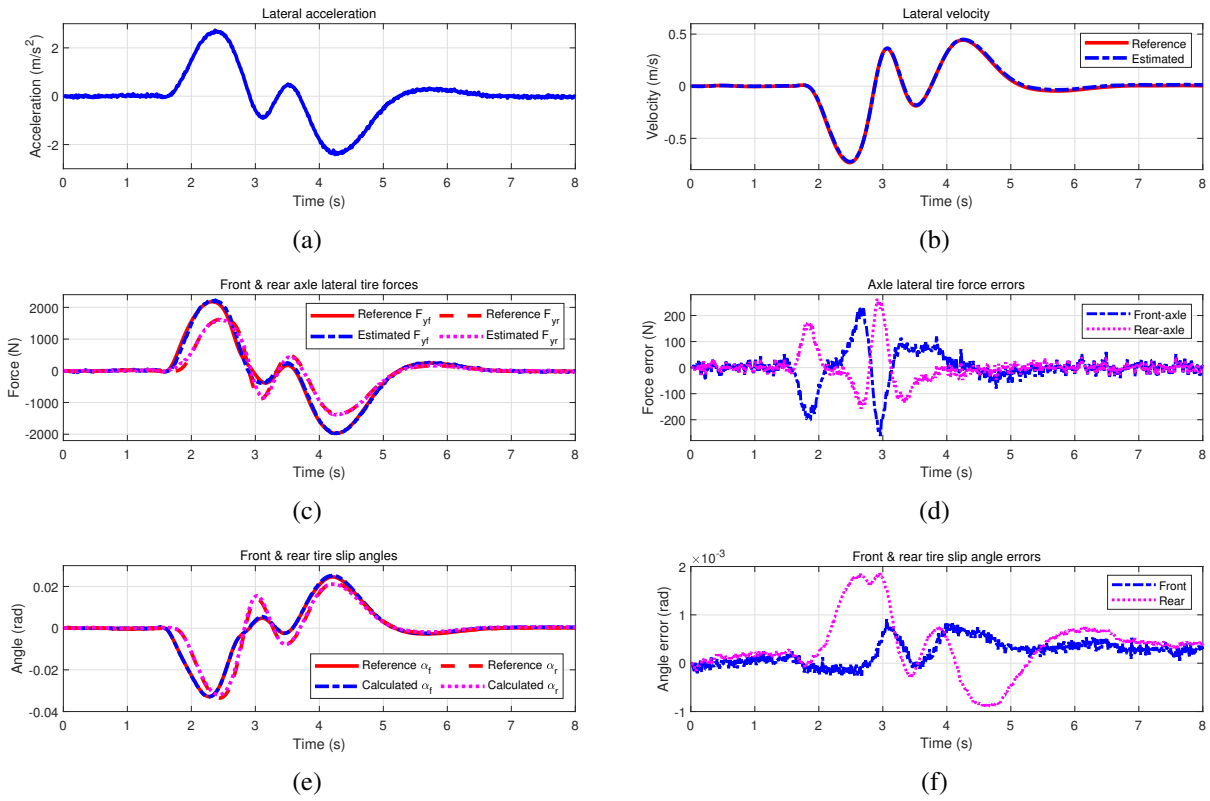

Figure 2.10: SLC simulation results on mid-μ road condition: (a) measured lateral acceleration, (b) estimated lateral velocity, (c) and (d) estimated axle forces and their errors, and (e) and (f) calculated tire slip angles and their errors.

maneuver. The estimated TRFC values, $\hat{\mu}_f$ and $\hat{\mu}_r$, rapidly decrease from the confined value of 1.0 to nearly 0.4, as the vehicle enters the curved track (Figure 2.12(a)). After $t = 4.2$ s when the generated tire side-slip angles decrease from a smaller peak value of only 0.025 rad to near zero, small overestimations of the estimated TRFCs are observed for both the front- and rear-axle due to lower tire side-slip angles during this period. $\hat{\mu}_f$ and $\hat{\mu}_r$ may finally converge to small different values (less than 0.01) as a result of the Gaussian white noises added to the measured signals. Nevertheless, the estimated TRFC values vary within a small band between 0.37 and 0.44 during and after the SLC maneuver.

The proposed algorithm also yields accurate and rapid estimations of the TRFC values on the basis of lateral dynamic responses to a SLC maneuver performed on the low-μ road condition, as seen in Figure 2.12(b). Owing to considerably larger variations in the steer angle and thus the

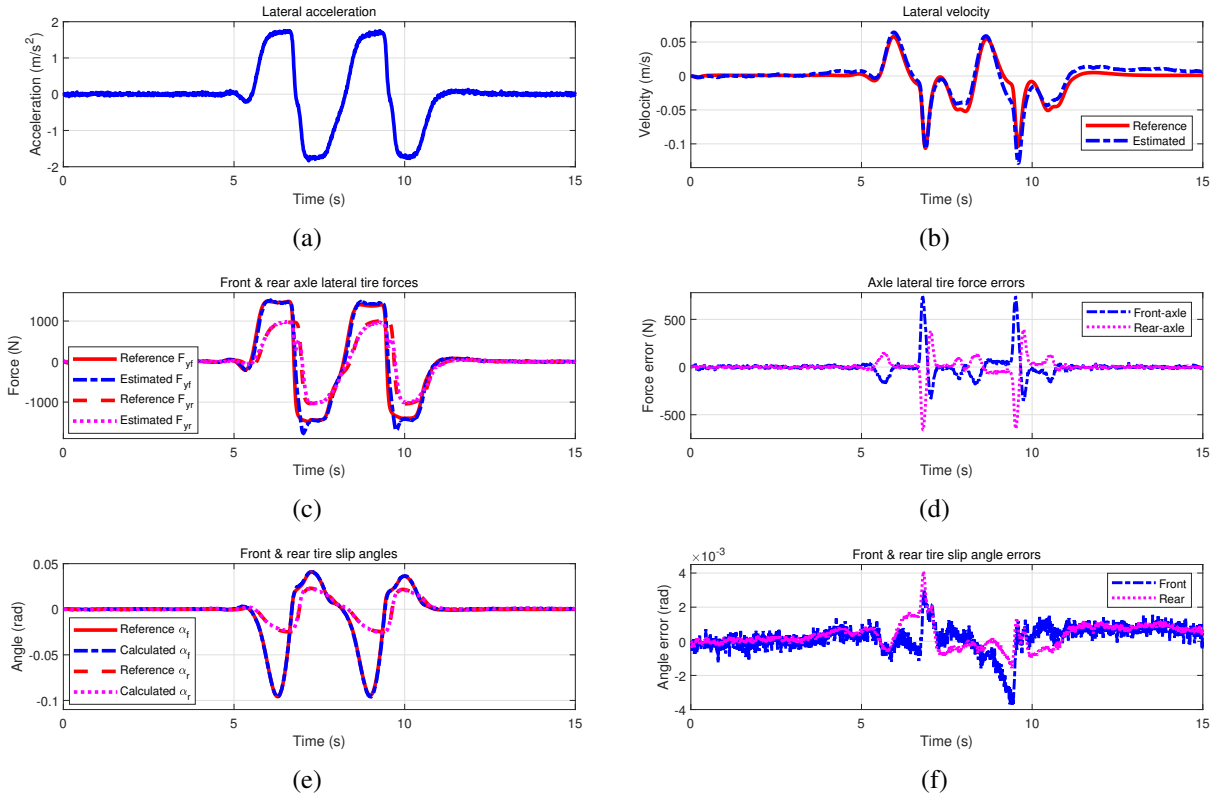

Figure 2.11: SLC simulation results on low-μ road condition: (a) measured lateral acceleration, (b) estimated lateral velocity, (c) and (d) estimated axle forces and their errors, and (e) and (f) calculated tire slip angles and their errors.

tire side-slip angles, the results show considerable deviations in the side force estimation. This is evident near $t = 6$ s and $t = 9$ s in Figure 2.11(d), which is likely caused by uncertainties in the tire cornering forces in the saturation region. The vehicle *CG* trajectories on mid- and low-μ road conditions during the SLC maneuver are compared in Figure 2.9(b). The vehicle trajectories remain within the defined bounds throughout the maneuver, irrespective of the TRFC value, although the SLC maneuver on the low-μ road condition yields greater path oscillations.

2.4.3 Discussion and Analysis

From the above simulation results, it is evident that the proposed EKF-and-UKF framework consisting of only standard EKF and UKF can ensure rapid TRFC estimation with acceptable

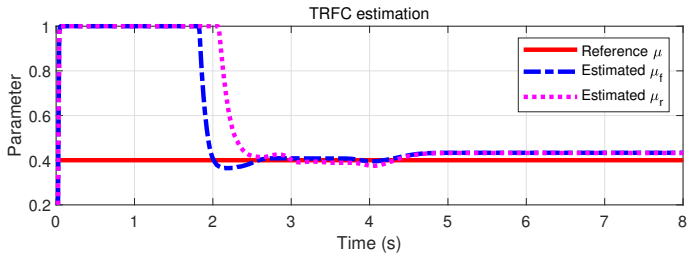

(a)

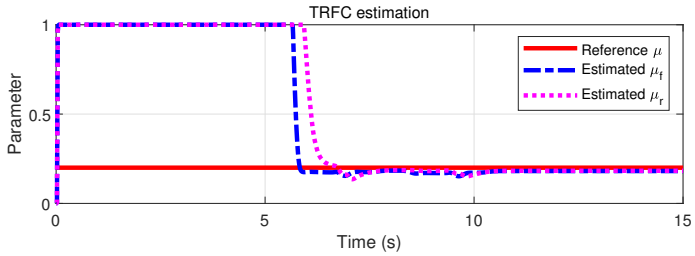

(b)

Figure 2.12: TRFC estimation under SLC maneuver on two different road conditions: (a) mid-μ road and (b) low-μ road.

accuracy on high-, mid- and low-μ road surfaces. Considering that the number of states to be estimated has large influence on the computational burden, the filtered wheel velocity (approximation of vehicle longitudinal velocity) and the estimated lateral velocity from EKF in the first stage are considered as measurements in the UKF1. Tire forces are thus remaining the only three unknown states to be estimated in (2–10). As a result, the overall computational demand for tire force estimation is reduced and much lower than the combined velocity and tire force estimation in the study by Qi et al [42]. The estimated axle lateral forces from UKF1 are then fed to the UKF2 for TRFC identification, the TRFC at the front and rear tires remain the only two parameters to be identified based on the brush tire model. The overall computational cost is still comparable to methods as described in the studies by Wang and Wang [24] and Chen et al. [100] considering the convergence rate of the estimated TRFC. However, the methods in these two studies are assuming known vehicle velocities. It should also be noted that re-setting of the sigma points of UKF1 during each interval is not attempted since the tire forces are not expected to vary abruptly under the considered vehicle maneuvers and this helps to further improve computational efficiency.

While the desired DLC maneuver realized effective TRFC estimation on all the three road

conditions (Figure 2.6), it can lead to large lateral acceleration close to the limit value (μg) on both the mid- and low-μ road conditions (Figures 2.7(a) and 2.8(a)), which is neither safe nor comfortable. Results in Figure 2.12 suggest that the TRFC can be accurately identified under the simpler SLC maneuver on both the mid- and low-μ road conditions. Moreover, the SLC maneuver generates smaller peak lateral acceleration with less oscillations than that observed under DLC maneuver. Therefore, it is not necessary to conduct a DLC maneuver for estimating the friction coefficient, especially for the mid- and low-friction road conditions. The TRFC estimation under a SLC maneuver is more practical for implementation, when compared to the relatively severe maneuvers employed in the reported studies [17, 41].

2.5 Summary

In this chapter, a new TRFC estimation framework based on the vehicle responses to more practical lane change maneuvers (including both DLC and SLC maneuvers) has been investigated. The framework is designed so as to utilize the measurements that are available directly from the onboard sensors. The lateral velocity constitutes the only exception, which is estimated in the initial stage of the framework. The overall computational burden is reasonably reduced due to the cascade structure of the estimation framework. The proposed two-stage method can yield rapid and accurate estimations of the TRFC values of various road conditions, although the estimations under the SLC maneuver are a little worse than those under the DLC maneuver. However, the effective TRFC identification even under the SLC maneuver makes the proposed method very promising towards its practical application. The TRFC estimation under lateral vehicular excitations, however, leads to undesired interference to vehicle motion, which would likely be perceived as annoying by the vehicle occupants. An alternate framework based on longitudinal dynamics of the vehicle is proposed in the following chapter in an attempt to minimize the interference to the vehicle motion during the TRFC estimation.

Chapter 3

TRFC Estimation based on Longitudinal Vehicle Dynamics

3.1 Introduction

Since unmanned vehicles should be able to perform driving tasks on different road conditions, the real-time knowledge of varying friction is vital for motion control and safe driving of the AVs. The available road surface friction coefficient may vary considerably with various environmental and operating conditions such as weather conditions, state of tires, road roughness, instantaneous traction/braking demand and more. Different TRFC estimation strategies have been proposed on the basis of longitudinal and/or lateral dynamic states of the vehicle, which tend to vary considerably depending on excitations and road conditions. The reported studies have used different tire models including Pacejka tire model [101], Dugoff tire model [43], brush tire model [41] and LuGre tire model [102], which suggest that the reliability of TRFC estimation also relies on effectiveness of the tire model used. Some of the most common dynamic vehicle models for friction estimation are wheel rotation dynamic model [21], bicycle model [16], quarter-car model [103] and four-wheel vehicle dynamic model [23]. Technical survey studies on vehicle and tire models used for friction estimation are referred to [104, 105].

Chen et al. [45] proposed a novel online gradient descent algorithm for vehicle side-slip angle and road friction estimation, though the effectiveness has not yet been verified by experiments in real vehicle. Ahn et al. [17] proposed an adaptive state and parameter observer to estimate friction coefficient and tire side-slip angle using the lateral acceleration and tire-aligning moment responses to a 0.25 Hz sinusoidal steering input, assuming negligible longitudinal tire force. Using total aligning torque of front-axle during steering, Shao et al. [38] designed a stability and robustness guaranteed TRFC estimation method. A 3-DOF vehicle model was used by Ren et al., [23] which proposed a hybrid friction estimator based on vehicle responses to a rapidly varying fish-hook steering maneuver. The lateral tire force or self-alignment was chosen to estimate TRFC depending on the excitation levels.

Choi et al. [41] employed linearized RLS technique for real-time identification of TRFC together with the tire stiffness on the basis of vehicle responses to combined braking and steering inputs. The study employed the brush tire model as described in the book written by Pacejka [101]. Gustafsson [106] and Rajamani et al. [29] obtained individual wheel TRFCs on the basis of the longitudinal slip slope which is estimated using RLS approach by assuming linear relationship between the longitudinal force and the slip. This linearity, however, can be considered valid only for very small slip deformations of the tire. Castro et al. [103] proposed a constrained RLS approach for real-time TRFC estimation using optimal linear parameterization of the non-linear Burckhardt tire model. Enisz et al. [40] proposed an EKF framework with road friction as a random-walk variable to facilitate TRFC estimation. The study employed a two-wheel longitudinal vehicle dynamic model together with the MF tire model. Another study employed a sliding-mode observer in conjunction with the RLS technique for identifying TRFC for synthesis of a traction control system [35]. The effectiveness of the method was illustrated for the vehicle accelerating on a high friction road. Zhao et al. [21] proposed a robust TRFC estimation algorithm for anti-lock braking system, where tire forces were observed by the discrete-time KF followed by TRFC estimation using the RLS method.

The aforementioned studies have shown that an accurate estimation of TRFC can be obtained

from lateral and/or longitudinal dynamic responses of the vehicle. The effective estimation of TRFC generally involves a trade-off between sufficient excitations and small disturbances on vehicle motion. Most of the traditional longitudinal dynamics-based methods, however, impose relatively large magnitudes of braking/acceleration to achieve sufficient variations in dynamic responses for identifying the TRFC. These maneuvers may not be practical during normal driving and may interfere with the desired vehicle motion in real driving situations. It is thus desirable to develop TRFC estimation methods involving adequate excitations to warrant convergence of the parameter estimation algorithm while ensuring minimal interference with the vehicle motion. It is noted that a disturbance along the longitudinal axis would be more practical for implementation as opposed to the lateral excitation in real driving conditions. Moreover, variations in longitudinal motion of the vehicle are more commonly encountered during routine driving and are considered acceptable to the occupants. This chapter presents the development of longitudinal dynamics-based TRFC estimation method, which ensures relatively small changes in the vehicle speed.

3.2 Estimation Approach and Tire Model

3.2.1 An Overview of the Methodology

A two-stage braking pressure pulse input is designed for generating sufficient longitudinal excitations while ensuring minimal interference with vehicle velocity. In the *Stage I*, a series of up to five braking pressure pulses with varying magnitude ($p_{pi}, i = 1, ..., 5$) is utilized to identify the desired minimal magnitude of the braking pulse (p_s) for TRFC estimation through a heuristic rule. In the *Stage II*, a single braking pressure pulse with magnitude of p_s is implemented for quantitative TRFC estimation. Qualitative TRFC estimation can be obtained from *Stage I* alone making *Stage II* unnecessary if such accuracy is acceptable. In order to make the whole estimation procedure more practical, a controlled normalized throttle position (n_{th}) is also formulated to restore the vehicle speed after applying the braking pulse in both the stages. It should be noted that the tire forces as well as the quantitative TRFC are estimated on the basis of longitudinal dynamic responses of the

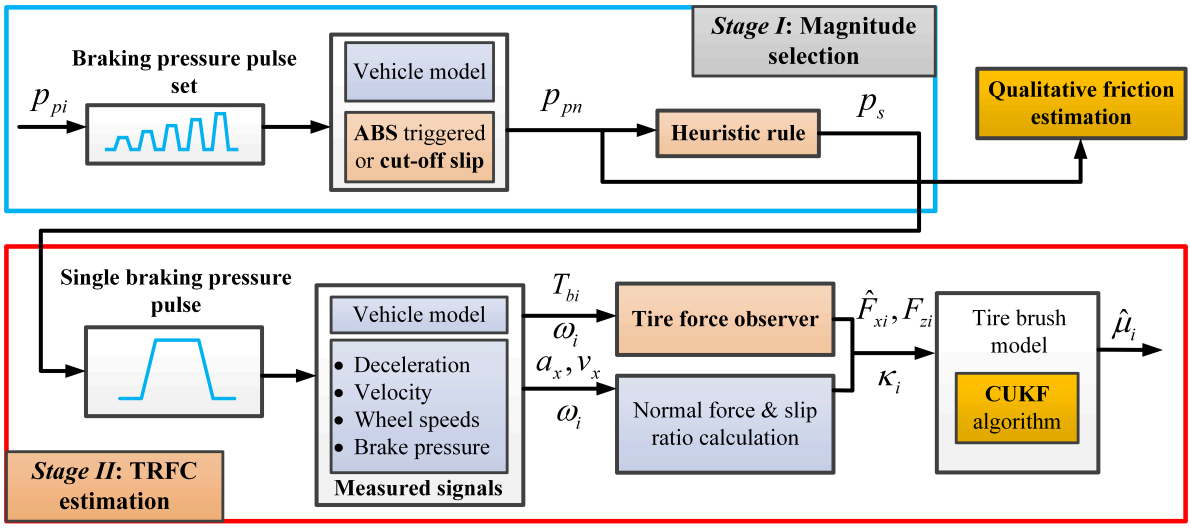

Figure 3.1: Block diagram of the estimation algorithm (braking pressure pulse).

vehicle subject to the braking pressure pulse in *Stage II*, when high accuracy of TRFC estimation is required.

Figure 3.1 illustrates the block diagram of the proposed algorithm, which involves following measured states related to the longitudinal responses of the vehicle:

- Longitudinal deceleration (a_x) and wheel's angular velocity (ω_i) that may be acquired from on-board sensors.
- Instantaneous forward velocity (v_x), which may be obtained from on-board sensors or measured using the GPS.
- Braking torque (T_{bi}), which can be obtained from the brake pressure.

While the normal force (F_{zi}) and slip ratio (κ_i) are computed from the available measured signals, a modified form of the tire force observer from [24] is formulated for estimating the braking force ($\hat{F}_{xi}$). An estimate of the TRFC ($\hat{\mu}_i$) is subsequently obtained from the estimated tire forces and the calculated slip ratio using the brush tire model [21]. For this purpose, a new constrained unscented Kalman filter (CUKF) algorithm is proposed to achieve rapid convergence and improved accuracy of the estimation, where the TRFC is considered as a state in the tire model.

Remark 3.1 *The tire force and TRFC estimations are designed with a focus on the rear-axle wheels as opposed to the front wheels. This is motivated by the fact that the contributions of the drive-train dynamics to rotational dynamics of the rear wheels can be neglected when the front-wheel drive vehicle is considered.*

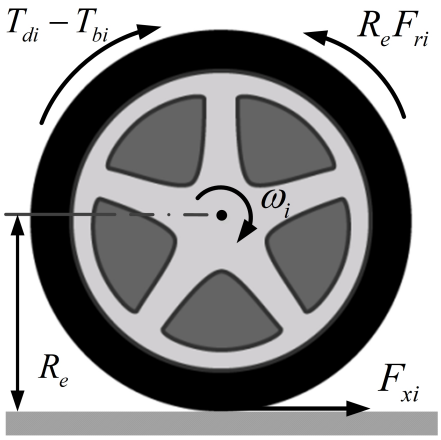

Figure 3.2: Wheel rotational dynamic model.

3.2.2 Wheel Rotational Dynamics

The governing equation of rotational dynamics of an individual vehicle's wheel, as shown in Figure 3.2, is obtained as:

$$I_\omega \dot{\omega}_i = T_{di} - T_{bi} - R_e F_{xi} - R_e F_{ri} \tag{3–1}$$

where I_w is the moment of inertia of the wheel, ω_i is the rotation angular speed of an individual wheel, R_e is the tire effective radius, and $i = 1, 2, 3, 4$ represent the front-left, front-right, rear-left and rear-right wheels, respectively. F_{xi} denotes the individual longitudinal tire force and $F_{ri} = F_{zi} f_r$ is the rolling resistance force with F_{zi} being the individual tire normal force. T_{di} and T_{bi} in the above equation denote the driving and braking torques, respectively. The braking torque is directly related to the hydraulic fluid pressure (p_i) and the brake force gain K_{Bi} of an individual tire [31]:

$$T_{bi} = K_{Bi} \cdot p_i \tag{3–2}$$

3.2.3 Tire Model

It has been reported that the nonlinear relation between the tire slip ratio and the braking force of a tire, including the force saturation, can be accurately described by the brush tire model [21,41]. The tire force predicted by the model directly relates to the road friction coefficient, such that:

$$F_{xi} = \frac{C_{xi} \cdot \kappa_i/(1+\kappa_i)}{f} F \tag{3–3}$$

where

$$f = \sqrt{C_{xi}^2 \cdot (\kappa_i/(1+\kappa_i))^2}$$

$$F = \begin{cases} f - \frac{f^2}{3\mu_i F_{zi}} + \frac{f^3}{27\mu_i^2 F_{zi}^2}, & \text{if } f \leqslant 3\mu_i F_{zi} \\ \mu_i F_{zi}, & \text{else} \end{cases}$$

in which C_{xi} is the longitudinal stiffness of the tire i, and μ_i is the TRFC.

Neglecting the lateral and roll motions of the vehicle, the instantaneous normal forces acting on the individual tire can be computed considering vehicle longitudinal deceleration, a_x, as:

$$F_{zi} = \begin{cases} \dfrac{mgl_r - ma_x h_c}{2 \cdot l}, i = 1,2 \\ \dfrac{mgl_f + ma_x h_c}{2 \cdot l}, i = 3,4 \end{cases} \tag{3–4}$$

where g is the acceleration due to gravity, h_c is the *CG* of the vehicle, l_f and l_r are the distances from the *CG* to the front- and rear-axle, respectively, and l is vehicle's wheelbase.

The longitudinal wheel slip of tire i, κ_i is defined as:

$$\kappa_i = \begin{cases} 1 - \dfrac{R_e \cdot \omega_i}{v_x}, \text{ if } v_x > R_e \cdot \omega_i, \ v_x \neq 0 \\ 1 - \dfrac{v_x}{R_e \cdot \omega_i}, \text{ if } v_x < R_e \cdot \omega_i, \ \omega_i \neq 0 \end{cases} \tag{3–5}$$

From (3–4) and (3–5), it is evident that the instantaneous normal force and tire slip ratio can be computed from the measured states, a_x, ω_i and v_x.

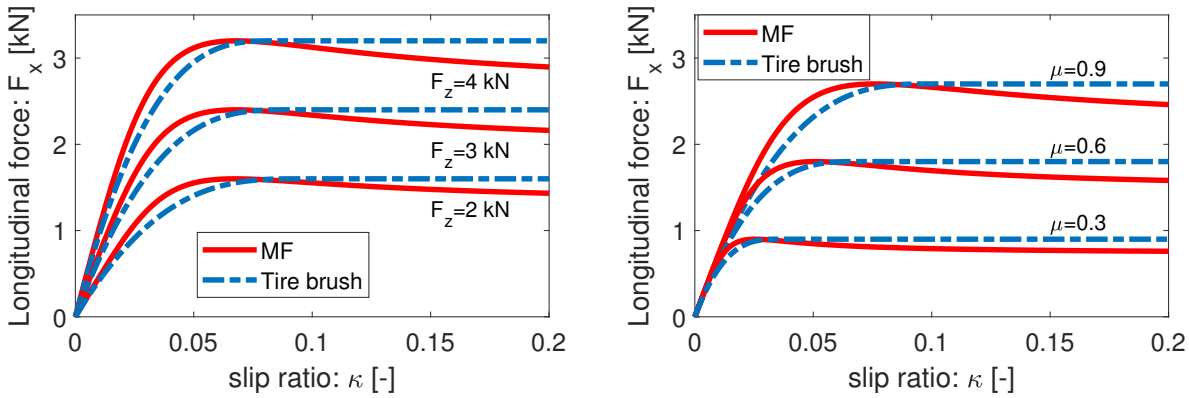

(a) (b)

Figure 3.3: Comparisons of longitudinal tire forces obtained from the brush tire model and the Magic formula (MF) formula as a function of the slip ratio considering variations in the (a) normal force ($\mu = 0.8$); and (b) road friction coefficient ($F_z = 3$ kN).

The adequacy of the brush tire model under pure slip ratio is examined by comparing the longitudinal force-slip characteristics of the tire obtained from the above relation with those obtained from the widely used MF tire model [107, 108], as seen in Figure 3.3. The comparisons are illustrated considering three different normal loads (2, 3 and 4 kN) in Figure 3.3(a), and three different road friction coefficients (0.3, 0.6 and 0.9) in Figure 3.3(b). The comparison results suggest that the brush tire model yields longitudinal force-slip properties comparable to those of the MF model up to about 15% slip, which is considered as commonly encountered slip range [21, 44]. Considering the tire longitudinal stiffness is largely affected by the tire normal load [94], the longitudinal stiffness is assumed to be constant when there are only small variations in the tire normal load.

3.3 Vehicle Maneuvers Design

The TRFC estimations generally involve relatively large excitation, which may constitute undesired disturbance on the vehicle motion [21, 41]. In the first method, the TRFC estimation algorithm is formulated under controlled braking inputs, which are imposed in the form of short duration pulses in the master cylinder brake pressure (p_{mc}) in order to reduce interference with the

vehicle motion.

3.3.1 Braking Pulse Design for TRFC Estimation

Braking pulse designed for TRFC estimation in the *Stage II* is firstly described in this section. With the purpose of minimizing interference with the vehicle motion, a triangular braking pressure pulse was firstly attempted, which revealed poor convergence of the estimation algorithm even under relatively high peak pressure. This was attributed to rapid decrease in the slip ratio following the braking pulse. Subsequently, a braking pressure in the form of a 2 s trapezoidal pulse was utilized, where the braking pressure p_{mc} was ramped from zero to a peak value of p_s for 0.5 s at the instant $t_0 = 1$ s. The peak pressure was held for 1 s and released to zero over the next 0.5 s in a ramp-down manner. For a road surface with nearly uniform friction (uniform-μ) over the observation period, the controlled braking pressure input is thus described as:

$$p_{mc} = \begin{cases} 0, & t \leqslant t_0,\ t > t_0 + 2 \\ 2p_s(t - t_0), & t_0 < t \leqslant t_0 + 0.5 \\ p_s, & t_0 + 0.5 < t \leqslant t_0 + 1.5 \\ p_s - 2p_s(t - (t_0 + 1.5)), & \text{else} \end{cases} \tag{3–6}$$

and shown in Figure 3.4(a). In order to reduce the interference with vehicle speed, it is essential to select minimal peak pressure as well as peak hold duration while ensuring sufficient slip ratio generation for the algorithm to converge to the actual friction value. Only uniform-μ road surfaces were considered in the first method and preliminary simulations revealed that the trapezoidal deceleration inputs with 1 s peak hold duration can lead to estimation algorithm to converge to a stable value. A low magnitude pressure peak may yield underestimation due to insufficient slip ratio, while too high a value will likely trigger the ABS. The generated slip ratio, however, is related to the tire-road friction in addition to the braking pressure. A constant value of p_s is thus not considered feasible. The desired minimal magnitude of p_s which is varying with road friction,

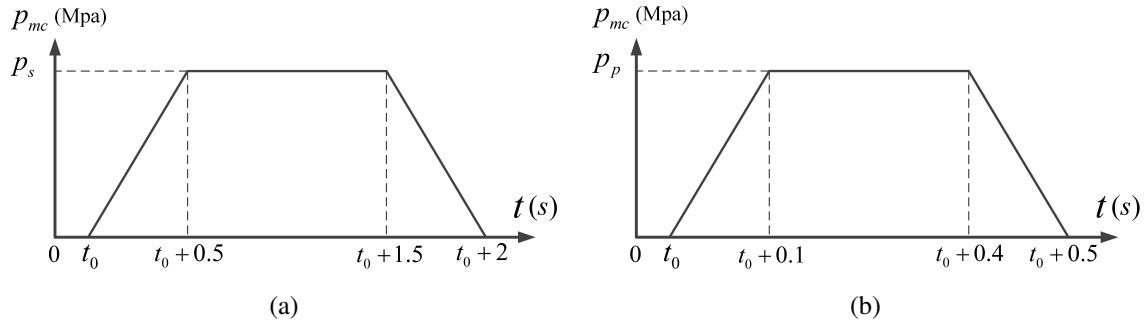

Figure 3.4: The designed braking pressure pulses for (a) TRFC estimation; and (b) identification of desired braking pulse magnitude.

should be priorly determined. For this purpose, a series of braking pressure pulses with increasing magnitude was designed in the *Stage I*, as described in the following subsection.

3.3.2 Identification of Desired Braking Pulse Magnitude

The widely used control principle of ABS is the slip ratio threshold-based algorithm. The ABS is triggered as the slip ratio exceeds a threshold value leading to oscillations in the wheel speed and the slip ratio [21]. The desired minimal braking pressure that leads to minimal slip ratio required for the TRFC algorithm to converge is identified so as to reduce the disturbance to the vehicle speed. Preliminary simulations suggested that the minimal slip ratio leading to satisfactory convergence of the estimation algorithm could range from 0.012 for the low friction road ($\mu = 0.2$) to 0.085 for the high friction road ($\mu = 0.9$). Furthermore, simulations were performed using a CarSim vehicle model (class-C) to determine the minimal braking pressure leading to triggering of the ABS considering road friction in the 0.2 to 0.9 range and different initial forward speeds (v_{x0}). The default slip-ratio threshold for activating the ABS of the class-C vehicle model was set as 0.12. The simulations were performed using short duration trapezoidal pulses (0.3 s peak hold)

Table 3.1: Variations in the peak pressure threshold (p_p^*) for different road surfaces.

Road surface friction (μ)	p_p^* (MPa)	Initial speeds (km/h)
0.2	0.8	40 and 30
0.4	1.5	60, 40 and 30
0.6	2.1	80, 60 and 40
0.8	2.5	100, 80 and 60
0.9	2.7	100, 80 and 60

so as to reduce interference with the vehicle speed, such that (as shown in Figure 3.4(b)):

$$p_{mc} = \begin{cases} 0, & t \leqslant t_0,\ t > t_0 + 0.5 \\ 10p_p(t - t_0), & t_0 < t \leqslant t_0 + 0.1 \\ p_p, & t_0 + 0.1 < t \leqslant t_0 + 0.4 \\ p_p - 10p_p(t - (t_0 + 0.4)), & \text{else} \end{cases} \tag{3–7}$$

where $t_0 = 1$ s and p_p is peak magnitude of the pulse. The threshold pressures (p_p^*) leading to triggering of the ABS were identified for different μ values by gradually increasing p_p. As examples, Figure 3.5 illustrates time-histories of the slip ratio for two different roads with $\mu = 0.9$ and $\mu = 0.4$. The results are presented only for values of p_p close to those leading to the ABS triggering at different initial speeds. The results clearly show that the threshold pressures vary substantially with μ and the threshold values were obtained as 2.7 MPa for $\mu = 0.9$ and 1.5 MPa for $\mu = 0.4$. The results also suggest relatively lower dependence of the threshold pressures on the forward speeds considered in the simulations. Similar trends were also observed for other road surfaces. Table 3.1 summarizes the threshold values of p_p^* leading to ABS activation on different road surfaces together with the considered speed ranges.

Owing to the strong dependency of the braking pressure threshold on the road surface, a method was designed to identify desired minimal pulse pressure (p_s) for TRFC estimation. The method was

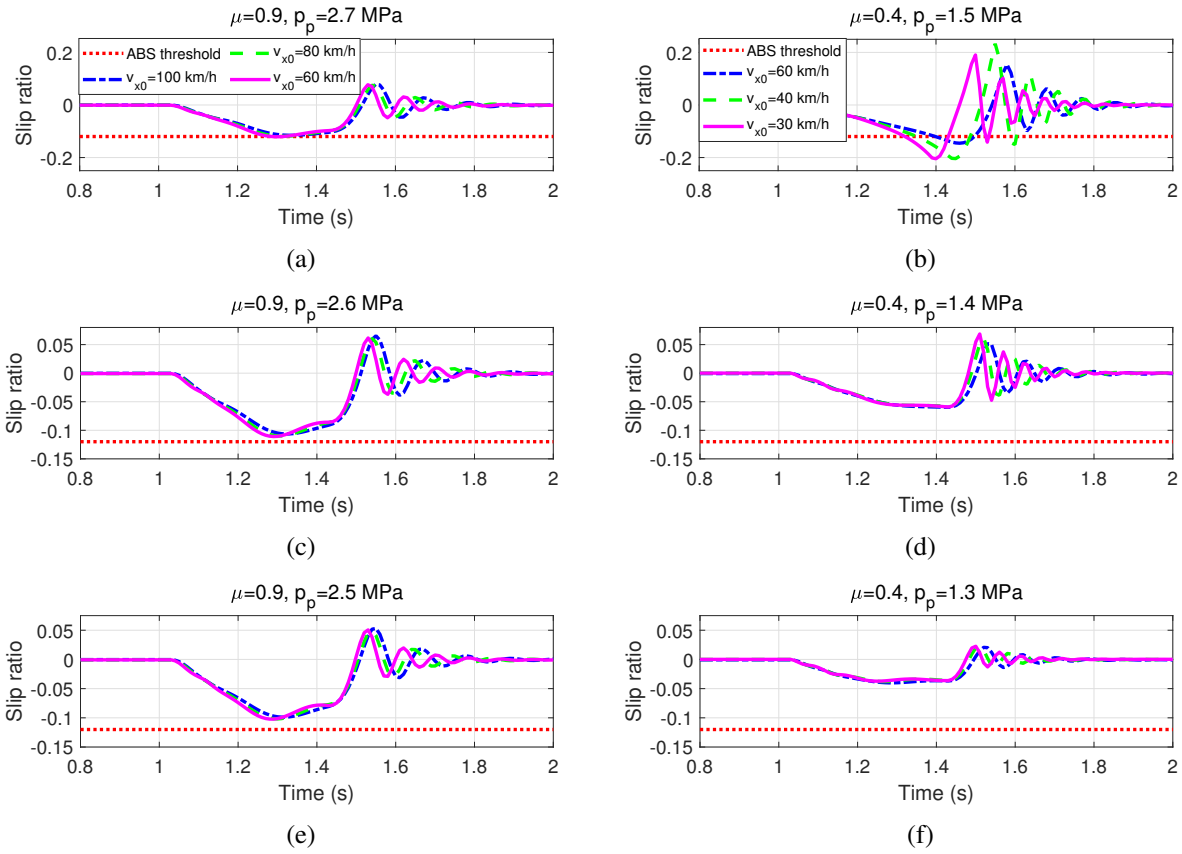

Figure 3.5: Time-histories of the slip ratio developed at the rear-left tire under different speeds and magnitudes of the braking pressure pulse considering two different TRFCs.

based on application of a series of up to five braking pulses with increasing peak magnitude. The interval between two consecutive pulses was set as 0.5 s. The variation in the braking pressure for each pulse was governed by (3–7). The magnitudes of the five consecutive pulses ($p_{pi}, i = 1, ..., 5$) were initially chosen to be 0.1 MPa below the threshold pressures triggering the ABS (p_p^*) identified for different forward speeds and road friction coefficients. The value of 0.1 MPa was selected such that slip ratio is limited to about 0.1, which is slightly below the ABS slip threshold and sufficient to achieve satisfactory convergence of the TRFC estimation algorithm even on a high friction road surface ($\mu = 0.9$), and thus considered as the cut-off slip ratio. This ensured the absence of the repeated ABS activations during the estimation process. However, the generated slip ratio is very sensitive to the magnitude of the braking pulse on low friction roads ($\mu \leqslant 0.4$). This is also evident in Figure 3.5, which suggests that even a small variation in the magnitude of the braking pressure,

in the order of 0.1 MPa, could lead to large variation in slip ratio. This constituted a challenge in identifying an appropriate magnitude of the braking pressure pulse so as to limit to the cut-off slip. The peak pressures of the first two pulses (p_{p1} and p_{p2}) corresponding to road surfaces with low friction coefficients ($\mu \leqslant 0.4$) were thus limited to the threshold values triggering the ABS. The magnitudes of the subsequent pulses ($p_{pi}, i = 3, 4, 5$) were ensured to be 0.1 MPa below their respective threshold pressures as summarized in Table 3.1. The magnitudes of the consecutive peaks were thus selected as $p_{p1} = 0.8$, $p_{p2} = 1.5$, $p_{p3} = 2.0$, $p_{p4} = 2.4$ and $p_{p5} = 2.6$ MPa.

The slip ratio of each wheel was monitored, and the input was terminated when the slip ratio approached or exceeded 0.1 or the ABS was triggered. As examples, Figure 3.6 illustrates the slip ratio responses of the vehicle model subject to series of braking pressure pulses for two different friction coefficients. It is evident that the $\mu = 0.6$ road and the $\mu = 0.9$ road yield desired slip ratio of 0.1 during applications of the third and fifth pulse, respectively.

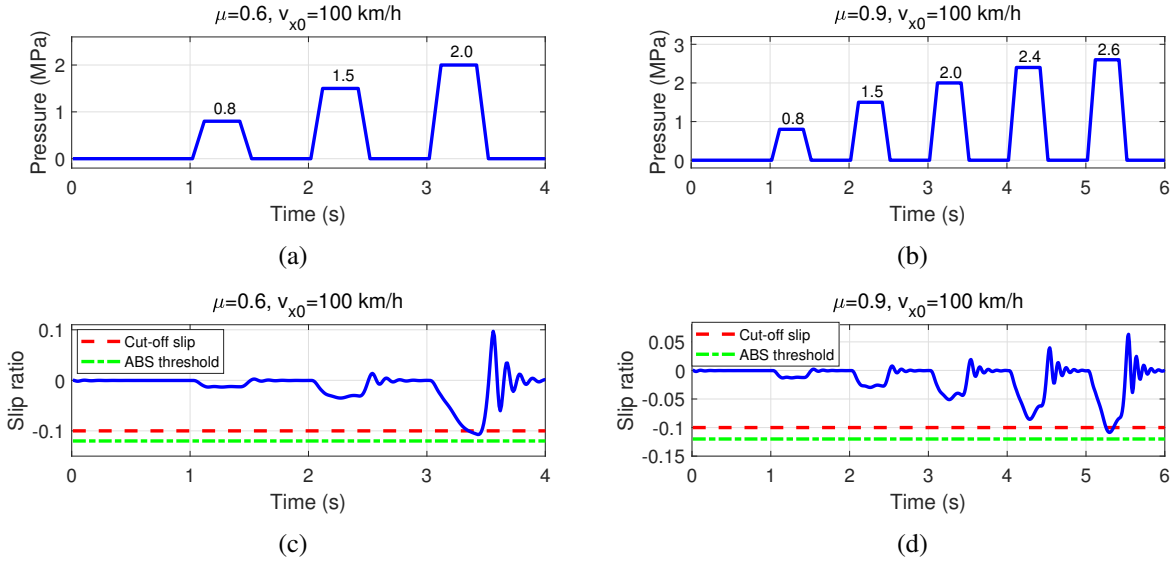

Figure 3.6: Magnitudes of the braking pressure pulses and the slip ratio developed at the rear-left tire.

The desired magnitude of the pressure (p_s) for the *Stage II* of the TRFC estimation algorithm was subsequently selected using the following heuristic rule, which was established based on the repeated simulations considering convergence of the proposed TRFC estimation algorithm for

Table 3.2: Qualitative friction estimation results.

Pulse number (n)	Friction range	Adhesion quality
1	<0.2	Very low
2	0.2–0.4	Low
3	0.4–0.6	Medium
4	0.6–0.8	High
5	>0.8	Very high

broad ranges of road surfaces. Based on which pulse ($n = 1, ..., 5$) leading to ABS activation or the cut-off slip ratio, the magnitude of p_s in the *Stage II* is set as follows:

$$p_s = \begin{cases} p_{ss} - 0.2, & \text{if } \kappa_i \geqslant 0.1 \\ p_{ss}, & \text{else} \end{cases} \tag{3–8}$$

where,

$$p_{ss} = \begin{cases} p_{pn} - 0.2, & \text{if } n = 1, 2 \\ p_{pn} - 0.1, & \text{if } n = 3, 4, 5 \end{cases} \tag{3–9}$$

and κ_i is the generated slip ratio under the braking pressure p_{ss}.

3.3.3 Relationship between *Stage I* and *Stage II*

Depending on the pulse that leads to ABS activation or the cut-off slip ratio during *Stage I*, a qualitative estimation of TRFC may be obtained. This helps identify the road adhesion quality into five different conditions, namely, 'very low', 'low', 'medium', 'high' and 'very high', as summarized in Table 3.2. Based on the tire responses, such qualitative results are more reliable than the traditional qualitative methods [25–27], which neglect the roles of the tire operating factors. The two stages are not mandatory and the *Stage II* may become unnecessary if a qualitative estimate of TRFC is acceptable in a given application. This may be true and reasonable considering the road

friction coefficient is not always a fixed value. It is worth noting that the approximated friction range for 'very low' and 'very high' friction roads ($n = 1$ and $n = 5$) has sufficient accuracy, making the *Stage II* unnecessary in these two cases. For other road conditions, *Stage II* is desirable for TRFC estimation with a higher accuracy.

3.4 Braking Force Estimation

The estimation algorithm is designed with a focus on the rear-axle wheels as opposed to the front wheels. This is motivated by the fact in our situation that rear wheels exhibit relatively higher slip ratio during braking despite the lower brake gain compared to the front wheels. Moreover, the contributions of the drive-train dynamics to rotational dynamics of the rear wheels can be neglected since the front-wheels drive vehicle is considered in the first method ($T_{di} = 0; i = 3, 4$).

The observer in [24, 109] was modified for estimating rear tire longitudinal force from the wheels' rotational dynamics. The proposed observer incorporates the contribution due to rolling resistance, and the estimated force $\hat{F}_{xi}$ $(i = 3, 4)$ can be expressed as:

$$\begin{cases} \hat{F}_{xi} = -\frac{I_w}{R_e}\chi_i - \frac{I_w}{R_e}\rho_i\omega_i \\ \dot{\chi}_i = -\rho_i\chi_i - \rho_i(\frac{-T_{bi}-R_eF_{ri}}{I_w} + \rho_i\omega_i) \end{cases} \tag{3–10}$$

where ρ_i is a positive gain, χ_i is an intermediate variable generated by the second equation in (3–10). From Eq. (3–1), the angular deceleration of the wheel can be expressed as:

$$\dot{\omega}_i = -\frac{R_e}{I_w}F_{xi} + \frac{-T_{bi} - R_eF_{ri}}{I_w} \tag{3–11}$$

Equations (3–10) and (3–11) yield following relationship between time derivative of $\hat{F}_{xi}$ and the

force estimation error, $\hat{F}_{xi} - F_{xi}$:

$$\begin{aligned}
\dot{\hat{F}}_{xi} =& -\frac{I_w}{R_e}\dot{\chi}_i - \frac{I_w}{R_e}\rho_i\dot{\omega}_i \\
=& -\frac{I_w}{R_e}\rho_i[-\chi_i - \frac{-T_{bi} - R_e F_{ri}}{I_w} - \rho_i\omega_i] \\
& -\frac{I_w}{R_e}\rho_i[-\frac{R_e}{I_w}F_{xi} + \frac{-T_{bi} - R_e F_{ri}}{I_w}] \\
=& -\frac{I_w}{R_e}\rho_i[-\chi_i - \rho_i\omega_i - \frac{R_e}{I_w}F_{xi}] \\
=& -\rho_i[-\frac{I_w}{R_e}\chi_i - \frac{I_w}{R_e}\rho_i\omega_i - F_{xi}] \\
=& -\rho_i(\hat{F}_{xi} - F_{xi})
\end{aligned} \tag{3–12}$$

Considering the Lyapunov function of the form [109]:

$$V_i = \frac{1}{2}(F_{xi} - \hat{F}_{xi})^2 \tag{3–13}$$

The time derivative of V_i is obtained, as:

$$\begin{aligned}
\dot{V}_i &= (F_{xi} - \hat{F}_{xi})(\dot{F}_{xi} - \dot{\hat{F}}_{xi}) \\
&= (F_{xi} - \hat{F}_{xi})[\dot{F}_{xi} + \rho_i(\hat{F}_{xi} - F_{xi})] \\
&= -\rho_i(F_{xi} - \hat{F}_{xi})^2 + \dot{F}_{xi}(F_{xi} - \hat{F}_{xi}) \\
&\leqslant -\rho_i(F_{xi} - \hat{F}_{xi})^2 + \frac{(F_{xi} - \hat{F}_{xi})^2}{2} + \frac{(\dot{F}_{xi})^2}{2}
\end{aligned} \tag{3–14}$$

Assuming that $\dot{F}_{xi}$ remains bounded, $|\dot{F}_{xi}| \leqslant C$, the above can be re-written as:

$$\dot{V}_i \leqslant -(\rho_i - \frac{1}{2})(F_{xi} - \hat{F}_{xi})^2 + \frac{C^2}{2} \tag{3–15}$$

As the right-hand side of (3–15) converges to zero, the estimation error $|F_{xi} - \hat{F}_{xi}|$ becomes bounded, as:

$$|F_{xi} - \hat{F}_{xi}| \leqslant \frac{C}{\sqrt{|2\rho_i - 1|}} \tag{3–16}$$

Since ρ_i can be arbitrarily chosen to be large, the estimation error can be bounded by a small constant.

3.5 TRFC Estimation Algorithm

3.5.1 CUKF Algorithm

The TRFC can be considered as a vehicle state embedded in the brush tire model, which yields tire force as a nonlinear and segmented function of the slip ratio and the TRFC. The linearization of the tire model around the operating point would require evaluations of the Jacobian matrices, which may not be computationally efficient [110]. The UKF, based on the unscented transformations instead of the linearization, is thus considered as a better alternative.

Defining the TRFC as a state $\tau_k = \mu_{i,k}$, and the measurement $y_k = F_{xi,k}$, where $F_{xi,k}$ are the braking forces developed at rear tires, $i = 3, 4$. The subscript k is the index for the time step. The brush tire model can be expressed as a one-state and one-measurement discrete-time nonlinear system as:

$$\begin{aligned} \tau_k &= F(\tau_{k-1}) + w_k, w_k \sim (0, M_k) \\ y_k &= H(\tau_k) + v_k, v_k \sim (0, N_k) \end{aligned} \tag{3–17}$$

where w_k and v_k are the process noise and measurement noise, respectively, and M_k and N_k are the respective covariances of w_k and v_k. The state transition F and observation H functions are expressed as:

$$F(\tau_{k-1}) = \tau_{k-1} = \mu_{i,k-1} \tag{3–18}$$

and

$$H(\tau_k) = H(\mu_{i,k}) = F^c_{xi,k} \tag{3–19}$$

where $F^c_{xi,k}$ is the longitudinal tire force obtained from the brush tire model considering the instantaneous normal force $F_{zi,k}$ and the tire slip ratio $\kappa_{i,k}$, together with the estimated TRFC at the preceding step $\hat{\mu}_{i,k-1}$.

The normal force at each sampling interval is obtained from Eq. (3–4), and the longitudinal tire force is expressed in the normalized form, as:

$$r_{i,k} = \frac{\hat{F}_{xi,k}}{F_{zi,k}},\ i = 3, 4 \tag{3–20}$$

where $\hat{F}_{xi,k}$ is the estimated braking tire force from the estimator (3–10). The TRFC of a passenger vehicle generally lies between 0 and 1 and it is physically greater than or equal to the normalized tire force $r_{i,k}$, such that:

$$\begin{cases} 0 < \mu \leqslant 1 \\ \quad \mu \geqslant r_{i,k} \end{cases} \tag{3–21}$$

Based on (3–21), practical varying constraints on the system state can be designed and a new CUKF framework is further formulated to enhance the rate of convergence. With L being the dimension of the state vector, the $2L + 1$ transformed sigma points $\Gamma^{ii}_{k|k-1}$ are updated according to the following rules:

$$\Gamma^{ii}_{k|k-1} = \begin{cases} 1, & \text{if } \Gamma^{ii}_{k|k-1} \geqslant 1 \\ r_{i,k}, & \text{else if } 0 < \Gamma^{ii}_{k|k-1} \leqslant r_{i,k} \\ 0, & \text{else if } \Gamma^{ii}_{k|k-1} < 0 \\ \Gamma^{ii}_{k|k-1}, & \text{else} \end{cases} \tag{3–22}$$

where $ii = 0, ..., 2L$. The pseudo-code of the CUKF algorithm is presented in Algorithm 1, where $\Gamma^{ii}_{k|k-1}$ and $\gamma^{ii}_{k|k-1}$ are the ii-th columns of the matrices, $\Gamma_{k|k-1}$ and $\gamma_{k|k-1}$, respectively, N is the total number of the time steps, $\lambda = \alpha_u^2(L + \sigma) - L$ is a scaling parameter with σ being a secondary scaling parameter which is usually set to 0 [99], and W_s^{ii} and W_c^{ii} are the weighting factors for

$2L + 1$ sigma points, given by:

$$
\begin{aligned}
W_s^0 &= \frac{\lambda}{L+\lambda} \\
W_c^0 &= \frac{\lambda}{L+\lambda} + (1 - \alpha_u^2 + \beta_u) \\
W_s^{ii} &= W_c^{ii} = \frac{1}{2(L+\lambda)}, ii = 1, ..., 2L
\end{aligned}
\tag{3–23}
$$

where α_u is a constant determining the spread of the sigma points around the mean of τ_k, the constant β_u permits the use of prior knowledge of the distribution of τ_k. For a Gaussian distribution, $\beta_u = 2$ has been suggested as the optimal [99]. As can be seen in Algorithm 1, both the *a priori* state estimate $\hat{\tau}_k^-$ and its error covariance P_k^- include the information of the constraints on the state. Following the procedure, the information of the constraints on state is further introduced to the predicted measurement $\hat{y}_k^-$ and covariances $P_{y_k y_k}$ and $P_{\tau_k y_k}$. While the formulated CUKF framework helps to enhance the rate of convergence, it is still easy to implement with a simple structure similar to the UKF. In the first method, the CUKF parameters are selected as $\alpha_u = 1, \beta_u = 2$ and $\sigma = 0$, which provided satisfactory estimations of TRFC. The UKF technique for nonlinear estimations has been described in detail in [96, 99, 111].

3.5.2 Conditions for Terminating Updates

The TRFC estimation algorithm considers controlled braking pressure input, which is released to zero at the end of the designed maneuver. The resulting low values of the slip ratio at the end of the maneuver can lead to considerable TRFC estimation error. It is thus essential to terminate the recursive updating and retain the TRFC being estimated prior to the slip ratio becoming too small.

For the braking pressure pulse inputs, described in (3–6), the brake pressure p_{mc} decreases from the peak value p_s to zero within 0.5 s near the end of the maneuver. The slip ratio decreases rapidly following the release of the braking pressure. Thus, the termination instant for the updating, t_{stop}, is set as the instant when the release of braking pressure is initiated. In order to further improve the accuracy, the estimated TRFC after t_{stop} is taken as the average of the estimations obtained during

Algorithm 1 Pseudo-code of the CUKF.

Input: Tire force $F_{xi,k}$, $F_{zi,k}$, and slip ratio $\kappa_{i,k}$

Output: Estimated TRFC $\hat{\mu}_{i,k}$

Initialization $\hat{\tau}_0 = E(\tau_0)$, $P_0 = E[(\tau_0 - \hat{\tau}_0)(\tau_0 - \hat{\tau}_0)^T]$

for $k \in \{1, ..., N\}$ **do**

  Calculate sigma points

  $\Gamma_{k-1} = [\hat{\tau}_{k-1}\ \hat{\tau}_{k-1} \pm \sqrt{(L+\lambda)P_{k-1}}]$

  Time update and constraints

  $\Gamma_{k|k-1} = F(\Gamma_{k-1})$

  if $\Gamma^{ii}_{k|k-1} \geqslant 1$ **then** $\Gamma^{ii}_{k|k-1} = 1$

  end if

  if $0 < \Gamma^{ii}_{k|k-1} \leqslant r_{i,k}$ **then** $\Gamma^{ii}_{k|k-1} = r_{i,k}$

  end if

  if $\Gamma^{ii}_{k|k-1} < 0$ **then** $\Gamma^{ii}_{k|k-1} = 0$

  end if

  $\hat{\tau}^-_k = \sum_{ii=0}^{2L} W^{ii}_s \Gamma^{ii}_{k|k-1}$

  $P^-_k = \sum_{ii=0}^{2L} W^{ii}_c [\Gamma^{ii}_{k|k-1} - \hat{\tau}^-_k][\Gamma^{ii}_{k|k-1} - \hat{\tau}^-_k]^T$

  $\Gamma_{k|k-1} = [\hat{\tau}^-_k\ \hat{\tau}^-_k \pm \sqrt{(L+\lambda)P^-_k}]$

  $\gamma_{k|k-1} = H(\Gamma_{k|k-1})$

  $\hat{y}^-_k = \sum_{ii=0}^{2L} W^{ii}_s \gamma^{ii}_{k|k-1}$

  Measurement update

  $P_{y_k y_k} = \sum_{ii=0}^{2L} W^{ii}_c [\gamma^{ii}_{k|k-1} - \hat{y}^-_k][\gamma^{ii}_{k|k-1} - \hat{y}^-_k]^T$

  $P_{\tau_k y_k} = \sum_{ii=0}^{2L} W^{ii}_c [\Gamma^{ii}_{k|k-1} - \hat{\tau}^-_k][\gamma^{ii}_{k|k-1} - \hat{y}^-_k]^T$

  $K_k = P_{\tau_k y_k} P^{-1}_{y_k y_k}$

  $\hat{\tau}_k = \hat{\tau}^-_k + K_k(y_k - \hat{y}^-_k)$

  $P_k = P^-_k - K_k P_{y_k y_k} K^T_k$

end for

the period (t_3, t_{stop}) with $t_3 = t_{stop} - 0.5$ as follows:

$$\hat{\mu}_{i,stop} = \frac{1}{k_2 - k_1 + 1} \sum_{k=k_1}^{k_2} \hat{\mu}_{i,k} \tag{3–24}$$

where $k_1 = t_3/T_s$, $k_2 = t_{stop}/T_s$ and T_s is the sampling interval. By doing so, the estimates of the TRFC corresponding to higher slip ratios, which are generally more reliable, can be integrated into the TRFC estimation results when the algorithm stops updating.

3.6 Simulation Results and Discussions

To evaluate the effectiveness of the proposed TRFC identification algorithm, the platforms of MATLAB/Simulink and CarSim were employed. The responses of the CarSim simulation model to braking pulse inputs were considered as the reference or measured states for assessing the performance of the algorithm. White Gaussian noise, however, was added to the model responses for assessing the estimation effectiveness in the presence of the measurement noise. Apart from the TRFC, the associated motion interference of the proposed algorithm was also evaluated in terms of change in the forward speed.

The simulations were performed under the braking inputs, defined in Section 3.3, considering different road surfaces and initial forward speeds. The estimation results were also obtained using UKF and RLS algorithms, as reported in [96] and [99], and compared with those obtained using the CUKF algorithm. The initial settings for CUKF, UKF and RLS are presented in Table 3.3 showing the fairness of the comparison of these three algorithms. It should be noted that the forgetting factor of RLS is tuned based on obtaining best estimation results. The main parameters of the class-C vehicle model are listed as: $l_f = 1.016$ m, $l_r = 1.562$ m, $m = 1416$ kg, $I_w = 0.9$ kgm^2, $R_e = 0.316$ m, $K_{B3} = 200$ N-m/MPa and $C_{x3} = 48$ kN/unit slip, and the sampling interval $T_s = 0.01$ s. Considering negligible roll motion, the forces developed by the left and right tires are identical. The TRFC estimation results obtained from rear-left tire alone are presented below.

Table 3.3: Initial settings of different algorithms.

Algorithm	$\hat{\tau}_0$	P_0	M_k	N_k	λ_k
CUKF	0	10	10^{-4}	4×10^4	—
UKF	0	10	10^{-4}	4×10^4	—
RLS	0	10	—	—	0.92

$\hat{\tau}_0$: initial state; P_0: initial state error covariance; M_k: process covariance; N_k: observation covariance; λ_k: forgetting factor; —: not applied.

3.6.1 High-μ Surface

Simulations were performed for a relatively high friction surface ($\mu = 0.8$) considering an initial forward speed of 100 km/h. Applications of series of braking pulses in the *Stage I* revealed that the cut-off slip ratio of 0.1 occurred during the fourth pulse. The initial stage simulations were thus terminated after the fourth pulse and a controlled throttle input pulse was subsequently applied to restore the vehicle speed. The magnitude of the braking pulse in the *Stage II* was subsequently determined as 2.3 MPa using the heuristic rule (3–8) and (3–9). The estimated longitudinal and normal forces developed at the rear-left tire, and the generated slip ratio are compared with the reference values obtained from CarSim simulations in Figures 3.7(a)-3.7(c). The comparisons suggest relatively small errors between the estimated and targeted values. The algorithm is updating during 1 s to 2.5 s interval. Peak errors in the longitudinal and normal tire forces were 3.3% and 2.5%, respectively, with respect to the reference values, while the peak slip ratio is in the order of 0.08. Figure 3.7(d) compares the TRFC estimated from the proposed algorithm based on CUKF with the reference value and those obtained from the UKF and RLS algorithms, reported in [96, 99]. Both the UKF- and RLS-based methods identified the TRFC with acceptable accuracy since the generated slip ratio was relatively high. The TRFC estimated from both the methods converged to 0.77 after $t = 2.1$ s (1.1 s following the application of the braking pulse), although the UKF approach exhibits very slight advantage in terms of the leading time. The proposed CUKF-based approach, however, resulted in more accurate TRFC and relatively faster convergence. The estimated value

approached very close to the target value of 0.8 at about 1.7 s. From these comparisons, it can be deduced that the CUKF did offer improved rate of convergence and estimation accuracy compared to the RLS and UKF algorithms.

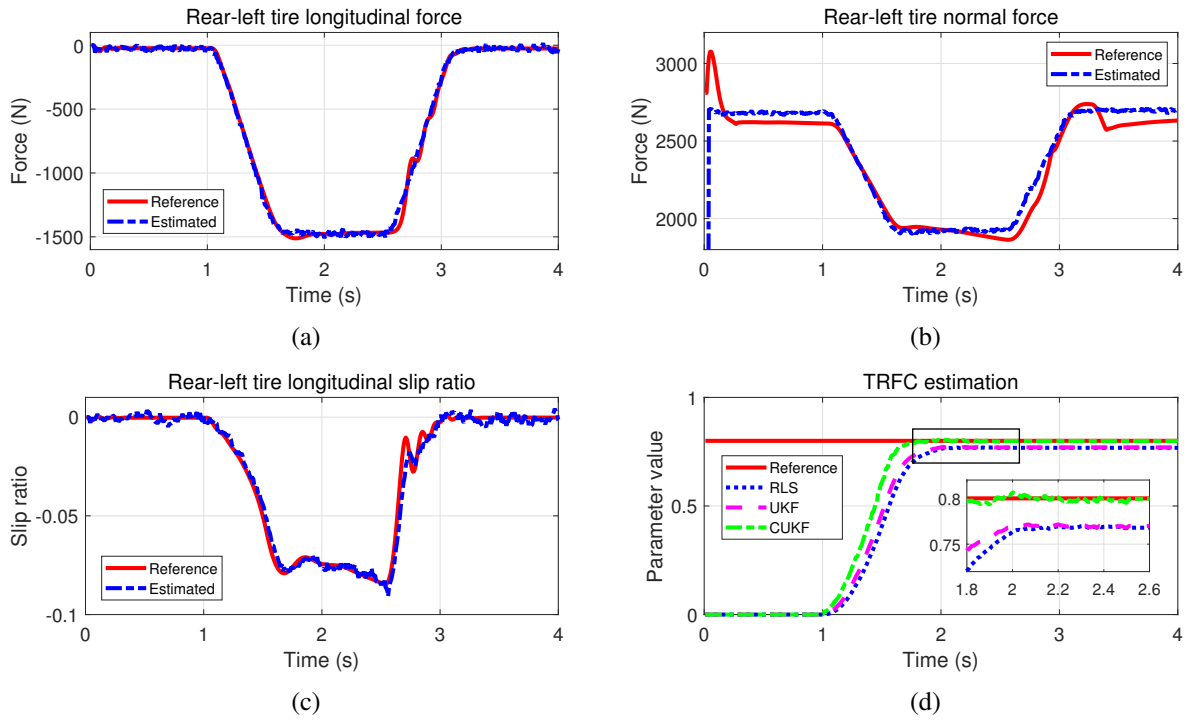

Figure 3.7: Comparisons of the estimated and reference signals at the rear-left tire ($\mu = 0.8$; $v_{x0} = 100$ km/h).

3.6.2 Mid-μ Surface

The TRFC estimation effectiveness of the proposed algorithm was further evaluated for mid-μ road surface ($\mu = 0.5$) considering a cruising speed of 60 km/h. Results obtained for the *Stage I* revealed that the desired slip ratio of 0.1 could be attained during the third pulse, which resulted in a small vehicle speed reduction and the vehicle speed was then restored to the initial cruising speed. According to the heuristic rule, the magnitude of p_s for TRFC estimation in the *Stage II* was set as 1.7 MPa. During the TRFC estimation process in the *Stage II*, both the longitudinal and normal tire force, and the slip ratio could be effectively estimated, as shown in Figures 3.8(a)-3.8(c). Peak errors in the estimated braking and the normal forces were about 8% and 5%, respectively, when

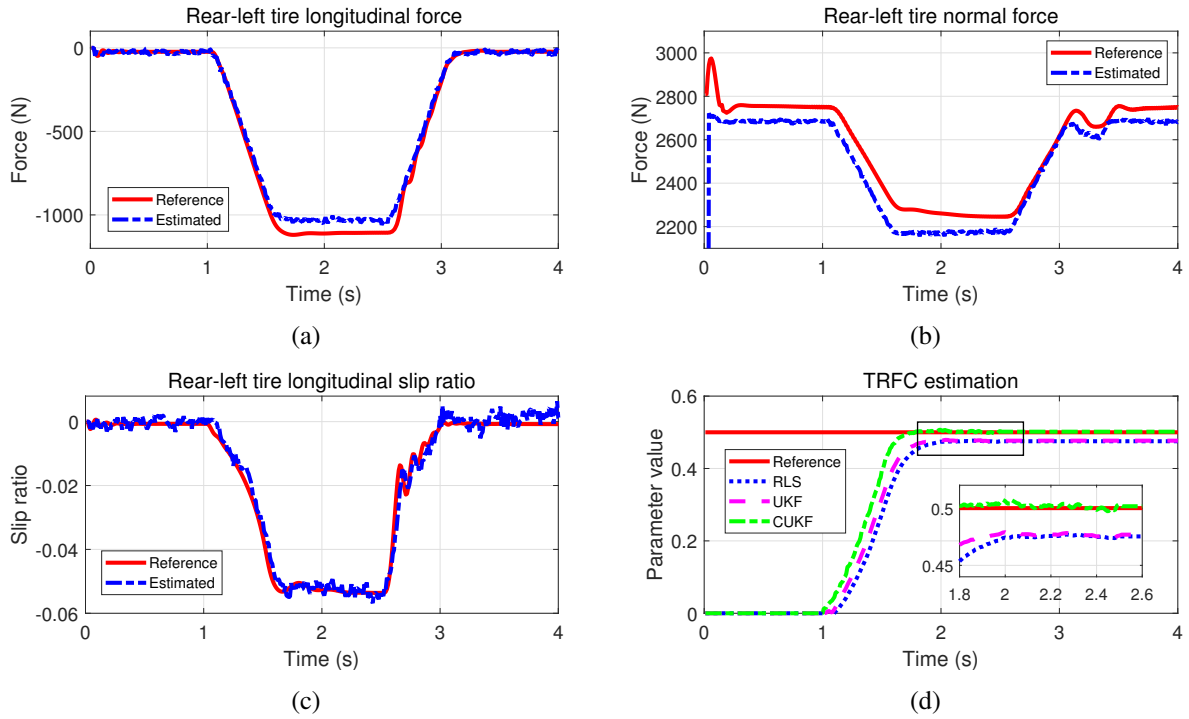

Figure 3.8: Comparisons of the estimated and reference signals at the rear-left tire ($\mu = 0.5$; $v_{x0} = 60$ km/h).

compared to the reference values. These are slightly higher than those observed for the high-μ road with initial speed of 100 km/h and suggest that the force estimator may be sensitive to the vehicle speed and the measurement noises. The slip ratio, however, was estimated more accurately as in case of the high-μ road, as seen in Figure 3.8(c). Under the magnitute of 1.7 MPa in the *Stage II*, the proposed algorithm resulted in accurate estimation of the TRFC, which converged to the target value of 0.5 near $t = 1.7$ s, as evidenced in Figure 3.8(d). As comparison, the TRFC estimated using the UKF and RLS algorithms converged to a slightly lower value of 0.47 until near to $t = 2$ s. It is clear to see that the CUKF was superior to the UKF and RLS algorithms again in terms of faster identification of the TRFC.

3.6.3 Low-μ Surface

Figure 3.9 illustrates the time histories of the estimated and reference tire forces together with the slip ratio, and the TRFC, respectively, for the low-μ road ($\mu = 0.2$) under a forward speed of

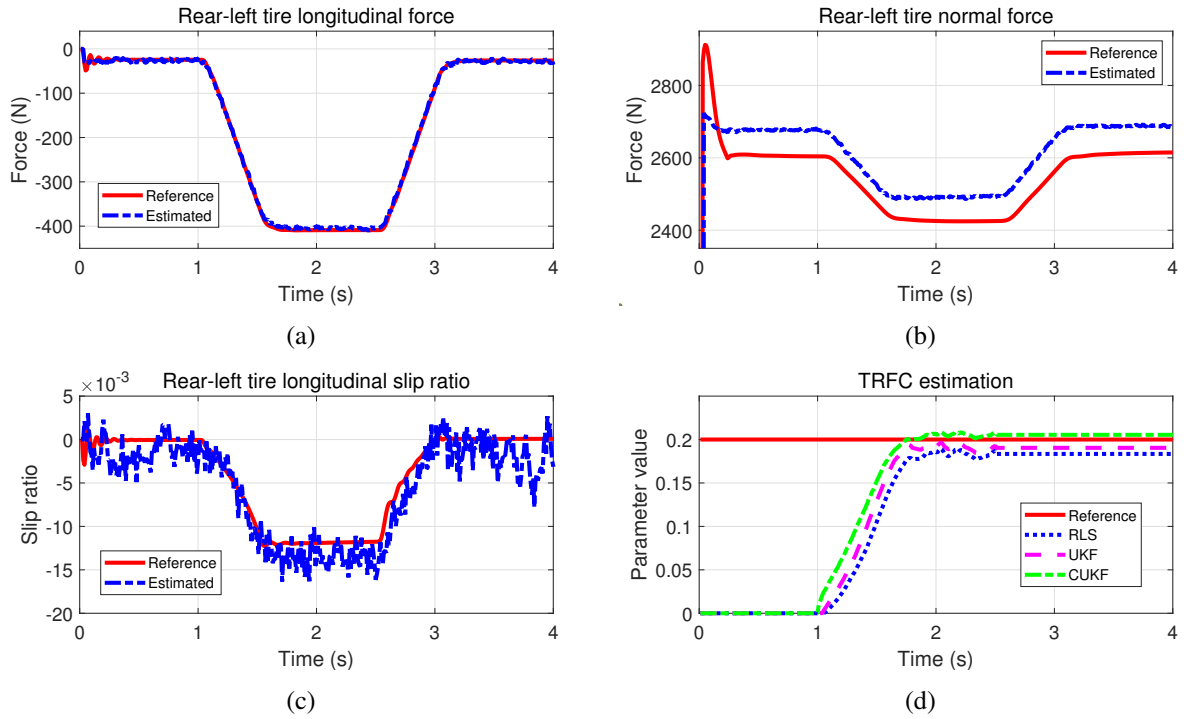

Figure 3.9: Comparisons of the estimated and reference signals at the rear-left tire ($\mu = 0.2$; $v_{x0} = 40$ km/h).

40 km/h. In the *Stage I*, the triggering of the ABS occurred during the first braking pressure pulse input, although the speed reduction was very small. The peak value of the braking pulse (p_s) was subsequently selected as 0.6 MPa in accordance with (3–8) and (3–9) for TRFC estimation in the *Stage II*. This resulted in significantly lower slip ratio, in the order of 1.2%, as seen in Figure 3.9(c). The deviation between the estimated and the targeted braking force was in the order of only 2.5%, while a relatively greater error (3.3%) was observed in the estimated tire normal force. Similar to the high- and mid-μ road conditions, all the three algorithms identified the friction coefficient with good accuracy under the designed braking maneuver. However, the difference in estimation accuracy between the CUKF and UKF is small. This was because the normalized tire force is around 0.16 showing that the tire is working at a slip range close to the optimal slip at which the maximum tire force is generated. Nevertheless, it was obviously noted that the CUKF did distinguish itself with relatively faster convergence, as shown in Figure 3.9(d).

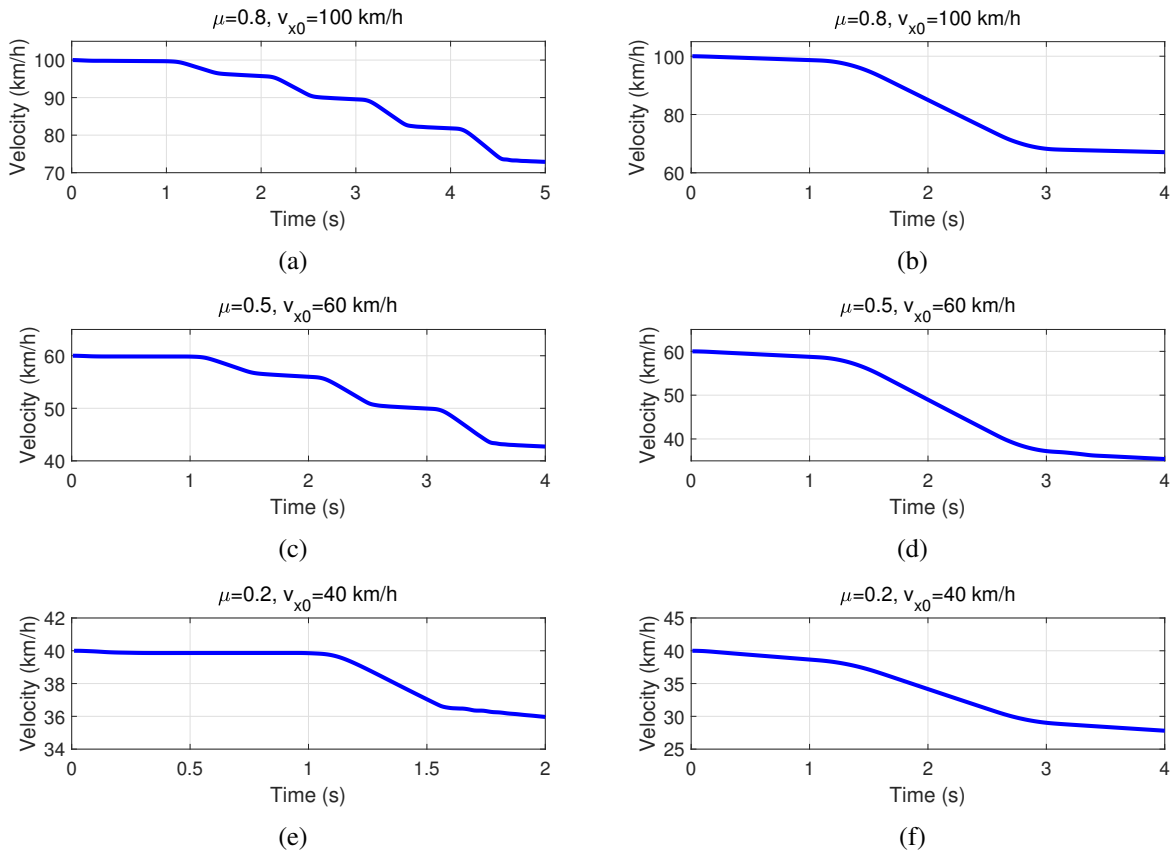

Figure 3.10: Speed variations on high-, mid- and low-μ road surfaces. (a), (c) and (e) are *Stage I*; (b), (d) and (f) are *Stage II*.

3.6.4 Discussions on Interference with Vehicle Motion

The speed variations caused by the braking pulse(s) in the *Stage I* and *Stage II* are presented in Figure 3.10. The speed reductions in the *Stage II* are slightly higher than those in the *Stage I* since the magnitude of the single braking pulse in the *Stage II* is much higher. In both the stages, the speed reductions are increasing with the TRFC, which shows more challenges in identifying a high friction coefficient. Moreover, the simulation results obtained from the proposed CUKF and the reported RLS and UKF algorithm invariably revealed that the accuracy of the TRFC estimation strongly depends on the slip ratio induced by the controlled braking pulse. TRFC estimations for the high- and mid-μ road conditions involved relatively higher slip ratios of about 8.5% and 5.5%, which could lead to unavoidable reductions in the vehicle forward speed. Thanks to the short duration of the braking pulse, the simulation results revealed the average speed reductions

of the two stages are about 28, 20 and 8 km/h for the high-, mid- and low-μ road conditions, respectively, as can be seen in Figure 3.10. These were attributed to the slip ratio required for determining the appropriate magnitude of pressure and for accurately estimating the TRFC, both of which constituted interference with the vehicle motion.

When focusing only on the absolute value of the average speed reductions on the three different roads, one may feel that the speed disturbances under TRFC estimation (*Stage II*) are not that small, especially for high-μ road. A trade-off exists between the accuracy of the TRFC estimation and the disturbance to the vehicle motion. However, those speed disturbances are indeed much smaller compared to the reported studies where constant braking inputs are always employed leading to considerable speed reductions or even a complete stop during the friction estimation process [16, 21, 29]. Moreover, the implemented braking pressure pulse for friction coefficient estimation process lasts only for 2 s, and the vehicle speed could further be restored quickly. In view of this, together with consideration of the three initial speeds (100, 60 and 40 km/h, respectively), we would say the motion interference by the proposed estimation method is still acceptable. It is also worth noting that the *Stage II* may become unnecessary when the approximated friction range from the *Stage I* has sufficient accuracy. In this case, further less speed reduction and thus minimal motion interference are expected.

3.7 Sensitivity Analysis

Simulations were finally performed to assess the sensitivity of the proposed tire-road friction identification algorithm to braking pressure and initial vehicle speed. Road friction $\mu = 0.8$, initial speed $v_{x0} = 100$ km/h and three different braking pressures $p_s = 2.3, 2.2, 2.1$ MPa were considered as examples. Figure 3.11 presents the errors in estimated rear-left tire longitudinal force, vertical force and slip ratio, and the estimated road friction coefficient. Moreover, the results are presented in the 1 to 2.5 s interval when the CUKF was updating. The figure also presents the computed slip ratio. The results show very small to negligible in errors of the estimated longitudinal and the

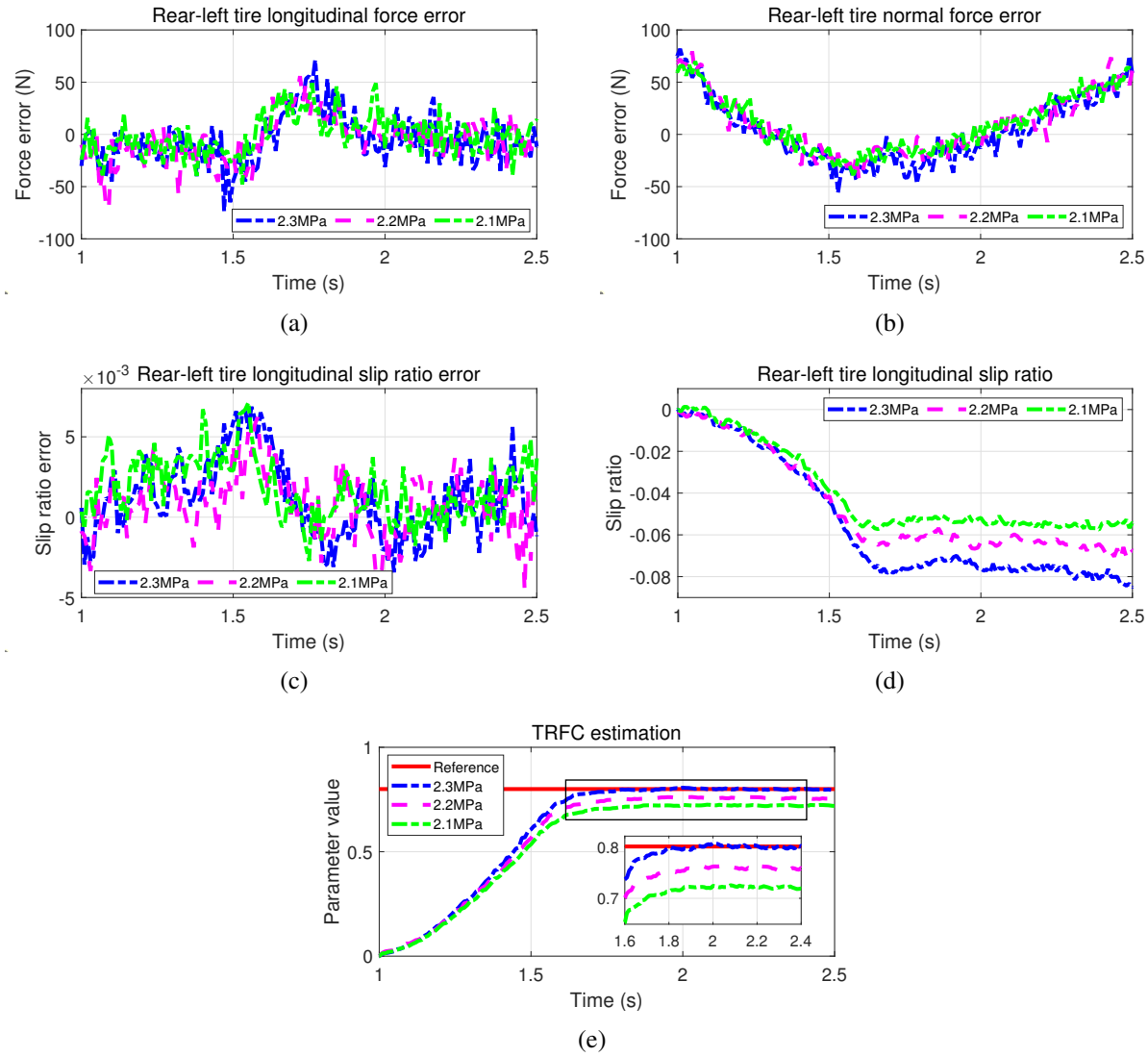

Figure 3.11: Sensitivity of the estimations to variations in the braking pulse pressure magnitude (p_s): (a) longitudinal force error; (b) normal force error; (c) slip ratio error; (d) slip ratio; and (e) friction estimation ($\mu = 0.8$; $v_{x0} = 100$ km/h).

normal tire forces, irrespective of the braking pressures. The slip ratio error also exhibits very low sensitivity to the braking pressure magnitude, as seen in Figure 3.11(c). Higher braking pressure, however, yields notably higher slip ratio, as shown in Figure. 3.11(d). The friction estimation error is thus also affected by the braking pulse pressure, as seen in Figure 3.11(e). The results suggest steady-state normalized friction errors of about 5% and 10% for the 2.2 and 2.1 MPa magnitude pressure pulses, respectively. This is due to insufficient slip ratio generated by the lower magnitude

pulses. Negligible friction error is evident for $p_s = 2.3$ MPa, and the algorithm converges to 0.8. The results also justify the choice of $p_s = 2.3$ MPa for ensuring high accuracy of the TRFC estimation on high-μ road condition.

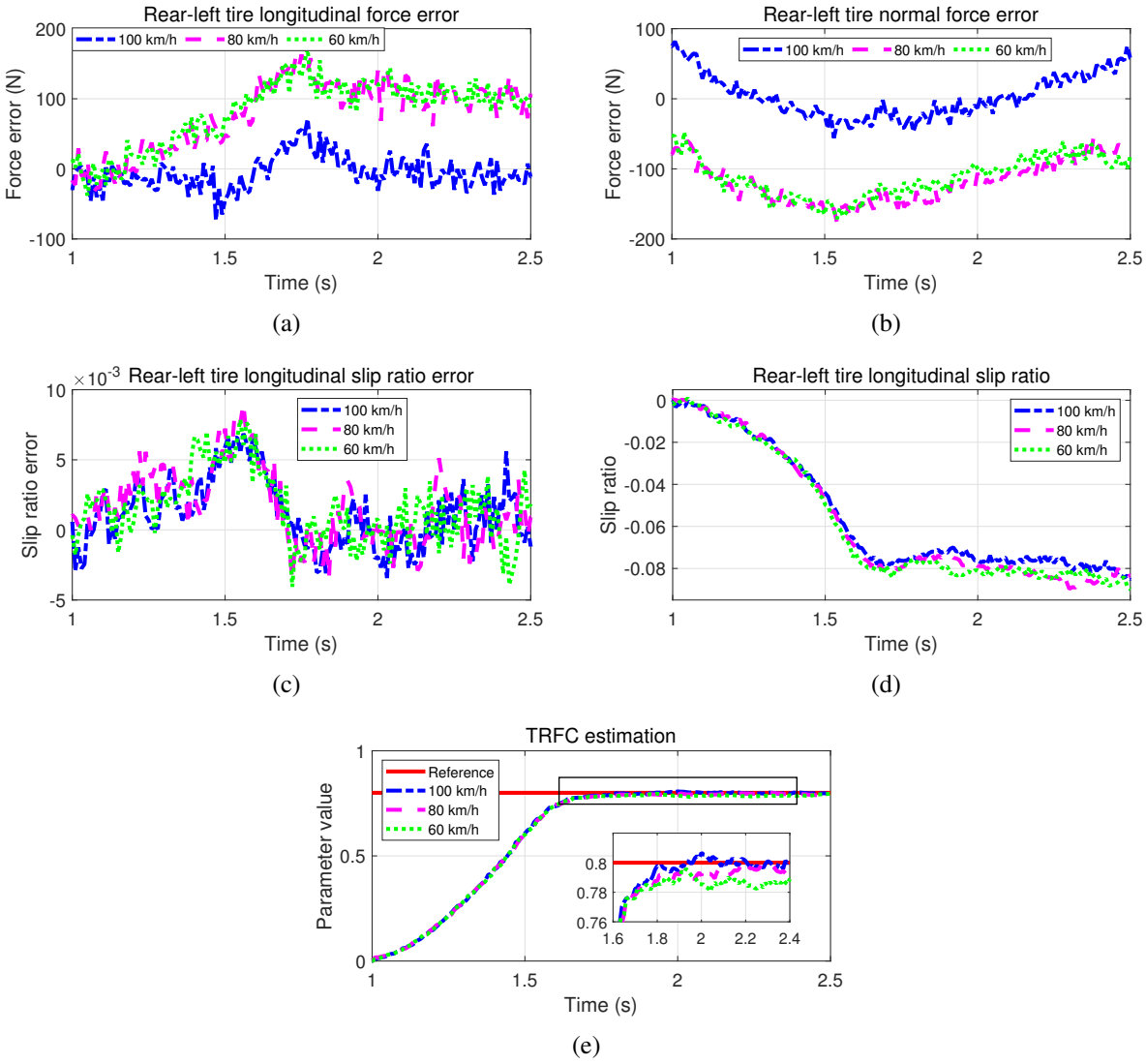

Figure 3.12: Sensitivity of the estimations to variations in initial vehicle speed (v_{x0}): (a) longitudinal force error; (b) normal force error; (c) slip ratio error; (d) slip ratio; and (e) friction estimation ($\mu = 0.8$; $p_s = 2.3$ MPa).

Figure 3.12 illustrates the sensitivity of the estimation errors to the initial vehicle speed considering road friction $\mu = 0.8$, braking pressure $p_s = 2.3$ MPa and forward speeds of $v_{x0} = 60, 80, 100$ km/h. The results suggest comparable errors in the tire longitudinal and normal forces

for 60 and 80 km/h, which are considerably greater than those obtained for 100 km/h. The errors in the slip ratio and TRFC, however, exhibit very low sensitivity to the vehicle speed, as evident in Figures 3.12(c) and 3.12(e), respectively. This is due to the fact that the slip ratio and thus the TRFC are mainly determined by the braking pressure magnitude instead of the initial vehicle speed. The normalized estimation error in the TRFC in the steady-state is less than 2.5% for all the three speeds considered. Similar trends were also observed for the other road surfaces. From the results, it was concluded that the proposed algorithm can provide effective estimations of TRFC under a wide range of initial vehicle speeds.

3.8 Summary

In this chapter, we present a more practical method for estimating TRFC of a road vehicle on the basis of its longitudinal dynamic response induced by short duration of braking pulse. It is shown that the accuracy of the TRFC estimation strongly relies on the magnitude of the slip ratio caused by the braking input, which may cause unreasonable interference with the vehicle motion. The initial stage of the proposed two-stage TRFC estimation algorithm ensures identification of the minimal braking pulse pressure required for accurate TRFC estimation so as to reduce its effect on the vehicle forward motion. A new CUKF algorithm is subsequently proposed in the second stage to improve the accuracy and convergence rate of the TRFC estimation. One distinguished feature is that either qualitative or quantitative estimation results can be obtained depending on the required estimation accuracy. The two stages are not mandatory and the second stage can become unnecessary when the qualitative results are acceptable in application. The effectiveness of the proposed TRFC estimation algorithms have been demonstrated via simulations carried out with a high-fidelity, full-vehicle model from CarSim considering different road surface conditions and initial vehicle speeds. The estimated TRFC will be integrated with the trajectory planning in the next chapter to show the significance of the TRFC in the AVs' trajectory generation.

Chapter 4

Adaptive Lane Change Trajectory Planning for AVs

4.1 Introduction

Developments of autonomous vehicles (AVs) have attracted considerable efforts during the past few decades due to their multi-faceted advantages such as enhanced road safety, effective traffic flow management, reduced fuel consumption and emission [3]. Trajectory planning is an integral module and a key enabler for the autonomous driving, which concerns trajectory generation that satisfies the safety requirements and motion model or state constraints while ensuring the occupants' comfort [47, 112, 113]. Among the various directional maneuvers, the lane changes constitute the most frequent maneuvers encountered in daily driving. The lane change maneuvers have thus been the primary focus of studies reporting trajectory planning of AVs [65, 68, 114, 115]. The generation of an appropriate trajectory for safe and comfortable lane change maneuver, however, is known to be quite complex as it involves both the lateral and longitudinal motions, which are constrained by the lane boundaries and traffic rules [10, 11]. The real-time variations in the road condition and the traffic flow, including the velocity changes of preceding vehicle(s), further contribute to the complexities [116].

The directional control and path tracking of a road vehicle is strongly influenced by the forces developed at the tire-road interface, which are primarily governed by the TRFC for a given normal load [16, 117]. The TRFC is thus strongly related to the directional control and driving safety of a road vehicle, which may vary considerably depending on the road and environment conditions. This coefficient is especially important for AVs since the autonomous driving should be robust to different road conditions [118]. Considering the limitation of the road friction earlier in the path planner can guarantee the generated trajectory physically feasible with reliable safety margin, in addition to the already achieved objectives including comfort driving and continuous curvature in the reported studies. With the knowledge of the TRFC, the design of the trajectory tracking controller can also be significantly simplified. The methods of integrating TRFC with the trajectory planning module, however, have not been sufficiently studied. Although there are some studies that do consider road friction saturation while generating the trajectories so far, like [56, 58, 65, 89], the limitations are obvious and summarized as:

(1) Most of the reported studies introduce the TRFC as a system constraint based on the friction ellipse. However, the obtained friction-based constraints (e.g., acceleration limits) are excessively large in terms of the comfort requirement.

(2) The upper limits defined by the comfort requirement are always set as fixed values, which may not be physically feasible when the TRFC changes, especially for the low friction roads.

(3) The variations in the TRFC in the existing approaches are within a small range and only one or two different road friction conditions are considered. The effects of the variations in the TRFC on the generating trajectories are not adequately studied.

How to realize more human-like or even personalized driving styles is another important factor related to the penetration of AVs. Although initial efforts have been attempted in self-driving shuttle bus [119] and passenger car [120, 121], how to effectively imitate the excellent drivers continues to be an important technical challenge. Moreover, the sensitivity of the outcomes of the trajectory planning schemes to variations in the forward speed have not been adequately studied.

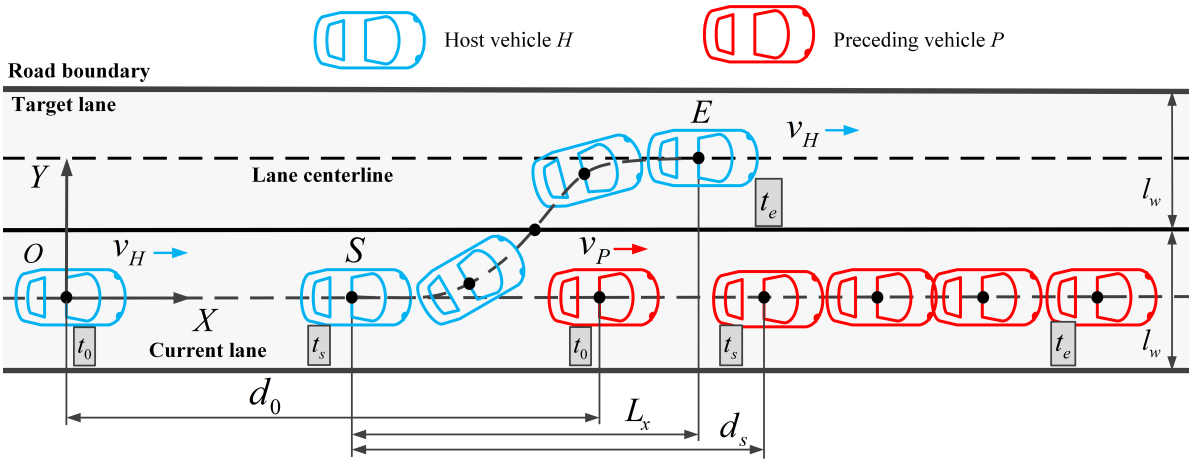

Figure 4.1: The schematic diagram of a typical lane change scenario (l_w is the lane width, S and E are the start and end point of the lane change maneuver, and their respective time instant are t_s and t_e).

In particular, the limits on the dynamic states of the vehicle are generally not well-defined in view of the occupant comfort and vehicle stability. Motivated by the aforementioned limitations, this chapter proposes a computationally efficient trajectory planning algorithm for typical lane change maneuvers over a wide range of forward speeds considering the available TRFC. A 7th-order polynomial function is used to represent the lane change trajectory with continuity up to the derivative of curvature (jerk). A wide range of road friction conditions and forward speeds are considered for trajectory planning and the main features of the yielded trajectory can be easily customized according to the passenger's personalized preferences.

4.2 Problem Formulation

Figure 4.1 illustrates a typical lane change scenario for an autonomous vehicle with no vehicles in the vicinity in the target lane. The forward velocities of the host vehicle (H) and the preceding vehicle (P) in the same lane are indicated by v_H and v_P, respectively, with v_H being a constant value and $v_H > v_P$. Both the vehicles are assumed to be positioned at the centerline of the current lane prior to the lane change performed by H. As the relative longitudinal distance between H and P is decreasing, H needs to gradually steer from the current lane to the target lane to avoid

a potential collision. S and E represent the coordinates of H at the start and end of the lane change maneuver, respectively, and t_s and t_e are the corresponding time instants. L_x defines the longitudinal distance traveled by H during the lane change, which is measured with reference to the position of the center of gravity (*CG*). The relative position and speed information of H and P are easily obtained from the onboard sensors. Focusing on the trajectory planning, it is also assumed that the TRFC is estimated prior to the lane change maneuver (before position S) using the TRFC estimation algorithms presented in authors' recent works [122,123]. For safety reasons, the relative distance between the *CG*s of the two vehicles at the start point S (d_s) should be carefully identified on the basis of the vehicle dimensions. Motion predictions of H and P, however, may be required for optimal selection of d_s. As more accurate motion predictions of the surrounding vehicles can be provided, V2VC-based lane change trajectory planning has been studied in [67, 68]. However, such methods will likely raise the issues related to communications which may make the simple lane change trajectory planning process unnecessarily complex. Thus, this study focuses on lane change trajectory planning using the AVs' on-board sensors alone.

Considering that the human drivers, invariably, use a safety margin distance in a qualitative sense without exactly knowing other vehicle's states when starting the lane change maneuver, the minimum threshold of d_s, d_{th} can be reasonably defined assuming the worse scenario the AVs may encounter. This assumption coincides with the basic idea formulating safe distance presented in [124]. In order to reduce the influence on the traffic, the host vehicle H starts lane change maneuver at the position where $d_s = d_{th}$. As AVs will drive on various roads with different friction conditions, the typical lane change problem is thus transferred to find a smooth trajectory linking the point S to the point E, while satisfying the comfort and friction limitations. It is noted that the assumption of constant forward speed of H is preferred by the human driver in view of driving comfort during the lane change maneuver.

4.3 Comfort Criteria for Autonomous Lane Change Maneuvers

For the purpose of trajectory planning for the comfortable autonomous driving, the selection of a comfort criteria constitutes the first challenge, which may vary widely due to different approaches used or varying objectives involved. The reported acceleration and jerk thresholds for driving comfort are reviewed together with the human-drivers' driving characteristics in an attempt to establish more appropriate criteria for a comfortable lane change maneuver.

4.3.1 Acceleration and Jerk Criteria

The vehicle's acceleration and its time rate of change, jerk, greatly affect the safety and comfort of passengers [120, 125]. As straight and flat road is considered in this chapter, longitudinal and lateral accelerations and their associated jerks are regarded as the major factors affecting the occupants' ride comfort. The reported studies have employed widely different comfort thresholds during the lane change maneuvers. Considering both seated and standing passengers in an autonomous public shuttle bus, Bae et al. [119] set the acceleration and jerk thresholds for comfort as 0.9 m/s^2 and 0.6 m/s^3, respectively, in both longitudinal and lateral directions. In the design of virtual desired trajectory for lane change maneuvers, the lateral jerk and acceleration limits were selected as 0.1 g/s and 0.05 g, respectively, considering passenger's ride comfort and transition time [126]. Guo et al. [61] designed maximum lateral jerk and acceleration as 0.1 g/s and 0.1 g, respectively, for lane changing on a curved road.

The above-stated acceleration and jerk thresholds, however, may be too conservative for autonomous lane change maneuvers. This is because the order of 1.0 m/s^3 (about 0.1 g/s) in jerk threshold is comparable to the range of lateral jerk (0.3-0.9 m/s^3) which is suggested to determine the minimum horizontal road curve radius [127]. Moreover, the lateral acceleration of human controlled vehicle can easily go over 3-4 m/s^2 within common range of driving speeds (0-20

m/s) [128]. In daily transportation vehicles such as subways, express trams and buses, the magnitudes of initial longitudinal and lateral accelerations up to 2.0 m/s^2 and 4.0 m/s^2 have been reported, while the initial jerks varied from 1.5 m/s^3 in the longitudinal direction to 3.5 m/s^3 in the transverse direction [129]. Some studies have suggested thresholds of lateral acceleration of 1.8 m/s^2 and 3.6 m/s^2 for very comfortable and medium comfort lane changes, respectively. An acceleration threshold of 5.0 m/s^2 has been associated with uncomfortable lane change maneuver [130, 131]. Svensson and Eriksson [132] have illustrated that the lane changes with peak lateral acceleration and jerk up to 2.0 m/s^2 and 3.5 m/s^3, respectively, are perceived comfortable by the passengers. The maneuver is considered as very uncomfortable when the maximum acceleration and jerk approach 4.5 m/s^2 and 10.9 m/s^3. With combined considerations of constrains imposed by the road conditions, engine power and passenger comfort, Lygeros and Godbole [133] suggested that the acceleration and jerk should lie in the range of [-5, 3] m/s^2 and [-5, 5] m/s^3 in perspective of vehicle automation. Shamir [134] recommended the maximum lateral jerk for passenger comfort as 2.4 m/s^3 and the threshold for passenger safety as 5 m/s^3 for overtaking a slower-moving vehicle. Another study considered the longitudinal acceleration in the range of 0.11 g to 0.15 g as acceptable for the public transport occupants, while the associated jerk larger than 0.30 g/s was not suggested [135]. Kahya and Schmidt [58] confined the longitudinal acceleration to 2 m/s^2 for comfortable driving during a lane change, which concurs with the reported limiting value of longitudinal acceleration controller by the human driver even on high-curvature roads [128]. Wu et al. [65] set the absolute acceleration and jerk limits in both longitudinal and lateral directions as 2 m/s^2 and 5 m/s^3, respectively, for autonomous vehicle lane change.

On the basis of the acceleration and jerk limits suggested in the reported studies, it is deduced that the comfort thresholds of longitudinal and lateral accelerations of 2 m/s^2 and 3.6 m/s^2, respectively, would be adequate for lane change maneuvers considering the practical ranges of forward speed and road conditions. Furthermore, the associated lateral jerk threshold should be limited to 5 m/s^3, as suggested in [65, 133, 134]. The trajectory planning in this chapter is based on these threshold limits, which are considered to permit sufficient maneuverability for a wide range of

driving scenarios.

4.3.2 Human Drivers' Lane Change Characteristics

The planned lane change trajectory based on the acceleration and jerk thresholds may differ from those assumed by a human driver. Accounting for human driver's characteristics in the process of trajectory planning can provide more natural riding experience for the occupants, which can also yield enhanced ride comfort [121]. This involves identifications of peak lateral velocity and acceleration, and the range of duration encountered during the human's lane change driving. Based on the lane change data collected for highways with lane width of 3.7 m, Yang et al. [136] conducted a comprehensive statistical analysis of these three parameters. The results suggested that the maximum lateral velocity and acceleration and the total duration of a single-lane change lie in the range of [0.8, 2.4] m/s, [0.5, 4] m/s^2 and [2.3, 6.3] s, respectively, for more than 80$\%$ human drivers. By considering a wide range of traffic conditions on highway, Toledo and Zohar [137] have revealed that the mean duration of a single lane change maneuver for passenger cars is 4.6 s. In order to account for the observed wide ranges of human drivers' characteristics in planning the trajectory, these three key parameters are permitted to vary in the reported ranges, which will be presented in details in Section 4.4.3.

4.4 Autonomous Lane Change Planning Scheme

4.4.1 7th-order Polynomial Trajectory

With the advantages of smooth curvature, closed-form expression and simple computation, quintic polynomial has been widely used for lane change trajectory planning [54, 68, 134, 138]. A quintic (5th-order) polynomial trajectory, however, ensures continuity only up to the curvature. The derivative of the curvature (jerk) can experience a sudden change at the starting point, while it does not converge to zero at the end point of the lane change maneuver. This may intrinsically cause

certain discomfort and may not be acceptable for lane change trajectory planning. A trajectory with zero jerk at the extremes of the maneuver would be desirable to achieve more comfortable vehicle motion. Motivated by the succinct form of a quintic polynomial curve [55], a 7th-order polynomial lane change trajectory is formulated as:

$$Y(x) = l_w \sum_{i=1}^{4} a_i (\frac{x}{L_x})^{3+i},\ x \in [0,\ L_x] \tag{4–1}$$

where l_w is the lane width and x is the longitudinal position of H relative to S. $Y(x)$ denotes the lateral position of H and $a_i, i = 1, ..., 4$ are four coefficients to be determined. The order of seven is selected since it is the least order required to realize the continuity in jerk. Although the derivatives of $Y(x)$ are normal to the lane instead of exactly normal to the vehicle's longitudinal direction, it is still reasonable to use $\dot{Y}(x)$, $\ddot{Y}(x)$ and $\dddot{Y}(x)$ to indicate lateral velocity, acceleration and jerk, respectively, considering the normal case that $L_x \gg l_w$. As can be seen from Eq. (4–1), the vehicle states including lateral position, velocity, acceleration and jerk at the starting point ($x = 0$) are naturally ensured as zero. The coefficients of a_i in in Eq. (4–1) are determined to satisfy the vehicle state constraints at the end of the lane change maneuver ($x = L_x$), by:

$$Y(L_x) = l_w,\ \dot{Y}(L_x) = 0,\ \ddot{Y}(L_x) = 0,\ \dddot{Y}(L_x) = 0 \tag{4–2}$$

Solution of Eq. (4–1) together with the above condition is expressed as $a_1 = 35$, $a_2 = -84$, $a_3 = 70$, $a_4 = -20$. The designed lane change trajectory is subsequently obtained upon substituting coefficient values in Eq. (4–1). For the constant forward speed v_H, $Y(x)$ can also be expressed as a function of time by letting $x = v_H(t - t_s)$ in Eq. 4–1, such that:

$$Y(t) = l_w \sum_{i=1}^{4} a_i (\frac{v_H(t - t_s)}{L_x})^{3+i},\ t \in [t_s,\ t_s + t_{slc}] \tag{4–3}$$

where t is the current time, t_s is the time instant when the lane change maneuver starts, and t_{slc} is the lane change duration which can be approximately calculated as L_x/v_H. The lateral position at

mid-point where $x = 0.5L_x$ or $t = t_s + 0.5t_{slc}$, and the maximum lateral velocity, acceleration and jerk during the lane change maneuver are calculated as:

$$\begin{aligned} Y_m &= Y(x)|_{x=0.5L_x} = Y(t)|_{t=t_s+0.5t_{slc}} = 0.5l_w, \\ v_{ymax} &= \left|\dot{Y}(x)|_{x=0.5L_x}\right| = 2.1875l_w\frac{v_H}{L_x} = \frac{2.1875l_w}{t_{slc}}, \\ a_{ymax} &= \left|\ddot{Y}(x)|_{x=0.7236L_x,\ x=0.2764L_x}\right| = 7.513l_w\frac{v_H^2}{L_x^2} = \frac{7.513l_w}{t_{slc}^2}, \\ j_{ymax} &= \left|\dddot{Y}(x)|_{x=0.5L_x}\right| = 52.5l_w\frac{v_H^3}{L_x^3}| = \frac{52.5l_w}{t_{slc}^3} \end{aligned} \tag{4–4}$$

Figure 4.2 illustrates comparisons of the lateral position, velocity, acceleration and jerk responses obtained using the proposed 7th-order polynomial trajectory and the 5th-order polynomial trajectory ($l_w = 3.5$ m, $L_x = 100$ m, $v_H^* = 72$ km/h and $X_S = 0$ m). The results confirm that the 7th-order polynomial trajectory not only retains the advantages of the 5th-order polynomial curve but also ensures a smooth variation in jerk from zero to zero. Under the same L_x, the 7th-order trajectory has slightly higher maximum lateral velocity, acceleration and jerk, as shown in Figures 4.2(b)-4.2(d). These results also demonstrate that a longer L_x is required by the 7th-order trajectory when the same maximum limits with the 5th-order polynomial are designated, which is the sacrifice of a smoother motion.

4.4.2 Safety Constraints

The coordinates of the start point S are determined so as to maintain a safe distance with respect to vehicle P to avoid a potential collision. A comprehensive study of how to design such safe distance for lane change maneuvers is referred to [124]. Here, we present a simple way of designing the safe distance by considering the worst scenario vehicle H may encounter: vehicle P suddenly applies maximum braking effort and holds it until to the complete stop. The maximum deceleration of P (a_P^m) in this case can be expressed as μg, with μ and g being the TRFC and the acceleration due to gravity, respectively. The time lapse for the preceding vehicle to reach a complete stop can be obtained as, $t_{stop} = v_P/\mu g$. In this scenario, the host vehicle is assumed

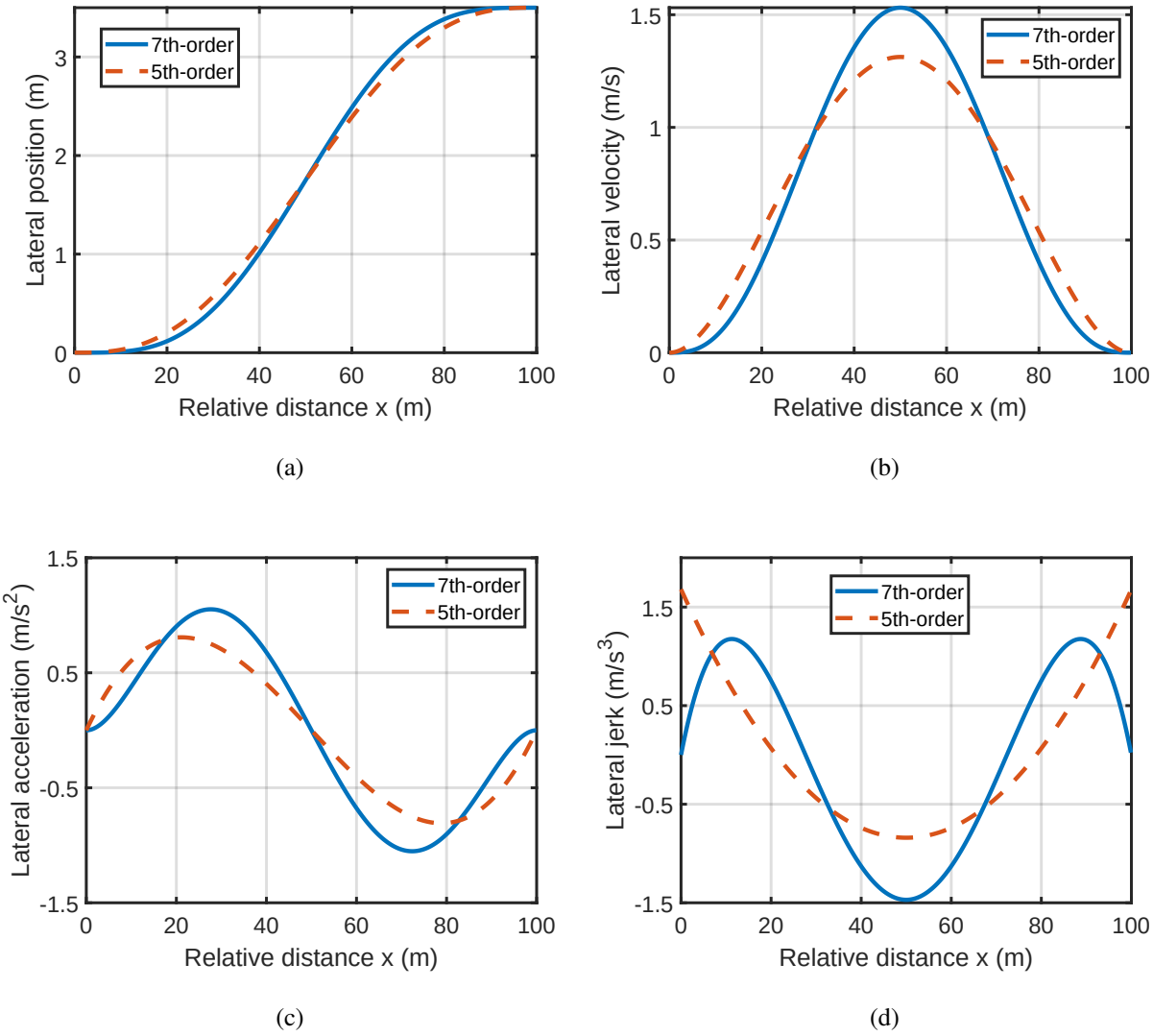

Figure 4.2: Comparisons of the proposed 7th-order polynomial trajectory with the 5th-order polynomial trajectory ($l_w = 3.5$ m, $L_x = 100$ m, $v_H^* = 72$ km/h, and $X_S = 0$ m).

to maintain its forward speed as the preceding vehicle starts braking, which requires additional distance margin to the initial relative distance d_s. Considering the lateral position at the mid-point (Y_m) of $0.5l_w$, it would require $0.5t_{slc}$ for H to cross the boundary between the current and the target lanes. If d_s is set as d_{th} and P starts braking with its maximum deceleration from the lane change starting time instant t_s, the relative distance (d_c) between H and P when H crosses the

lane boundary is calculated as:

$$d_c = \begin{cases} d_s + v_P \cdot t_{stop} - v_H \frac{\tilde{t}_{slc}}{2} - \frac{a_P^m}{2}(\frac{t_{stop}}{2})^2, & \text{if } t_{stop} \leqslant \frac{\tilde{t}_{slc}}{2} \\ d_s + (v_P - v_H)\frac{\tilde{t}_{slc}}{2} - \frac{a_P^m}{2}(\frac{\tilde{t}_{slc}}{2})^2, & \text{else} \end{cases} \tag{4–5}$$

where $\tilde{t}_{slc}$ is the duration used for predicting the positions of H and P vehicles during the lane change maneuver. In order to avoid a collision, the longitudinal distance between the *CG*s of H and P, d_c, should be larger than the vehicle's length (l_v) assuming H and P have the same dimensions. Thus, the initial distance starting the lane change maneuver d_s should satisfy:

$$d_s \geqslant \begin{cases} v_H \frac{\tilde{t}_{slc}}{2} - v_P \cdot t_{stop} + \frac{a_P^m}{2}(\frac{t_{stop}}{2})^2 + l_v, & \text{if } t_{stop} \leqslant \frac{\tilde{t}_{slc}}{2} \\ (v_H - v_P)\frac{\tilde{t}_{slc}}{2} + \frac{a_P^m}{2}(\frac{\tilde{t}_{slc}}{2})^2 + l_v, & \text{else} \end{cases} \tag{4–6}$$

The minimum safe distance corresponding to the start of the lane change maneuver (or called threshold distance), d_{th}, is then selected as:

$$d_{th} = \begin{cases} v_H \frac{\tilde{t}_{slc}}{2} - v_P \cdot t_{stop} + \frac{a_P^m}{2}(\frac{t_{stop}}{2})^2 + l_v, & \text{if } t_{stop} \leqslant \frac{t_{slc}}{2} \\ (v_H - v_P)\frac{\tilde{t}_{slc}}{2} + \frac{a_P^m}{2}(\frac{\tilde{t}_{slc}}{2})^2 + l_v, & \text{else} \end{cases} \tag{4–7}$$

As summarized in Section 4.3.2, the lane change duration for more than 80% human drivers lies in 2.3 s to 6.3 s. $\tilde{t}_{slc} = 6.3$ s is thus considered adequate for estimating d_{th}.

4.4.3 Comfort Constraints

Since there are no vehicles in the vicinity in the target lane, the planned trajectory mainly depends on the occupants' comfort, which can be related to the acceleration and jerk within the comfort limits [65, 68]. The studies reporting trajectory planning generally consider fixed comfort limits, irrespective of the speed and available road friction. The variations in the vehicle forward speed and road friction, however, may have the impact on the vehicle's allowable acceleration and

Table 4.1: Designed constraint parameters.

Symbol	Value	Unit	Symbol	Value	Unit
a_{xmax}^{low}	0	g	v_{ymax}^{up}	2.3	m/s
a_{xmax}^{up}	0.204	g	j_{ymax}^{low}	0.0749	g/s
a_{ymax}^{low}	0.0675	g	j_{ymax}^{up}	0.510	g/s
a_{ymax}^{up}	0.246	g	t_{slc}^{low}	3.3	s
v_{ymax}^{low}	1.2	m/s	t_{slc}^{up}	6.3	s

jerk limits [11]. Consideration of comfort limits adaptive to forward speed and TRFC can lead to more effective trajectory planning.

The comfort limits for longitudinal and lateral accelerations, and lateral jerk established in Section 4.3.1 are $a_{xmax} \leqslant 2$ m/s^2, $a_{ymax} \leqslant 3.6$ m/s^2 and $j_{ymax} \leqslant 5$ m/s^3, respectively, and the maximum lateral velocity (v_{ymax}) and lane change duration of more than 80% human drivers lie in [0.8, 2.4] m/s and [2.3, 6.3] s ranges, respectively. It should be noted that the main characteristics of the 7th-order lane change trajectory are correlated to each other as evidenced from Eq. (4–4). For instance, the a_{ymax}, j_{ymax} and t_{slc} can be computed according to the given v_{ymax}. Taking into account all the comfort limits confined by each characteristic, the compromised comfort limits of the main characteristics of the lane change maneuver are obtained as:

$$\begin{aligned} &a_{xmax}^{low} \leqslant |a_{xmax}| \leqslant a_{xmax}^{up},\ a_{ymax}^{low} \leqslant |a_{ymax}| \leqslant a_{ymax}^{up},\ v_{ymax}^{low} \leqslant |v_{ymax}| \leqslant v_{ymax}^{up} \\ &j_{ymax}^{low} \leqslant |j_{ymax}| \leqslant j_{ymax}^{up},\ t_{slc}^{low} \leqslant t_{slc} \leqslant t_{slc}^{up} \end{aligned} \tag{4–8}$$

where the values of all the constraint parameters are listed in Table 4.1.

4.4.3.1 TRFC-Adaptive Acceleration Limit

It is evident that the available maximum longitudinal and lateral accelerations positively change with increase in the TRFC. For very low friction roads (e.g., $\mu = 0.2$), the designed upper bounds of longitudinal and lateral accelerations a_{xmax}^{up} and a_{ymax}^{up} in Table 4.1 are not physically achievable,

though both of them lie within the comfort limits. A straightforward method to solve this problem is to design the adaptive acceleration limit which changes with the TRFC. Based on the friction ellipse, the two minimum friction values to provide a_{xmax}^{up} and a_{ymax}^{up}, a_{xmax}^{low} and a_{ymax}^{low}, denoted as μ_m and μ_o, respectively, are calculated as:

$$\mu_m = \frac{\sqrt{(a_{xmax}^{up})^2 + (a_{ymax}^{up})^2}}{g},\ \mu_o = \frac{\sqrt{(a_{xmax}^{low})^2 + (a_{ymax}^{low})^2}}{g} \tag{4–9}$$

and their values are shown in Table 4.1. The lane change maneuver is considered unsafe when $\mu < \mu_o$. The TRFC of the most frequently encountered roads, however, is generally greater than μ_o. Theoretically, it is possible to set a_{ymax} as the value of a_{ymax}^{up} only if $\mu \geqslant \mu_m$. Letting $a_{ymax}(\mu_o) = a_{ymax}^{low}$ and $a_{ymax}(\mu_m) = a_{ymax}^{up}$, the a_{ymax} can be simply designed as a linear function of TRFC, when $\mu_o \leqslant \mu \leqslant \mu_m$. The slope of this linear function is expressed as:

$$K = \frac{a_{ymax}(\mu_m) - a_{ymax}(\mu_o)}{\mu_m - \mu_o} = \frac{a_{ymax}^{up} - a_{ymax}^{low}}{\mu_m - \mu_o} \tag{4–10}$$

The linear TRFC-adaptive lateral acceleration limit (L-AccLim) is subsequently expressed as:

$$a_{ymax}^{L}(\mu) = \begin{cases} \dfrac{a_{ymax}^{up} - a_{ymax}^{low}}{\mu_m - \mu_o}(\mu - \mu_o) + a_{ymax}^{low},\ \mu_o \leqslant \mu \leqslant \mu_m \\ a_{ymax}^{up},\ \mu > \mu_m \end{cases} \tag{4–11}$$

However, this method would make the available longitudinal acceleration very limited for certain range of TRFC, especially for the low- and middle-friction roads. Circumventing this limitation, an appropriate margin between the allowable a_{ymax} and the available acceleration μg may be introduced to ensure vehicle's operation considerably below the road's adhesion limit. A quadratic function is designed such that a_{ymax} is permitted to increase at a relatively slower rate with TRFC. a_{ymax} increases to its upper limit a_{ymax}^{up} at $\mu = \mu_p$ (where μ_p is taken as $2\mu_m$ to allow for leaving acceleration margin). With smaller magnitude of a_{ymax} allowed on low- and middle-friction roads, the newly designed quadratic acceleration limit would result in a safer and more comfortable lane

change maneuver than L-AccLim. It is worth noting that the resulting redundant longitudinal acceleration also shows implications with regard to our future research on trajectory planning for varying-speed lane change maneuver, though only constant forward speed is considered in this study. The quadratic TRFC-adaptive lateral acceleration limit (Q-AccLim, $a_{ymax}^{Q}(\mu)$) is described as:

$$a_{ymax}^{Q}(\mu) = \begin{cases} b_0 + b_1\mu + b_2\mu^2, \, \mu_o \leqslant \mu \leqslant \mu_p \\ a_{ymax}^{up}, \, \mu > \mu_p \end{cases} \tag{4–12}$$

where b_0, b_1 and b_2 are three coefficients to be determined. The above function is satisfied by the following boundary conditions:

$$a_{ymax}^{Q}(\mu_o) = a_{ymax}^{low}, \; a_{ymax}^{Q}(\mu_p) = a_{ymax}^{up} \tag{4–13}$$

The first derivative of a_{ymax}^{Q} is assumed continuous at $\mu = \mu_p$ to ensure smoother changing in a_{ymax}^{Q}, which is:

$$\dot{a}_{ymax}^{Q}(\mu_p) = 0 \tag{4–14}$$

Substituting Eqs. (4–13) and (4–14) into Eq. (4–12) yields the coefficients b_0, b_1 and b_2, which are acquired as follows:

$$\begin{bmatrix} b_0 \\ b_1 \\ b_2 \end{bmatrix} = \begin{bmatrix} 1 & \mu_o & \mu_o^2 \\ 1 & \mu_p & \mu_p^2 \\ 0 & 1 & 2\mu_p \end{bmatrix}^{-1} \begin{bmatrix} a_{ymax}^{low} \\ a_{ymax}^{up} \\ 0 \end{bmatrix} \tag{4–15}$$

The Q-AccLim is subsequently obtained upon substituting for the coefficients in Eq. (4–12). Figure 4.3(a) compares the variations in Q-AccLim and L-AccLim with TRFC, while the variations in the available longitudinal accelerations on low- and middle-friction roads (μ=0.1-0.5) are presented in Figure 4.3(b).

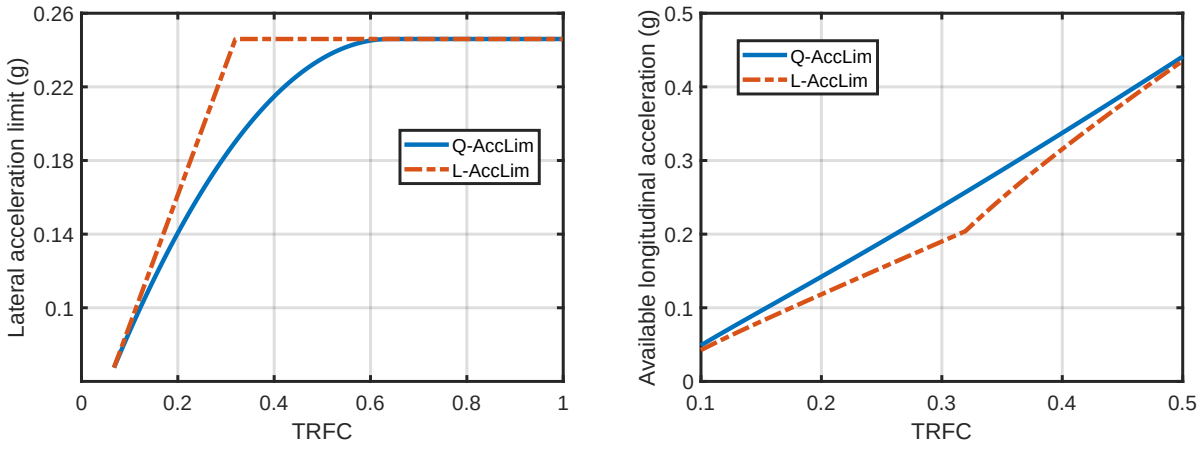

(a) (b)

Figure 4.3: (a) Comparisons of Q-AccLim and L-AccLim. (b) Comparisons of the available longitudinal acceleration under Q-AccLim and L-AccLim.

4.4.3.2 Speed-Adaptive Jerk Limit

Although the 7th-order polynomial trajectory exhibits continuity up to jerk, the maximum lateral jerk j_{ymax} should be confined to ensure comfort and safety. It is evident from Eq. (4–4) that a larger j_{ymax} will lead to a faster lane change with shorter duration and higher lateral acceleration and velocity. Although the upper bound of the maximum lateral jerk is confined as 5 m/s^3 (Table 4.1), it may still lead to uncomfortable or even unsafe driving when the forward speed is high. Bearing this in mind, a speed-adaptive jerk limit is necessary to design for enhanced comfort and safety.

In general, the allowable j_{ymax} can be designed to gradually decrease with the forward speed. When the vehicle speed increases from zero to the speed limit (v_{lim}), the designed j_{ymax} decreases from j_{ymax}^{up} to j_{ymax}^{low}. This is because higher jerk corresponding to faster maneuver is more acceptable at lower speed, and low jerk should be ensured at high speed for safety. Considering that the daytime speed limits on freeways (urban) and undivided (rural) are 70-100 km/h and 80-90 km/h in Quebec province, the threshold speed (v_{th}) is selected as 80 km/h. As the vehicle speed exceeds v_{th}, the designed j_{ymax} should be rapidly decreased to a smaller value to ensure safety and comfort.

On the contrary, the designed j_{ymax} for low and middle speeds should be kept close to the confined values so as to conduct prompt lane change maneuvers. In order to reduce the effects on the traffic, shortest lane change duration is maintained by setting the designed j_{ymax} to the maximum allowable value. Based on this, the speed-adaptive jerk limit is designed as a piecewise function:

$$j_{ymax}(v_H^*) = \begin{cases} c_1(v_H^*/v_{lim})^2 + c_2,\ 0 \leqslant v_H \leqslant v_{th} \\ c_3 c_4^{(v_H^* - v_{th})/(v_{lim} - v_{th})} + c_5,\ v_{th} < v_H \leqslant v_{lim} \end{cases} \tag{4–16}$$

where v_H^*, v_{lim} and v_{th} are the host vehicle's forward speed, limiting speed and threshold speed in km/h, respectively. v_{lim} is chosen as 120 km/h, assuming that typical driving speeds may range from 0 to 120 km/h, and c_1 to c_5 are constant coefficients. The above function satisfies the following boundary conditions at zero speed and limiting speed:

$$j_{ymax}(0) = j_{ymax}^{up},\ j_{ymax}(v_{lim}) = j_{ymax}^{low} \tag{4–17}$$

As shown in [137], the mean lane change duration for passenger cars is 4.6 s on highways. From Eq. (4–4), the corresponding maximum lateral jerk can be easily calculated as $j_{ymax}^m = 0.1924$ g/s. In order to guarantee comfort and safety, the designed j_{ymax} at high speeds ($v_H^* > v_{th}$) should be confined no larger than j_{ymax}^m. Thus, we set j_{ymax} at v_{th} as j_{ymax}^m. In addition, it is assumed that the designed j_{ymax} is continuous up to first derivative to assure smooth variation in lateral jerk limit. Thus, the designed j_{ymax} should satisfy the following conditions:

$$\begin{cases} j_{ymax}(v_{th}) = j_{ymax}^m \\ c_1(v_{th}/v_{lim})^2 + c_2 = c_3 + c_5 \\ 2c_1 v_{th}/(v_{lim}^2) = c_3 \ln c_4/(v_{lim} - v_{th}) \end{cases} \tag{4–18}$$

By manipulating Eqs. (4–17) and (4–18), the five coefficients c_1-c_5 can be solved accordingly. c_1

and c_2 are identified as:

$$c_1 = (j_{ymax}^{m} - j_{ymax}^{up})/(v_{th}/v_{lim})^2,\ c_2 = j_{ymax}^{up} \tag{4–19}$$

and c_3 and c_5 are expressed as:

$$c_3 = (j_{ymax}^{low} - j_{ymax}^{m})/(c_4 - 1),\ c_5 = j_{ymax}^{m} - c_3 \tag{4–20}$$

where c_4 is satisfied with the following equation:

$$(j_{ymax}^{low} - j_{ymax}^{m})\ln(c_4) + 2c_1 v_{th}(v_{lim} - v_{th})(1 - c_4)/(v_{lim})^2 = 0 \tag{4–21}$$

Once c_4 is solved through Eq. (4–21), c_3 and c_5 are subsequently known according to Eq. (4–20). Figure 4.4 illustrates speed-adaptive jerk limit obtained from the above relations.

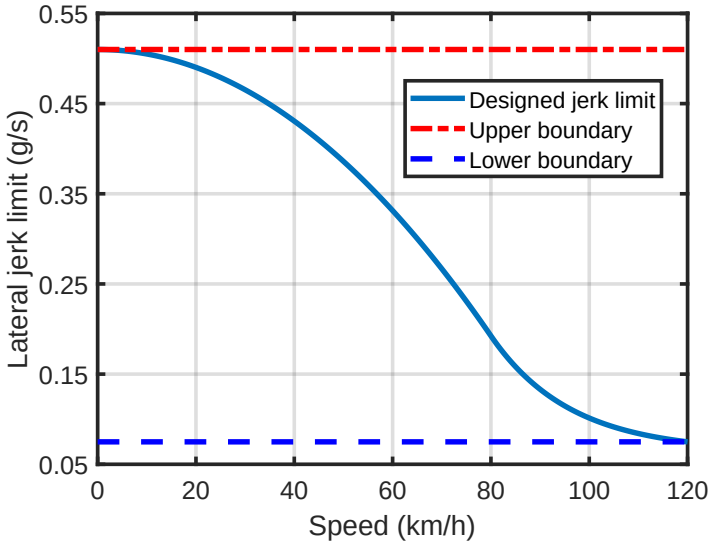

Figure 4.4: The designed speed-adaptive jerk limit.

4.4.4 Trajectory Planning Procedure

The host vehicle H is considered to initially cruise at speed v_H well behind the preceding vehicle P. While following the centerline of the current lane, the TRFC is firstly estimated based on the longitudinal dynamics using the algorithms reported in [122, 123]. The speed of H is restored to the original forward speed following the TRFC estimation. Since $v_H > v_P$, the initial distance (d_0) between H and P gradually decreases to d_{th} where the lane change maneuver starts and the corresponding longitudinal position of H is labeled as X_S. Based on the available μ and v_H information, the adaptive lateral acceleration and jerk limits are calculated according to Eq. (4–12) and Eq. (4–16), respectively. It is evident from Eq. (4–3) that the planned trajectory is known once L_x is known after the start point is determined. Therefore, the lane change problem is now transferred to find the optimal value for L_x. As t_{slc} can be approximated as L_x/v_H, the optimal selection of L_x can be further transferred to find the optimal t_{slc} at a given v_H.

According to Eq. (4–4), a_{ymax} and j_{ymax} during the lane change maneuver can be expressed as:

$$a_{ymax} = \frac{7.513 l_w}{t_{slc}^2},\ j_{ymax} = \frac{52.5 l_w}{t_{slc}^3} \tag{4–22}$$

Both a_{ymax} and j_{ymax} decrease as t_{slc} increases, and we assume the shortest lane change duration while satisfying safety and comfort constraints as the optimal maneuver. Thus, the choice of the admissible lane change trajectory can be made by the selection of the smallest value of t_{slc}, t_{slc}^{min}, by:

$$t_{slc}^{min} = \max\left\{\sqrt{\frac{7.513 l_w}{g \cdot a_{ymax}^{Q}(\mu)}},\ \sqrt[3]{\frac{52.5 l_w}{g \cdot j_{ymax}(v_H^*)}}\right\} \tag{4–23}$$

After t_{slc}^{min} is selected, L_x is calculated as $v_H t_{slc}^{min}$, and the planned trajectory is determined accordingly. The framework of the proposed trajectory planning scheme is shown in Figure 4.5.

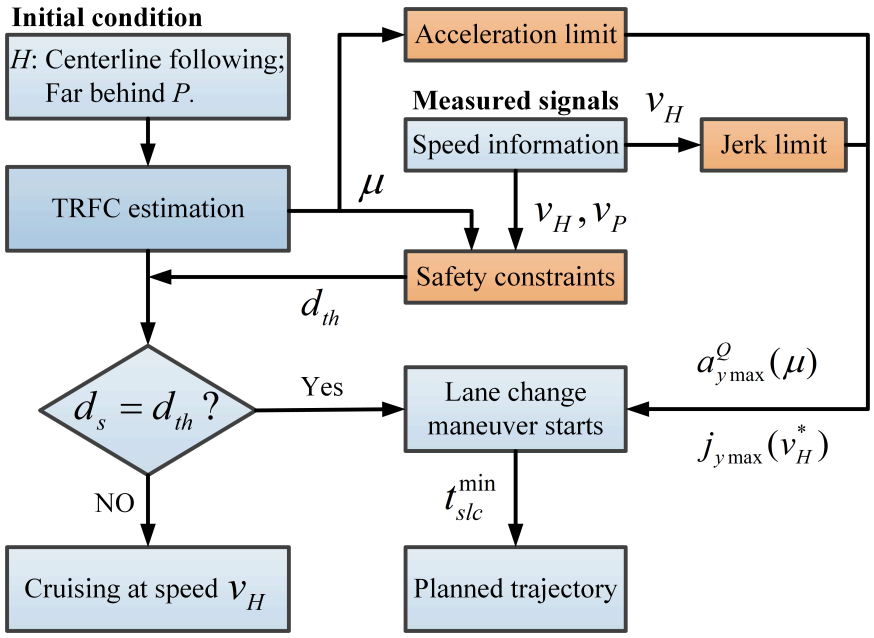

Figure 4.5: The planning diagram of the lane change scheme (H and P represent host and preceding vehicle, respectively).

4.5 Simulations and Results Analysis

To study the performance of the proposed trajectory planning scheme, simulations were performed using MATLAB and CarSim considering a series of highway scenarios involving different forward speeds and road friction conditions. The trajectory planning was conducted in the MATLAB/Simulink environment for the chosen speed and TRFC, which was subsequently fed to CarSim as the target path to be followed. The traceability of the planned path is evaluated by observing the vehicle's responses obtained in the CarSim platform.

4.5.1 Trajectory Planning Simulations

In this section, the proposed trajectory planning scheme was validated considering different scenarios, where the preceding vehicle P may be stationary or moving at different constant speeds. At the initial instant t_0, the origin of the global coordinate system XOY (Figure 4.1) was taken as *CG* of H, while the initial distance d_0 was set as 150 m. The key test parameters were taken as follows: vehicle length, $l_v = 3.35$ m; vehicle width, $T = 1.74$ m; lane width $l_w = 3.5$ m and

$v_{lim} = 120$ km/h.

4.5.1.1 Stationary Preceding Vehicle

The simulations were initially performed assuming stationary preceding vehicle, which may be caused by a breakdown or an accident. Trajectory planning was carried out considering multiple forward speeds and road friction values to verify the effectiveness and robustness of the proposed planning scheme.

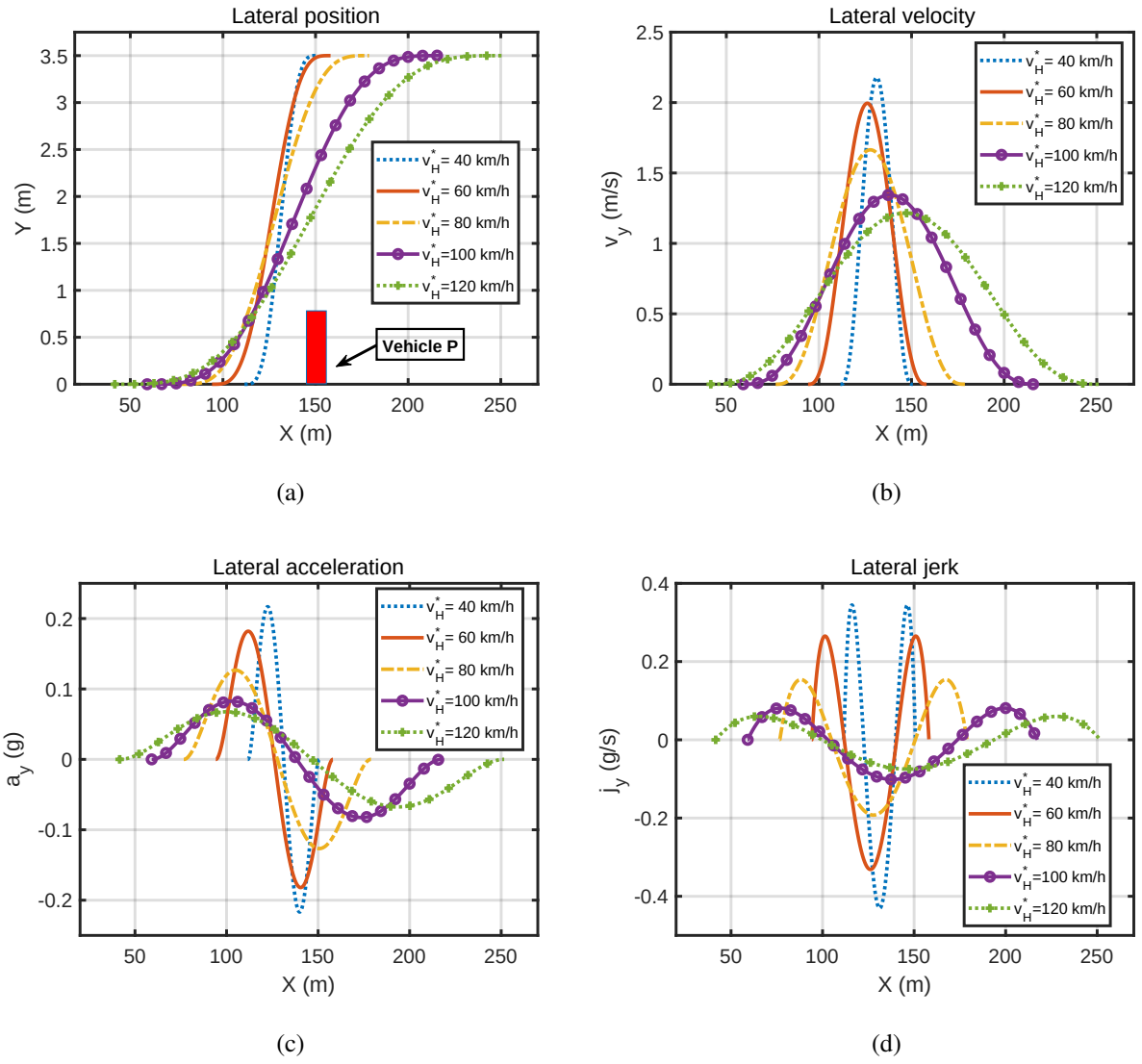

Figure 4.6: Lateral positions, velocities, accelerations and jerks of the host vehicle's *CG* under different speeds ($\mu = 0.8$, $v_P^* = 0$ km/h).

Table 4.2: The main performance parameters under different forward speeds ($v_P^* = 0$ km/h, $\mu = 0.8$).

v_H^* (km/h)	$\lvert v_{ymax}\rvert$ (m/s)	$\lvert a_{ymax}\rvert$ (g)	$\lvert j_{ymax}\rvert$ (g/s)	X_S (m)	L_x (m)	t_{slc} (s)
40	2.18	0.2176	0.4306	111.65	39.08	3.52
60	1.99	0.1820	0.3314	94.15	63.96	3.84
80	1.66	0.1276	0.1924	76.65	102.23	4.60
100	1.34	0.0826	0.1013	59.15	158.24	5.70
120	1.22	0.0675	0.0749	41.65	210.01	6.30

Trajectory Planning under Different Speeds Since the forward speed on low friction roads would be lower for safety, a high value of TRFC ($\mu = 0.8$) was selected so as to cover a wide range of allowable forward speeds. Five different forward speeds of H ($v_H^* = 40, 60, 80, 100$ and 120 km/h) were considered for path planning and conducting the lane change maneuver. Figure 4.6 illustrates the variations in the lateral position, velocity, acceleration and jerk of H with the longitudinal positions, as a function of the forward speed. As it can be seen in Figure 4.6(a), the distance between the lane change start point and the stationary vehicle P (located at 150 m from the origin) increases with the forward speed to ensure safety, and the planned trajectory becomes smoother as the forward speed increases for both the safety and comfort reasons. The required longitudinal distance travelled during the lane change maneuver (L_x) also increases with the forward speed, which is consistent with the designed lane change duration. Moreover, the higher the forward speed is, the smaller the maximum values in lateral velocity, acceleration and jerk are, as seen in Figures 4.6(b)-4.6(d). Values of the main performance parameters during the lane change maneuver are presented in Table 4.2 for different forward speeds, namely peak lateral velocity (v_{ymax}), acceleration (a_{ymax}) and jerk (j_{ymax}) in absolute values, lane change duration (t_{slc}) and start position (X_S) and the distance travelled during the maneuver (L_x). Considering the lane change start points and the maximum values of the generated lateral accelerations and jerks, the results show that the proposed planning scheme ensures safe and comfortable lane change maneuvers.

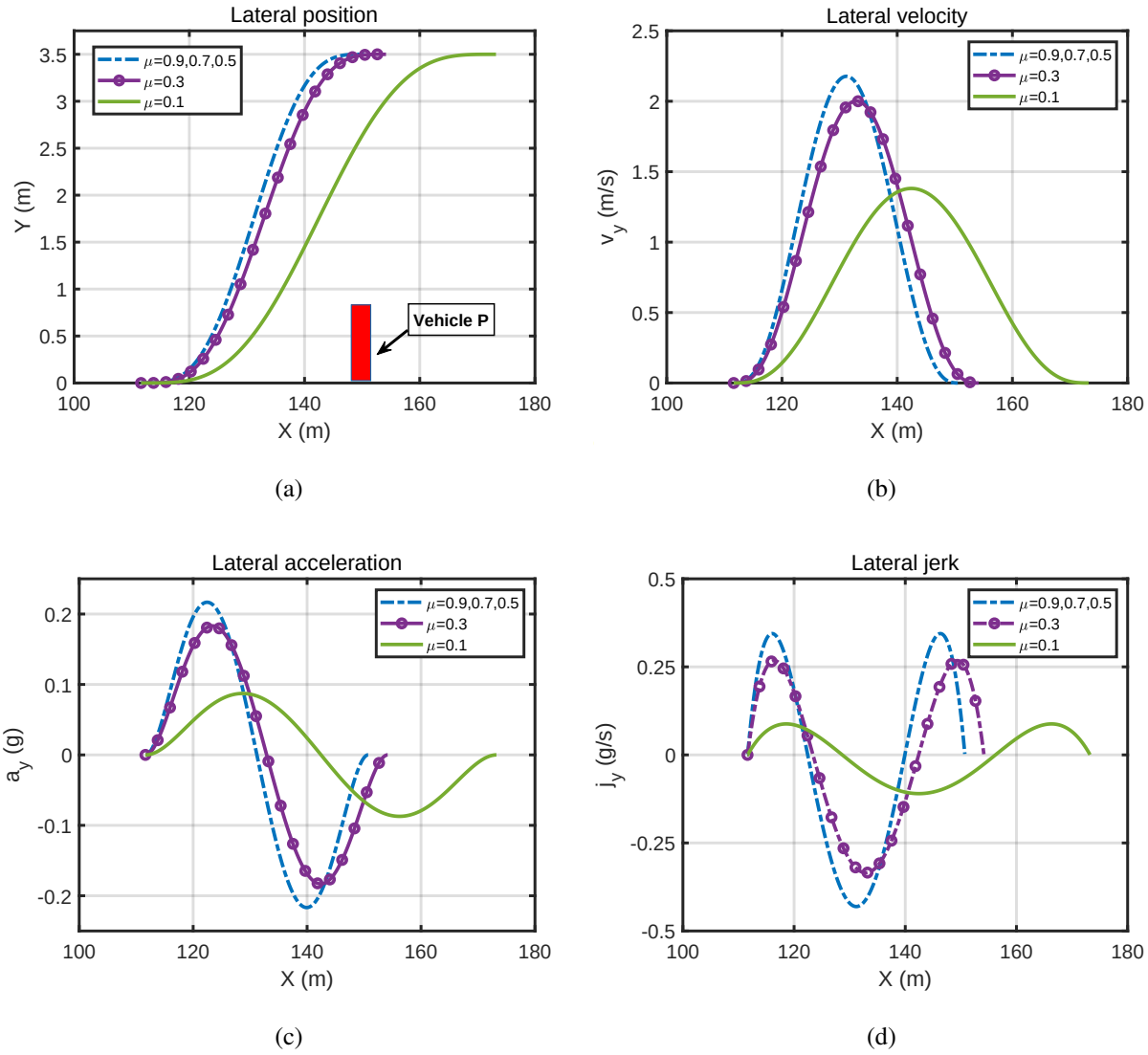

Figure 4.7: Lateral positions, velocities, accelerations and jerks of the host vehicle's *CG* on different friction roads ($v_H^* = 40$ km/h, $v_P^* = 0$ km/h).

Trajectory Planning under Different Friction Conditions In this section, the proposed trajectory planning scheme was conducted for lane change maneuvers on straight roads with different friction coefficients. In order to conduct the lane change maneuvers under a wide range of friction conditions, a lower forward speed of 40 km/h was selected for the host vehicle. Trajectory planning for lane change maneuvers was realized for five different friction values ($\mu = 0.1, 0.3, 0.5, 0.7$ and 0.9). The effects of road friction on the lateral position, velocity, acceleration and jerk of the host

Table 4.3: The main performance parameters under different friction conditions ($v_P^* = 0$ km/h, $v_H^* = 40$ km/h).

μ	$\lvert v_{ymax}\rvert$ (m/s)	$\lvert a_{ymax}\rvert$ (g)	$\lvert j_{ymax}\rvert$ (g/s)	X_S (m)	L_x (m)	t_{slc} (s)
0.1	1.38	0.0872	0.1099	111.65	61.60	5.54
0.3	2.00	0.1832	0.3346	111.65	42.50	3.83
0.5	2.18	0.2167	0.4306	111.65	39.08	3.52
0.7	2.18	0.2167	0.4306	111.65	39.08	3.52
0.9	2.18	0.2167	0.4306	111.65	39.08	3.52

vehicle are shown in Figure 4.7 as a function of the longitudinal position. Since the preceding vehicle is stationary ($t_{stop} = 0$) and the host vehicle is traveling at the same constant speed (40 km/h), identical lane change start position is obtained for all the roads, which is evident in Figure 4.7(a). Since the allowable jerk corresponding to 40 km/h is relatively large according to Eq. (4–16), the planned trajectories on low friction roads are mainly determined by the lateral acceleration limit, which is constrained by the friction coefficient. As can be seen from Figure 4.7(c), the desired maximum lateral acceleration increases with friction coefficient to achieve a quicker lane change maneuver when the road friction is less than $\mu = 0.5$. Increasing the friction coefficient up to 0.5 resulted in higher peak lateral velocity, acceleration and jerk, as seen in Figures 4.7(b)-4.7(d) and Table 4.3. The length of the maneuver and thus the duration, however, decreases with the increase in the road friction. For higher μ values, the lateral responses are constrained by the defined limits. The maximum allowable lateral acceleration, however, does not always increase with the friction coefficient. Since the constraints defined for comfortable and safe driving are related to both the friction coefficient and the forward speed, the desired maximum lateral acceleration tends to saturate at 0.2167 g even though the lateral acceleration corresponding to the road adhesion limit may be considerably larger than the limiting value. The results also show saturation of peak lateral jerk to 0.4306 g/s.

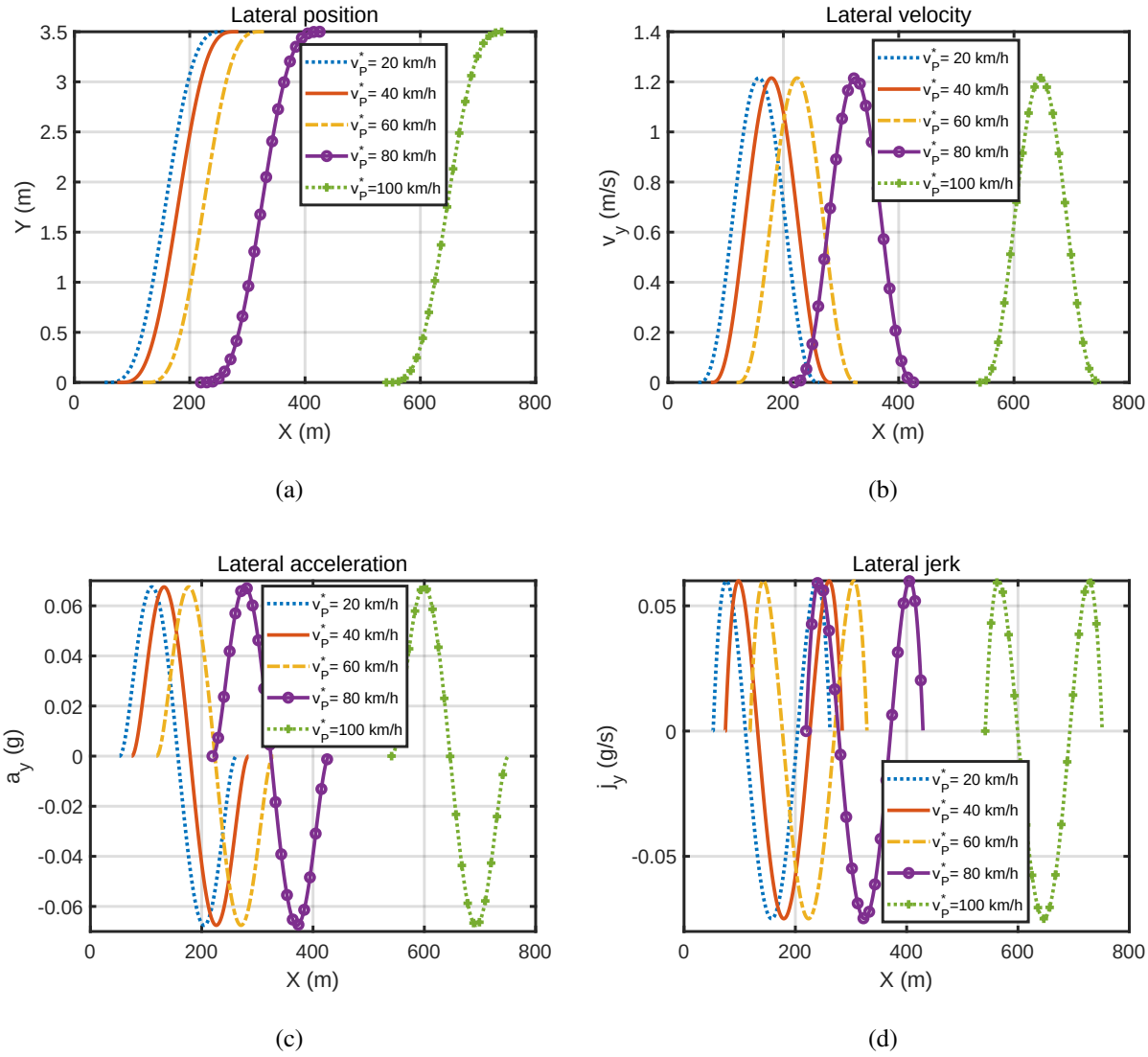

(a) (b) (c) (d)

Figure 4.8: Lateral positions, velocities, accelerations and jerks of the host vehicle's *CG* under different preceding vehicle speeds ($\mu = 0.8$ and $v_H^* = 120$ km/h).

4.5.1.2 Moving Preceding Vehicle

Simulations were subsequently performed for moving preceding vehicle, which is a more representative driving scenario. As it can be seen from Eq. (4–23), t_{slc}^{min} varies only with the designed acceleration and jerk limits $a_{ymax}^{Q}(\mu)$ and $j_{ymax}(v_H^*)$. It should be noted that $a_{ymax}^{Q}(\mu)$ and $j_{ymax}(v_H^*)$ are related to the friction coefficient μ and host vehicle's forward speed v_H^* regardless of the preceding vehicle's forward speed v_P, as evident in Eqs. (4–12) and (4–16). For given values

of μ and v_H^*, identical curvature of the lane trajectories is obtained, irrespective of v_P. However, the position of the start point S with respect to the origin, X_S, changes with v_P. This is because the threshold distance d_{th} changes with v_P to ensure safety, as it is seen in Eq. (4–7). The trajectory planning was conducted for relatively higher host vehicle speed, $v_H^* = 120$ km/h, and higher friction coefficient, $\mu = 0.8$, which permitted broad variations in v_P. Figure 4.8(a) illustrates the trajectories obtained for five different speeds of the preceding vehicle v_P^* of 20, 40, 60, 80 and 100 km/h, where v_P^* is the transformed v_P in km/h. The results clearly show identical path curvatures, irrespective of v_P^*. An increase in v_P^*, however, leads to initial of the maneuver at a higher relative position of H with respect to the origin. The peak values of the resulting lateral velocity, acceleration and jerk are also identical, as seen in Figures 4.8(b)-4.8(d).

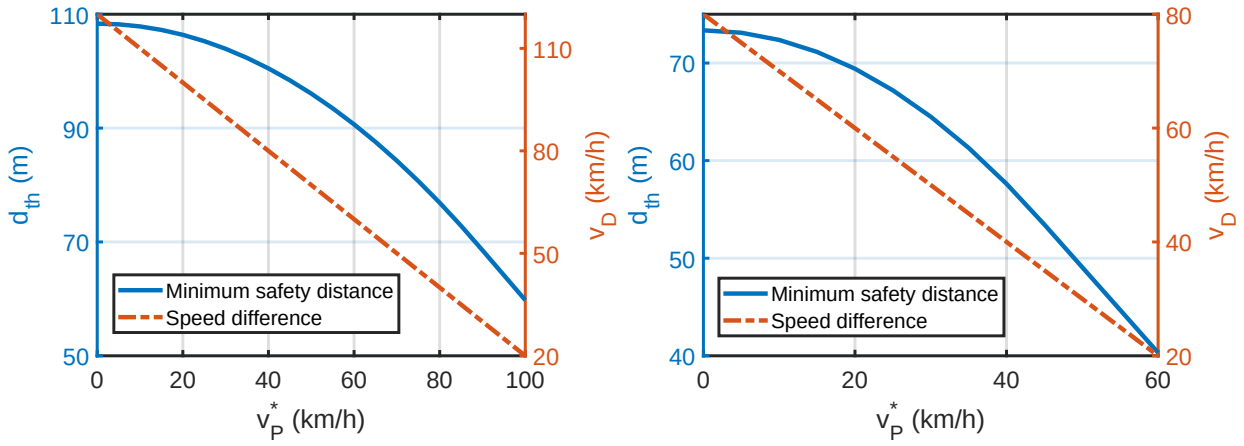

(a) $\mu = 0.8, v_H^* = 120$ km/h

(b) $\mu = 0.4, v_H^* = 80$ km/h

Figure 4.9: Variations in threshold distance and relative speed as a function of the preceding vehicle speed.

To clearly show how does the preceding vehicle speed v_P^* affect the threshold distance starting the lane change maneuver, d_{th} and speed difference ($v_D = v_H^* - v_P^*$) as a function of v_P^* are simultaneously plotted in Figure 4.9. Two representative scenarios ($\mu = 0.8, v_H^* = 120$ km/h; and $\mu = 0.4, v_H^* = 80$ km/h) were investigated. For $\mu = 0.8, v_H^* = 120$ km/h, d_{th} was computed for v_P^* range of $0 - 100$ km/h at every 5 km/h; and for $\mu = 0.4, v_H^* = 80$ km/h, d_{th} was computed for v_P^* range of $0 - 60$ km/h at every 5 km/h. The results suggest that the threshold distance decreases with

Table 4.4: The main parameters of the full-vehicle model.

Symbol	Parameter	Value	Unit
m	Vehicle mass	1416	kg
l_f	Distance between *CG* and front axle	1.016	m
l_r	Distance between *CG* and rear axle	1.562	m
t_d	Track width	1.539	m
T	Vehicle width	1.739	m
l_v	Vehicle length	3.35	m
R_e	Effective tire radius	0.316	m
h_c	Height of *CG*	0.54	m
C_{yf}	Front-axle cornering stiffness	94	kN/rad
C_{yr}	Rear-axle cornering stiffness	76	kN/rad

the increase of v_P^* (or the decrease of v_D), which is consistent with human driving experience of leaving more space when the relative speed of the following vehicle with respect to the preceding vehicle is higher.

4.5.2 Realization and Evaluation Simulations

This section evaluates the traceability of the planned lane change trajectories using a high-fidelity, full-vehicle model in CarSim. The driver-model module, available in the CarSim, was used to compute the steering angle required to track the planned path under different speeds and road surface conditions. Comparative tracking simulations were performed for the planned trajectories based on the proposed 7th-order polynomial and the classic 5th-order polynomial functions. Two scenarios ($\mu = 0.8$, $v_H^* = 80$ km/h; and $\mu = 0.3$, $v_H^* = 40$ km/h) were considered and the stationary preceding vehicle was initially located at 150 m ahead of the host vehicle. The full vehicle model of a typical C-class hatchback, available in CarSim, was employed to verify path tracking for the two lane-change scenarios. The key parameters of the vehicle are listed in Table 4.4. The driver model parameters, namely, driver preview time and driver time lag, were set as 0.75 s and 0.15 s, respectively, as suggested in [139].

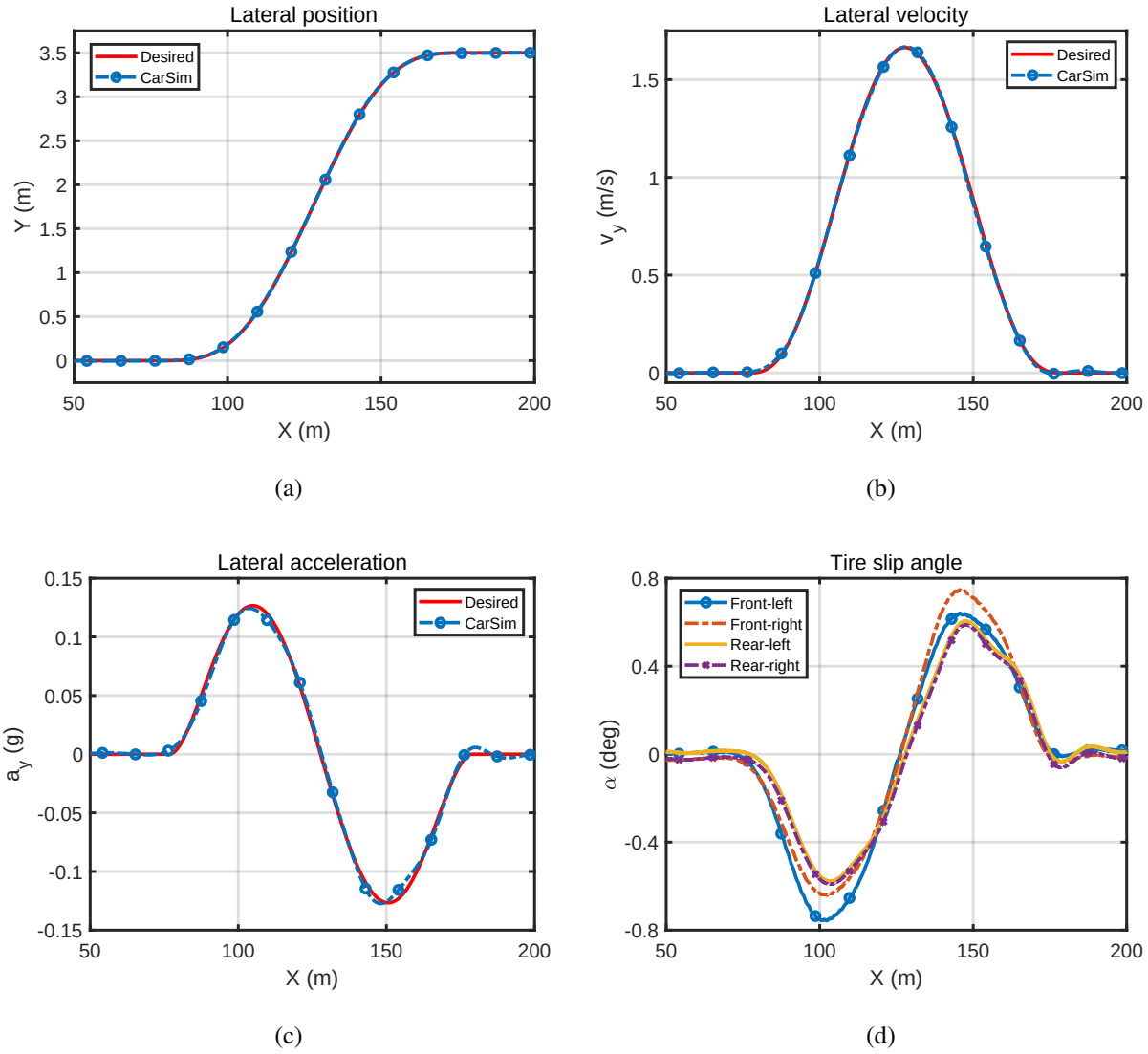

Figure 4.10: The CarSim vehicle's responses to the proposed 7th-order trajectory ($\mu = 0.8$ and $v_H^* = 80$ km/h).

Figure 4.10 demonstrates the CarSim vehicle's responses to the proposed 7th-order trajectory in lateral position, velocity, acceleration and tire slip angles under the scenario $\mu = 0.8$ and $v_H^* = 80$ km/h. The results show that the planned 7th-order trajectory can be well tracked by the CarSim vehicle with small peak tracking errors. Figure 4.11 further compares the tracking errors of the proposed 7th-order polynomial trajectory with those of the 5th-order polynomial trajectory. The tracking errors in both the lateral position and velocity are obviously smaller than those of the 5th-order trajectory, as can be seen in Figures 4.11(a) and 4.11(b). Figure 4.11(c) shows that the

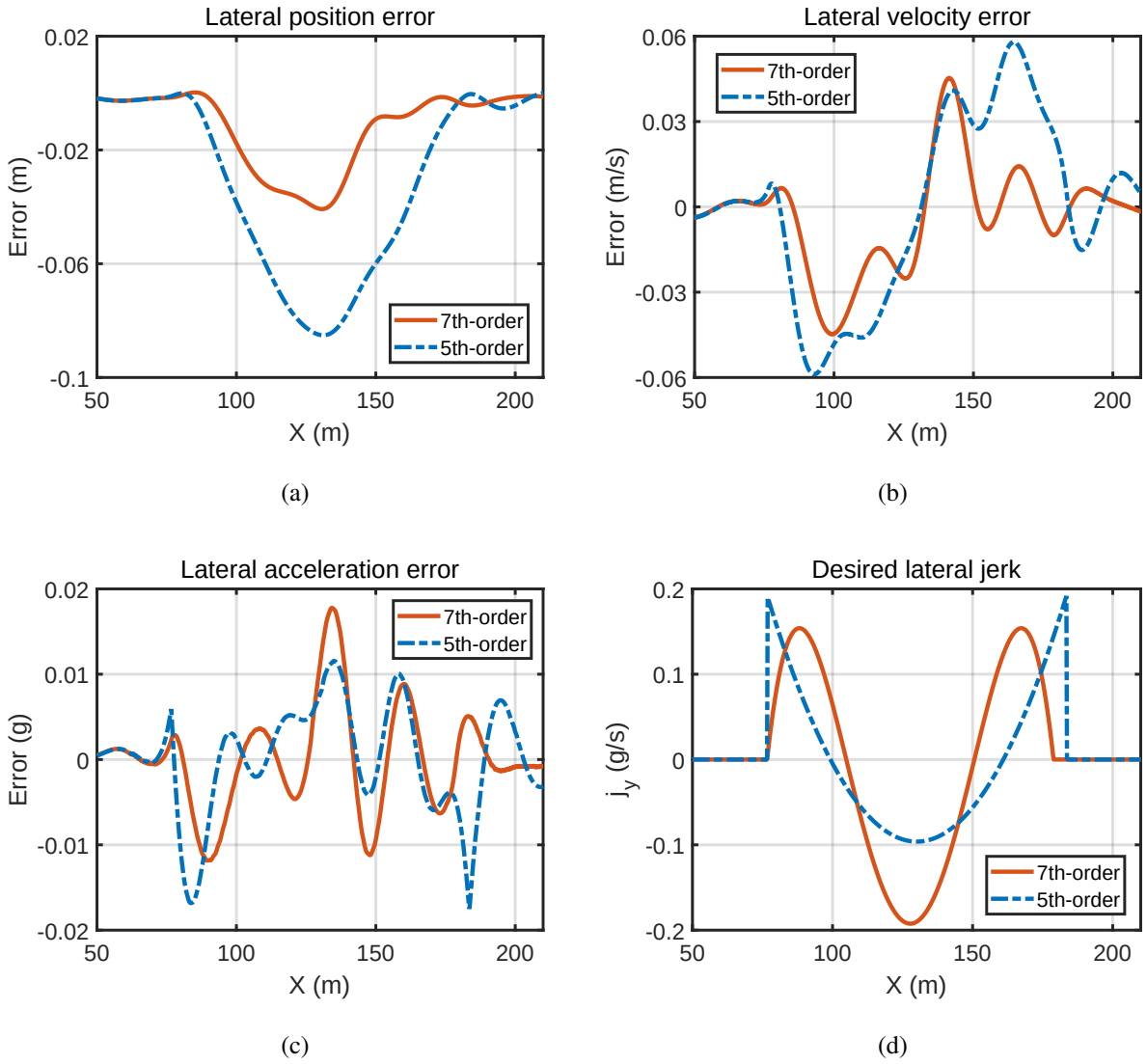

Figure 4.11: Tracking errors and the desired lateral jerks of the proposed 7th-order polynomial trajectory and the classic 5th-order polynomial trajectory ($\mu = 0.8$ and $v_H^* = 80$ km/h).

5th-order trajectory is comparable to the 7th-order trajectory in view of the peak value of lateral acceleration error. However, more severe oscillations are observed near the lane change start and end points. This is attributed to the sharp changes in the desired lateral jerk of the 5th-order trajectory at the corresponding time instants, which are clearly seen in Figure 4.11(d).

The tracking results of the proposed 7th-order trajectory on road $\mu = 0.3$ with $v_H^* = 40$ km/h are presented in Figure 4.12. As can be seen in Figures 4.12(b) and 4.12(c), greater deviations from the desired values are observed for lateral velocity and acceleration. This is due to a poor

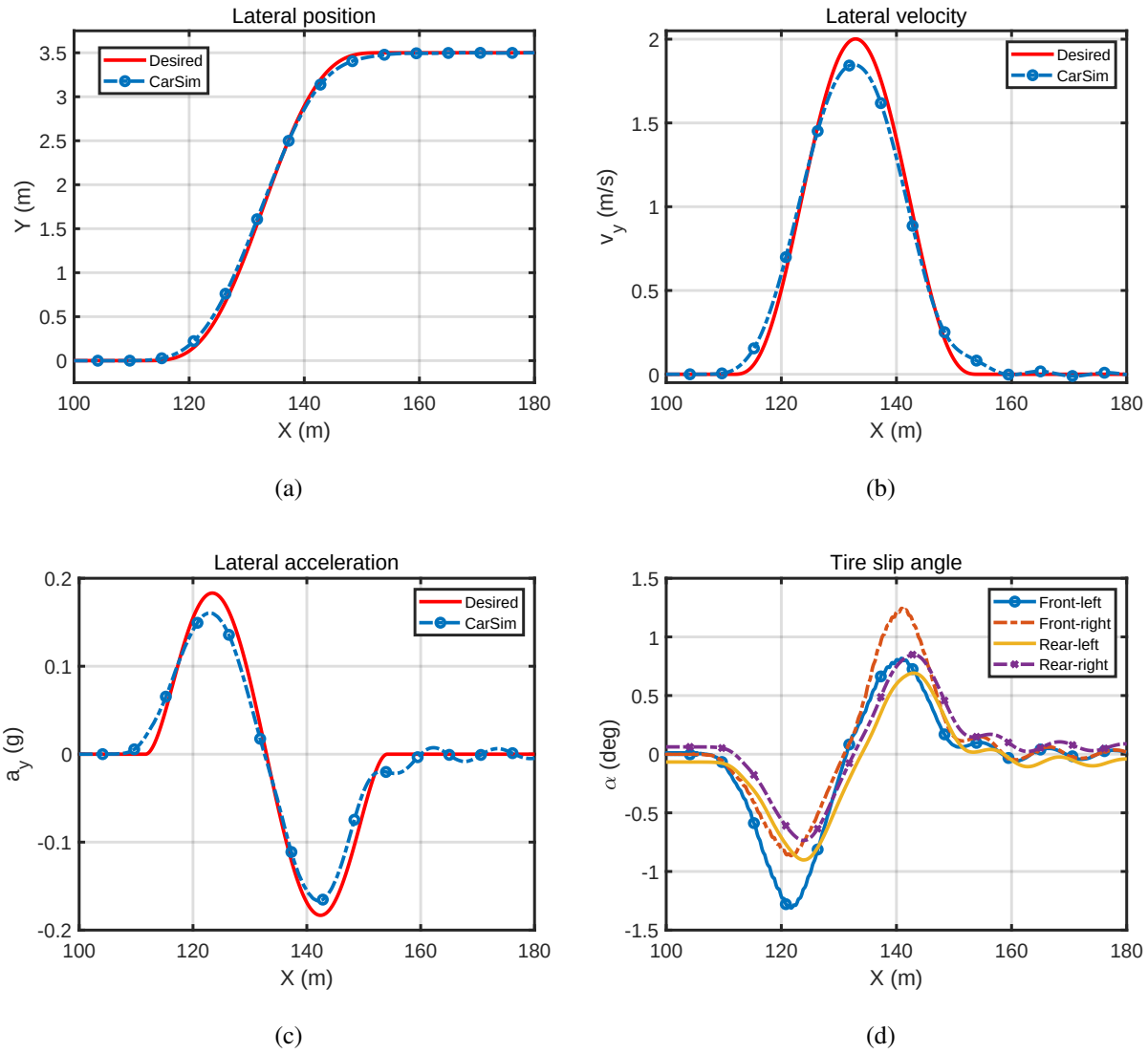

Figure 4.12: The CarSim vehicle's responses to the proposed 7th-order trajectory ($\mu = 0.3$ and $v_H^* = 40$ km/h).

adhesion in this scenario. The tracking errors of the proposed 7th-order trajectory and the 5th-order trajectory are illustrated in Figures 4.13(a)-4.13(c). While the magnitudes of the lateral position errors of the two trajectories are close to each other, obviously smaller tracking errors of lateral velocity are observed for the proposed 7th-order trajectory. Owing to smooth changes in the desired lateral jerk at both the start and end points of the lane change maneuver, the 7th-order trajectory resulted in smoother variations in lateral acceleration error than that of the 5th-order trajectory, as clearly seen in Figures 4.13(c) and 4.13(d). It is further seen from Figure 4.13(d) that

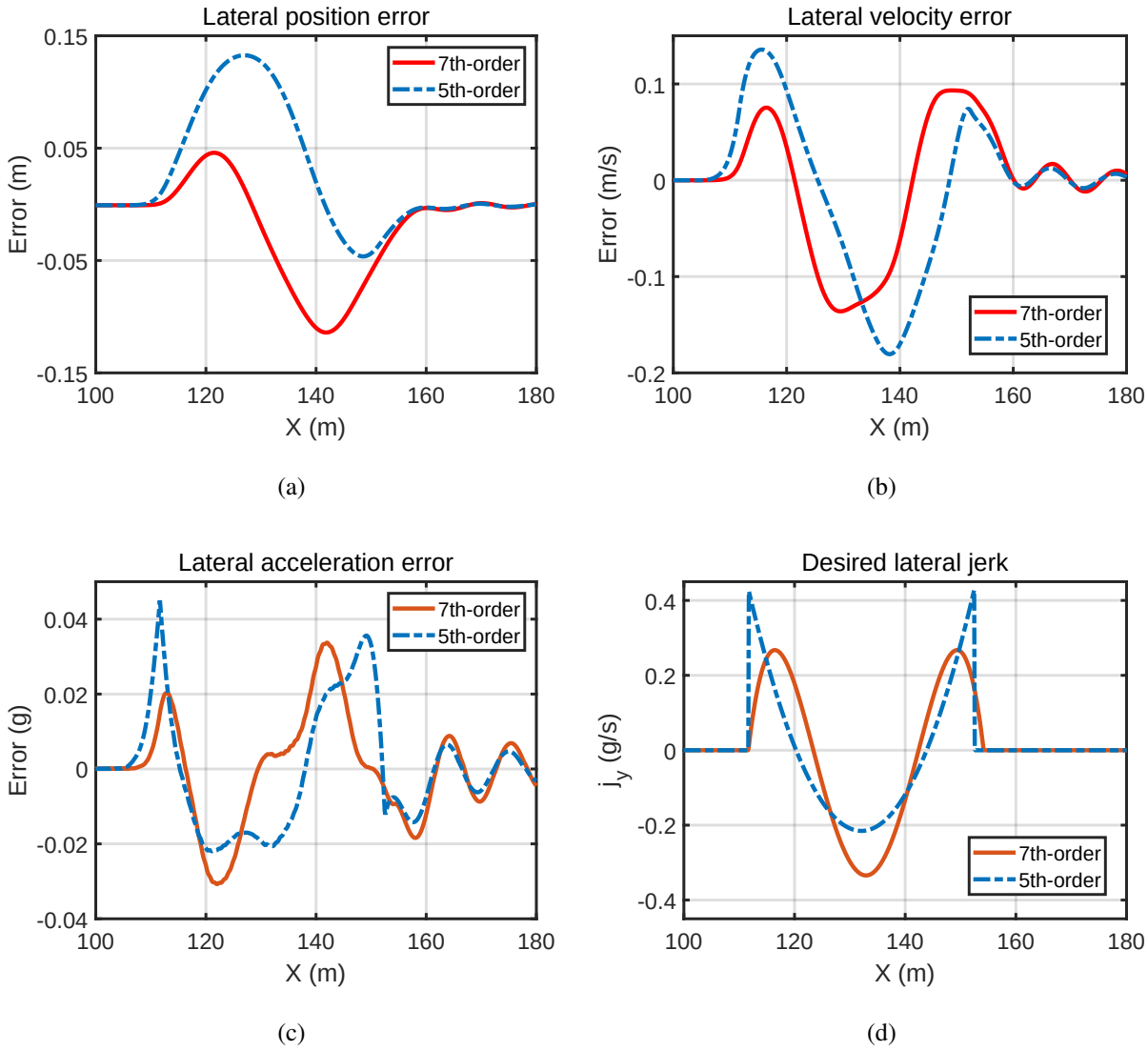

Figure 4.13: Tracking errors and the desired lateral jerks of the proposed 7th-order polynomial trajectory and the classic 5th-order polynomial trajectory ($\mu = 0.3$ and $v_H^* = 40$ km/h).

the 7th-order trajectory has a farther lane change end point (a longer longitudinal length of the lane change maneuver), which yields a smoother trajectory and thus achieving higher safety on the low friction road, when compared to the 5th-order trajectory.

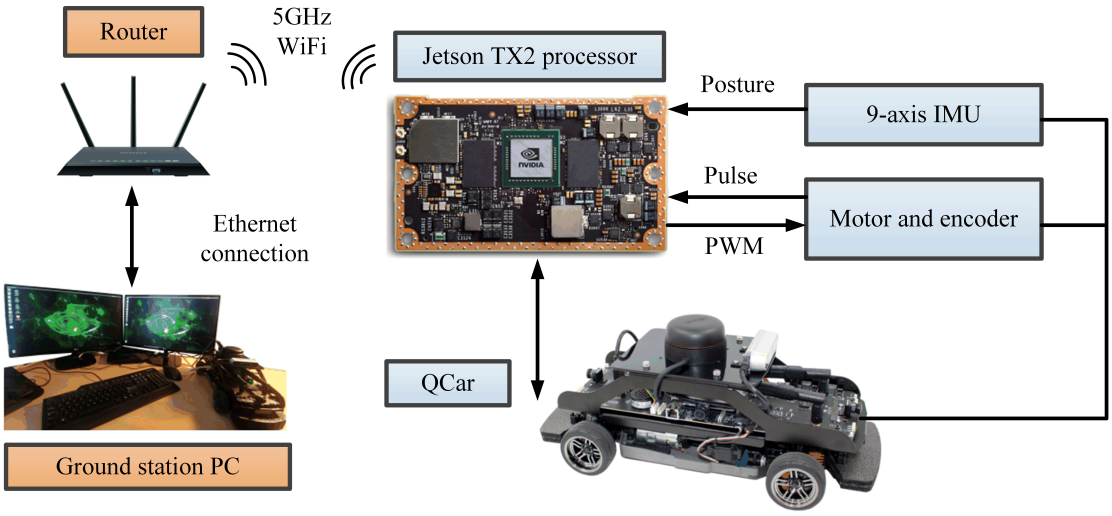

Figure 4.14: The schematic of the Quanser self-driving car (QCar) experiment setup.

4.6 Experimental Results

To further demonstrate the practical effectiveness of the proposed lane change trajectory planning scheme, experimental tests were conducted on the QCar platform, which is a 1/10 scale model car. The effectiveness is verified by comparison of the QCar's responses with the desired characteristics of the trajectory based on the proposed planning scheme.

4.6.1 Description of the Experimental Setup

The architecture of the experiment setup is demonstrated in Figure 4.14. The key parameters of the QCar are summarized in Table 4.5. The desired trajectory is generated in the ground station PC based on the proposed planning scheme, and is fed to the QCar as the reference trajectory. The motion of the QCar is controlled by a drive and steering servo motor. The onboard 9-axis inertial measurement unit (IMU) is used to obtain the real-time posture of the QCar. The control algorithm is written with Simulink blocks and compiled to C-code running on an embedded Linux-based system, which is powered by an onboard NVIDIA Jetson TX2 processor using a Quad-Core ARM Cortex-A57 micro-controller. The onboard processor receives the commanded inputs from the ground station PC, sends the data collected from the IMU and the motor encoder to the ground

Table 4.5: The key parameters of the QCar.

Symbol	Description	Value	Unit
l_v	Length	0.425	m
l_w	Width	0.192	m
h	Height	0.182	m
l	Wheelbase	0.256	m
T	Track width	0.170	m
R_e	Tire radius	0.066	m
u_1^m	Maximum speed	1.5	m/s
u_2^m	Maximum steering angle	0.5	rad

station through Wi-Fi wireless communication, and generates appropriate pulse-width modulation (PWM) signal to the servo motor.

4.6.2 QCar Test Results

In the experiment, the road friction μ is about 0.5. The lane width was set as $l_w^* = 0.35$ m and the speed of the QCar was selected as 0.83 m/s which corresponds to a full-scale speed of about $v_H^* = 30$ km/h (considering a 1/10 scale model). With utilization of the friction and speed information, the adaptive acceleration and jerk limits, $a_{ymax}^Q(u)$ and $j_{ymax}(v_H^*)$, can be obtained according to Eqs. (4–12) and (4–16), respectively. However, as compressed lanes and scale model car were used in the experiment, the minimum lane change duration calculated from Eq. (4–23) should be multiplied by a factor ρ in this case, as:

$$t_{slc}^{min} = \rho \cdot \max\left\{\sqrt{\frac{7.513 l_w^*}{g \cdot a_{ymax}^Q(\mu)}},\ \sqrt[3]{\frac{52.5 l_w^*}{g \cdot j_{ymax}(v_H^*)}}\right\} \tag{4–24}$$

for achieving reasonable planning and tracking results, where $\rho = \sqrt[3]{l_w / l_w^*}$ is a tuned coefficient related to the width ratio of the real lane over the compressed lane. After t_{slc}^{min} is achieved, the planned trajectory is determined accordingly.

The lane change start point is now the only unknown parameter which is related to the motion

of the host and the preceding vehicle. Without loss of generality, the scenario of stationary preceding vehicle was considered. The minimum safe distance d_{th} is thus only related to v_H in this case according to Eq. (4–7). For simplification, d_{th} is set as $1.5v_H$ for ensuring safety. At the initial instant, the QCar was stationary at the origin of the global coordinate system, the stationary preceding vehicle was located at 1.5 m ahead in the current lane.

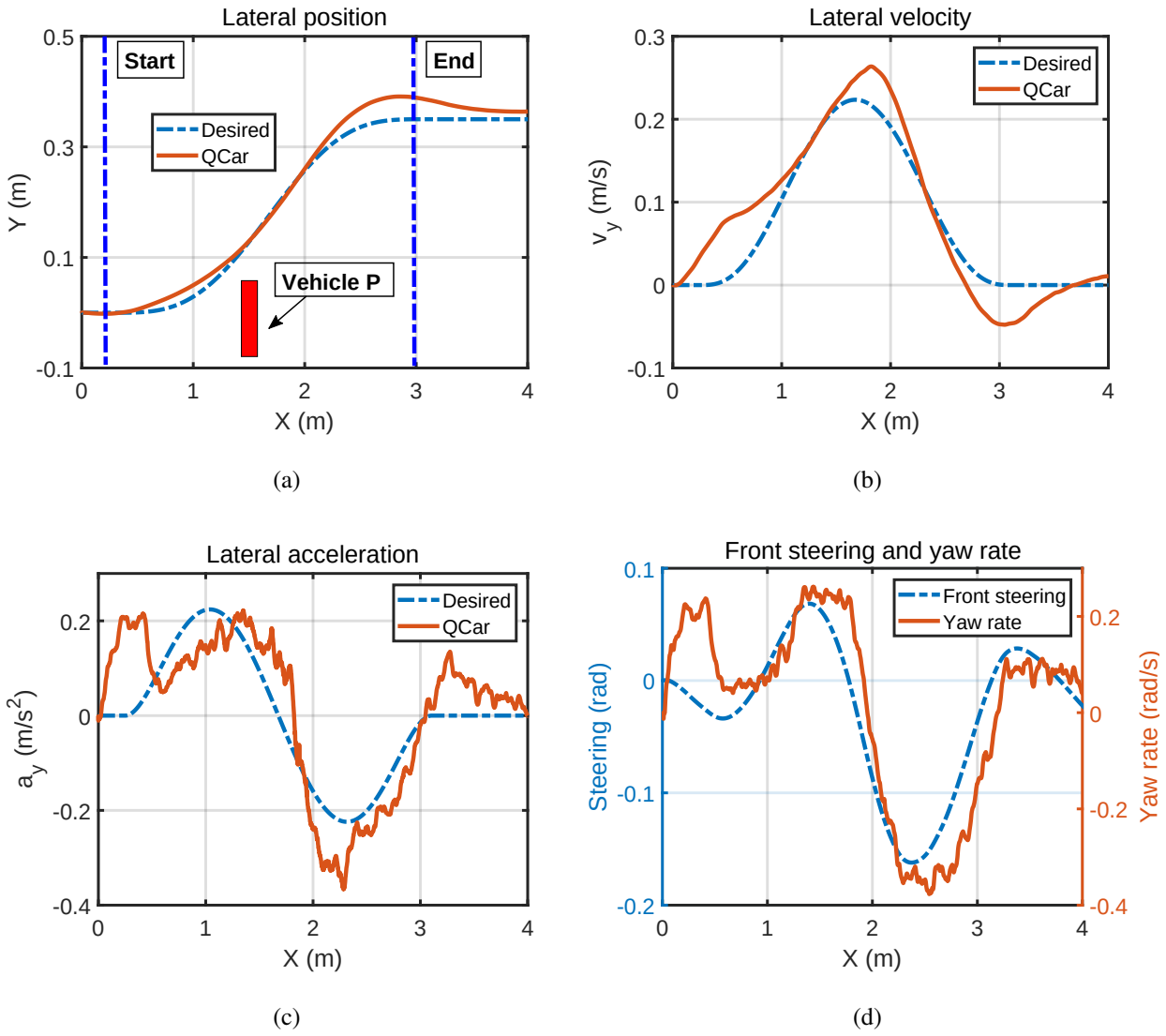

Figure 4.15: The QCar's responses to the proposed 7th-order trajectory in lateral position, velocity, acceleration together with front steering angle and yaw rate.

Figure 4.15 presents the planning and tracking results of the QCar based on the proposed lane change planning scheme. In view of the planned trajectory, the QCar starts lane changing

maneuver at $X = 0.26$ m and completes the maneuver near $X = 3$ m. The achieved comfort can be demonstrated by the fact that the desired lateral position, velocity and acceleration vary smoothly and the peak lateral velocity and acceleration of the QCar are less than 0.25 m/s and 0.35 m/s^2, respectively. Overall, the QCar can track the desired values of lateral position, velocity and acceleration with acceptable accuracy. However, obvious tracking errors are observed near the lane change start and end points. The initial tracking errors are caused by the rapid acceleration of the QCar when $X < 0.5$m, as the QCar needs to track the desired speed from initial zero speed in a short distance (which is due to limited space of the indoor laboratory). As a result, similar increases in lateral acceleration and yaw rate are witnessed near the start point, as shown in Figures 4.15(c) and 4.15(d). After the QCar reaches the desired speed, the QCar closely tracks the desired values until near the lane change end point. The measurement noises and the relatively low accuracy in the localization of the QCar may contribute to the discrepancy between the QCar's trajectory and the planned trajectory near the end point. The smooth variations in front steering angle with the maximum magnitude less than 0.18 rad, as shown in Figure 4.15(d), also illustrate the comfort of the lane change maneuver.

4.7 Summary

In this chapter, a safe and comfortable lane change trajectory planning scheme is proposed for AVs on straight highway. Human driving characteristics are reviewed and integrated to achieve natural driving experience which is regarded as part of comfortable driving. As partly required by the natural driving, 7th-order polynomial function is used to represent the planned trajectory to ensure the continuity of the planned trajectory up to jerk. Dealing with the fact that vehicle dynamic limits are affected by road conditions and vehicle motions, friction-adaptive acceleration and speed-adaptive jerk limits have been designed. After the lane change starting point is determined by the desired worst-scenario-based longitudinal distance criteria, the problem of lane change trajectory planning is reduced to a problem of selecting the approriate lane change duration. There

is no need to solve a constrained optimization problem and only fast algebraic computations are needed to select this single coefficient. Both numerical simulation and QCar experimental results have revealed the effectiveness and practicability of the proposed lane change trajectory planning scheme. The generated trajectories based on the proposed planning scheme can be well tracked by the AVs. In order to achieve robust lane change trajectory tracking under a wide range of forward speeds, an MPC-based adaptive controller is designed in the following chapter with combined consideration of the estimated TRFC.

Chapter 5

MPC-based Lane Change Trajectory Tracking for AVs

5.1 Introduction

Path planning and tracking control play a critical role in autonomous driving, which refer to determine and track the collision-free trajectory from the vehicle's current location to a designated target in accordance with the traffic rules, safety, comfortability and vehicular dynamics. There is substantial research on path planning and tracking control for AVs and very good reviews on various planning algorithms and control methods can be found in [10, 114]. In order to find the best trajectory to follow, different types of constraints imposed by vehicle dynamics, actuator saturation, road boundary, should be taken into consideration while meeting the requirement of obstacle avoidance.

Due to its capability of handling constraints in a systematic way, the MPC technique has recently become an appealing method to solve the AVs' path planning and tracking control problems [86, 140]. The approach involves optimizing a performance index under operation constraints with respect to a sequence of control inputs to generate a desired path or to track a given trajectory by applying the first element of such optimal input sequence to the vehicle system [11, 86]. Two

different research directions can be seen in the reported studies. Some researchers integrated the control module with the path planner respecting the fact that path planning and tracking control have strong connection to each other. Jalalmaab et al. [87] investigated a road-adaptive MPC strategy to track the centerline of the lane while avoiding the obstacle. Although path planning and tracking were realized within one linear MPC framework, it should be noted that only kinematic point-mass vehicle model was used to ensure real-time implementation. In order to take into account both the tire force saturation and the vehicle nonlinearities, a nonlinear MPC based on the four-wheel vehicle model and the MF tire model was designed to conduct path re-planning and tracking task in [86]. The experimental results have shown that the computation time increases rapidly and induced an issue of real-time implementation when the vehicle speed is over 40 km/h.

To avoid complex optimization process which may result in excessive computational demand, an alternative way is to address the path planning and tracking problem separately in a hierarchical architecture. In the project of PRORETA 3, Bauer et al. [88] utilized a potential field-based trajectory planner to calculate the optimal vehicle trajectory, which was then fed into the control layer to achieve collision avoidance in the critical traffic situations. In [89], the collision-free trajectory for AVs was generated based on a three-dimensional potential field method considering the road boundary conditions and the vehicle's kinematic model. The commanded steering angle to track the generated trajectory was then obtained from a multi-constrained MPC framework. Similarly, Shim et al. [90] designed a collision avoidance system which determined a collision-free trajectory based on sixth-order polynomials, and the front steering and individual wheel torques were controlled by an MPC scheme to track the reference trajectory. When the nonlinear vehicle model was used in the MPC, the linearization technique can be applied in each prediction step to reduce the computational burden, as shown in [91]. In addition to the computational burden, the structure of the cost function and the tuning weights on outputs and inputs also have heavy impact on the performance of MPC. Unfortunately, relatively less efforts have been made toward this field. Another issue is related to the TRFC, which reflects the limitation of the available force the road can provide to a vehicle. This coefficient is closely linked to the direction control and the

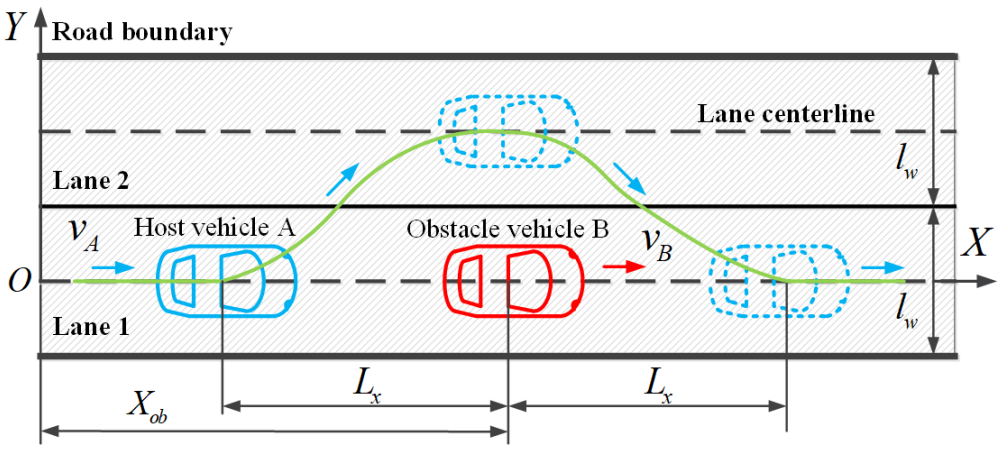

Figure 5.1: A DLC scenario of vehicle collision avoidance.

stability performance of an on-road vehicle and is especially important for AVs since they should be able to perform driving tasks on different road conditions. Most of the previous works in a hierarchical architecture only introduce the TRFC to the trajectory tracking module as input and/or state constraints, such as [86, 89, 91]. Actually, the quality or smoothness of the reference path has a significant influence on the tracking control performance. Thus, considering the limitation of the road friction earlier in the high-level path planner can significantly simplify the design of the low-level tracking controller.

In this chapter, we focus on the two-level path planning and tracking for an autonomous vehicle to avoid vehicle collision on a straight one-way, two-lane highway. In the high-level planning module, a TRFC-based DLC trajectory is generated by making use of the road friction and vehicle speed information. With the front tire steer angle as the control input, a linear dynamic MPC with adaptive weights on outputs in the cost function is further designed to track the planned trajectory as close as possible under a wide range of forward speeds. The proposed lane change trajectory tracking control method will be described in detail in the following sections.

5.2 DLC Trajectory Planning

The scenario of a DLC vehicle collision avoidance is shown in Figure 5.1. XOY is the absolute inertial frame with X-axis defined positive to the right along the centerline of the Lane 1, Y-axis

defined positive upward along the perpendicular of the lane centerline. To simplify the generation of the collision-free trajectory, the study in this chapter only focuses on the following conditions:

(1) The host vehicle A is driving at a constant forward speed v_A all the time and moving along the centerline of the Lane 1 before the lane changing maneuver.

(2) The obstacle vehicle B is static or moving at a very low speed $v_B \leqslant \frac{v_A}{3}$ ahead of the vehicle A along the centerline of the Lane 1.

(3) There is no vehicle in the Lane 2 which is available for lane changing.

As the host vehicle A is approaching to the obstacle vehicle B, lane change maneuver has to be conducted when a collision cannot be avoided through braking alone. A conservative safety distance relevant to both the TRFC (μ) and the vehicle speeds (v_A, v_B) is used to determine where the lane changing maneuver starts, which is defined as:

$$L_x = (v_A^2 - v_B^2)/2\mu g + v_A * h_0 + d_0^* + l_v \tag{5–1}$$

where the first term represents the minimum braking distance required to reduce speed from v_A to v_B, with $g = 9.81$ m/s^2 being the acceleration due to gravity; h_0 and d_0^* are headway time and standstill distance, respectively; l_v is the vehicle length which is added here for consideration of vehicle geometry. Based on the continuous-curvature path proposed by Nelson [55], the safety distance is utilized to generate the desired trajectory of the host vehicle A, which is defined by representing lateral position Y_d as a function of the longitudinal position X, and is expressed as:

$$Y_d = \begin{cases} l_w[10(\frac{X_3}{L_x})^3 - 15(\frac{X_3}{L_x})^4 + 6(\frac{X_3}{L_x})^5], X_1 \leqslant X \leqslant X_{ob} \\ l_w[10(\frac{X_4}{L_x})^3 - 15(\frac{X_4}{L_x})^4 + 6(\frac{X_4}{L_x})^5], X_{ob} < X \leqslant X_2 \\ 0, \text{else} \end{cases} \tag{5–2}$$

where l_w is the lane width, $X_1 = X_{ob} - L_x$, $X_2 = X_{ob} + L_x$, $X_3 = X - X_1$, $X_4 = 2X_{ob} - X_1 - X$, with X_{ob} being the longitudinal position of the vehicle B as shown in Figure 5.1. By following

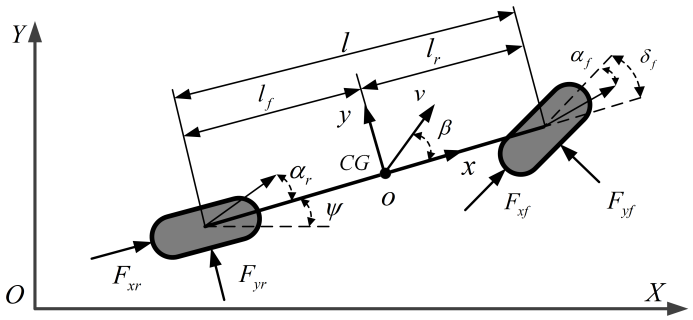

Figure 5.2: Simplified one-track model used for path tracking.

the reference trajectory (5–2), vehicle A starts steering from the centerline of the Lane 1 to the adjacent Lane 2 at $X = X_1$, reaches the centerline of the Lane 2 at $X = X_{ob}$, and goes back to the original centerline at $X = X_2$. The smoothness of the desired trajectory and the duration of the DLC maneuver are determined by the safety distance L_x, and thus related to the TRFC and the vehicle speeds. This is a simple way which may mimic a skillful driver taking the road friction condition and vehicle speed into account on highway.

Remark 5.1 *It is evident from (5–1) and (5–2) that the lower v_A the sharper trajectory will be generated. It may become difficult to follow the desired trajectory when the host vehicle is running at a very low speed. $v_A \geqslant 30$ km/h is thus considered in this study and this is reasonable especially for studying DLC maneuver on highway.*

Remark 5.2 *The friction coefficient (μ) is assumed having been estimated before the DLC maneuver when the vehicle is driving on the straight road. More details about the TRFC estimation can be referred to the authors' previous works [122, 123].*

5.3 DLC Trajectory Tracking Controller Design

5.3.1 Vehicle Dynamic Model

Considering constant longitudinal velocity, a simplified one-track model of a vehicle is selected to describe the lateral motion, as shown in Figure 5.2. The vehicle body frame xoy is centered

on the *CG*, with x defined positive to the right along the centerline of the vehicle and y defined positive upward along the perpendicular of x. With assumption of small tire steering angle and small vehicle yaw angle, the motion equations of this model can be derived with the help of force and torque balances with respect to the *CG* and coordinate transformations between the inertial frame and the vehicle body frame, as:

$$\begin{aligned} m(\dot{v}_y + v_x\dot{\psi}) &= F_{yf} + F_{yr} \\ I_z\ddot{\psi} &= l_f F_{yf} - l_r F_{yr} \\ \dot{Y} &= v_x\psi + v_y \end{aligned} \tag{5–3}$$

where m is the vehicle mass, I_z is the rotational inertia about the z-axis, l_f and l_r are the distances from the *CG* to the front- and rear-axle, respectively. v_x, v_y are the vehicle longitudinal and lateral velocities in the body frame. $\psi, \dot{\psi}$ and Y are yaw angle, yaw rate and lateral position of the host vehicle in the inertial frame, respectively. For small tire slip angle, the unknown cornering force of front- and rear-axle, F_{yf} and F_{yr}, are approximated as a linear function of tire slip angle as:

$$F_{yi} = -2C_i \cdot \alpha_i,\ i = f, r \tag{5–4}$$

where C_i and α_i are the individual tire cornering stiffness and the tire slip angle, $i = f, r$ represents front and rear tires, respectively. Using small angle approximation, the tire slip angle (α_f, α_r) are described by [17]:

$$\begin{aligned} \alpha_f &= (v_y + l_f\dot{\psi})/v_x - \delta_f \\ \alpha_r &= (v_y - l_r\dot{\psi})/v_x \end{aligned} \tag{5–5}$$

where δ_f is the front tire steer angle.

5.3.2 MPC Controller Formulation

The state-space vehicle model for the MPC optimization process is derived based on the equations (5–3)-(5–5), and this model can be compactly written as:

$$\begin{aligned} \dot{x}(t) &= Ax(t) + Bu(t) \\ z(t) &= Cx(t) \end{aligned} \tag{5–6}$$

where $x(t) \in \mathbb{R}^n$ is the state of the system, $u(t) \in \mathbb{R}^m$ is the input and $z(t) \in \mathbb{R}^p$ is the output, $n = 4$ is the number of states, $m = 1$ is the number of input and $p = 3$ is the number of outputs. The four states are lateral velocity in the body frame, yaw angle, yaw rate, and lateral coordinates of the *CG* of the host vehicle in the inertial frame. These are denoted respectively as $x = [v_y, \psi, \dot{\psi}, Y]'$. The only input for lateral control is the front tire steering angle $u = \delta_f$. The three outputs are denoted as $z = [\dot{\psi}, Y, \beta]'$ where β is the vehicle's sideslip angle. The matrices A, B and C in (5–6) are listed as:

$$A = \begin{bmatrix} -\frac{2C_f+2C_r}{mv_x} & 0 & -v_x - \frac{2C_f l_f - 2C_r l_r}{mv_x} & 0 \\ 0 & 0 & 1 & 0 \\ -\frac{2l_f C_f - 2l_r C_r}{I_z v_x} & 0 & -\frac{2l_f^2 C_f + 2l_r^2 C_r}{I_z v_x} & 0 \\ 1 & v_x & 0 & 0 \end{bmatrix} \tag{5–7}$$

$$B = \begin{bmatrix} \frac{2C_f}{m} \\ 0 \\ \frac{2l_f C_f}{I_z} \\ 0 \end{bmatrix}, \; C = \begin{bmatrix} 0 & 0 & 1 & 0 \\ 0 & 0 & 0 & 1 \\ \frac{1}{v_x} & 0 & 0 & 0 \end{bmatrix} \tag{5–8}$$

In order to obtain a finite-dimensional optimal control problem, we discretize the system dynamics (5–6) with a fixed sampling time T_s using Euler's method:

$$\begin{aligned} x(k+1|k) &= A_d \cdot x(k|k) + B_d \cdot u(k|k) \\ z(k|k) &= C_d \cdot x(k|k) \end{aligned} \tag{5–9}$$

where $A_d = E + AT_s$, $B_d = BT_s$ and $C_d = C$, with E an n-dimensional unit matrix.

Let k be the current time step, $x_k = x(k|k)$ is the state vector at k-th step and consider the following cost function:

$$\begin{aligned} J(x_k, \mathcal{U}_k, \epsilon_k) = &\sum_{i=1}^{H_p} \|\eta(k+i|k) - \eta^r(k+i|k)\|_Q^2 \\ &+ \sum_{i=0}^{H_c-1} \|\Delta u(k+i|k)\|_R^2 + \rho\epsilon_k^2 \end{aligned} \tag{5–10}$$

where $\eta(k+i|k) = z(k+i|k)$ represent the predictive outputs and $\eta^r(k+i|k)$ are the corresponding reference signals at sampling step $k+i$. $\Delta u(k+i|k) = u(k+i|k) - u(k+i-1|k)$ are the differences of the control inputs at sampling step $k+i$ and $u(k-1|k)$ are the known inputs from the previous control interval. $\mathcal{U}_k = [u(k|k)', ..., u(k+H_c-1)']'$ is the optimization vector at time step k. H_p and H_c are the prediction and control horizon, respectively, and $H_p > H_c$. To reduce computational requirement, the control signal sequences $u(k+i|k)$ hold equal to $u(k+H_c-1|k)$ while $H_c \leqslant i \leqslant H_p$. The term $\rho\epsilon_k^2$ penalizes the violation of the constraint, ϵ_k is a slack variable and ρ is a weighting coefficient. Q and R are diagonal matrices with the squares of those output weights and input rate weights, respectively, being the diagonal elements. They are written as $Q = \text{diag}(\lambda_1^2, \lambda_2^2, \lambda_3^2)$, $R = \lambda_4^2$.

The objective of the MPC controller is to track the desired trajectory generated in Section 5.2. As shown in (5–2), only reference lateral position is directly generated. However, the host vehicle is driving on a straight line before and after the lane change maneuver. Considering the physical characteristics, the reference values of both the yaw rate and vehicle sideslip angle can be set zero

Table 5.1: Constraints on outputs.

Outputs	Minimum value	Maximum value
$\dot{\psi}$	$-0.85\mu g/v_x$	$0.85\mu g/v_x$
Y	$-l_w/2 + T/2$	$3l_w/2 - T/2$
β	$-\arctan(0.02\mu g)$	$\arctan(0.02\mu g)$

Table 5.2: Adaptive weights.

v_x (km/h)	(30, 50]	(50, 60]	(60, 70]	(70, 80]	(80, 92]
λ_1	0.4	1.0	2.8	4.0	6.0

before and after the DLC maneuver. Still, the reference vehicle sideslip angle and yaw rate during the DLC maneuver are unknown. In this case, the problem of minimizing (5–10) can not be solved through the traditional MPC scheme. Here, we propose a new way to deal with this problem and the prerequisite is only the reference lateral position.

Remind that the higher the output weights, the higher demand on tracking the corresponding reference signal. The controller will ignore the setpoints with zero weight and allow the output to vary freely. Based on this, the weight on the predictive output is set to zero when there is lack of its reference value. Thus, the output weight on yaw rate (λ_1) is set zero during the DLC maneuver and a nonzero value otherwise. Unlike yaw rate being an easily measured signal, vehicle sideslip angle is hard to be directly measured, its output weight is thus setting to zero all the time ($\lambda_3 = 0$). Doing so will enable the vehicle sideslip angle and yaw rate to vary freely around their respective setpoints when no reference values are given. The setpoints of vehicle sideslip angle and yaw rate are assigned both zero in $\eta^r(k+i|k)$ for respecting the fact that the host vehicle is starting from the centerline and going back to the same centerline. Moreover, it is not safe when the generated yaw rate or vehicle sideslip angle is beyond the value the road is able to provide [141]. At high vehicle sideslip angle, the tires may lose their linear behavior and cause large tracking errors. Hence the magnitude of these two outputs should be bounded by the friction-related constraints. At each time

step k, the following finite horizon optimal control problem is solved:

$$
\begin{aligned}
&\min_{\mathcal{U}_k,\epsilon_k} J(x_k,\mathcal{U}_k,\epsilon_k)\\
\text{s.t. }\ & x(k+1|k)=A_d\cdot x(k|k)+B_d\cdot u(k|k)\\
& \eta(k|k)=C_d\cdot x(k|k)\\
& u(k-1|k)=u(k-1)\\
& \Delta u(k+i|k)=u(k+i|k)-u(k+i-1|k)\\
& \Delta u_{min}\leqslant \Delta u(k+i|k)\leqslant \Delta u_{max}\\
& u_{min}\leqslant u(k+i|k)\leqslant u_{max}\\
& i=0,...,H_c-1\\
& \Delta u(k+i|k)=0,\ i=H_c,...,H_p\\
& \begin{bmatrix}\dot{\psi}_{min}\\ Y_{min}\\ \beta_{min}\end{bmatrix}-\epsilon_k\leqslant \eta(k+i|k)\leqslant \begin{bmatrix}\dot{\psi}_{max}\\ Y_{max}\\ \beta_{max}\end{bmatrix}+\epsilon_k\\
& i=1,...,H_p,\ \epsilon_k\geqslant 0\\
& x(k|k)=x_k,\ \eta^r(k+i|k)=[0\ \ Y_d\ \ 0]'
\end{aligned}
\tag{5–11}
$$

where u_{min} and Δu_{min}, u_{max} and Δu_{max} are the constraints imposed on the control signals. The constraints exerted on the output variables are denoted in Table 5.1 with l_w and T being lane width and vehicle width, respectively. The empirical selection of the friction-related upper and lower bounds of $\dot{\psi}$ and β can be referred to [141].

Remark 5.3 *Vehicle sideslip angle β is approximated as v_y/v_x and the output constraint $\beta_{min}-\epsilon_k\leqslant\beta\leqslant\beta_{max}+\epsilon_k$ is transferred to state constraint on vehicle lateral velocity.*

The optimization problem (5–11) can be recast as a quadratic programming and it does not require any complex optimization software. Denoted by $\mathcal{U}_k^*=[u^*(k|k)',...,u^*(k+H_c-1)']'$, the sequence of optimal inputs are computed at time step k by solving (5–11) for the current system

states x_k, then the first sample of $\mathcal{U}_k^*$ is applied to the vehicle at time k. At time $k+1$, a new optimization is solved over a shifted prediction horizon starting from the newly measured states $x(k+1|k+1) = x_{k+1}$.

5.3.3 Adaptive Weights in Cost Function

The performance of the above MPC is strongly related to the tuning weight set $[\lambda_1, \lambda_2, \lambda_3, \lambda_4]$. Given a vehicle forward speed, it is easy to tune a set of $[\lambda_1, \lambda_2, \lambda_3, \lambda_4]$ to achieve acceptable tracking results. However, the performance of the controller with fixed values of $\lambda_i, i = 1, 2, 3, 4$ will be degraded or even unacceptable (cause oscillations and instability) when the vehicle is moving under a different velocity. A straightforward method is to design the adaptive weights varying with vehicle speed. While there are four weights to be tuned, the output weights on yaw rate and lateral position (λ_1, λ_2) have larger influence on the performance of the controller than the input weight. Noted that the output weight on vehicle sideslip angle λ_3 is zero as explained in Section 5.3.2, only λ_1 and λ_2 are needed to set as speed-adaptive values by setting $\lambda_4 = 0.5$. In order to further simplify the tuning process, we set output weight on lateral position as fixed value of $\lambda_2 = 1$. Based on the principle that the higher forward speed, the higher weights should be imposed on yaw rate to ensure vehicle's stability. The adaptive weights on yaw rate were selected after extensive simulations under a wide range of speeds, as shown in Table 5.2.

5.4 Simulation Results

To test the performance of the proposed planning and tracking framework, a series of collision avoidance maneuvers at different forward speeds have been conducted using CarSim and MATLAB/Simulink software. Two different road surfaces with friction coefficients of 0.8 and 0.3, denoted as high-μ and low-μ road, respectively, have been set in CarSim. The main parameters for the vehicle model and the highway road used in simulation are shown as:

- $m = 1,416$ kg, $I_z = 1,523$ kgm^2, $l_f = 1.016$ m, $l_r = 1.562$ m, $l = 2.578$ m, $T = 1.739$ m,

$C_f = 47,000$ N/rad, $C_r = 38,000$ N/rad, $l_w = 3.5$ m, $h_0 = 2$ s, $d_0 = 2$ m

The adaptive MPC (5–11) is with the following parameters:

- $T_s = 0.05$ s, $H_p = 15$, $H_c = 5$
- $u \in [-10^\circ, 10^\circ]$, $\Delta u \in [-1^\circ, 1^\circ]$
- $Q = \text{diag}(\lambda_1^2, 1, 0)$, $R = 0.5^2$, $\rho = 10^5$

5.4.1 High-μ Road

A relatively high friction coefficient ($\mu = 0.8$) was firstly selected to simulate the usual running condition on concrete or asphalt surfaces for highway vehicles. The host and the obstacle vehicles were initially located at longitudinal position 0 and 150 m, respectively. The host vehicle's DLC maneuvers under three constant forward speeds $v_x = 90, 60, 40$ km/h, respectively, have been conducted. The three desired trajectories, corresponding to the different speeds, are computed based on (5–2), as shown in Figure 5.3(a). The higher the forward speed, the earlier the host vehicle starts steering to the adjacent lane and thus leaving larger safety distance. The designed MPC tracks the desired trajectories well and tightly confines the vehicle's position within the road boundaries, though a slightly larger error is observed under 90 km/h. The generated yaw rate, vehicle sideslip angle and wheel steer angle are shown in Figures 5.3(c), 5.3(e) and 5.3(g), respectively. All of these three variables are varying with peak values much smaller than their respective bounds showing the smoothness of the generated trajectories. As can be seen from Figure 5.3(e), the magnitude of the generated vehicle sideslip angle under 90 km/h is much larger than those under two lower speeds. This shows that the vehicle forward speed has a strong influence on the sideslip angle and high vehicle speed may generate high sideslip angle leading to unstable system. Higher sideslip angle also results in larger vehicle modeling errors, which partly explains a slight tracking oscillation under 90 km/h. It is also pointed out that the designed MPC is able to obtain acceptable closed-loop performance up to $v_x = 92$ km/h on high-μ road.

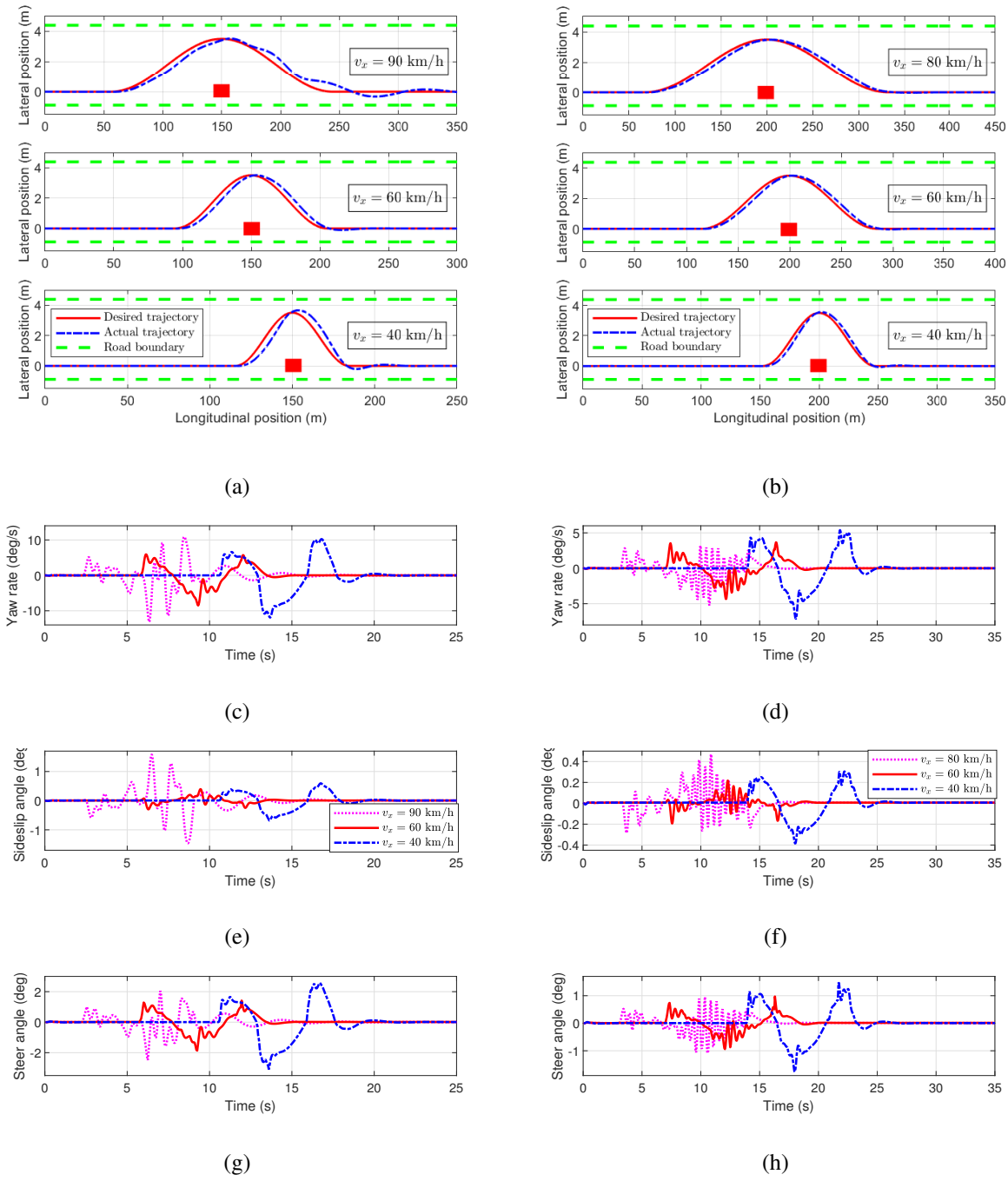

Figure 5.3: Simulation results on two road conditions. (a), (c), (e) and (g) are $\mu = 0.8$ road under three different forward speeds. (b), (d), (f) and (h) are $\mu = 0.3$ road under three different speeds. (Note the red box in (a) and (b) represents the obstacle vehicle).

5.4.2 Low-μ Road

The friction coefficient was set as $\mu = 0.3$ to simulate road conditions covered by snow in winter of highway. The host vehicle was initialized at longitudinal position 0 m. The location of the obstacle vehicle was set as $X_{ob} = 200$ m considering that larger safety distance is required on a slippery road under the same speed. Collision avoidance scenarios under three speeds $v_x = 80, 60, 40$ km/h have been investigated. The desired and the actual trajectories are shown in Figure 5.3(b). Compared to those results obtained on high-μ road, the designed MPC can achieve better tracking performances on this low-μ road. This is because the generated trajectories based on a larger safety distance on the slippery road are smoother. Figures 5.3(d), 5.3(f) and 5.3(h) demonstrate the generated yaw rate, vehicle sideslip angle and the road wheel steer angle, respectively, during the DLC maneuver. Due to a poor road adhesion, the commanded wheel steer angle changes more frequently than that on high-μ road to closely track the desired trajectory. As a result, both the yaw rate and the vehicle sideslip angle also rapidly change with time during the lane-change maneuver. The higher the forward speed, the more rapid changes are observed. Again, it is also pointed out that the upper bound of the forward speed for the MPC to stabilize the vehicle and accurately track the desired trajectory is $v_x = 82$ km/h.

5.5 Summary

In this chapter, an MPC-based path planning and tracking framework for AVs using the estimated TRFC is presented. The desired DLC trajectory is generated based on the safety distance between the host vehicle and the obstacle vehicle, which is related to both the TRFC and the vehicle speed. With integrated consideration of output weights in the cost function and the constraints on the magnitude of the outputs defined by the TRFC, a linear dynamic MPC with adaptive output weights is designed so that only lateral position is required to track the desired trajectory. Moreover, the adaptive weights on outputs in the cost function have been identified for a wide range of

speeds making the designed controller very promising in practical applications. While the advantage of integration of TRFC with the trajectory tracking is obvious, to validate the effectiveness of the proposed method through lab experiments is not that easy since it is hard to simulate the real tire-road interface and obtain the accurate value of the real TRFC in the indoor lab. It is also noted that the trajectory tracking controllers should be designed according to the operating conditions and environments. Based on the available scaled model QCar self-driving platform in our lab, an adaptive trajectory tracking control scheme for AVs operating at low speeds is proposed in the following chapter. Comparative simulations and experimental tests have been carried out to demonstrate its advantages in tracking accuracy while meeting the requirements by the implementation capability of the actuators.

Chapter 6

Adaptive Trajectory Tracking for Low-Speed AVs with Input Constraints

6.1 Introduction

Car-like vehicles have attracted considerable attention and efforts from academia and industry due to their flexible mobility [142–144]. These developments have been further fueled by the emerging of AVs with the help of significant advancements in sensing and computing technologies. It is believed that AVs have great potential to improve safety, comfort and efficiency of the transportation [112, 140, 145–147]. Under nonholonomic constraints, a challenging problem in car-like vehicles is trajectory tracking control which aims at driving the vehicle along a pre-defined trajectory [143, 144, 148, 149]. As an integral part of autonomous systems, the trajectory tracking control problem of car-like vehicles has been widely studied. Depending on the utilized vehicle model, the tracking control approaches in the literature can be generally divided into geometric, dynamic and kinematic based controllers. When the AVs are operating at low speeds, most dynamic effects are negligible. The designed controllers based on kinematic model alone may still achieve acceptable trajectory tracking performances.

There are two paramount concerns in the problem of trajectory tracking for car-like vehicles

based on kinematic model. One is the input constraints arising from the implementation capability of the physical actuator(s). Large tracking errors or even system instability would occur when the commanded inputs surpass the maximum capability of the actuator(s). Besides, the overlarge inputs will reduce the operational life of the actuator(s) in real applications. Some studies utilized the MPC [150–152] or neural network (NN) [153,154] methodologies to handle system constraints and nonlinearities. However, the presence of nonlinear dynamics, time-varying states and input constraints may contribute to the issue of heavy computation [11]. The design of tracking controllers based on non-optimization-based methods may thus be a good alternative. Unfortunately, most of these methods in the reviewed studies focus on stabilizing the vehicle at zero equilibrium without imposing constraints on inputs. Accurate trajectory tracking with consideration of input constraints would thus still be desirable for practical implementation. The other concern is the operational range. In order to increase the controller's operational range, the majority of the existing studies research on achieving control robustness against model uncertainties and external disturbances considering only constant control gains [155–157]. Clearly, a set of constant gains seldom meets all the driving scenarios especially when there are variations in initial errors and desired speeds. It should be noted that the controller's gains have a great influence on the tracking performance and adaptive gains are of highly practical importance in real applications. The design of adaptive gains not only enhances the tracking accuracy for various scenarios but also reduces the time and efforts dedicated to the tuning of the gains.

In this chapter, a new trajectory tracking control scheme with adaptive gains is designed for the low-speed AVs. While the input constraints are considered for practical application, backstepping method is used to ensure zero deviations of the car-like vehicle based on the kinematic model. To make the trajectory tracking control more explicit, the lateral position error is creatively taken as a virtual input in the first step of the backstepping method to determine the commanded velocity and steering angle. The proposed controller's gains are automatically adjusted according to the tracking errors and the desired vehicle speed, which can largely reduce the tuning time and efforts. Compared to traditional controllers with constant gains, the proposed adaptive control scheme has a

faster convergence rate of the tracking errors, especially for lateral position error. In the meanwhile, the commanded inputs of the proposed controller are guaranteed not violating the input constraints. The proposed trajectory tracking scheme will be described in detail in the following sections.

6.2 Problem Formulation

6.2.1 Kinematic Bicycle Model

A bicycle model is constructed by lumping the two wheels on front- and rear-axle, respectively, as a single wheel located at the midpoint of each axle, as shown in Figure 6.1(a). The front-wheel is the steering wheel, and the rear-wheel's orientation is fixed. Assuming that the vehicle only has planar motions, a posture consisting of three coordinates in the global coordinate frame (OXY) is required to describe the motion of the vehicle:

$$\boldsymbol{p_c} = [X_c, Y_c, \psi_c]' \tag{6–1}$$

where (X_c, Y_c) are global coordinates of the control point C (midpoint of rear-axle) and ψ_c describes the orientation of the vehicle whose positive direction is taken counterclockwise from the X-axis. For low-speed motion of the vehicle, it is reasonable to assume both the wheels roll with no slipping [141]. The lines FO' and CO' are drawn perpendicular to the orientation of the front and rear wheels, respectively. The intersection O' is the instantaneous rolling center for the vehicle. The radius of the vehicle (R) is calculated by:

$$R = l/\tan\delta \tag{6–2}$$

where l is the vehicle's wheelbase, δ is the steering angle of the front wheel (turning left is positive steering). With assumption of low vehicle speed, the yaw rate of the vehicle ($\dot{\psi}_c$) is expressed by:

$$\dot{\psi}_c = V/R = V/l \cdot \tan\delta \tag{6–3}$$

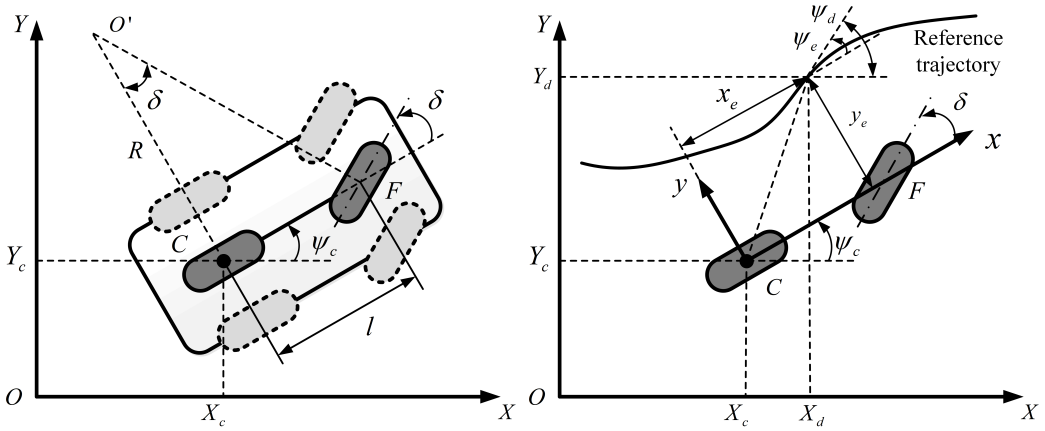

Figure 6.1: Kinematic bicycle model and posture errors.

where V is the forward speed at the point C. The kinematic model of the vehicle's motion is derived as:

$$\begin{cases} \dot{X}_c = V\cos\psi_c \\ \dot{Y}_c = V\sin\psi_c \\ \dot{\psi}_c = V/l\cdot\tan\delta \end{cases} \tag{6–4}$$

6.2.2 Posture Error

For trajectory tracking control problem, the vehicle's current posture $\boldsymbol{p_c}$ must follow the reference posture ($\boldsymbol{p_d} = [X_d, Y_d, \psi_d]'$). In terms of control, it is better to define a posture error in the local coordinate frame (Cxy) whose origin is at point C, x-axis is in the direction of ψ_c, and y-axis is perpendicular to x-axis with positive upwards, as seen in Figure 6.1(b). Based on the geometric relationship, the difference between $\boldsymbol{p_d}$ and $\boldsymbol{p_c}$, $\boldsymbol{p_d} - \boldsymbol{p_c}$ is transformed to local coordinate frame as $\boldsymbol{p_e}$, which is described as:

$$p_e = \begin{bmatrix} x_e \\ y_e \\ \psi_e \end{bmatrix} \begin{bmatrix} \cos\psi_c & \sin\psi_c & 0 \\ -\sin\psi_c & \cos\psi_c & 0 \\ 0 & 0 & 1 \end{bmatrix} \begin{bmatrix} X_d - X_c \\ Y_d - Y_c \\ \psi_d - \psi_c \end{bmatrix} \tag{6–5}$$

where x_e, y_e and ψ_e are longitudinal position, lateral position and yaw angle errors between the desired trajectory and the actual trajectory tranformed into the local coordinate frame. Taking the time derivative of Eq. (6–5) and combining it with Eq. (6–4), the dynamic equations of the posture errors are obtained as:

$$\begin{cases} \dot{x}_e = -V + V_d \cos\psi_e + y_e \dfrac{V}{l} \tan\delta \\ \dot{y}_e = V_d \sin\psi_e - x_e \dfrac{V}{l} \tan\delta \\ \dot{\psi}_e = \dot{\psi}_d - \dot{\psi}_c = \dfrac{V_d}{l} \tan\delta_d - \dfrac{V}{l} \tan\delta \end{cases} \tag{6–6}$$

where V_d, δ_d and $\dot{\psi}_d$ are the desired forward speed, steering angle and yaw rate, respectively. In which, $\dot{\psi}_d$ can be calculated as $(V_d \tan\delta_d)/l$ according to Eq. (6–3). In this chapter, only forward motion is considered ($V > 0$), the steering angle δ and the yaw angle ψ_c are confined within $[-0.5, 0.5]$ and $(-\pi, \pi]$, respectively, and it is also assumed $|\psi_e| < \pi$.

6.2.3 Problem Statement

The actual controlled inputs to the car-like vehicle are the forward speed V and the steering angle δ, the output of the vehicle is the current posture $\boldsymbol{p_c}$. Obviously, both the two inputs have physical constraints in real applications. It is assumed that a feasible and smooth trajectory has been generated and the reference posture $\boldsymbol{p_d}$ together with the desired steering angle δ_d are known information to the vehicle all the time. The trajectory tracking problem has now transferred to find an appropriate input vector $\boldsymbol{u} = [u_1, u_2]' = [V, \delta]'$ to make the posture error $\boldsymbol{p_e}$ to converge to zero subject to the following constraints:

$$|u_i| \leqslant u_i^m,\ i = 1, 2 \tag{6–7}$$

where $u_i^m, i = 1, 2$, are the maximum values of the inputs which are determined by the implementation ability of the actuator.

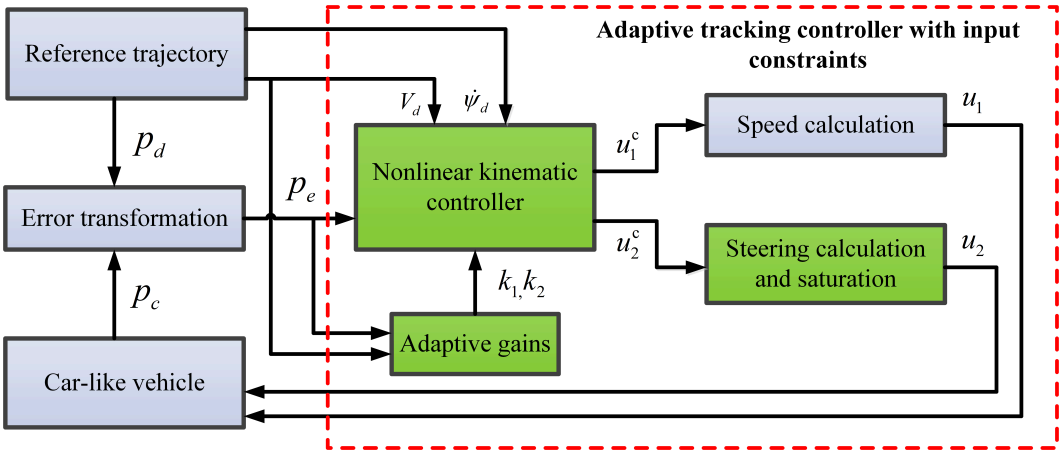

Figure 6.2: The architecture of the proposed adaptive trajectory tracking control system.

6.3 Adaptive Tracking Control Scheme

In this section, the adaptive nonlinear kinematic controller will be designed to stabilize the posture error dynamics given by Eq. (6–6) (i.e., $\boldsymbol{p_e} \to 0$ as $t \to \infty$) with combined consideration of the input constraints in Eq. (6–7). The backstepping control method is utilized in the control scheme design since it can provide a systematic way to derive globally stabilizing control laws [155]. The architecture of the proposed adaptive trajectory tracking control system is depicted in Figure 6.2. The details about the green blocks inside the red rectangle will be discussed in the following sections.

6.3.1 Backstepping Control Scheme without Input Constraints

First, the kinematic model without input constraints is considered. As $\dot{\psi}_c$ equals to $V \tan\delta / l$, Eq. (6–6) can be written in a compact form, as:

$$\begin{cases} \dot{x}_e = -V + V_d \cos\psi_e + y_e \dot{\psi}_c \\ \dot{y}_e = V_d \sin\psi_e - x_e \dot{\psi}_c \\ \dot{\psi}_e = \dot{\psi}_d - \dot{\psi}_c \end{cases} \tag{6–8}$$

Under this compact form of posture error dynamic equations, the tracking problem is transformed to find an appropriate control input $\boldsymbol{u^*} = [u1^*, u2^*]' = [V, \dot{\psi}_c]'$ such that $\boldsymbol{p_e} \to 0$ as $t \to \infty$. In purpose of this objective, the following subsystem is firstly considered:

$$\begin{aligned} \dot{x}_e &= -V + V_d \cos\psi_e + y_e \dot{\psi}_c \\ \dot{y}_e &= V_d \sin\psi_e - x_e \dot{\psi}_c \end{aligned} \tag{6–9}$$

We choose the Lyapunov function candidate for this subsystem as:

$$V_1 = \frac{1}{2}(x_e^2 + y_e^2) \tag{6–10}$$

The derivative of V_1 along Eq. (6–9) is:

$$\dot{V}_1 = x_e(-u_1^* + V_d \cos\psi_e) + y_e V_d \sin\psi_e \tag{6–11}$$

As lateral position error y_e has an explicit reflection of trajectory tracking performance, we here regard it as a virtual input. If y_e varies along:

$$y_e^d = -\frac{k_2 \sin\psi_e}{V_d} \tag{6–12}$$

and the input u_1^* is selected as:

$$u_1^* = V_d \cos\psi_e + k_1 x_e \tag{6–13}$$

then we have:

$$\dot{V}_1 = -k_1 x_e^2 - k_2 (\sin\psi_e)^2 \tag{6–14}$$

where k_1 and k_2 are positive constant gains. Therefore, V_1 will converge to zero asymptotically, which is equal to that both the longitudinal and lateral position errors will converge to zero asymptotically. While the actual input u_1 can be selected as u_1^* given by Eq. (6–13), the lateral position error y_e has no guarantee to track y_e^d precisely in this stage. Define the tracking error between y_e

and y_e^d as:

$$\tilde{y}_e = y_e - y_e^d \tag{6–15}$$

The derivative of $\tilde{y}_e$ is calculated as:

$$\dot{\tilde{y}}_e = V_d \sin\psi_e - (x_e + \frac{k_2 \cos\psi_e}{V_d})u_2^* + \frac{k_2 \cos\psi_e \dot{\psi}_d}{V_d} - \frac{k_2 \sin\psi_e \dot{V}_d}{V_d^2} \tag{6–16}$$

where $\dot{V}_d$ is the first-order derivative of the desired forward speed and can be calculated from the reference trajectory. In order to ensure $\tilde{y}_e \to 0$ or $y_e \to y_e^d$ as $t \to \infty$, we consider the Lyapunov function as:

$$V_2 = V_1 + \frac{1}{2}\tilde{y}_e^2 \tag{6–17}$$

The time derivative of V_2 along Eqs. (6–11) and (6–16) is:

$$\begin{aligned}\dot{V}_2 =& x_e(-u_1^* + V_d \cos\psi_e) + y_e V_d \sin\psi_e \\ &+ \tilde{y}_e \left[V_d \sin\psi_e - (x_e + \frac{k_2 \cos\psi_e}{V_d})u_2^* + \frac{k_2 \cos\psi_e \dot{\psi}_d}{V_d} - \frac{k_2 \sin\psi_e \dot{V}_d}{V_d^2} \right]\end{aligned} \tag{6–18}$$

Substituting Eqs. (6–12), (6–13) and (6–15) into Eq. (6–18), $\dot{V}_2$ can be derived as:

$$\begin{aligned}\dot{V}_2 =& -k_1 x_e^2 - k_2(\sin\psi_e)^2 \\ &+ \tilde{y}_e \left[2V_d \sin\psi_e - (x_e + \frac{k_2 \cos\psi_e}{V_d})u_2^* + \frac{k_2 \cos\psi_e \dot{\psi}_d}{V_d} - \frac{k_2 \sin\psi_e \dot{V}_d}{V_d^2} \right]\end{aligned} \tag{6–19}$$

We select u_2^* in Eq. (6–19) as:

$$u_2^* = \frac{k_3 \tilde{y}_e + 2V_d \sin\psi_e + \frac{k_2 \cos\psi_e \dot{\psi}_d}{V_d} - \frac{k_2 \sin\psi_e \dot{V}_d}{V_d^2}}{x_e + \frac{k_2 \cos\psi_e}{V_d}} \tag{6–20}$$

where

$$\tilde{y}_e = y_e + \frac{k_2 \sin\psi_e}{V_d} \tag{6–21}$$

and k_3 is a positive constant gain. Then, $\dot{V}_2$ is obtained as:

$$\dot{V}_2 = -k_1 x_e^2 - k_2 (\sin \psi_e)^2 - k_3 \tilde{y}_e^2 \tag{6–22}$$

Obviously, $\dot{V}_2 \leqslant 0$ for $\forall\ t \in (0, +\infty)$. It can be concluded that for all initial conditions, the control system will converge to the set defined as $\{x_e = 0,\ y_e = 0,\ \tilde{y}_e = 0\}$. As $\tilde{y}_e \to 0$, $y_e \to y_e^d = -k_2 \sin \psi_e / V_d$. Since $k_2 > 0$, $V_d > 0$ and $|\psi_e| < \pi$, the yaw angle error ψ_e also converges to 0 when the lateral position error $y_e \to 0$. The control objective of $p_e \to 0$ as $t \to \infty$ is thus achieved. The proposed control laws are given as:

$$\begin{aligned} u_1^* &= V_d \cos \psi_e + k_1 x_e \\ u_2^* &= \frac{k_3 \tilde{y}_e + 2 V_d \sin \psi_e + \frac{k_2 \cos \psi_e \dot{\psi}_d}{V_d} - \frac{k_2 \sin \psi_e \dot{V}_d}{V_d^2}}{x_e + \frac{k_2 \cos \psi_e}{V_d}} \end{aligned} \tag{6–23}$$

As the actual input of the car-like system is $\boldsymbol{u}$ instead of $\boldsymbol{u^*}$, the above control laws should be transferred to u as:

$$\begin{aligned} u_1 =& u_1^* = V_d \cos \psi_e + k_1 x_e \\ u_2 =& \arctan \left(\frac{l}{u_1^*} u_2^* \right) \\ =& \arctan \left(\frac{l(k_3 \tilde{y}_e + 2 V_d \sin \psi_e + \frac{k_2 \cos \psi_e \dot{\psi}_d}{V_d} - \frac{k_2 \sin \psi_e \dot{V}_d}{V_d^2})}{u_1 (x_e + \frac{k_2 \cos \psi_e}{V_d})} \right) \end{aligned} \tag{6–24}$$

where $\tilde{y}_e$ is given in Eq. (6–21).

6.3.2 Adaptive Gains and Input Constraints

The proposed control laws in Eq. (6–24) are functions of control gains and posture errors: $\boldsymbol{u} = f(\boldsymbol{K}, \boldsymbol{p_e})$, where $\boldsymbol{K} = [k_1, k_2, k_3]'$ and $\boldsymbol{p_e} = [x_e, y_e, \psi_e]'$. Given a set of constant gains $\boldsymbol{K}$, the commanded inputs based on Eq. (6–24) may be outside the physically allowed range of the inputs given by Eq. (6–7), especially for the scenarios where there are large initial errors. Due

to implementation limits of the actuators, such too large inputs will lead to large tracking errors or even instability of the system. Moreover, it is always expected to drive the vehicle close to the reference trajectory as soon as possible when the vehicle is far away from the reference trajectory. Taking into account these effects, adaptive control gains are designed together with consideration of input constraints in this section.

From the equation of u_1 in Eq. (6–24), the following result can be obtained:

$$|u_1| \leqslant V_d + k_1|x_e| \tag{6–25}$$

Define d_x as the threshold distance of $|x_e|$ and $d_x > 0$. If $|x_e| \leqslant d_x$, then:

$$|u_1| \leqslant V_d + k_1 d_x \tag{6–26}$$

In order to ensure $|u_1| \leqslant u_1^m$, then $V_d + k_1 d_x$ should be no larger than u_1^m. If we select k_1 at position where $|x_e| = d_x$ as:

$$k_1|_{|x_e|=d_x} = \frac{u_1^m - V_d}{d_x} \tag{6–27}$$

$|u_1|$ will then be ensured no larger than u_1^m for $|x_e| \leqslant d_x$. When $|x_e| > d_x$ showing the vehicle is far away from the reference trajectory, and the vehicle is expected to drive at the maximum speed to move close to the trajectory quickly. Based on this, k_1 is designed to vary as a reciprocal function of $|x_e|$ when $|x_e| > d_x$, such that:

$$k_1(|x_e|) = \frac{\Delta}{|x_e|},\ |x_e| > d_x \tag{6–28}$$

where Δ is obtained based on the condition that the commanded speed is u_1^m at position where $|x_e| = d_x$, thus:

$$\Delta = u_1^m - V_d \tag{6–29}$$

The reciprocal function increases quickly with decrease of $|x_e|$. For $|x_e| \leqslant d_x$, only if the value

of k_1 is under the curve of reciprocal function, the commanded u_1 is less than u_1^m. Generally, a larger k_1 corresponds to a faster response rate given a set of $|x_e|$ and V_d. However, too large k_1 will lead to excessive accelerations or even speed oscillations of the vehicle. Based on this, k_1 is set to be adaptive to $|x_e|$ following a quadratic function as follows:

$$k_1(|x_e|) = -a_1|x_e|^2 + a_2,\ |x_e| \leqslant d_x \tag{6–30}$$

where a_1 and a_2 are two constant coefficients. It is assumed that the completed curve of k_1 is continuous up to first-order derivative at position $|x_e| = d_x$, thus:

$$\begin{aligned} -a_1 d_x^2 + a_2 &= \frac{\Delta}{d_x} \\ -2a_1 d_x &= -\frac{\Delta}{d_x^2} \end{aligned} \tag{6–31}$$

By manipulating the above equations, a_1 and a_2 are obtained as $\Delta/(2d_x^3)$ and $3\Delta/(2d_x)$, respectively. The designed control gain k_1, as a piecewise function of $|x_e|$, is thus described as:

$$k_1(|x_e|) = \begin{cases} -\dfrac{\Delta}{2d_x^3}|x_e|^2 + \dfrac{3\Delta}{2d_x}, |x_e| \leqslant d_x \\ \dfrac{\Delta}{|x_e|}, |x_e| > d_x \end{cases} \tag{6–32}$$

where Δ is given as Eq. (6–29). As required by the system stability, k_1 should always be positive. However, k_1 may become zero when V_d is equal to u_1^m as seen in Eq. (6–32). In order to avoid this from occurrence, the function of $\tanh()$ is introduced to Δ as:

$$\Delta = u_1^m - V_d \tanh(\frac{V_d}{\sigma}) \tag{6–33}$$

where $\sigma > 0$ is a tuning parameter. The designed control gain k_1, as a piecewise function of $|x_e|$,

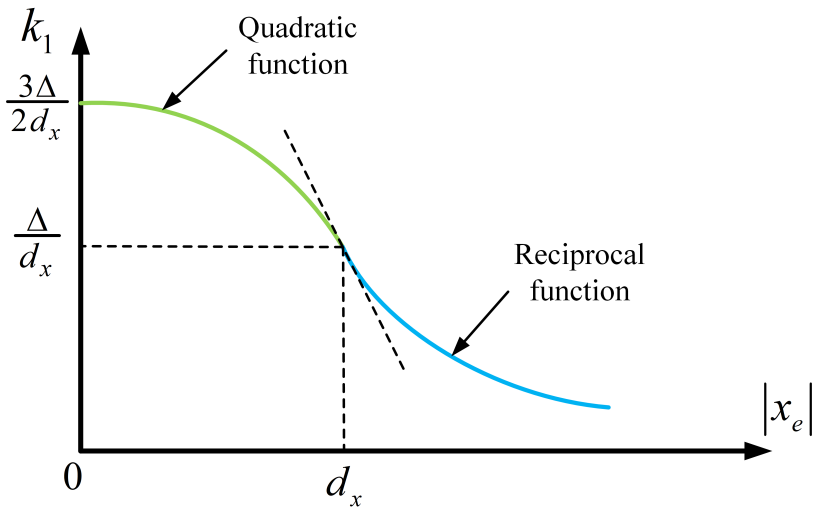

Figure 6.3: Variation of k_1 as a function of $|x_e|$.

is finally described as:

$$k_1(|x_e|) = \begin{cases} -\dfrac{u_1^m - V_d \tanh(\frac{V_d}{\sigma})}{2d_x^3}|x_e|^2 + \dfrac{3(u_1^m - V_d \tanh(\frac{V_d}{\sigma}))}{2d_x}, |x_e| \leqslant d_x \\ \dfrac{u_1^m - V_d \tanh(\frac{V_d}{\sigma})}{|x_e|}, |x_e| > d_x \end{cases} \tag{6–34}$$

The schematic of k_1 as a function of $|x_e|$ is plotted in Figure 6.3. As seen in the figure, k_1 gently decreases as the increase of $|x_e|$ for achieving compromised performance with combined consideration of both the response rate and the input constraints.

Looking at the equation of u_2 in Eq. (6–24), it has complex expression and is related to all the three errors x_e, y_e and ψ_e. It is hard to design adaptive k_2 and k_3 in a straight way similar to k_1 with integrated consideration of the input constraint of u_2. A compromised method is proposed here. Recall that we expect y_e to vary along y_e^d, as shown in Eq. (6–12), k_2 can be selected as a function of V_d to compensate the influence of the forward speed on tracking results (especially for enhancing the convergence rate of lateral position error). For simplicity, k_2 is set as proportional to V_d:

$$k_2 = \alpha V_d \tag{6–35}$$

where $\alpha > 0$ is a constant tuning parameter. Then, $\dot{k}_2 = \alpha \dot{V}_d$ and y_e^d becomes $-\alpha \sin \psi_e$, regardless

of the desired speed. By doing so, the convergence rate of lateral position error is obviously improved. Following the procedure from (6–10)-(6–24), the new input vector $u^c = [u_1^c, u_2^c]'$ is obtained as:

$$\begin{aligned} u_1^c =& V_d \cos\psi_e + k_1(|x_e|)x_e \\ u_2^c =& \arctan\left(\frac{l\left[k_3(y_e + \alpha\sin\psi_e) + 2V_d\sin\psi_e + \alpha\cos\psi_e\dot{\psi}_d\right]}{u_1^c(x_e + \alpha\cos\psi_e)}\right) \end{aligned} \tag{6–36}$$

It is worth noting that both $\dot{k}_2$ and $\dot{V}_d$ disappeared because of algebraic simplification by selecting k_2 according to (6–35). Since $u_1^c \leqslant u_1^m$ is always satisfied, the actual input of vehicle speed is thus set as:

$$u_1 = u_1^c \tag{6–37}$$

Due to the complex form of u_2^c, adjusting k_3 alone cannot guarantee the steering angle not violating the constraint. In order to simplify the problem, after setting constant gain k_3, we use the following steering control law:

$$u_2 = \begin{cases} u_2^c, if\ |u_2^c| < u_2^m \\ u_2^m, if\ u_2^c \geqslant u_2^m \\ -u_2^m, if\ u_2^c \leqslant -u_2^m \end{cases} \tag{6–38}$$

to achieve acceptable trajectory tracking results for car-like vehicles.

Theorem 6.1 *For low-speed car-like vehicles, using the control laws given by Eqs. (6–37) and (6–38) will result in an approximate globally asymptotically stable equilibrium at $\boldsymbol{p_e} = 0$ for $V_d > 0$ and $|\psi_e| < \pi$.*

Proof 6.1 *The speed control law (6–37) and the steering control law (6–38) can make system globally asymptotically stable at $\boldsymbol{p_e} = 0$ when $|u_2^c| < u_2^m$, as evident in Section 6.3.1.*

In order to analyze the system stability for $|u_2^c| \geqslant u_2^m$, we consider a Lyapunov function candidate as:

$$V_3 = \frac{1}{2}(x_e^2 + y_e^2) + u_1^m(1 - \cos\psi_e) \tag{6–39}$$

where $u_1^m > 0$ is the maximum forward speed of the vehicle. Clearly, $V_3 \geqslant 0$. If $\boldsymbol{p_e} = 0$, $V_3 = 0$. If $\boldsymbol{p_e} \neq 0$, $V_3 > 0$. The time derivative of V_3 along the error dynamics (6–6) with the control laws (6–37) and (6–38) is:

$$\begin{aligned} \dot{V}_3 &= -k_1(|x_e|)x_e^2 + y_e V_d \sin\psi_e + (\frac{V_d}{l}\tan\delta_d - \frac{u_1^c}{l}\tan u_2)\sin\psi_e u_1^m \\ &= -k_1(|x_e|)x_e^2 + y_e V_d \sin\psi_e + (\dot{\psi}_d \mp \dot{\psi}_m)\sin\psi_e u_1^m \end{aligned} \tag{6–40}$$

where $\dot{\psi}_m = (u_1^c \tan u_2^m)/l > 0$ is the maximum yaw rate at current speed. The first term $-k_1(|x_e|)x_e^2 \leqslant 0$. Note that $u_2^c \geqslant u_2^m$ when $\psi_e > 0$; $u_2^c \leqslant -u_2^m$ when $\psi_e < 0$, and $|\psi_e| < \pi$, the third term $(\dot{\psi}_d \mp \dot{\psi}_m)\sin\psi_e u_1^m$ is thus always non-positive. Under the saturated steering input $u_2 = \pm u_2^m$, $|\sin\psi_e|$ decreases, $|y_e V_d \sin\psi_e|$ can be bounded. It should also be emphasized that the posture errors y_e and ψ_e will dramatically decrease during the period when $|u_2^c| < u_2^m$. Although $\dot{V}_3$ has the possibility to become positive, the corresponding magnitude and duration are both very small, imposing little influence on the convergence of the tracking errors to zero. The proposed adaptive control scheme results in a closed-loop system with an approximate globally asymptotically stable equilibrium at $\boldsymbol{p_e} = 0$. Once the initial errors of x_e, y_e and ψ_e are appropriately selected, $\dot{V}_3$ can still be ensured non-positive all the time, which makes the tracking system globally asymptotically stable even under the influence of steering saturation. Both the simulation and experimental results in the following sections will prove this.

Remark 6.1 *The designed adaptive k_1 in Eq. (6–34), which increases with decrease of $|x_e|$, also positively contributes to make $\dot{V}_3$ negative.*

Remark 6.2 *When steering saturation is considered under $|u_2^c| \geqslant u_2^m$, the globally asymptotically stable region is quite large under the control laws given by Eqs. (6–37) and (6–38), although the accurate determination may be difficult.*

Table 6.1: The initial conditions for circular trajectory.

$\boldsymbol{p_d}(0)$	$\boldsymbol{p_c}(0)$	$\boldsymbol{p_e}(0)$
$[0.998, -1.470, 0.2]'$	$[-0.128, 0, 0]'$	$[1.126, -1.47, 0.2]'$

6.4 Simulation Results

In order to demonstrate the effectiveness and superiority of the proposed control scheme, a numerical simulation study was firstly conducted in the MATLAB/Simulink. The car-like vehicle was required to track a circular trajectory which is governed by the following equations:

$$\begin{aligned} X_d(t) &= 1.5\sin(0.4t + 0.2) + 0.7 \\ Y_d(t) &= 1.5(1 - \cos(0.4t + 0.2)) - 1.5 \end{aligned} \tag{6–41}$$

From (6–41), the reference vehicle speed, yaw angle and yaw rate can be obtained as:

$$\begin{aligned} V_d(t) &= \sqrt{\dot{X}_d^2(t) + \dot{Y}_d^2(t)} \\ \psi_d(t) &= \text{atan2}\{\dot{Y}_d(t), \dot{X}_d(t)\} \\ \dot{\psi}_d(t) &= \frac{\ddot{Y}_d(t)\dot{X}_d(t) - \ddot{X}_d\dot{Y}_d(t)}{V_d^2(t)} \end{aligned} \tag{6–42}$$

The initial conditions for the tracking of the car-like vehicle are listed in Table 6.1. For the sake of comparative study, the performances of a backstepping controller in [155] (marked as Controller 1) and a classic stable tracking controller presented in [158] (marked as Controller 2) were also investigated. The control gains of the Controller 1 and Controller 2 were tuned as $[1.98, 1.98, 1.98]'$ and $[1.65, 1.65, 1.65]'$, respectively, so that acceptable tracking results were obtained. The control parameters of the proposed controller in Eqs. (6–34) and (6–35) were chosen as $d_x = 1$ m, $\sigma = 0.3$, $\alpha = 0.75$, and the fixed gain k_3 in Eq. (6–36) was also selected as 1.65 for the fairness of performance comparisons.

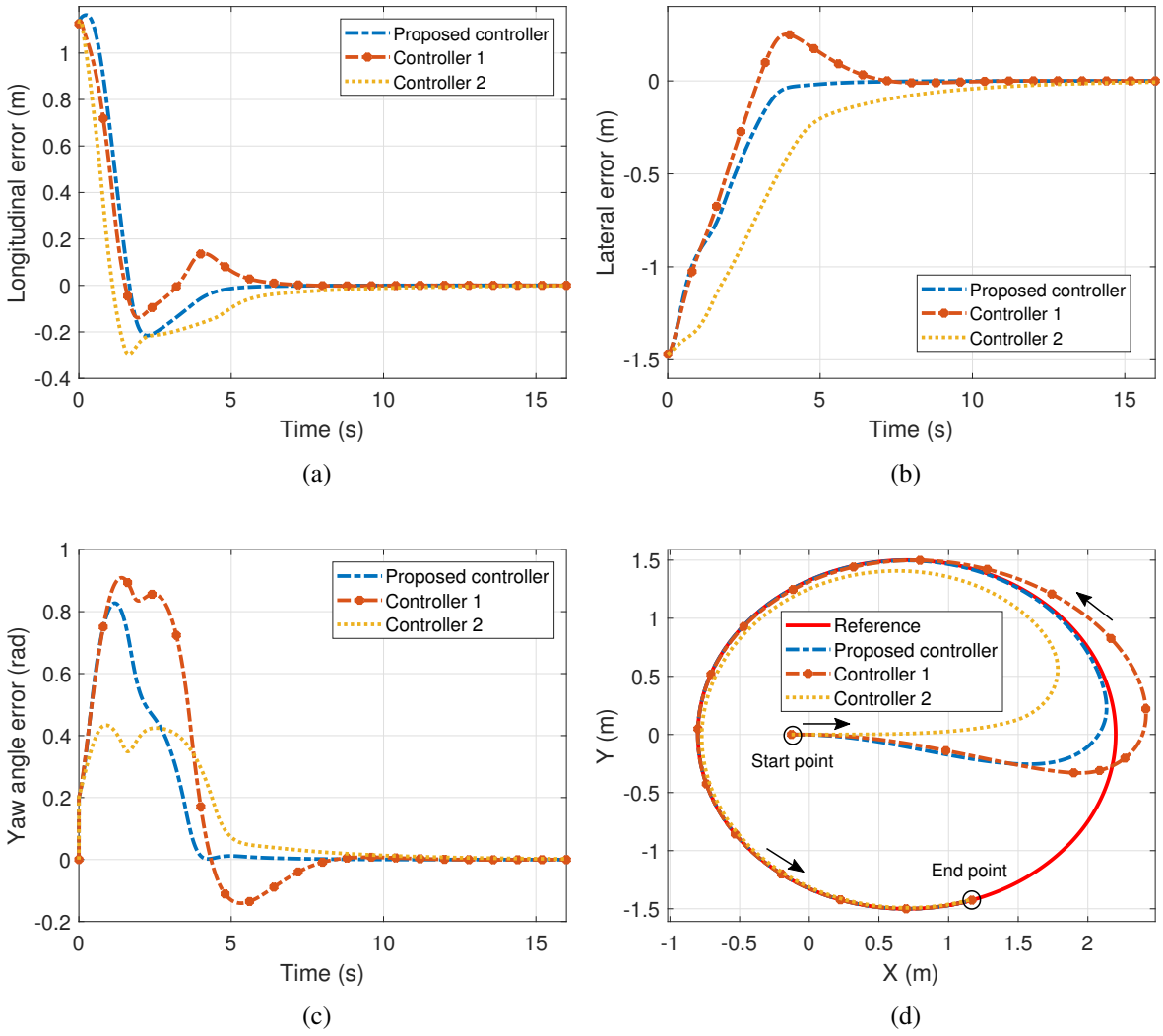

Figure 6.4: Posture tracking results of the circular trajectory. (a) Longitudinal position error. (b) Lateral position error. (c) Yaw angle error. (d) Reference and actual trajectories.

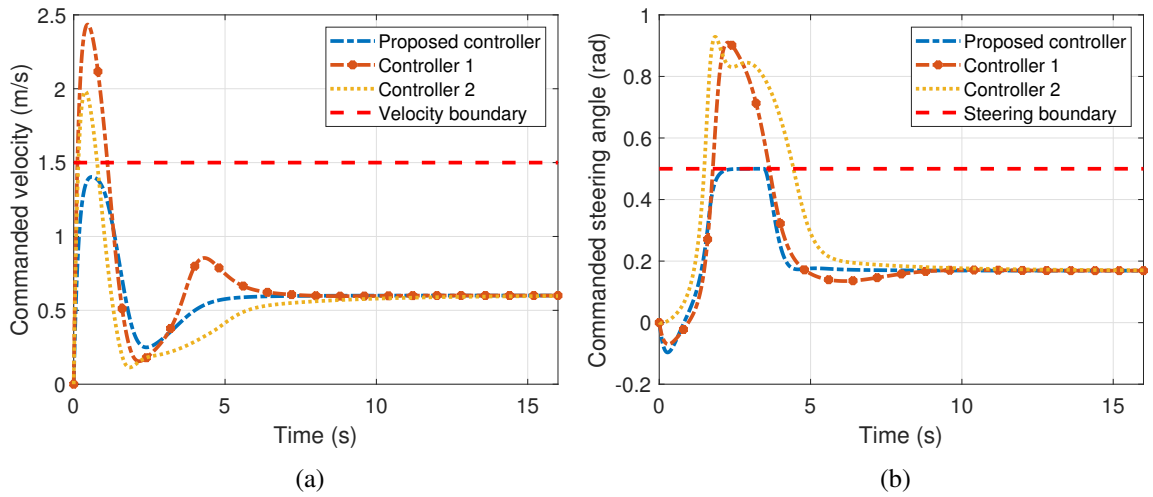

(a) (b)

Figure 6.5: Commanded inputs of the three controllers for tracking the circular trajectory. (a) Velocity input. (b) Steering angle input.

Figure 6.4 presents the tracking results of the circular trajectory. Although all the three controllers can ensure longitudinal position, lateral position and yaw angle tracking errors to finally converge to zero, significant differences in the transient performances are observed. The proposed controller enables all the three tracking errors to vary smoothly and the transient time is less than 5 s. While the Controller 1 has obvious oscillations in all the three tracking errors, the Controller 2 has slow convergence rate in both the lateral position and yaw angle errors. Consequently, the actual trajectories by the three controllers differ considerably, as shown in Figure 6.4(d). It seems that the Controller 1 steers too late leading the car-like vehicle to go outside the circular trajectory, though it then tracks the reference trajectory well in a moderate convergence rate. The Controller 2 steers too early and follows the reference trajectory with a slow rate in decreasing the deviations from the reference trajectory. Noted that it takes more than 12 s for the Controller 2 to converge all the three tracking errors to zero, as evident in Figure 6.4(b).

The commanded inputs of the three controllers are shown in Figure 6.5. Due to large initial errors, both the commanded velocity and steering angle from Controller 1 and Controller 2 have significantly exceeded the input limits. Although the trajectory tracking results of Controller 1 and Controller 2 are acceptable in the simulation, as seen in Figure 6.4(d), applying such overlarge

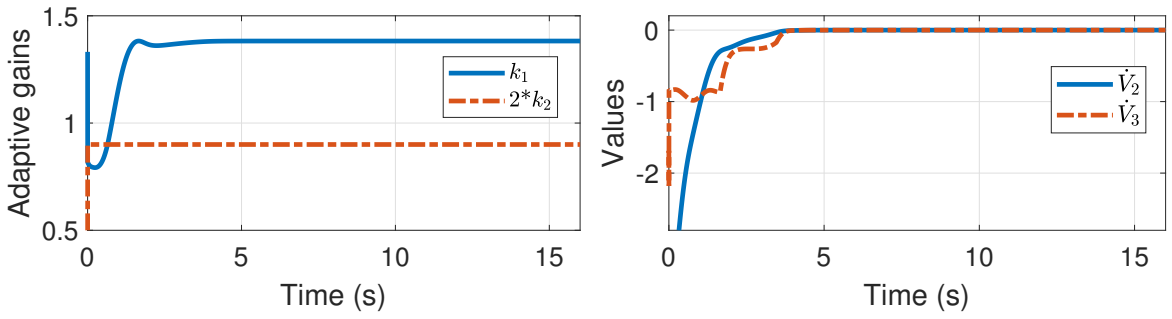

(a) (b)

Figure 6.6: Evolutions of the adaptive gains and the first-order derivative of the Lyapunov functions of the proposed controller for tracking the circular trajectory.

inputs to the real platform may lead to instability of the control system resulting in failures of trajectory tracking. In contrast, the commanded inputs from the proposed controller are ensured within the input boundaries. These are realized by the design of adaptive gains and the consideration of steering saturation. The evolutions of the adaptive gains, k_1 and k_2 are shown in Figure 6.6(a). During the first 1.5 s, k_1 increases with the decrease of the absolute value of the longitudinal position error to drive the vehicle close to the reference trajectory in a short time. After that, k_1 stabilizes around 1.4 since the longitudinal position tracking error has become very small. k_2 keeps a constant value in this case since the desired velocity of a circular trajectory is constant. As can be seen from Figure 6.5(b), the steering angle of the proposed controller is saturated during around 2-3 s. As a result, oscillations can be observed in the evolution of $\dot{V}_3$, as shown in Figure. 6.6(b). However, $\dot{V}_2$ and $\dot{V}_3$ are both non-positive during the whole simulation showing the effectiveness and stability of the proposed control laws given by (6–37) and (6–38), as seen in Figure 6.6(b).

6.5 Experimental Results

To further verify the effectiveness of the proposed control strategy in practice, experimental tests have been conducted on the Quanser self-driving car (QCar) platform. Similar to the simulation study, the trajectory tracking results of the Controller 1 [155] and Controller 2 [158] were also demonstrated for the sake of comparative study. In order to compare conveniently, all the

Table 6.2: The initial conditions for S-shape trajectory under experimental tests.

Scenario	$[a_{11}, a_{12}, a_{21}]$	$\boldsymbol{p_d}(0)$	$\boldsymbol{p_e}(0)$
I	$[0.2, -0.1, -2.4]$	$[0.120, -0.211, 0.137]'$	$[0.248, -0.211, 0.137]'$
II	$[0.7, 0.1, -2.2]$	$[0.780, -0.011, -0.137]'$	$[0.908, -0.011, -0.137]'$

control parameters of the three controllers were set as the same as those in simulation study. The description of the experimental setup is referred to Section 4.6.1. The schematic of the experiment setup is demonstrated in Figure 4.14. The key parameters of the QCar are summarized in Table 4.5. The QCar test videos can be viewed at `https://youtu.be/JTpX6-I-hxo` in our Lab's website.

6.5.1 Initial Conditions

In the experiment, a more complex but more similar to an actual road S-shape trajectory was chosen as the reference trajectory. The equations of this trajectory were considered as follows:

$$\begin{aligned} X_d(t) &= a_{11} + 0.8\sin(0.4t + a_{12}) \\ Y_d(t) &= a_{21} + 2.2\cos(0.2t + a_{12}) \end{aligned} \tag{6–43}$$

where a_{11}, a_{12} and a_{21} are coefficients used to define the initial conditions of the trajectory tracking. Two scenarios corresponding to small (Scenario I) and large (Scenario II) initial errors were considered, and the initial conditions were listed in Table 6.2. From the real-time reference positions $X_d(t)$ and $Y_d(t)$ in Eq. (6–43), the reference vehicle speed, yaw angle and yaw rate were obtained according to Eq. (6–42).

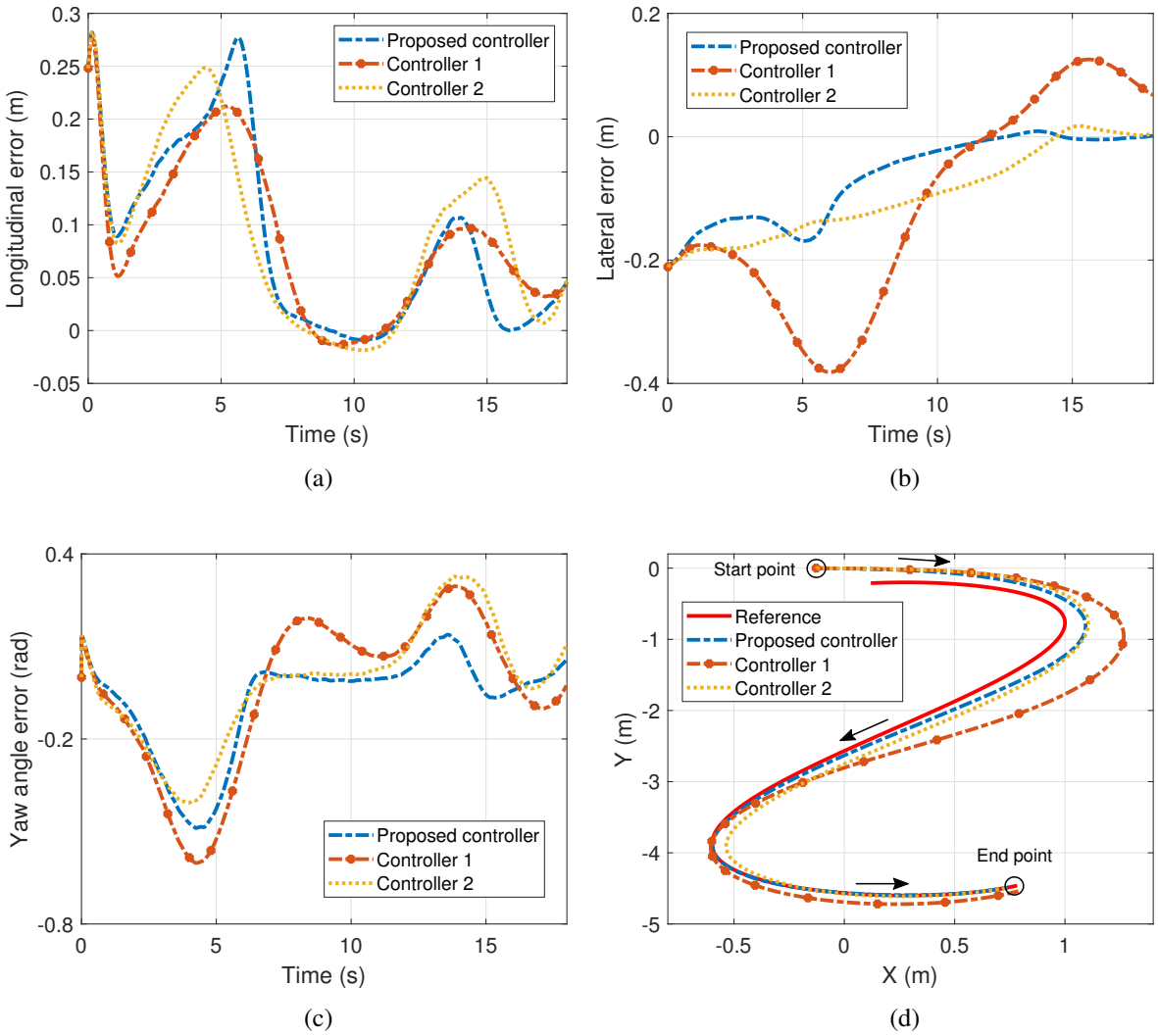

Figure 6.7: Posture tracking results of the S-shape trajectory (Scenario I). (a) Longitudinal position error. (b) Lateral position error. (c) Yaw angle error. (d) Reference and actual trajectories.

6.5.2 QCar Test Results

6.5.2.1 Scenario I

The tracking results of the S-shape trajectory under small initial posture errors are presented in Figure 6.7. The longitudinal position errors of the three controllers are comparable to each other as can be seen in Figure 6.7(a). However, the proposed controller has shown its obvious advantage in eliminating the lateral position error. As seen in Figure 6.7(b), the lateral position error of the proposed controller not only has a much faster convergence rate but also a smaller magnitude of oscillation compared to the other two controllers. While the yaw angle error of the Controller 2 is slightly smaller than that of the proposed controller at the first corner (during 3-5 s), it increases to a much larger value than the proposed controller when the QCar comes to the second corner (during 12-14 s), as seen in Figure 6.7(c). The reference S-shape trajectory and the actual trajectories of the QCar under the three controllers are shown in Figure 6.7(d). The proposed controller tracks the reference trajectory with the highest accuracy during the whole experiment, though a small deviation from the reference trajectory exists at the first corner due to the initial error. Although the Controller 2 has shown comparable accuracy in tracking with the proposed controller during the most time of the experiment, it is the only controller which has evident deviation at the second corner. The Controller 1, however, generates a large deviation from the reference trajectory even from the first corner. Despite the deviation gradually decreases to zero when the QCar enters the second corner, small cutting corner error is observed thereafter.

The commanded inputs of the three controllers are depicted in Figure 6.8. Since small initial posture errors are considered in this scenario, both the velocity and steering angle inputs are within the input boundaries. The saturated steering angle input of the proposed controller in Figure 6.8(b) reflects that the proposed controller makes full use of the steering capability to track the reference trajectory at the first corner. By using the adaptive gains whose evolutions with time are shown in Figure 6.9(a), the commanded steering input of the proposed controller at the second corner is much smaller than that of the Controller 2 (whose commanded steering input is very close to the

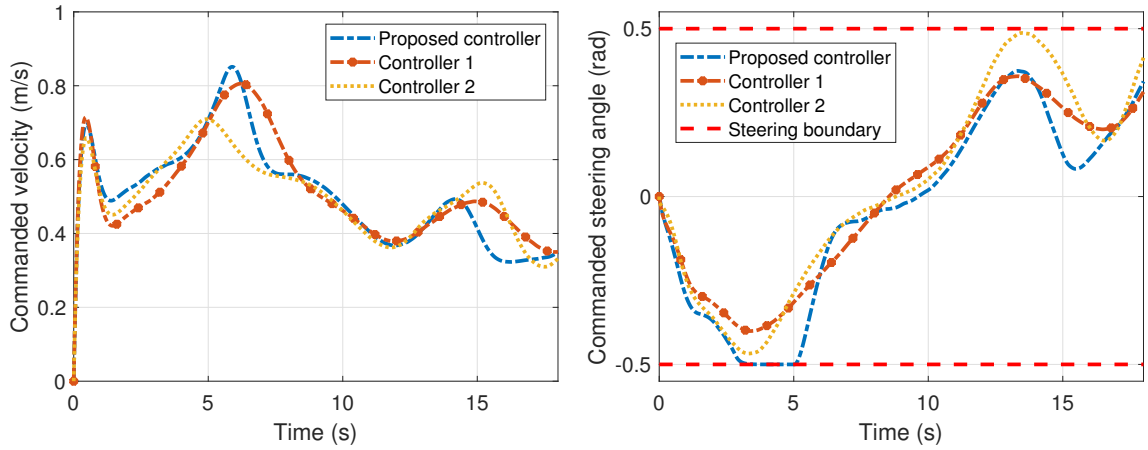

(a) (b)

Figure 6.8: Commanded inputs of the three controllers for tracking the S-shape trajectory (Scenario I). (a) Velocity input. (b) Steering angle input.

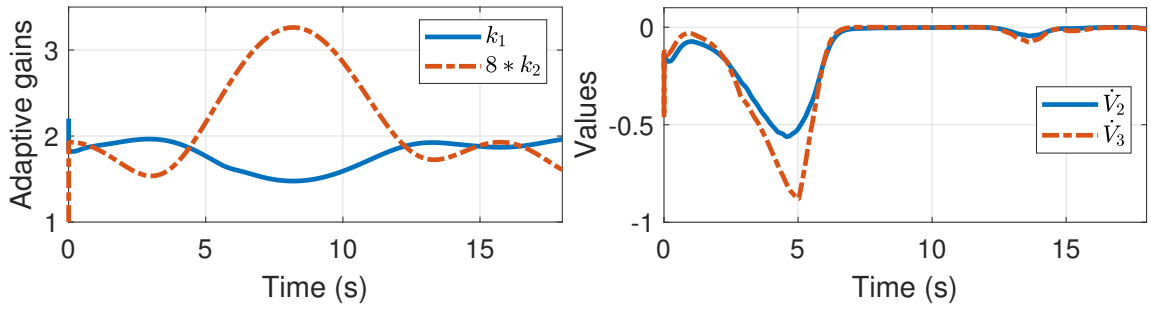

(a) (b)

Figure 6.9: Evolutions of the adaptive gains and the first-order derivative of the Lyapunov functions of the proposed controller for tracking the S-shape trajectory (Scenario I).

steering boundary). The variations of $\dot{V}_2$ and $\dot{V}_3$ with time are demonstrated in Figure 6.9(b). It is clear to see that both $\dot{V}_2$ and $\dot{V}_3$ are indeed ensured non-positive though the commanded steering is saturated at the first corner (during 3-5 s).

6.5.2.2 Scenario II

The tracking results of the S-shape trajectory under large initial posture errors are presented in Figure 6.10. The tracking performance of the Controller 1 is the worst, though the longitudinal position error is close to that of the other two controllers. Compared to Controller 2 and the

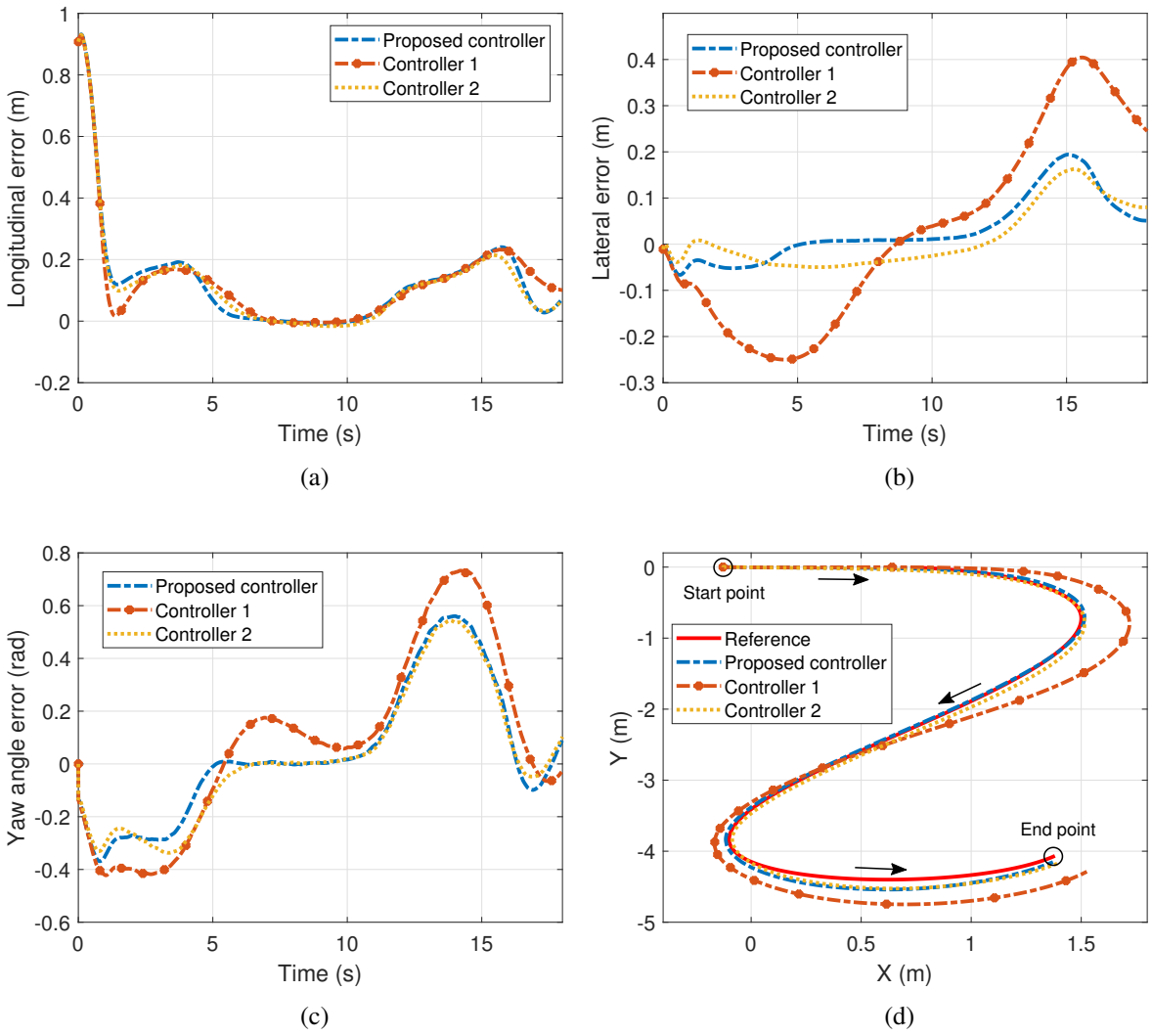

Figure 6.10: Posture tracking results of the S-shape trajectory (Scenario II). (a) Longitudinal position error. (b) Lateral position error. (c) Yaw angle error. (d) Reference and actual trajectories.

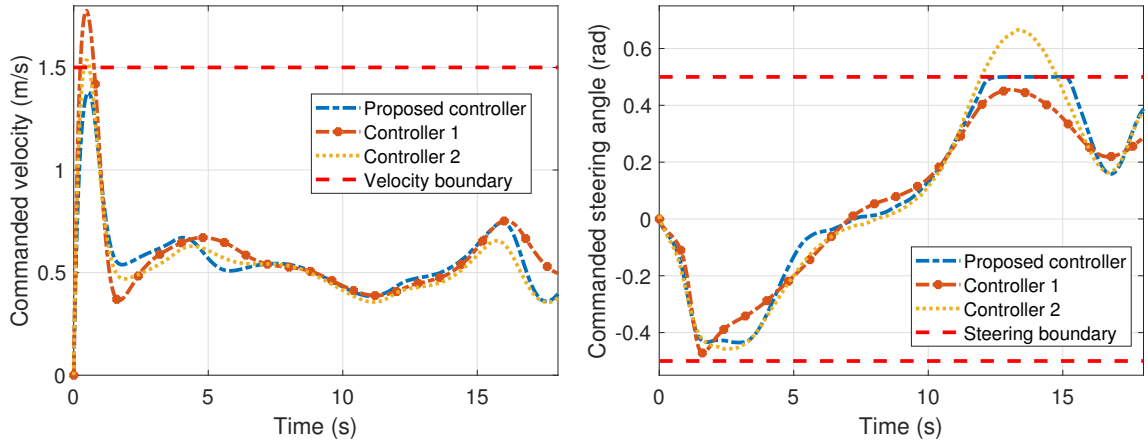

(a) (b)

Figure 6.11: Commanded inputs of the three controllers for tracking the S-shape trajectory (Scenario II). (a) Velocity input. (b) Steering angle input.

proposed controller, the Controller 1 leads to much larger magnitudes of the lateral position and yaw angle errors. By contrast, the Controller 2 and the proposed controller have comparable tracking performances in longitudinal and lateral position and yaw angle. The resulting trajectories of the QCar are plotted in Figure 6.10(d). As seen from the figure, the proposed controller achieves a slightly higher accuracy over the Controller 2 in tracking the reference trajectory, especially when the QCar is located between the first and the second corner (during 5-14 s). However, the Controller 1 seems to steer the QCar too late and contributes to a large deviation from the reference trajectory at the first corner. After that the Controller 1 gradually drives the QCar close to the reference trajectory, however, a large cutting-corner error is observed after the second corner.

While the actual trajectories of the proposed controller and the Controller 2 are close to each other, the big difference lies in the commanded inputs as seen in Figure 6.11. Due to large initial posture errors considered in this scenario, the commanded velocity of the Controller 1 at about 1 s and the commanded steering angle of the Controller 2 during the second corner (during 12-14 s) have exceeded their respective input boundary, 1.5 m/s and 0.5 rad to be specific. These overlarge inputs may exert harmful effects on the motor and sometimes even cause instability of the QCar. In contrast, the commanded velocity and steering angle of the proposed controller are

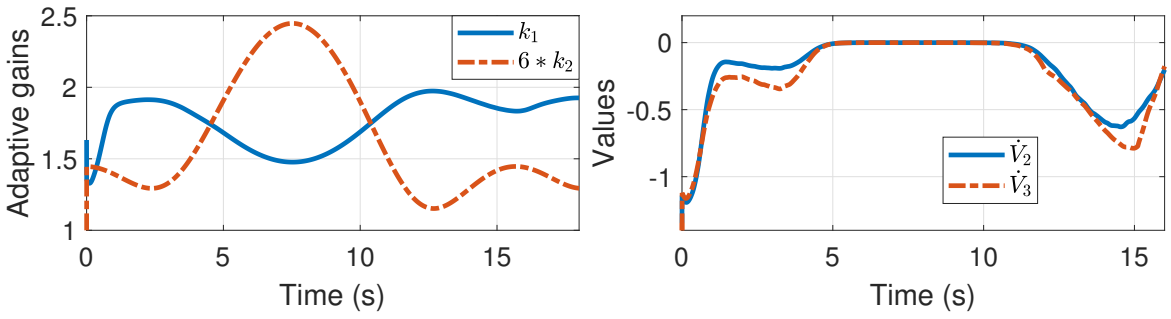

(a) (b)

Figure 6.12: Evolutions of the adaptive gains and the first-order derivative of the Lyapunov functions of the proposed controller for tracking the S-shape trajectory (Scenario II).

both guaranteed within the input boundaries. At a slight sacrifice of the steering saturation of the proposed controller, a small cutting-corner error exists after the second corner, as can be seen from Figure 6.10(d). Anyway, the tracking result of the proposed controller are still comparable to that of the Controller 2. The variations of the designed adaptive gains k_1 and k_2 are presented in Figure 6.12(a). Even under the influence of the steering saturation at the second corner, the first-order derivatives of the Lyapunov functions, $\dot{V}_2$ and $\dot{V}_3$ are again guaranteed non-positive, as evident in Figure 6.12(b).

6.6 Summary

In this chapter, the problem of trajectory tracking control of low-speed AVs under input constraints is investigated. Based on kinematic model, the design of adaptive control gains and consideration of steering saturation are combined within the backstepping technique in an interesting way to construct an adaptive trajectory tracking control scheme addressing the input constraints. The design of adaptive control gains not only reduces the demanded tuning efforts, which are generally neglected by the conventional methods, but also enhances the convergence rate of tracking errors (especially for lateral position error). While under the influence of steering saturation, the globally asymptotically stable region of the proposed control scheme is quite large, although the accurate

determination may be difficult. Comparative simulations and experimental tests have been carried out to demonstrate the advantages of the proposed control scheme in tracking accuracy while meeting the requirements by the implementation capability of the actuators.

Chapter 7

Hightlights, Conclusions and Suggestions for Further Studies

7.1 Major Contributions and Highlights

This thesis research contributed towards the design and development of trajectory planning and tracking strategies integrating with the estimated TRFC so as to enhance the safety and reliability of the AVs under varying road friction conditions. Unlike the reported GNC architectures for AVs, which have mostly ignored the road friction, this study integrates the estimated TRFC information in the planning and/or tracking stages for future AVs on roads. The consideration of the estimated road friction during the planning stage is vital for AVs since the vehicle motion is directly influenced by the forces and moments developed at the tire-road interface. The major contributions and highlights of this thesis are summarized below:

- A hierarchical TRFC estimation framework is developed making full use of both the EKF and the UKF techniques to effectively reduce the computational demand, while ensuring the estimation accuracy. A CUKF framework is further designed so as to achieve rapid convergence and improved accuracy of the TRFC estimation considering longitudinal dynamics of the vehicle.

- The TRFC estimation framework is developed on the basis of the measurements available from the conventional on-board sensors to facilitate its practical applicability. The lateral velocity constitutes the only exception, which is easily estimated within the proposed estimation framework.

- Inputs in terms of short duration braking pressure pulses are defined for generating sufficient longitudinal excitations for TRFC estimation, while ensuring only small disturbance in the vehicle motion.

- The robustness and estimation accuracy of the TRFC framework are illustrated considering a wide range of vehicle speeds, road friction coefficients, lane-change maneuvers.

- A new computationally efficient trajectory planning scheme is designed for AVs where the lane change trajectory planning problem is reduced to the selection of an appropriate lane change duration. The main features of the proposed trajectory planning scheme can be easily customized according to the vehicle occupant's preferences.

- TRFC-adaptive acceleration and speed-adaptive jerk limits are designed for intelligent driving, while ensuring occupant's comfort. These are integrated in the trajectory planning scheme considering a wide range of road friction conditions and forward speeds.

- A new MPC scheme is designed by integrating the output weights in the cost function together with the constraints on the magnitude of the outputs defined by the TRFC. The proposed MPC scheme requires only lateral position input for tracking the desired path.

- The adaptive weights of the outputs in the cost function are identified to ensure effectiveness of the proposed MPC scheme over a wide range of speeds. The adaptive trajectory tracking control scheme thus enhances its operational range.

- The command inputs of the low-speed AVs are ensured within the defined boundaries by integrating adaptive control gains with consideration of steering saturation using the backstepping technique. The proposed scheme resulted in rapid convergence of the tracking error,

especially for the lateral deviation from the reference trajectory.

- An experiment is designed to verify the effectiveness of the proposed adaptive trajectory tracking control scheme using the scaled model QCar test platform. The experimental results demonstrated the efficacy of the proposed control scheme under low-speed operations.

7.2 Major Conclusions

The major conclusions drawn from various aspects of this thesis research are summarized below:

- The proposed hierarchical TRFC estimation framework using both the EKF and the UKF techniques could provide accurate estimations of TRFC on the basis of lateral dynamic responses of the vehicle to stimuli attributed to typical single and double lane-change maneuvers.

- The accuracy of the TRFC estimation framework strongly relies on the magnitudes of the vehicle responses to maneuver-induced excitations. Relatively larger lateral tire excitation encountered under a DLC input resulted in accurate estimations, although it would cause greater disturbance to vehicle motion and occupants' discomfort. The SLC input is thus considered meritorious to limit the disturbance to vehicle motion, while ensuring equally accurate estimations of TRFC, especially when the friction coefficient is below 0.8.

- The friction estimation error of the braking pressure pulse-based method is affected by the magnitude of the braking pressure. Too small a magnitude of the braking pressure generates insufficient slip ratio, which can lead to underestimation of the TRFC.

- Once the magnitude of the braking pressure is appropriately selected, the errors in the slip ratio and the TRFC revealed very low sensitivity to variations in the vehicle speed. The proposed short duration braking pressure pulse-based method can provide effective estimations

of TRFC under a wide range of initial vehicle speeds with substantially smaller disturbances to the vehicle motion.

- The trajectory planning on the basis of the proposed 7th-order polynomial curve can ensure a smooth trajectory corresponding to a SLC maneuver with adequate, while satisfying target occupant's comfort.

- Integration of the friction-adaptive acceleration and speed-adaptive jerk limits into the planning scheme can help achieve the trajectory similar to that tracked by an experienced human driver. The traceability of the planned trajectory was verified considering the tracking error attained with the driver-model module.

- It is shown that a DLC trajectory of a skillfull driver can be simply simulated by taking into account both the TRFC and the vehicle speed. By manipulating the output weights in the cost function of the MPC, the DLC trajectory can be effectively tracked with knowledge of only the lateral position.

- The magnitude of the tracking error of the MPC scheme strongly relies on the speed. Increasing the output weight of the yaw rate with the forward speed can lead to improved tracking performance. Moreover, the maximum forward speed should be bounded to ensure stability of the MPC.

- Design of a trajectory tracking controller with vehicle speed- and position error-adaptive control gains can not only facilitate the tuning of the controller but also yield enhanced tracking performance.

- When steering saturation is considered, the globally asymptotically stable region is quite large under the proposed control law for low-speed car-like vehicles. However, the accurate determination of such region may be difficult.

- The experimental results based on the scaled model QCar platform suggest that the tracking performance of the kinematic controller is acceptable when the AVs are driving under

relatively low speeds.

- Long time input saturation should be avoided, which may lead to instability of the QCar in the experimental tests.

7.3 Recommendations for Future Studies

The current thesis research offers attractive potentials for enhancing practical applications of AVs by synthesizing planning and tracking methods with TRFC information while imposing minimal interference with the vehicle motion. Far more efforts, however, are desirable in developing more reliable and robust path planning and path tracking for the AVs. Some of the suggested future directions are briefly described below:

- TRFC estimation methods, invariably, require lateral or longitudinal excitations to the vehicle to detect changes in the dynamic responses. Such excitations, however, cause notable disturbances to the vehicle motion, which are perceived annoying for the occupant. It is thus desirable to seek TRFC estimation methods that permit detection of changes in dynamic states of the vehicle under relatively low side-slip or slip ratio variations.

- The proposed TRFC estimation methods for AVs in this thesis are only validated using CarSim^{TM} platform coupled with MATLAB/Simulink^{TM}. It is recommended that the effectiveness of the TRFC estimators be evaluated through road tests considering different road friction conditions, vehicle speeds and lateral/longitudinal excitations.

- The trajectory planning framework and the MPC-based tracking scheme proposed in this thesis are limited to a specific directional maneuver at a constant speed. The effectiveness of the proposed schemes should be investigated considering widely different maneuvers performed under varying speed. Alternatively, varying-speed trajectory planning and tracking schemes should be explored for more practical applications in AVs.

- The TRFC estimation methods on the basis of longitudinal dynamics have been limited to vehicle operation on a straight-line course with uniform friction. The efficacy of the estimation algorithm needs to be investigated for vehicle operations on curved roads, and road segments with split or varying friction conditions. These would help increase the robustness and effectiveness of the proposed trajectory planning and tracking schemes.

- In the present study, the trajectory planning and tracking control are limited to lane change situations without considering the vehicles in the target lane (adjacent lane). It is important to develop the trajectory planning and tracking framework applicable to coordinated driving considering multiple vehicles around the host vehicle in both the current and the adjacent lanes.

- In view of the practicality of trajectory tracking for low-speed AVs, the constraints on acceleration and steering rate are equally important and they should be considered in the adaptive control scheme.

Bibliography

[1] J. M. Anderson, K. Nidhi, K. D. Stanley, P. Sorensen, C. Samaras, and O. A. Oluwatola, *Autonomous vehicle technology: A guide for policymakers*. Rand Corporation, 2014.

[2] S. A. Bagloee, M. Tavana, M. Asadi, and T. Oliver, "Autonomous vehicles: challenges, opportunities, and future implications for transportation policies," *Journal of Modern Transportation*, vol. 24, no. 4, pp. 284–303, 2016.

[3] R. Hussain and S. Zeadally, "Autonomous cars: research results, issues, and future challenges," *IEEE Communications Surveys & Tutorials*, vol. 21, no. 2, pp. 1275–1313, 2018.

[4] S. A. Cohen and D. Hopkins, "Autonomous vehicles and the future of urban tourism," *Annals of Tourism Research*, vol. 74, pp. 33–42, 2019.

[5] J. DiClemente, S. Mogos, and R. Wang, "Autonomous car policy report," 2014.

[6] R. Shanker, A. Jonas, S. Devitt, K. Huberty, S. Flannery, W. Greene, B. Swinburne, G. Locraft, A. Wood, K. Weiss, *et al.*, "Autonomous cars: Self-driving the new auto industry paradigm," *Morgan Stanley Blue Paper, Morgan Stanley & Co. LLC*, 2013.

[7] Mercedes-Benz, "The Mercedes-Benz F2015 Luxury in Motion," 2020. [Online; accessed 21-June-2020].

[8] Wikipedia contributors, "Guidance, navigation, and control — Wikipedia, the free encyclopedia." `https://en.wikipedia.org/w/index.php?title=Guidance,`

_navigation,_and_control&oldid=961757278, 2020. [Online; accessed 14-July-2020].

[9] P. Zhao, J. Chen, T. Mei, and H. Liang, "Dynamic motion planning for autonomous vehicle in unknown environments," in *2011 IEEE Intelligent Vehicles Symposium (IV)*, pp. 284–289, 2011.

[10] C. Katrakazas, M. Quddus, W.-H. Chen, and L. Deka, "Real-time motion planning methods for autonomous on-road driving: State-of-the-art and future research directions," *Transportation Research Part C: Emerging Technologies*, vol. 60, pp. 416–442, 2015.

[11] S. Dixit, S. Fallah, U. Montanaro, M. Dianati, A. Stevens, F. Mccullough, and A. Mouzakitis, "Trajectory planning and tracking for autonomous overtaking: State-of-the-art and future prospects," *Annual Reviews in Control*, vol. 45, pp. 76–86, 2018.

[12] H. Cheng, *Autonomous Intelligent Vehicles: Theory, Algorithms, and Implementation*. Springer Science & Business Media, 2011.

[13] R. Kala, *On-Road Intelligent Vehicles: Motion Planning for Intelligent Transportation Systems*. Butterworth-Heinemann, 2016.

[14] D. Watzenig and M. Horn, *Automated Driving: Safer and More Efficient Future Driving*. Springer, 2016.

[15] D. González, J. Pérez, V. Milanés, and F. Nashashibi, "A review of motion planning techniques for automated vehicles," *IEEE Transactions on Intelligent Transportation Systems*, vol. 17, no. 4, pp. 1135–1145, 2015.

[16] J. Wang, L. Alexander, and R. Rajamani, "Friction estimation on highway vehicles using longitudinal measurements," *Journal of Dynamic Systems, Measurement, and Control*, vol. 126, no. 2, pp. 265–275, 2004.

[17] C. Ahn, H. Peng, and H.-E. Tseng, "Robust estimation of road frictional coefficient," *IEEE Transactions on Control Systems Technology*, vol. 21, no. 1, pp. 1–13, 2013.

[18] K. B. Singh and S. Taheri, "Estimation of tire-road friction coefficient and its application in chassis control systems," *Systems Science & Control Engineering*, vol. 3, no. 1, pp. 39–61, 2015.

[19] X. Zhang and D. Göhlich, "A hierarchical estimator development for estimation of tire-road friction coefficient," *PLoS ONE*, vol. 12, no. 2, p. e0171085, 2017.

[20] K. Han, E. Lee, M. Choi, and S. B. Choi, "Adaptive scheme for the real-time estimation of tire-road friction coefficient and vehicle velocity," *IEEE/ASME Transactions on Mechatronics*, vol. 22, no. 4, pp. 1508–1518, 2017.

[21] J. Zhao, J. Zhang, and B. Zhu, "Development and verification of the tire/road friction estimation algorithm for antilock braking system," *Mathematical Problems in Engineering*, vol. 2014, 2014.

[22] J. Villagra, B. D'Andréa-Novel, M. Fliess, and H. Mounier, "A diagnosis-based approach for tire-road forces and maximum friction estimation," *Control Engineering Practice*, vol. 19, no. 2, pp. 174–184, 2011.

[23] H. Ren, S. Chen, T. Shim, and Z. Wu, "Effective assessment of tyre-road friction coefficient using a hybrid estimator," *Vehicle System Dynamics*, vol. 52, no. 8, pp. 1047–1065, 2014.

[24] R. Wang and J. Wang, "Tire-road friction coefficient and tire cornering stiffness estimation based on longitudinal tire force difference generation," *Control Engineering Practice*, vol. 21, no. 1, pp. 65–75, 2013.

[25] M. Yamada, K. Ueda, I. Horiba, and N. Sugie, "Discrimination of the road condition toward understanding of vehicle driving environments," *IEEE Transactions on Intelligent Transportation Systems*, vol. 2, no. 1, pp. 26–31, 2001.

[26] A. Niskanen and A. Tuononen, "Three three-axis IEPE accelerometers on the inner liner of a tire for finding the tire-road friction potential indicators," *Sensors*, vol. 15, no. 8, pp. 19251–19263, 2015.

[27] D. Dogan and P. Boyraz, "Smart traction control systems for electric vehicles using acoustic road-type estimation," *IEEE Transactions on Intelligent Vehicles*, vol. 4, no. 3, pp. 486–496, 2019.

[28] C. Ahn, H. Peng, and H. E. Tseng, "Robust estimation of road friction coefficient using lateral and longitudinal vehicle dynamics," *Vehicle System Dynamics*, vol. 50, no. 6, pp. 961–985, 2012.

[29] R. Rajamani, G. Phanomchoeng, D. Piyabongkarn, and J. Y. Lew, "Algorithms for real-time estimation of individual wheel tire-road friction coefficients," *IEEE/ASME Transactions on Mechatronics*, vol. 17, no. 6, pp. 1183–1195, 2012.

[30] B. Li, H. Du, and W. Li, "Comparative study of vehicle tyre-road friction coefficient estimation with a novel cost-effective method," *Vehicle System Dynamics*, vol. 52, no. 8, pp. 1066–1098, 2014.

[31] C. Lee, K. Hedrick, and K. Yi, "Real-time slip-based estimation of maximum tire-road friction coefficient," *IEEE/ASME Transactions on Mechatronics*, vol. 9, no. 2, pp. 454–458, 2004.

[32] G. Erdogan, L. Alexander, and R. Rajamani, "Estimation of tire-road friction coefficient using a novel wireless piezoelectric tire sensor," *IEEE Sensors Journal*, vol. 11, no. 2, pp. 267–279, 2011.

[33] C.-S. Kim, J.-O. Hahn, K.-S. Hong, and W.-S. Yoo, "Estimation of tire-road friction based on onboard 6-DoF acceleration measurement," *IEEE Transactions on Vehicular Technology*, vol. 64, no. 8, pp. 3368–3377, 2015.

[34] A. K. Madhusudhanan, M. Corno, M. A. Arat, and E. Holweg, "Load sensing bearing based road-tyre friction estimation considering combined tyre slip," *Mechatronics*, vol. 39, pp. 136–146, 2016.

[35] J. Zhao, J. Zhang, and B. Zhu, "Coordinative traction control of vehicles based on identification of the tyre-road friction coefficient," *Proceedings of the Institution of Mechanical Engineers, Part D: Journal of Automobile Engineering*, vol. 230, no. 12, pp. 1585–1604, 2016.

[36] T. Kim, J. Lee, and K. Yi, "Enhanced maximum tire-road friction coefficient estimation based advanced emergency braking algorithm," in *2015 IEEE Intelligent Vehicles Symposium (IV)*, pp. 883–888, 2015.

[37] C. Hu, R. Wang, Z. Wang, M. Chadli, and F. Yan, "Integrated optimal dynamics control of 4WS4WD electric ground vehicles with tire-road frictional coefficient estimation," in *2015 American Control Conference (ACC)*, pp. 5426–5431, 2015.

[38] L. Shao, C. Jin, C. Lex, and A. Eichberger, "Robust road friction estimation during vehicle steering," *Vehicle System Dynamics*, vol. 57, no. 4, pp. 493–519, 2019.

[39] C.-F. Zong, P. Song, and D. Hu, "Estimation of vehicle states and tire-road friction using parallel extended Kalman filtering," *Journal of Zhejiang University-SCIENCE A*, vol. 12, no. 6, pp. 446–452, 2011.

[40] K. Enisz, I. Szalay, G. Kohlrusz, and D. Fodor, "Tyre-road friction coefficient estimation based on the discrete-time extended Kalman filter," *Proceedings of the Institution of Mechanical Engineers, Part D: Journal of Automobile Engineering*, vol. 229, no. 9, pp. 1158–1168, 2015.

[41] M. Choi, J. J. Oh, and S. B. Choi, "Linearized recursive least squares methods for real-time identification of tire-road friction coefficient," *IEEE Transactions on Vehicular Technology*, vol. 62, no. 7, pp. 2906–2918, 2013.

[42] Z. Qi, S. Taheri, B. Wang, and H. Yu, "Estimation of the tyre-road maximum friction coefficient and slip slope based on a novel tyre model," *Vehicle System Dynamics*, vol. 53, no. 4, pp. 506–525, 2015.

[43] L. Chen, M. Bian, Y. Luo, and K. Li, "Estimation of road-tire friction with unscented Kalman filter and MSE-weighted fusion based on a modified Dugoff tire model," SAE Technical Paper 2015-01-1601, 2015.

[44] D. Paul, E. Velenis, F. Humbert, D. Cao, T. Dobo, and S. Hegarty, "Tyre-road friction μ-estimation based on braking force distribution," *Proceedings of the Institution of Mechanical Engineers, Part D: Journal of Automobile Engineering*, vol. 233, no. 8, pp. 2030–2047, 2019.

[45] W. Chen, D. Tan, and L. Zhao, "Vehicle sideslip angle and road friction estimation using online gradient descent algorithm," *IEEE Transactions on Vehicular Technology*, vol. 67, no. 12, pp. 11475–11485, 2018.

[46] J.-H. Yoon, S. E. Li, and C. Ahn, "Estimation of vehicle sideslip angle and tire-road friction coefficient based on magnetometer with GPS," *International Journal of Automotive Technology*, vol. 17, no. 3, pp. 427–435, 2016.

[47] S. Zhang, W. Deng, Q. Zhao, H. Sun, and B. Litkouhi, "Dynamic trajectory planning for vehicle autonomous driving," in *IEEE International Conference on Systems, Man, and Cybernetics*, pp. 4161–4166, 2013.

[48] S. M. LaValle, "Rapidly-exploring random trees: A new tool for path planning," Technical Report 98-11, Iowa State University, 1998.

[49] Y. Kuwata, J. Teo, G. Fiore, S. Karaman, E. Frazzoli, and J. P. How, "Real-time motion planning with applications to autonomous urban driving," *IEEE Transactions on Control Systems Technology*, vol. 17, no. 5, pp. 1105–1118, 2009.

[50] S. Karaman and E. Frazzoli, "Sampling-based algorithms for optimal motion planning," *The International Journal of Robotics Research*, vol. 30, no. 7, pp. 846–894, 2011.

[51] M. Likhachev and D. Ferguson, "Planning long dynamically feasible maneuvers for autonomous vehicles," *The International Journal of Robotics Research*, vol. 28, no. 8, pp. 933–945, 2009.

[52] T. Gu, J. Snider, J. M. Dolan, and J.-W. Lee, "Focused trajectory planning for autonomous on-road driving," in *2013 IEEE Intelligent Vehicles Symposium (IV)*, pp. 547–552, 2013.

[53] W. Xu, J. Wei, J. M. Dolan, H. Zhao, and H. Zha, "A real-time motion planner with trajectory optimization for autonomous vehicles," in *IEEE International Conference on Robotics and Automation*, pp. 2061–2067, 2012.

[54] I. Papadimitriou and M. Tomizuka, "Fast lane changing computations using polynomials," in *Proceedings of the IEEE American Control Conference*, vol. 1, pp. 48–53, 2003.

[55] W. Nelson, "Continuous-curvature paths for autonomous vehicles," in *Proceedings of the IEEE International Conference on Robotics and Automation*, pp. 1260–1264, 1989.

[56] H. Sazgar, S. Azadi, and R. Kazemi, "Trajectory planning and combined control design for critical high-speed lane change manoeuvres," *Proceedings of the Institution of Mechanical Engineers, Part D: Journal of Automobile Engineering*, vol. 234, no. 2-3, pp. 823–839, 2020.

[57] A. Kelly and B. Nagy, "Reactive nonholonomic trajectory generation via parametric optimal control," *The International Journal of Robotics Research*, vol. 22, no. 7-8, pp. 583–601, 2003.

[58] A. H. M. A. Kahya and K. W. Schmidt, "Clothoid-based lane change trajectory computation for self-driving vehicles," *Çankaya Üniversitesi Bilim ve Mühendislik Dergisi*, vol. 14, no. 2, pp. 152–179, 2017.

[59] L. Ma, J. Yang, and M. Zhang, "A two-level path planning method for on-road autonomous driving," in *Second International Conference on Intelligent System Design and Engineering Application*, pp. 661–664, 2012.

[60] D. Korzeniowski and G. Ślaski, "Method of planning a reference trajectory of a single lane change manoeuver with bezier curve," in *IOP Conference Series: Materials Science and Engineering*, vol. 1, p. 012012, 2016.

[61] L. Guo, P.-S. Ge, M. Yue, and Y.-B. Zhao, "Lane changing trajectory planning and tracking controller design for intelligent vehicle running on curved road," *Mathematical Problems in Engineering*, vol. 2014, 2014.

[62] J. Feng, J. Ruan, and Y. Li, "Study on intelligent vehicle lane change path planning and control simulation," in *IEEE International Conference on Information Acquisition*, pp. 683–688, 2006.

[63] H. Sun, W. Deng, S. Zhang, S. Wang, and Y. Zhang, "Trajectory planning for vehicle autonomous driving with uncertainties," in *Proceedings of the IEEE International Conference on Informative and Cybernetics for Computational Social Systems (ICCSS)*, pp. 34–38, 2014.

[64] C. Götte, M. Keller, T. Nattermann, C. Haß, K.-H. Glander, and T. Bertram, "Spline-based motion planning for automated driving," *IFAC-PapersOnLine*, vol. 50, no. 1, pp. 9114–9119, 2017.

[65] X. Wu, B. Qiao, and C. Su, "Trajectory planning with time-variant safety margin for autonomous vehicle lane change," *Applied Sciences*, vol. 10, no. 5, p. 1626, 2020.

[66] C. Wei, Y. Wang, Y. Asakura, and L. Ma, "A nonlinear programing model for collision-free lane-change trajectory planning based on vehicle-to-vehicle communication," *Journal of Transportation Safety & Security*, vol. 11, pp. 1–21, 2019.

[67] H. Bai, J. Shen, L. Wei, and Z. Feng, "Accelerated lane-changing trajectory planning of automated vehicles with vehicle-to-vehicle collaboration," *Journal of Advanced Transportation*, vol. 2017, 2017.

[68] Y. Luo, Y. Xiang, K. Cao, and K. Li, "A dynamic automated lane change maneuver based on vehicle-to-vehicle communication," *Transportation Research Part C: Emerging Technologies*, vol. 62, pp. 87–102, 2016.

[69] G. Cesari, G. Schildbach, A. Carvalho, and F. Borrelli, "Scenario model predictive control for lane change assistance and autonomous driving on highways," *IEEE Intelligent Transportation Systems Magazine*, vol. 9, no. 3, pp. 23–35, 2017.

[70] J. Nilsson, M. Brännström, E. Coelingh, and J. Fredriksson, "Longitudinal and lateral control for automated lane change maneuvers," in *American Control Conference (ACC)*, pp. 1399–1404, 2015.

[71] X. Li, Z. Sun, Q. Zhu, and D. Liu, "A unified approach to local trajectory planning and control for autonomous driving along a reference path," in *IEEE International Conference on Mechatronics and Automation*, pp. 1716–1721, 2014.

[72] B. Mashadi, P. Ahmadizadeh, M. Majidi, and M. Mahmoodi-Kaleybar, "Integrated robust controller for vehicle path following," *Multibody System Dynamics*, vol. 33, no. 2, pp. 207–228, 2015.

[73] N. H. Amer, H. Zamzuri, K. Hudha, V. R. Aparow, Z. A. Kadir, and A. F. Z. Abidin, "Modelling and trajectory following of an armoured vehicle," in *2016 SICE International Symposium on Control Systems (ISCS)*, pp. 1–6, 2016.

[74] S. Salehpour, Y. Pourasad, and S. H. Taheri, "Vehicle path tracking by integrated chassis control," *Journal of Central South University*, vol. 22, no. 4, pp. 1378–1388, 2015.

[75] C. Hu, H. Jing, R. Wang, F. Yan, and M. Chadli, "Robust H_∞ output-feedback control for path following of autonomous ground vehicles," *Mechanical Systems and Signal Processing*, vol. 70, pp. 414–427, 2016.

[76] M. Elbanhawi, M. Simic, and R. Jazar, "Receding horizon lateral vehicle control for pure pursuit path tracking," *Journal of Vibration and Control*, vol. 24, no. 3, pp. 619–642, 2018.

[77] C.-I. Kim, M.-S. Kim, K.-S. Lee, H.-S. Jang, and T.-S. Park, "Development of a full speed range path-following system for the autonomous vehicle," in *2015 15th International Conference on Control, Automation and Systems (ICCAS)*, pp. 710–715, 2015.

[78] D. G. Wilson and I. Robinett, "Robust adaptive backstepping control for a nonholonomic mobile robot," in *IEEE International Conference on Systems, Man and Cybernetics. e-Systems and e-Man for Cybernetics in Cyberspace (Cat. No. 01CH37236)*, vol. 5, pp. 3241–3245, 2001.

[79] P. Setlur, J. R. Wagner, D. M. Dawson, and D. Braganza, "A trajectory tracking steer-by-wire control system for ground vehicles," *IEEE Transactions on Vehicular Technology*, vol. 55, no. 1, pp. 76–85, 2006.

[80] T. Hiraoka, O. Nishihara, and H. Kumamoto, "Automatic path-tracking controller of a four-wheel steering vehicle," *Vehicle System Dynamics*, vol. 47, no. 10, pp. 1205–1227, 2009.

[81] A. El Hajjaji and S. Bentalba, "Fuzzy path tracking control for automatic steering of vehicles," *Robotics and Autonomous Systems*, vol. 43, no. 4, pp. 203–213, 2003.

[82] D. Gu and H. Hu, "Neural predictive control for a car-like mobile robot," *Robotics and Autonomous Systems*, vol. 39, no. 2, pp. 73–86, 2002.

[83] N. R. Kapania and J. C. Gerdes, "Path tracking of highly dynamic autonomous vehicle trajectories via iterative learning control," in *2015 American Control Conference (ACC)*, pp. 2753–2758, 2015.

[84] F. A. Cheein and G. Scaglia, "Trajectory tracking controller design for unmanned vehicles: A new methodology," *Journal of Field Robotics*, vol. 31, no. 6, pp. 861–887, 2014.

[85] R. Lenain, B. Thuilot, C. Cariou, and P. Martinet, "Mixed kinematic and dynamic sideslip angle observer for accurate control of fast off-road mobile robots," *Journal of Field Robotics*, vol. 27, no. 2, pp. 181–196, 2010.

[86] Y. Gao, T. Lin, F. Borrelli, E. Tseng, and D. Hrovat, "Predictive control of autonomous ground vehicles with obstacle avoidance on slippery roads," in *ASME 2010 Dynamic Systems and Control Conference*, pp. 265–272, 2010.

[87] M. Jalalmaab, M. Pirani, B. Fidan, and S. Jeon, "Cooperative road condition estimation for an adaptive model predictive collision avoidance control strategy," in *2016 IEEE Intelligent Vehicles Symposium (IV)*, pp. 1072–1077, 2016.

[88] E. Bauer, F. Lotz, M. Pfromm, M. Schreier, B. Abendroth, S. Cieler, A. Eckert, A. Hohm, S. Lüke, P. Rieth, *et al.*, "Proreta 3: An integrated approach to collision avoidance and vehicle automation," *at-Automatisierungstechnik Methoden und Anwendungen der Steuerungs-, Regelungs-und Informationstechnik*, vol. 60, no. 12, pp. 755–765, 2012.

[89] J. Ji, A. Khajepour, W. W. Melek, and Y. Huang, "Path planning and tracking for vehicle collision avoidance based on model predictive control with multiconstraints," *IEEE Transactions on Vehicular Technology*, vol. 66, no. 2, pp. 952–964, 2016.

[90] T. Shim, G. Adireddy, and H. Yuan, "Autonomous vehicle collision avoidance system using path planning and model-predictive-control-based active front steering and wheel torque control," *Proceedings of the Institution of Mechanical Engineers, Part D: Journal of Automobile Engineering*, vol. 226, no. 6, pp. 767–778, 2012.

[91] B. Yi, S. Gottschling, J. Ferdinand, N. Simm, F. Bonarens, and C. Stiller, "Real time integrated vehicle dynamics control and trajectory planning with MPC for critical maneuvers," in *2016 IEEE Intelligent Vehicles Symposium*, pp. 584–589, 2016.

[92] M. Jalalmaab, M. Pirani, B. Fidan, and S. Jeon, "Cooperative estimation of road condition based on dynamic consensus and vehicular communication," *IEEE Transactions on Intelligent Vehicles*, vol. 4, no. 1, pp. 90–100, 2018.

[93] H. B. Pacejka and E. Bakker, "The magic formula tyre model," *Vehicle System Dynamics*, vol. 21, no. S1, pp. 1–18, 1992.

[94] J. Y. Wong, *Theory of Ground Vehicles*. John Wiley & Sons, 2008.

[95] ISO Central Secretary, "Passenger cars – test track for a severe lane-change manoeuvre – part 1: Double lane-change," Standard ISO 3888-1:1999, International Organization for Standardization, Geneva, CH, 1999.

[96] D. Simon, *Optimal State Estimation: Kalman, H_∞, and Nonlinear Approaches*. John Wiley & Sons, 2006.

[97] G. Baffet, A. Charara, D. Lechner, and D. Thomas, "Experimental evaluation of observers for tire-road forces, sideslip angle and wheel cornering stiffness," *Vehicle System Dynamics*, vol. 46, no. 6, pp. 501–520, 2008.

[98] H. Hamann, J. K. Hedrick, S. Rhode, and F. Gauterin, "Tire force estimation for a passenger vehicle with the unscented Kalman filter," in *IEEE Intelligent Vehicles Symposium Proceedings*, pp. 814–819, 2014.

[99] E. A. Wan and R. Van Der Merwe, "The unscented Kalman filter for nonlinear estimation," in *Proceedings of the IEEE 2000 Adaptive Systems for Signal Processing, Communications, and Control Symposium (AS-SPCC)*, pp. 153–158, 2000.

[100] L. Chen, M. Bian, Y. Luo, and K. Li, "Real-time identification of the tyre-road friction coefficient using an unscented Kalman filter and mean-square-error-weighted fusion," *Proceedings of the Institution of Mechanical Engineers, Part D: Journal of Automobile Engineering*, vol. 230, no. 6, pp. 788–802, 2016.

[101] H. Pacejka, *Tire and Vehicle Dynamics*. Elsevier, 2005.

[102] M. Jalalmaab, M. Pirani, B. Fidan, and S. Jeon, "Cooperative estimation of road condition based on dynamic consensus and vehicular communication," *IEEE Transactions on Intelligent Vehicles*, vol. 4, no. 1, pp. 90–100, 2019.

[103] R. De Castro, R. E. Araújo, and D. Freitas, "Real-time estimation of tyre-road friction peak with optimal linear parameterisation," *IET Control Theory & Applications*, vol. 6, no. 14, pp. 2257–2268, 2012.

[104] S. Khaleghian, A. Emami, and S. Taheri, "A technical survey on tire-road friction estimation," *Friction*, vol. 5, no. 2, pp. 123–146, 2017.

[105] L. Li, F.-Y. Wang, and Q. Zhou, "Integrated longitudinal and lateral tire/road friction modeling and monitoring for vehicle motion control," *IEEE Transactions on Intelligent Transportation Systems*, vol. 7, no. 1, pp. 1–19, 2006.

[106] F. Gustafsson, "Slip-based tire-road friction estimation," *Automatica*, vol. 33, no. 6, pp. 1087–1099, 1997.

[107] J. A. Cabrera, J. J. Castillo, J. Pérez, J. M. Velasco, A. J. Guerra, and P. Hernández, "A procedure for determining tire-road friction characteristics using a modification of the magic formula based on experimental results," *Sensors*, vol. 18, no. 3, p. 896, 2018.

[108] A. Ortiz, J. Cabrera, A. Guerra, and A. Simon, "An easy procedure to determine magic formula parameters: a comparative study between the starting value optimization technique and the imma optimization algorithm," *Vehicle System Dynamics*, vol. 44, no. 9, pp. 689–718, 2006.

[109] R. Wang and J. Wang, "Fault diagnosis method utilizing actuator redundancy and identicalness with applications to electric vehicles," in *Proceedings of the 2012 ASME Dynamic Systems and Control Conference*, pp. 111–118, 2012.

[110] A. Rezaeian, R. Zarringhalam, S. Fallah, W. W. Melek, A. Khajepour, S.-K. Chen, N. Moshchuck, and B. Litkouhi, "Novel tire force estimation strategy for real-time implementation on vehicle applications.," *IEEE Transactions on Vehicular Technology*, vol. 64, no. 6, pp. 2231–2241, 2015.

[111] S. Haykin, *Kalman Filtering and Neural Networks*. John Wiley & Sons, 2004.

[112] B. Paden, M. Čáp, S. Z. Yong, D. Yershov, and E. Frazzoli, "A survey of motion planning and control techniques for self-driving urban vehicles," *IEEE Transactions on Intelligent Vehicles*, vol. 1, no. 1, pp. 33–55, 2016.

[113] B. Li, T. Acarman, Y. Zhang, L. Zhang, C. Yaman, and Q. Kong, "Tractor-trailer vehicle trajectory planning in narrow environments with a progressively constrained optimal control approach," *IEEE Transactions on Intelligent Vehicles*, vol. 5, no. 3, pp. 414–425, 2020.

[114] F. You, R. Zhang, G. Lie, H. Wang, H. Wen, and J. Xu, "Trajectory planning and tracking control for autonomous lane change maneuver based on the cooperative vehicle infrastructure system," *Expert Systems with Applications*, vol. 42, no. 14, pp. 5932–5946, 2015.

[115] B. Li, Y. Zhang, Y. Feng, Y. Zhang, Y. Ge, and Z. Shao, "Balancing computation speed and quality: A decentralized motion planning method for cooperative lane changes of connected and automated vehicles," *IEEE Transactions on Intelligent Vehicles*, vol. 3, no. 3, pp. 340–350, 2018.

[116] Y. Chen, C. Hu, and J. Wang, "Motion planning with velocity prediction and composite nonlinear feedback tracking control for lane-change strategy of autonomous vehicles," *IEEE Transactions on Intelligent Vehicles*, vol. 5, no. 1, pp. 63–74, 2019.

[117] J. Hu, S. Rakheja, and Y. Zhang, "Real-time estimation of tire–road friction coefficient based on lateral vehicle dynamics," *Proceedings of the Institution of Mechanical Engineers, Part D: Journal of Automobile Engineering*, vol. 234, no. 10-11, pp. 2444–2457, 2020.

[118] J. Hu, Y. Zhang, and S. Rakheja, "Path planning and tracking for autonomous vehicle collision avoidance with consideration of tire-road friction coefficient," in *21st IFAC World Congress*, 2020.

[119] I. Bae, J. Moon, and J. Seo, "Toward a comfortable driving experience for a self-driving shuttle bus," *Electronics*, vol. 8, no. 9, p. 943, 2019.

[120] I. Bae, J. Moon, J. Jhung, H. Suk, T. Kim, H. Park, J. Cha, J. Kim, D. Kim, and S. Kim, "Self-driving like a human driver instead of a robocar: Personalized comfortable driving experience for autonomous vehicles," *arXiv preprint arXiv:2001.03908*, 2020.

[121] G. Geng, Z. Wu, H. Jiang, L. Sun, and C. Duan, "Study on path planning method for imitating the lane-changing operation of excellent drivers," *Applied Sciences*, vol. 8, no. 5, p. 814, 2018.

[122] J. Hu, S. Rakheja, and Y. Zhang, "Tire-road friction coefficient estimation under constant vehicle speed control," *IFAC-PapersOnLine*, vol. 52, no. 8, pp. 136–141, 2019.

[123] J. Hu, S. Rakheja, and Y. Zhang, "Tire-road friction coefficient estimation based on designed braking pressure pulse," *Proceedings of the Institution of Mechanical Engineers, Part D: Journal of Automobile Engineering*, vol. 235, no. 7, pp. 1876–1891, 2021.

[124] C. Pek, P. Zahn, and M. Althoff, "Verifying the safety of lane change maneuvers of self-driving vehicles based on formalized traffic rules," in *2017 IEEE Intelligent Vehicles Symposium (IV)*, pp. 1477–1483, 2017.

[125] D. Martin and D. H. Litwhiler, "An investigation of acceleration and jerk profiles of public transportation vehicles," in *Proceedings of ASEE Annual Conference and Exposition*, pp. AC 2008–1330, 2008.

[126] W. Chee, M. Tomizuka, S. Patwardhan, and W.-B. Zhang, "Experimental study of lane change maneuver for AHS applications," in *Proceedings of the American Control Conference*, vol. 1, pp. 139–143, 1995.

[127] A. S. Kilinç and T. Baybura, "Determination of minimum horizontal curve radius used in the design of transportation structures, depending on the limit value of comfort criterion lateral jerk," in *TS06G-Engineering Surveying, Machine Control and Guidance*, 2012.

[128] P. Bosetti, M. Da Lio, and A. Saroldi, "On the human control of vehicles: an experimental study of acceleration," *European Transport Research Review*, vol. 6, no. 2, pp. 157–170, 2014.

[129] B. D. Graaf and W. Van Weperen, "The retention of blance: An exploratory study into the limits of acceleration the human body can withstand without losing equilibrium," *Human Factors*, vol. 39, no. 1, pp. 111–118, 1997.

[130] J. Xu, K. Yang, Y. Shao, and G. Lu, "An experimental study on lateral acceleration of cars in different environments in sichuan, southwest China," *Discrete Dynamics in Nature and Society*, vol. 2015, 2015.

[131] Z. Y. Wang, C. B. Li, and J. Xu, "Analysis on usage comfort of highway based on lateral acceleration and lateral acceleration change rate," *Applied Mechanics and Materials*, vol. 427, pp. 320–324, 2013.

[132] L. Svensson and J. Eriksson, "Tuning for ride quality in autonomous vehicle: Application to linear quadratic path planning algorithm," Master's Thesis, Uppsala University, 2015.

[133] J. Lygeros and D. N. Godbole, "An interface between continuous and discrete-event controllers for vehicle automation," *IEEE Transactions on Vehicular Technology*, vol. 46, no. 1, pp. 229–241, 1997.

[134] T. Shamir, "Overtaking a slower-moving vehicle by an antonomous vehicle," in *Proceedings of Fourth International ICSC Symposium on Engineering in Intelligent Systems*, 2004.

[135] L. L. Hoberock, "A survey of longitudinal acceleration comfort studies in ground transportation vehicles," Tech. Rep., Council for Advanced Transportation Studies, 1976.

[136] D. Yang, L. Zhu, F. Yang, and Y. Pu, "Modeling and analysis of lateral driver behavior in lane-changing execution," *Transportation Research Record*, no. 2490, pp. 127–137, 2015.

[137] T. Toledo and D. Zohar, "Modeling duration of lane changes," *Transportation Research Record*, no. 1999, pp. 71–78, 2007.

[138] Y. Ding, W. Zhuang, Y. Qian, and H. Zhong, "Trajectory planning for automated lane-change on a curved road for collision avoidance," SAE Technical Paper, 2019.

[139] J. Wang, G. Zhang, R. Wang, S. C. Schnelle, and J. Wang, "A gain-scheduling driver assistance trajectory-following algorithm considering different driver steering characteristics," *IEEE Transactions on Intelligent Transportation Systems*, vol. 18, no. 5, pp. 1097–1108, 2016.

[140] X. Li, Z. Sun, D. Cao, D. Liu, and H. He, "Development of a new integrated local trajectory planning and tracking control framework for autonomous ground vehicles," *Mechanical Systems and Signal Processing*, vol. 87, pp. 118–137, 2017.

[141] R. Rajamani, *Vehicle Dynamics and Control*. Springer Science & Business Media, 2011.

[142] X. Wu, P. Jin, T. Zou, Z. Qi, H. Xiao, and P. Lou, "Backstepping trajectory tracking based on fuzzy sliding mode control for differential mobile robots," *Journal of Intelligent & Robotic Systems*, vol. 96, no. 1, pp. 109–121, 2019.

[143] H. Mirzaeinejad, "Optimization-based nonlinear control laws with increased robustness for trajectory tracking of non-holonomic wheeled mobile robots," *Transportation Research Part C: Emerging Technologies*, vol. 101, pp. 1–17, 2019.

[144] R. Solea and D. Cernega, "Super twisting sliding mode controller applied to a nonholonomic mobile robot," in *19th International Conference on System Theory, Control and Computing (ICSTCC)*, pp. 87–92, 2015.

[145] M. Cibooglu, U. Karapinar, and M. T. Söylemez, "Hybrid controller approach for an autonomous ground vehicle path tracking problem," in *25th Mediterranean Conference on Control and Automation (MED)*, pp. 583–588, 2017.

[146] L. Chen, Y. Chen, X. Yao, Y. Shan, and L. Chen, "An adaptive path tracking controller based on reinforcement learning with urban driving application," in *IEEE Intelligent Vehicles Symposium (IV)*, pp. 2411–2416, 2019.

[147] G. M. Hoffmann, C. J. Tomlin, M. Montemerlo, and S. Thrun, "Autonomous automobile trajectory tracking for off-road driving: Controller design, experimental validation and racing," in *2007 American Control Conference*, pp. 2296–2301, 2007.

[148] N. H. Amer, H. Zamzuri, K. Hudha, and Z. A. Kadir, "Modelling and control strategies in path tracking control for autonomous ground vehicles: A review of state of the art and challenges," *Journal of Intelligent & Robotic Systems*, vol. 86, no. 2, pp. 225–254, 2017.

[149] K. Majd, M. Razeghi-Jahromi, and A. Homaifar, "A stable analytical solution method for car-like robot trajectory tracking and optimization," *IEEE/CAA Journal of Automatica Sinica*, vol. 7, no. 1, pp. 39–47, 2019.

[150] D. Wang, W. Wei, Y. Yeboah, Y. Li, and Y. Gao, "A robust model predictive control strategy for trajectory tracking of omni-directional mobile robots," *Journal of Intelligent & Robotic Systems*, vol. 98, no. 2, pp. 439–453, 2020.

[151] W. Gan, D. Zhu, Z. Hu, X. Shi, L. Yang, and Y. Chen, "Model predictive adaptive constraint tracking control for underwater vehicles," *IEEE Transactions on Industrial Electronics*, vol. 67, no. 9, pp. 7829–7840, 2019.

[152] C. Shen, Y. Shi, and B. Buckham, "Trajectory tracking control of an autonomous underwater vehicle using Lyapunov-based model predictive control," *IEEE Transactions on Industrial Electronics*, vol. 65, no. 7, pp. 5796–5805, 2017.

[153] C. Yang, D. Huang, W. He, and L. Cheng, "Neural control of robot manipulators with trajectory tracking constraints and input saturation," *IEEE Transactions on Neural Networks and Learning Systems*, 2020. (Early Access).

[154] C. Yang, Y. Jiang, Z. Li, W. He, and C.-Y. Su, "Neural control of bimanual robots with guaranteed global stability and motion precision," *IEEE Transactions on Industrial Informatics*, vol. 13, no. 3, pp. 1162–1171, 2016.

[155] H. Fang, R. Fan, B. Thuilot, and P. Martinet, "Trajectory tracking control of farm vehicles in presence of sliding," *Robotics and Autonomous Systems*, vol. 54, no. 10, pp. 828–839, 2006.

[156] G. Bayar, M. Bergerman, A. B. Koku, and E. Ilhan Konukseven, "Localization and control of an autonomous orchard vehicle," *Computers and Electronics in Agriculture*, vol. 115, pp. 118–128, 2015.

[157] X. Wang, G. Zhang, F. Neri, T. Jiang, J. Zhao, M. Gheorghe, F. Ipate, and R. Lefticaru, "Design and implementation of membrane controllers for trajectory tracking of nonholonomic wheeled mobile robots," *Integrated Computer-Aided Engineering*, vol. 23, no. 1, pp. 15–30, 2016.

[158] Y. Kanayama, Y. Kimura, F. Miyazaki, and T. Noguchi, "A stable tracking control method for an autonomous mobile robot," in *IEEE International Conference on Robotics and Automation*, pp. 384–389, 1990.

List of Publications

Journal Papers

(1) **Juqi Hu**, Subhash Rakheja, and Youmin Zhang, "Real-time estimation of tire-road friction coefficient based on lateral vehicle dynamics," *Proceedings of the Institution of Mechanical Engineers, Part D: Journal of Automobile Engineering*, vol. 234, no. 10-11, pp. 2444-2457, 2020. (DOI:10.1177/0954407020929233)

(2) **Juqi Hu**, Subhash Rakheja, and Youmin Zhang, "Tire-road friction coefficient estimation under designed braking pressure pulse," *Proceedings of the Institution of Mechanical Engineers, Part D: Journal of Automobile Engineering*, vol. 235, no. 7, pp. 1876-1891, 2021. (DOI: 10.1177/0954407020983580)

(3) **Juqi Hu**, Youmin Zhang, and Subhash Rakheja, "Adaptive trajectory tracking for car-like vehicles with input constraints," *IEEE Transactions on Industrial Electronics*. (Early Access), Date of Publication: Mar. 30, 2021. (DOI:10.1109/TIE.2021.3068672)

(4) **Juqi Hu**, Youmin Zhang, and Subhash Rakheja, "Adaptive lane change trajectory planning scheme for autonomous vehicles with consideration of road friction and vehicle speed," *IEEE Transactions on Intelligent Vehicles*. (Under revision).

(5) **Juqi Hu**, Youmin Zhang, and Subhash Rakheja, "Road-condition adaptive model predictive control of autonomous vehicles for obstacle avoidance," *IEEE Transactions on Vehicular Technology*. (To be submitted).

Conference Papers

(1) **Juqi Hu**, Subhash Rakheja, and Youmin Zhang, "Tire-road friction coefficient estimation based on longitudinal measurements," in *2017 International Conference on Advanced Mechatronic System (ICAMechS)*, pp. 190-195, Dec. 6-9, 2017, Xiamen, China.

(2) **Juqi Hu**, Subhash Rakheja, and Youmin Zhang, "Tire-road friction coefficient estimation under constant vehicle speed control," *IFAC-PapersOnLine*, vol. 52, no. 8, pp. 136-141, Jul. 3-5, 2019, Gdansk, Poland. (DOI:10.1016/j.ifacol.2019.08.061)

(3) **Juqi Hu**, Youmin Zhang, and Subhash Rakheja, "Path planning and tracking for autonomous vehicle collision avoidance with consideration of tire-road friction coefficient," in *21st IFAC World Congress*, Jul. 13-17, 2020, Berlin, Germany.

(4) **Juqi Hu**, Youmin Zhang, and Subhash Rakheja, "An adaptive trajectory tracking algorithm for car-like vehicles in presence of input constraints," in *17th International Conference on Intelligent Unmanned Systems (ICIUS'21)*, Aug. 25-27, 2021, Ho Chi Minh, Vietnam. (To be submitted).